



**HAL**  
open science

# Vers un modèle numérique fiable du fonctionnement d'une torche de projection plasma à courant continu

Rodion Zhukovskii

► **To cite this version:**

Rodion Zhukovskii. Vers un modèle numérique fiable du fonctionnement d'une torche de projection plasma à courant continu. Mécanique des matériaux [physics.class-ph]. Université de Limoges, 2020. Français. NNT : 2020LIMO0021 . tel-03114779

**HAL Id: tel-03114779**

**<https://theses.hal.science/tel-03114779v1>**

Submitted on 19 Jan 2021

**HAL** is a multi-disciplinary open access archive for the deposit and dissemination of scientific research documents, whether they are published or not. The documents may come from teaching and research institutions in France or abroad, or from public or private research centers.

L'archive ouverte pluridisciplinaire **HAL**, est destinée au dépôt et à la diffusion de documents scientifiques de niveau recherche, publiés ou non, émanant des établissements d'enseignement et de recherche français ou étrangers, des laboratoires publics ou privés.

## Université de Limoges

ED 609 - Sciences et Ingénierie des Matériaux, Mécanique,  
Énergétique (SIMME)

Institut de Recherche sur les Céramiques (IRCER) – UMR CNRS 7315

Thèse pour obtenir le grade de  
Docteur de l'Université de Limoges  
Matériaux Céramiques et Traitements de Surface

Présentée et soutenue par  
**Rodion ZHUKOVSKII**

Le 16 janvier 2020

### **Vers un modèle numérique fiable du fonctionnement d'une torche de projection plasma à courant continu**

Thèse dirigée par **Christophe CHAZELAS, Armelle VARDELLE, Vincent RAT**

#### JURY :

##### Rapporteurs

M. **Javad MOSTAGHIMI**, Directeur de CACT, Professeur, Université de Toronto  
M. **Vandad ROHANI**, Enseignant Chercheur, HDR, PERSEE, MINES ParisTech

##### Examineurs

M. **Pascal ANDRÉ**, Professeur, LPC, Université Clermont-Auvergne  
M. **Erick MEILLOT**, Dr., HDR, Senior Fellow, LPTth, CEA Le Ripault  
M. **Alexander BARTH**, Dr., Leader New Materials Technology, Oerlikon Metco AG  
M. **Christophe CHAZELAS**, Professeur, IRCER, Université de Limoges  
M. **Vincent RAT**, Directeur de recherche, CNRS, IRCER, Université de Limoges  
Mme. **Armelle VARDELLE**, Professeure, IRCER, Université de Limoges

##### Invités

M. **Ron Molz**, Thermal Spray Core Technologies, Oerlikon Metco (US) inc





## Université de Limoges

ED 609 - Sciences et Ingénierie des Matériaux, Mécanique,  
Énergétique (SIMME)

Institute of Research on Ceramics (IRCER) – UMR CNRS 7315

A thesis presented for the degree of

Doctor of philosophy of the University of Limoges

Ceramic Materials and Surface Treatments

Presented by

**Rodion ZHUKOVSKII**

January 16, 2020

### **Towards a reliable numerical model of DC plasma spray torch operation**

Supervisors: **Christophe CHAZELAS, Armelle VARDELLE, Vincent RAT**

JURY :

Referees

Mr. **Javad MOSTAGHIMI**, Director of CACT, Professor, University of Toronto

Mr. **Vandad ROHANI**, Associate Professor, HDR, PERSEE, MINES ParisTech

Examiners

Mr. **Pascal ANDRÉ**, Full Professor, LPC, University of Clermont Auvergne

Mr. **Erick MEILLOT**, Dr., HDR, Senior Fellow, LPTth, CEA Le Ripault

Mr. **Alexander BARTH**, Dr., Leader New Materials Technology, Oerlikon Metco AG

Mr. **Christophe CHAZELAS**, Full Professor, IRCER, University of Limoges

Mr. **Vincent RAT**, Research director, CNRS, IRCER, University of Limoges

Mme. **Armelle VARDELLE**, Full Professor, IRCER, University of Limoges

Invited members

Mr. **Ron Molz**, Thermal Spray Core Technologies, Oerlikon Metco (US) inc





Dedicated to freedom of speech

*Stadtluft macht frei nach Jahr und Tag*  
**Rechtsgrundsatz im Mittelalter**

## Acknowledgments

---

I would like to express my sincerest gratitude to my supervisors Christophe Chazelas, Armelle Vardelle, and Vincent Rat for their immense patience, smooth guidance and extensive support.

I would like to thank the laboratory IRCER for the opportunity to work in an inspiring and friendly environment with hi-end computational resources and discover France and the French society. I am also very grateful to the Région Nouvelle-Aquitaine for providing the financial support for this thesis.

I would like to give special thanks to Alexander Barth and Hartmut Koschnitzke, Oerlikon Metco Wohlen, Switzerland; Ron Molz, Bernd Distler and Jose Colmenares, Oerlikon Metco, Westbury, USA for providing valuable experimental data and tested hardware needed for my model validation. I would like to thank Yvan Fournier, EDF R&D, Chatou, France for help with Code\_Saturne and Frederic Bernaudeau and Nicolas Calvé, IRCER, for their technical help with the computers.

I thank Prof. Javad Mostaghimi and Prof. Vandad Rohani for their time and efforts in reviewing the manuscript. Also I am grateful to Prof. Pascal André, Dr. Erick Meillot and Dr. Alexander Barth for attending the defense and being a part of the jury.

In addition, I would like to thank my friends Allison, Dmitrii, Angel, Alexey, Mikhail, Egor and Nikita for being my great motivation to work harder and push the limits. And, finally, I thank my family for their continuous encouragement.



## Submitted articles and presentations

---

### Articles:

1. Zhukovskii, R., Chazelas, C., Vardelle, A., Rat, V., Distler B., 2020. Effect of boundary conditions on reliability of DC plasma models. Submitted for publication in the J Therm Spray Tech 19/08/2019
2. Zhukovskii, R., Chazelas, C., Vardelle, A., Rat, V., 2020. Control of the Arc Motion in DC Plasma Spray Torch with a Cascaded Anode. Accepted for publication in the J Therm Spray Tech 29, 1-2. <https://doi.org/10.1007/s11666-019-00969-8>

### Conference presentations:

1. Rodion Zhukovskii, Christophe Chazelas, Armelle Vardelle, Vincent Rat. Effect of an external magnetic field on a DC plasma spray torch with a cascaded anode, HTTP 15, Jul 2018, Toulouse, France
2. Rodion Zhukovskii, Christophe Chazelas, Armelle Vardelle, Vincent Rat. Effect of Boundary conditions on the reliability of DC plasma model. ITSC 2018, May 2018, Orlando, United States
3. Rodion Zhukovskii, Christophe Chazelas, Armelle Vardelle, Vincent Rat. Control of the arc motion in DC plasma spray torch with a cascaded anode. ITSC 2019, May 27, 2019, Yokohama, Japan

### Posters

1. Rodion Zhukovskii, C. Chazelas, A. Vardelle, V. Rat. Arc cathode coupling and boundary conditions on predicted plasma flow field in a DC plasma torch. Salome\_CFD User Day, 2019, April 5-6, 2018, EDF Lab Paris-Saclay, France
2. Rodion Zhukovskii, C. Chazelas, A. Vardelle, V. Rat. Control of the Movement of the Arc in a Segmented Anode Torch. CAE 14<sup>ème</sup>, March 18-19, 2019, Bourges, France
3. Rodion Zhukovskii, C. Chazelas, A. Vardelle, V. Rat. Control of the Movement of the Arc in a cascaded-anode plasma torch. Salome\_CFD User Day, 2019, May 7, 2019, EDF Lab Paris-Saclay, France

## Authors' rights

---

This work is distributed under the terms of the license:

« **Attribution-NonCommercial-NoDerivs 3.0 France** »

a copy of which is available at: <http://creativecommons.org/licenses/by-nc-nd/3.0/fr/>



## Table of Contents

---

Acknowledgments .....	7
Submitted articles and presentations.....	8
Authors' rights .....	9
Table of Contents .....	10
Abbreviations, Symbols and Nomenclature .....	13
General introduction .....	17
Chapter I. DC non-transferred arc plasma spray torches: literature review .....	23
I.1. Introduction.....	25
I.2. Components of a conventional arc plasma torch .....	26
I.3. Principle of operation of a non-transferred arc conventional DC plasma torch .....	28
I.4. Electric arc.....	30
I.4.1. Thermodynamic aspect.....	30
I.4.2. Electromagnetic aspect.....	33
I.4.3. Arc electrodes interaction: near cathode and near anode area .....	34
I.4.3.1. Near cathode area.....	34
I.4.3.2. Near anode area .....	36
I.4.4. Energy balance at the electrodes.....	39
I.4.4.1. Cathode.....	39
I.4.4.2. Anode .....	39
I.5. Fluctuations of a DC plasma jet .....	40
I.5.1. General process of interaction of the arc and the cold boundary layer .....	40
I.5.2. Arc instabilities. Steady, take-over and restrike modes .....	41
I.5.3. Pressure-voltage fluctuation correlation.....	44
I.6. Toward more stable plasma torches .....	46
I.6.1. Types of plasma torches .....	47
I.6.2. Swirling gas injection.....	49
I.6.3. External magnetic field .....	50
I.7. Plasma torch operation model and its validation.....	52
I.7.1. Individual assumptions of various existing models of free burning arc and electric arc plasma torches.....	53
I.7.2. Models dealing with control of anode arc attachment rotation.....	59
I.7.2.1. Swirling gas injection.....	59
I.7.2.2. External magnetic field.....	59
I.7.3. Models validation.....	60
I.8. Approach of this study: Selection of the plasma torch and numerical model .....	60

I.8.1. Plasma torch .....	61
I.8.2. Plasma torch operation model .....	61
Chapter II. LTE and 2T models of plasma torch operation .....	63
II.1. Introduction.....	65
II.2. Model assumptions .....	65
II.3. LTE Model governing equations.....	67
II.4. Modification of the enthalpy equations for 2T model.....	70
II.5. Modelling of a cascaded-anode plasma torch with Code_Saturne.....	76
II.5.1. Operating Conditions of the plasma torch.....	76
II.5.2. Numerical features .....	76
II.5.3. Basic features of model.....	78
II.5.3.1. Computational domain of model .....	78
II.5.3.2. Mesh size limitations .....	78
II.5.3.3. Mesh configuration.....	79
II.5.3.4. Boundary conditions.....	82
II.5.3.5. Boundary condition for electric potential: Arc voltage scaling algorithm.....	84
II.5.3.6. Boundary conditions for magnetic vector potential .....	85
II.5.3.7. Initialization.....	90
II.5.3.8. Inclusion of electrodes .....	91
II.5.4. Fluid-electrode coupling .....	91
II.5.4.1. Coupling of solved variables .....	93
II.5.4.2. Heat transfer to electrodes dues to electric current .....	95
II.5.4.3. Mimicking disequilibrium effects at the electrode arc attachment in LTE model .....	97
II.6. Conclusion.....	98
Chapter III. Simulation results.....	101
III.1. Introduction.....	103
III.2. LTE model .....	103
III.2.1. Effect of boundary condition for magnetic vector potential .....	103
III.2.2. Effect of inclusion of electrodes into computational domain .....	106
III.2.3. Case study .....	110
III.3. Swirling gas injection in LTE model.....	116
III.3.1. Modelling of the gas injection.....	116
III.3.2. Results .....	116
III.4. Use of external magnetic field in LTE model.....	122
III.4.1. Predicted flow field .....	122
III.4.2. Results .....	124

III.5. 2T simulation results .....	132
III.5.1. Distribution of electric current density predicted by 2T model .....	132
III.5.2. Computed plasma flow fields .....	134
III.6. Validation of the simulation results .....	141
III.6.1. LTE model predictions for various arc current intensity and gas flow rate .....	142
III.6.2. Validation of the 2T model predictions .....	143
III.7. Conclusion .....	146
General Conclusion and Perspectives .....	147
1. General features of the developed model .....	149
2. LTE model .....	150
3. Arc rotation .....	150
4. 2T model .....	151
5. Perspective of the model .....	152
References .....	153
Annexes .....	167
Annex A. Argon plasma composition .....	168
Annex B. Argon plasma transport properties .....	171
Annex B.1. Electrical conductivity .....	171
Annex B.2. Thermal conductivity .....	172
Annex B.2.1. Electron translational thermal conductivity .....	172
Annex B.2.2. Heavy species translational thermal conductivity .....	172
Annex B.2.3. Reaction thermal conductivity .....	173
Annex B.2.4. Results of thermal conductivity computation .....	175
Annex B.3. Viscosity .....	176
Annex B.4. Collision integrals .....	177
Annex B.5. Basic data for collisions in argon .....	177
Annex B.6. Exchange coefficient .....	178
Annex B.7. Volumetric net radiation energy losses .....	179
List of Illustrations .....	181
List of Tables .....	189

## Abbreviations, Symbols and Nomenclature

---

### List of Abbreviations

2T	Two-temperature approximation
BS	Biot&Savart boundary condition for magnetic vector potential
CFD	Computational fluid dynamics
DC	Direct current
FEM	Finite element method
FVM	Finite volume method
LTE	Local thermodynamic equilibrium
NLPM	Normal Liter Per Minute
PLTE	Partial local thermodynamic equilibrium
PVNF	Null flux and null value boundary condition for magnetic vector potential
SLPM	Standard Liter Per Minute

### Latin Symbols

$\vec{A}$	Magnetic vector potential	V·s/m
$A_G$	Corrected Richardson constant	$A/(m^2 \cdot K^2)$
$A_V$	Voltage fluctuation amplitude factor	unitless
$\vec{B}$	Magnetic field	T
$C$	Courant number	unitless
$C_p$	Specific heat	J/kg
$e$	Electron charge	C
$\vec{E}$	Electric field	V/m
$E_\zeta$	Ionization energy of the particle $Ar^{(\zeta-1)+}$ to $Ar^{\zeta+}$	eV
$\vec{F}_L$	Lorentz force density	$N/m^3$
$G$	Plasma-forming gas flow rate	NLPM
$h$	Enthalpy	J/kg
$h_e$	Electron enthalpy	J/kg

$h_h$	Heavy species enthalpy	J/kg
$h_p$	Planck's constant	J·s
$I$	Total electric current intensity	A
$\overline{Id}$	Identity matrix	
$\vec{j}$	Electric current density	A/m <sup>2</sup>
$\vec{j}_e$	Electric current density due to electrons	A/m <sup>2</sup>
$\vec{j}_{ion}$	Electric current density due to ions	A/m <sup>2</sup>
$J_{em}$	Electron emission flux	1/(m <sup>2</sup> ·s)
$J_i$	Plasma ions flux	1/(m <sup>2</sup> ·s)
$J_{ebd}$	Counterdiffusing electrons flux	1/(m <sup>2</sup> ·s)
$k_B$	Boltzmann constant	J/K
$m_e$	Electron mass	kg
$m_h$	Mass of a heavy particle (atom or ion)	kg
$n_h^{\zeta+}$	Number density of the argon particle with charge $\zeta +$	1/m <sup>3</sup>
$n_e$	Electron number density	1/m <sup>3</sup>
$p$	Plasma and gas pressure	Pa
$r$	Radial coordinate	m
$R$	Radius	m
$q$	Energy flux	W/m <sup>2</sup>
$Q_\zeta^{int}$	Internal partitioning function of the argon particle with charge $\zeta +$	unitless
$Q_J$	Joule power density	J/m <sup>3</sup>
$Q_R$	Volumetric net radiation losses	J/m <sup>3</sup>
$S$	Cross section area	m <sup>2</sup>
$S_{VT}$	Voltage fluctuation shape factor	unitless
$t$	Time	s

$T$	Temperature	K
$T_e$	Electron temperature	K
$T_h$	Heavy species temperature	K
$\vec{u}$	Flow velocity	m/s
$U_A$	Anode sheath voltage drop	V
$U_C$	Cathode sheath voltage drop	V
$V$	Arc voltage	V
$\Delta V$	Amplitude of arc voltage fluctuations	
$W$	Tungsten work function	eV
$\Delta W$	Schottky reduction of the work function	eV
$z$	Axial coordinate	m

### Greek Symbols

$\alpha_{inj}$	Gas injection angle	degree
$\Gamma$	Source term	various
$\delta_e$	Continuum contribution to volumetric net radiation losses	unitless
$\epsilon_0$	Vacuum permittivity	F/m
$\zeta$	Ion charge	unitless
$\eta$	Torch efficiency	%
$\theta$	Ratio of electron temperature and heavy species temperature; or azimuthal component	unitless
$\lambda$	Total thermal conductivity	W/(m·K)
$\lambda_e$	Electron thermal conductivity	W/(m·K)
$\lambda_h$	Heavy species thermal conductivity	W/(m·K)
$\lambda_r$	Reactive thermal conductivity	W/(m·K)
$\lambda_R$	Material-specific correction factor of the Richardson constant	unitless
$\mu$	Dynamic viscosity	kg/m/s



$\mu_0$	Magnetic permeability	N/A <sup>2</sup>
$\sigma$	Electrical conductivity	S/m
$\tau$	Viscous stress tensor	N/m <sup>2</sup>
$\varphi$	Electric potential	V
$\Phi_i$	Argon ionization potential	eV
$\psi$	Conserved property in general	
$\omega$	Relaxation coefficient	unitless

### Dimensionless Numbers

Sw	Swirl number
Re	Reynolds number

### Indices

<i>azim</i>	Azimuthal
<i>calc</i>	Calculated
<i>cath</i>	Cathode
<i>e</i>	Electron
<i>eff</i>	Effective
<i>emis</i>	Emission
<i>expl</i>	Explicit
<i>ext</i>	External
<i>h</i>	Heavy species
<i>impl</i>	Implicit
<i>inj</i>	injection
<i>n</i>	Normal
<i>plsm</i>	Plasma
<i>prev</i>	Previous time step
<i>rad</i>	Radiation

# General introduction

---



Coatings are commonly used on industrial parts to allow the surface to fulfill functions distinct from those demanded from the bulk of the material (ASM Handbook, Cotell et al., 1994). These functions include protection of the parts against wear, corrosion and heat flux but also friction reduction, improved thermal and electrical insulation, antibacterial and anti-icing properties.

Plasma spraying is one of the leading coating technologies for applying a thick coating (a few hundred of micrometers up to a few millimeters thick) on a substrate to protect its surface or improve its function. The first plasma spray coating was made by Reinecke in 1939 and the technology is now used in most of the industrial sectors including aeronautics, industrial gas turbines, automotive, materials mining and processing, biomedical and electronics (ASM Handbook, Tucker, 2013).

The success of this technology is explained by its ability to deposit thick coating on large parts with diverse shapes at a high deposition rate (up to a few kilograms per hour) as compared, for example, with electroplating and vapor deposition methods. It is also a very flexible coating process that makes it possible to deposit metal, metal alloy, ceramic and cermet coatings onto a large number of base materials. In addition, plasma spraying can be considered as rather simple to use as it can be operated at the atmospheric pressure and, the core of the spray system consists of a plasma torch and a material feed system that delivers the coating material in the form of a powder or a liquid (suspension or solution). This coating material is injected into a plasma jet formed thanks to an electric arc struck between two metal electrodes in a plasma torch (Figure 1). The particles are then accelerated, heated and finally, impact onto the substrate where the coating is built by the piling of the impinging particles.

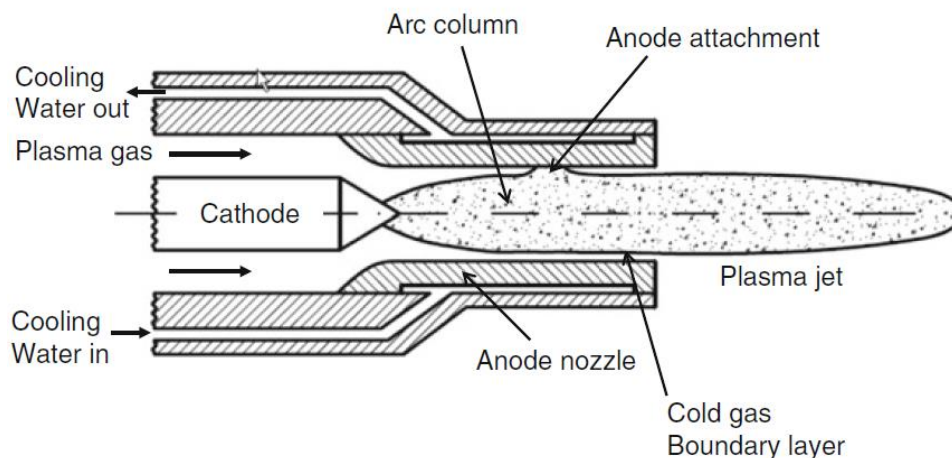


Figure 1: Schematic drawing of a typical conventional plasma spray gun (Fauchais et al., 2014)

A large part of industrial applications uses a plasma torch of simple design, involving a rod-shaped doped-tungsten cathode with a conical tip and a concentric water-cooled copper anode as shown in Fig. 1. High temperatures (12000 - 20000 K), specific enthalpy (up to 30 kJ/g) and velocity (up to about 2500 m/s) characterize the plasma jet issuing from the torch.

Because of these characteristics, plasma spray is the favorite technology to apply thick ceramics coatings. A recent market survey by Transparency Market valued the global high performance ceramic coatings market at US\$ 9,209.2 millions in 2019 and anticipated a raise up to US\$ 12,980.4 millions by 2024. About 50% of these ceramic coatings are applied by plasma spraying (Transparency Market Research, 2018).

The coating market increase combined with global pressures on prices has encouraged the development of plasma torches that meet better the needs of industry: acceleration of production, increase in throughput and consistency in quality of the coating. To fulfill these needs, the main improvements required for a plasma torch involve a more stable plasma jet, reduced electrode erosion, a broad range of specific enthalpy and velocity, high thermal efficiency and deposition rate, possibility of use of different plasma gases including diatomic gases. The new designs of plasma torches are generally based on a multi-electrode concept (Marqués et al., 2009). The commercial ones involve i) the combination of three individual plasma torches whose plasma jets converge in a nozzle where the powder is injected along the line of symmetry of the three plasma torches, ii) a single cathode with an arrangement of three anode segments and iii) a cascaded anode with a single cathode or an arrangement of three cathodes. In the former case, the plasma jets fluctuate independently and so the arc voltage fluctuations has little effect on the axially-injected coating material. In the latter cases, the lengthening of the arcs by inter-electrode inserts yields an increase in gas enthalpy resulting from the increase in arc voltage (typically around 100–120 V as compared with about 70 V for conventional plasma torch) and also a decrease in voltage fluctuation as the movement of the arc(s) is restricted to the anode-ring of the nozzle (Bobzin et al., 2016; Fauchais et al., 2014; Vardelle et al., 2015). As all these plasma torches are generally operated at lower arc current than a conventional torch, they also benefit from a decrease in electrode erosion. Actually (Landes et al., 2002), the anode erosion increases roughly as the square of the arc current.

If the new-design plasma torches correspond better to the requirements of industrial use, their operation still raises some issues: unexplained electrode erosion mode, requirement of a minimum gas flow rate generally higher than conventional plasma torches, rather narrow operating windows for some conditions, etc (Vardelle et al., 2016). A better understanding of the arc behavior inside the plasma torch and the effect of torch geometry and operating parameters on this behavior would help to address these issues.

The experimental measurements are limited to the static and dynamic current-voltage characteristics, torch thermal efficiency and inner pressure, acoustic emission and post-mortem analysis of electrode erosion (Fauchais et al., 2014). Therefore, mathematical modeling is essential for further improvement of plasma torches. However, the model should be first reliable and predictive.

This study takes place in this context. It deals with a cascaded-anode commercial plasma torch (SinplexPro™ from Oerlikon Metco) that is used at the IRCER laboratory to produce coatings for various applications including thermal barrier coatings and multifunctional coatings. It aims to:

- Develop a 3-D, time-dependent electric arc model tolerant to numerical effects in an open-source software (Code\_Saturne). For given torch operating conditions and geometry, the model will predict the arc voltage, electro-magnetic fields, velocity, enthalpy and temperature fields.
- Implement the electrodes inside the computational domain with flexible coupling in order to predict the heat fluxes and temperature distribution inside the electrodes. However, no detailed electrode sheath model will be implemented in this electric arc model.

- Reconsider the existing options for boundary conditions in terms of coupled simulation of fluid phase and electrodes.
- Find the limitations of LTE assumption for simulation of non-transferred arc plasma torch with inter-electrode inserts and suggest a way to mitigate the disadvantages of the assumption.
- Estimate and compare the ways to control the arc motion inside the plasma torch.
- And finally, examine the feasibility to implement a dynamic 2T electric arc plasma torch simulation coupled with electrodes in an open-source software, investigate its pitfalls and problems.

This report summarizes the work done to meet these objectives; it is organized in three chapters.

Chapter 1 is an introduction to DC non-transferred plasma torches used in plasma spray. Based on the published literature, it first describes the main components of the torch and its operation modes. It, then, explains the most common solutions to improve the stability of the plasma jet and/or decrease electrode erosion and briefly describes the numerical models used to better understand these solutions. Finally, building on these solutions and the models proposed in the literature, it presents the approach followed in this study.

Chapter 2 presents the two numerical models of plasma torch operation used in this work; i.e. LTE and 2T models. It lists the model equations and describes the computational domain, assumptions, boundary conditions and initialization. Then, it focusses on the implementation of the electrodes in the computational domain.

Chapter 3 gathers the main results of the numerical simulations. It begins with an analysis of the effect on the plasma flow fields of i) the boundary conditions imposed to the magnetic vector potential on the predicted magnetic and velocity fields and ii) the inclusion of electrodes into the computation domain. Next, this chapter presents the predictions about the arc dynamics obtained with the LTE model; A series of numerical simulations was designed to investigate the effect of i) the angle of injection of the plasma-forming gas in the arc chamber and ii) an external magnetic field on the rotation of the arc attachment at the anode wall and on the anode temperature evolution. Then it presents i) the predictions obtained with the 2T model and ii) validation of predictions against experimental data provided by the torch manufacturer, mainly arc voltage and plasma torch cooling losses.

Finally, the last chapter reports the main conclusions drawn from this work and discusses the possibilities to improving the model and research work.

The report is completed with a list of references and appendices. The latter mainly deal with the argon plasma composition and non-LTE transport properties of argon that have been used in the model.



# **Chapter I. DC non-transferred arc plasma spray torches: literature review**

---





## I.1. Introduction

DC arc plasma torches have been used in the industry since the 1960s (ASM Handbook, Tucker, 2013; Venkatramani, 2002). Their configurations are adapted to their use. They can be distinguished according to:

- The type of the cathode: hot cathode in refractory material (doped tungsten or graphite) or cold cathode in copper,
- Their mode of operation: transferred arc or blown arc.

In plasma spraying, the plasma torches are equipped with hot cathodes made of doped tungsten and work in blown mode, unlike the plasma torches used in cutting and welding that work in the transferred arc mode. The blown arc mode makes modeling the operation of a plasma spray torch much more complex than that of a transferred arc torch.

Indeed, the arc issuing from the cathode tip connects to the wall of the anode in the form of a plasma channel through the cold boundary layer which develops in parallel to the plasma flow along the anode. Depending on the operating conditions, the anodic arc root, under the combined action of viscous hydrodynamic forces, Joule heating instabilities and Lorentz force, may exhibit an erratic behavior on the wall of the nozzle, which induces, for a given arc current intensity, a variation of the arc voltage and, therefore, of the enthalpy dissipated in the plasma jet. This displacement is, however, necessary for the survival of the anode which, depending on the geometry of the arc root (constricted or diffuse), can be subject to thermal fluxes of the order of  $10^7$ - $10^9$  W/m<sup>2</sup>.

Although these torches have been industrially used for more than 60 years, the dynamics of the electric arc that controls their operation is not yet fully understood and is still a challenging and topical subject (Chazelas et al., 2017). The main issues are:

- The interactions of the arc with the magnetic field induced by the arc current circulation, cold plasma-forming gas flow and electrodes.
- The local thermodynamic equilibrium (LTE) deviations (Freton et al., 2012; Huang et al., 2013; Trelles, 2007) close to the walls and in the plasma fringes.
- The effect of the geometry of the arc chamber and especially that of the volume upstream of the cathode tip on the stability of the arc. This point is the subject of specific but essentially experimental attention yet (Rat and Coudert, 2011, 2010a).

Before describing the two models used in this study (Chapter II) and the main results obtained with both models (Chapter III), this chapter presents the operation of a non-transferred arc mono-cathode, mono-anode plasma torch fed with direct current. This type of hot-cathode plasma torch is the most used in plasma spraying with an electric power ranging between 10 and 100 kW.

The chapter begins with the presentation of the main elements of the torch, the characteristics of the electric arc established within the torch and, its connections with the electrodes. The operation of the torch and main phenomena that may affect it are then presented and analyzed. Finally, the potential contribution of numerical simulations of the plasma torch operation and main features of the "ideal model" for such simulations are discussed. The purpose of this literature review is not an exhaustive survey of the literature dealing with the non-transferred arc plasma torch models but a presentation of the hypotheses of this ideal model for the physical conditions and geometry relevant to plasma spray torches, on the basis of the

advances presented in the literature. The last section of this chapter gives the reasons of the selection of the plasma spray torch used in this study, and presents the models that will be used to investigate its operation.

## 1.2. Components of a conventional arc plasma torch

The electric arc generators used in thermal spraying correspond to resistive-type discharges, bursting between a thermo-emissive conical cathode and a concentric anode which also acts as a nozzle. Electric arc is a source of intense heat production, which is transported to the electrodes by electric current, thermal conduction and radiation. Therefore the electrodes cooling is vital for long-term plasma torch operation. Usually the thermal load to electrodes is withdrawn by cold water circulating around the external surfaces of the electrodes. The cooling water system also allows to estimate the fraction of energy input to the torch that is lost in the cooling water and so estimate the torch thermal efficiency.

The essential parts of the plasma torch are the electrodes: cathode and anode. A conventional plasma torch is shown in Figure 1. In plasma spray torches the cathode is the source of electrons which are necessary to maintain the electric current intensity, while the anode mostly collect the electrons and also acts as a nozzle. The electric arc attaches to the cathode tip where the plasma jet originates. The anode is usually in copper. The whole internal cylindrical surface is available for interaction with the arc and the inner wall is generally protected from arc erosion and copper pitting by a tungsten liner. The exit diameter of the nozzle ranges between 6 and 10 mm in diameter. It has a significant effect on the characteristics of the plasma jet issuing from the torch: a decrease in nozzle diameter leads to an increase in plasma jet velocity and usually in maximum plasma temperature for a given gas mass flow rate because of a higher heat loss to the anode and a higher electric field, which may result in higher plasma heating (Fauchais et al., 2014).

The cathode and anode liner of commercial plasma spray torches are usually made of tungsten which has a melting temperature around 3695 K. However, during the torch operation the maximum temperature of the electrode material at the arc attachment spot may exceed the tungsten melting point because of the high heat load to electrodes. This is favored by a constricted arc attachment and high electric current density.

The electric current at the cathode tip is composed of the electrons emitted from the cathode surface and the plasma ions coming to the cathode surface. The electrons carry away thermal energy from the cathode surface and thus cool it, while the ions are deposited on the surface with their kinetic energy and heat it. The electron flux from the cathode depends on the surface temperature according to the Richardson-Dushman emission law supplemented with Schottky correction (Nottingham, 1956):

$$j_{em} = A_G T_{cathode}^2 \exp\left(-\frac{W - \Delta W}{k_B T_{cathode}}\right) \quad (1.1)$$

$$\text{Where } A_G = \lambda_R \frac{4\pi k_B^2 e M_e}{h_p^3} \quad (1.2)$$

Where  $W$  is the cathode material work function (4.2-4.5 eV for tungsten),  $\Delta W$  the Schottky reduction of the work function,  $h_p$  the Planck's constant,  $\lambda_R$  the material-specific correction factor which is around 0.5 (Crowell, 1965; Kiziroglou et al., 2008; Shannon and Nieuwesteeg,

1993). The material-specific correction factor is conditioned by the reflection of emitted electrons back to the cathode surface (Reimann, 1934). With these data the factor before the exponent  $A_G = 6 \cdot 10^5 \text{ A} \cdot \text{m}^{-2} \cdot \text{K}^{-2}$ , which corresponds to the empirical value for pure tungsten given in (Fomenko, 1981; Neumann, 1987; Reimann, 1934; Wright, 1953).

The dependence of the electron flux emitted from the cathode surface on the temperature (1.1) requires to heat the cathode tip up to high temperatures. That is why the tungsten is doped in order to reduce the material work function  $W$ , and, thus decrease the maximum temperature of the cathode tip needed for the torch operation. The common dopants are rare earth metal oxides such as Thorium dioxide or Lanthanum (III) oxide with work function between 2.6 and 2.7 eV (Neumann, 1987; Paschen, 1996). The second dopant is now generally used in the plasma spray torches as thorium is a radioactive material that emits alpha radiation. The dopants have lower melting temperature than tungsten and, thus, melt faster and diffuse towards the cathode surface. On the cathode surface due to very high temperature the dopants evaporate and end up in plasma jet. Therefore eventually after the dopants depletion the cathode's work function significantly increases leading to further temperature increase (Harris, 2002; Nemchinsky, 2014).

The cathode erosion can also be intensified by further constriction of the arc attachment due to pointed conical shape of the cathode tip or high thermal conductivity of plasma gas, as for hydrogen or nitrogen. Additional damage to the cathode can be caused by too high current intensity. Examples of erosion of conic tip cathode can be seen on Figure 2.



Figure 2: Examples of conic tip cathodes erosion in F4 plasma torch (by courtesy of IRCER, University of Limoges)

The anode surface is also subjected to significant heat load brought by the electrons collected by the anode from the arc and by the thermal energy of plasma interacting with the anode surface. The anode erosion is enhanced by constricted anode arc attachment with high electric current density. Spots of high electric current density and therefore erosion can appear due to electron overheating instability which is conditioned by disturbances in plasma heating-cooling balance (Baksht et al., 1997; Yang and Heberlein, 2007a). The anode arc attachment is further constricted by gas flow parallel to the anode surface which constricts the anode arc attachment (Yang et al., 2006). Several hours after the plasma torch operation starts, the arc forms preferred attachment spots and tracks, which intensify the anode erosion even further leading

to formation of spikes and splashes on the anode surface, as illustrated in Figure 3. The cooling of the anode has a significant role in the anode temperature, arc attachment shape and erosion (Neumann, 1976).

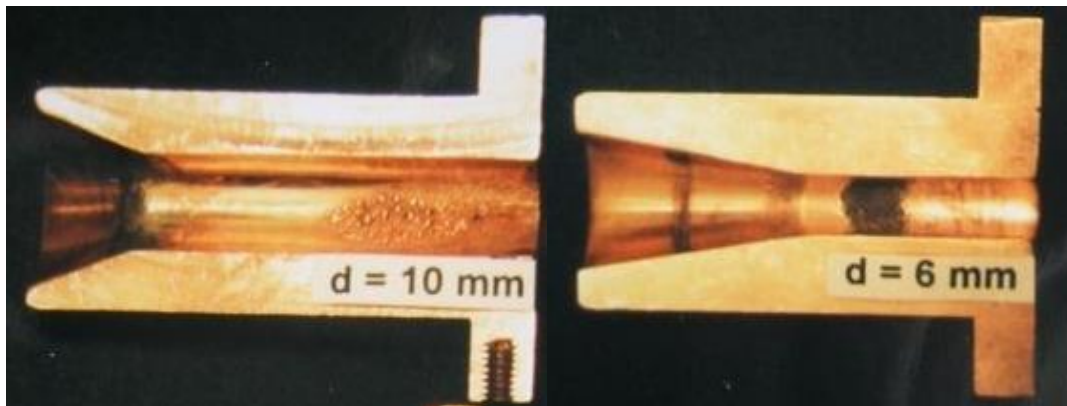


Figure 3: Examples of anode erosion with 600 A, 45 NLPM of argon plus 15 NLPM of H<sub>2</sub> (Planche, 1995)

The constriction of the anode arc attachment and increase in electric current density can also be conditioned by an increase in the thickness of the cold gas boundary layer that develops in parallel to the anode wall. Thicker cold boundary layer result from increased nozzle diameter, lower current intensity or higher thermal conductivity of the plasma-forming gas. That may result in a counterintuitive situation: higher arc current results in a decrease of the cold boundary layer thickness and change in the arc operation mode that may decrease the electric current density at the anode arc attachment and so decrease anode erosion (Fauchais et al., 2014). Generally, anode erosion comes along with lower mean arc voltage and increased voltage fluctuations. (Leblanc and Moreau, 2002) showed that for a conventional plasma torch, the arc voltage, torch power and plasma net energy decreased significantly on a 50-hour time scale.

The erosion of anode erosion can also happen when the arc is started since the high-frequency starter exerts a very high voltage (in the order of 10,000V) on the electrodes. For this reason the starting current intensity is low in order to keep the anode erosion as low (< 1A) as possible. Multiple arc starts result in multiple erosion traces on the anode surface (Fauchais et al., 2014).

### 1.3. Principle of operation of a non-transferred arc conventional DC plasma torch

A conventional DC arc plasma torch employs electrical energy supplied by a current generator to produce the plasma flow. The electric arc is maintained between the cathode tip and nozzle-anode. The arc interacts with the plasma-forming gas and produces heat and kinetic energy through the Joule effect (Mostaghimi et al., 2017). The initiation of the arc is performed using a radiofrequency discharge (a few MHz) at high voltage (5-10 kV). The electric arc is then maintained under low voltage (<100 V) and high current (generally between 100 and 1000A).

In a plasma spray torch, the confinement of the arc is ensured by the water-cooled walls of the anode and the cold gas flow between the arc column and water-cooled walls. The initial acceleration of the plasma flow is produced by the “magnetic constriction and thrust” (the Maecker effect) near the cathode tip (Maecker, 1955). The Joule effect that increases the enthalpy in the confined arc, balanced by the conduction-convection and radiation losses further accelerates the plasma flow in the plasma torch channel. The peripheral cooling, conditioned by the gas flow rate and thermo-physical properties, tends to reduce the radius of

the arc column (i.e.; electrical radius), and increase the electric field inside the column whereas an increase in the intensity of the arc current leads to an increase of this electric radius.

The latter is defined as the radius of the current-conducting channel. For current intensity above 100 A, the arc radius is close to the luminous diameter, especially if the arc is confined in a cooled channel. The luminous diameter can be estimated from photographs taken by a high-speed camera in front of the torch nozzle as done in (Bobzin et al., 2019; Duan and Heberlein, 2002; Wang et al., 2019a). The mean current density can be also roughly estimated from the current-conducting radius of the arc from photographs of the arc. Experimental measurements show that, depending on the gas type, the mean current density in the arc column lies in the range  $10^4$ – $10^7$  A/m<sup>2</sup>, whereas the mean current density near the electrodes may reach  $10^7$ – $10^{12}$  A/m<sup>2</sup> (Zhukov and Zasytkin, 2007). In (Zhukov et al., 1981) another technique of experimental observation of the electric arc was used: a 1 mm glass window shielded by additional gas flow in order to get time sweep of arc element luminosity by the high-speed camera. Such measurements allow to get an insight into the arc size and dynamics and understand how the flow develops from the cathode to the anode.

The volt-ampere characteristic is an essential electrical characteristic of plasma torch operation since it defines the torch behavior when changing the arc current intensity. For stabilized arc length plasma torches operated with an arc below 100-200 A the volt-ampere characteristic is usually falling, meaning that an increase of current leads to a decrease of voltage (Zhukov and Zasytkin, 2007). In other words, in the low current range (<100 A) a high voltage is necessary to maintain the arc, while any increase in arc current towards 200 A makes the plasma temperature and electrical conductivity higher, and thus lower voltage is needed for the arc existence. Meanwhile, with a high arc current above 200 A, the volt-ampere characteristic is usually growing, meaning that for higher current the torch requires higher voltage as illustrated in Figure 4. A similar result was demonstrated in (Bora et al., 2010) for a cascaded DC plasma torch: the falling volt-ampere characteristic below 150 A and growing above that current value.

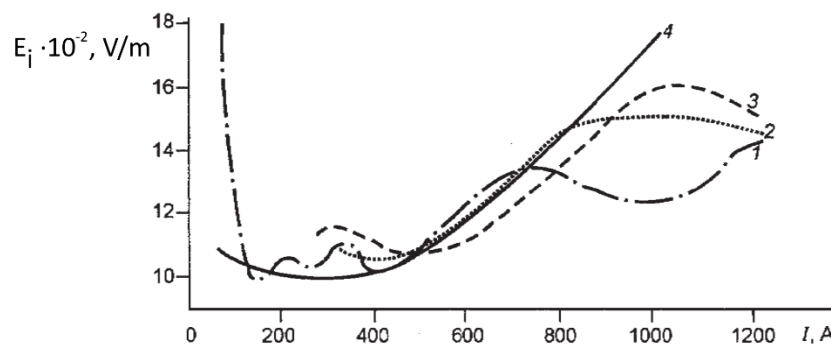


Figure 4 E-I characteristics of the arc in the initial section of the channel of plasma torch with stabilized arc length. Air, nozzle diameter 30 mm, gas flow rate 1) 36 g/s; 2) 70 g/s; 3) 84 g/s; 4) calculated for 36 g/s (Zhukov and Zasytkin, 2007)

In addition it is worth mentioning that with further increase of the current intensity beyond 600-800 A, an inflection of the volt-ampere characteristic from growing to falling can appear. Such inflection can result in the arc being unstable and even fading away (Zhukov et al., 1981).

The stabilization of the arc column being ensured by both the peripheral gas flow and cold walls, a "good" confinement corresponds to an arc radius close to that of the nozzle radius  $R$ . These conditions are generally met for high current intensity (typically more than 200 A) or a

low value of  $R$  (typically of the order of 3 to 4 mm). Finally, it is in the arc column that the "useful" conversion of electrical energy into heat takes place.

The energy provided by the arc makes it possible to raise the temperature of the gas injected upstream, dissociate the molecules and ionize the atoms. The exothermic recombination of the atoms or ions and electrons makes it possible to maintain, downstream of the arc root, a quenching plasma which forms the jet of plasma at the outlet of the nozzle. The arc column attaches to the wall of the anode in the form of a plasma loop through the cold boundary layer which develops parallel to the plasma flow along the anode.

This loop, at high temperature and low density, is subjected to hydrodynamic forces related to gas flow, Lorentz electromagnetic forces and thermal effects. As a result of these forces, the electric arc root moves continuously: the arc lengthens, shortens and exhibits erratic behavior. If these fluctuations of the arc can be profitable to limit the anode erosion, they induce, at given arc current intensity, modifications of the total power dissipated by the electric arc by modification of the arc voltage. These variations in the dissipated power generate fluctuations in the characteristics of the plasma jet at the nozzle outlet (dynamic pressure, temperature, speed, viscosity, density, etc.) and in particular at the point of injection of the particles of powder or liquid precursors. They modify their penetration into the plasma jet and the fragmentation of the liquid precursors and thus impair the reproducibility of the process and the quality of the deposits obtained (Vardelle et al., 2001).

The development of a more stable plasma source with limited erosion of the electrodes is necessary to improve the reliability of the process, in particular for the production of coatings from suspensions or solutions (Fauchais et al., 2008). It goes through a better understanding of the phenomena acting on the stability of the arc discharge and its interaction with the electrodes.

## **I.4. Electric arc**

### **I.4.1. Thermodynamic aspect**

Electric arc is a discharge with intensity above 1 A for pressure around 1 atmosphere. Below 1 A, the discharge is a glow discharge with electric current intensity around  $10^2$  A/m<sup>2</sup>. In high-pressure environment the discharge transition from glow to arc happens around 10 A (Neumann, 1977). Electric current density typical for a high-intensity arc is around or above  $10^6$  A/m<sup>2</sup> (Pfender and Heberlein, 2007).

The arc cannot be considered as a solid body since it has no solid surface on which we might exert a mechanical force and the arc has an intensive two-way exchange of substance with the surrounding gas (Maecker and Stablein, 1986). Furthermore, the arc is not merely a hot gas; it is rather a hot electrically conductive channel produced by the Joule heating due to the electric current in the channel and surrounded by a cold gas environment.

The arc-plasma interaction consists in the balance between Joule heating, cooling by the flow of cold gas, heat dissipation by conduction and convection and plasma radiation loss. The cold gas penetrates the arc, heats up, expands, accelerates and moves away from the arc core while enhancing the heat transport (Maecker and Stablein, 1986). Near the cooled metal electrodes, the plasma is efficiently cooled down. The decrease of plasma temperature results in a lower electrical conductivity. Due to the conservation of total current intensity, the decrease of electrical conductivity leads to an increase in Joule heating expressed by the formula (1.3). Prominent Joule heating leads to intensive expansion of plasma, thus, plasma jets may be

observed near the electrodes. In some cases, the arc may constrict, while lowering the arc diameter and increasing the Joule heating even more.

$$Q_J = \frac{\vec{j} \cdot \vec{j}}{\sigma} \quad (1.3)$$

Due to high Joule heating in the region near the cathode and anode, the maximum temperature occurs near the electrodes. On the arc axis, near the electrodes, the temperature may reach 10 ÷ 20 kK while it rapidly decreases in the radial direction (Zhukov and Zasyupkin, 2007).

The electrons in the arc are heated by the applied electric field and transfer energy to the heavy species through collisions. In contrast to the collisions between only heavy species, the collisions between electrons and heavy species are less efficient for kinetic energy exchange because of the significant difference in mass. In order to reach a thermal equilibrium between electrons and heavy species, more than  $10^3$  collisions are necessary, which is possible only inside the arc where a single Maxwellian distribution for all the particles is reached (Boulos et al., 1994). For that reason, the electrons inside the arc and close to it have a temperature close to the heavy species temperature.

The ionization equilibrium corresponds to the plasma composition that can be described by the Saha equation (Chen and Han, 1999; Gleizes et al., 1999; Gomes, 1983). The excitation and ionization processes in electric arc plasma torches are assumed to be mostly collisional. The contribution of photons to the excitation and ionization processes is negligible. Also, the considered plasma satisfies the principle of microreversibility of the collision process, meaning that for every reaction in plasma a reverse process exists and in every given element of volume their rates are equal (Boulos et al., 1994). However, the microreversibility of specifically photoabsorptions and photoemissions in excitation and ionization may be violated because the plasma produced by the electric arc is considered optically thin. But this issue is insignificant due to the small share of photoprocesses in the ionization process and only the total microreversibility matters. A small shortage of photoabsorptions can be compensated by collisional ionization. The ionization equilibrium is violated only near the arc electrode attachments.

Finally, the electric arc is a medium in which strong interactions occur at the collisional and radiative level between atoms, electrons, ions, excited species and photons. Such an environment will be in equilibrium if (Vacquie, 2000):

- The radiation obeys the Planck's law,
- The "chemical" equilibrium is introduced by means of the Saha's law for the ionization of the medium and the Guldberg-Waage law for the dissociation of the molecular species (law of action of the masses),
- The distribution of populations on the energy levels of each chemical species is governed by the Boltzmann law,
- And, the distribution of translational velocities is governed by the Maxwell's law.

If they are respected, then the medium is in complete thermodynamic equilibrium (CTE): one and the same temperature governs all the statistical distributions and the medium does not present gradients. At this temperature, each elementary process (excitation, ionization, emission, etc.) is then exactly counterbalanced by the inverse process (respectively deexcitation, recombination, absorption, etc.).



In the case of an electric arc and plasma jet produced by a plasma spray torch, the escape of light radiation breaks the radiation balance, by lack of absorption, and the Planck's law must be replaced by the Kirchhoff's law. In addition, the temperature on the discharge axis is greater than that of the periphery and the temperature gradient gives rise to a radial material flow. The CTE is no longer maintained. However, the collisions, short-range interactions, can restore a state of equilibrium at a local level if they are sufficiently numerous and energetic: all laws, except Planck's law, are then respected. Nevertheless, the diffusion processes generated by the temperature and partial pressure gradients of the different species must be negligible in comparison with the collision terms so that the characteristics (concentration, temperature) of the flow at that point are only representative of this point and not of his "neighborhood". This is called local thermodynamic equilibrium (LTE). This balance requires, however, high temperatures and electron concentrations (Griem criterion) (Griem, 1964; Vacquie, 2000) so that the collisions, mainly due to electrons, restore this state of equilibrium. In addition, the LTE is valid only when the plasma temperature changes slowly over the equilibration time, also changes smoothly and continuously over the equilibration length (Griem, 1963).

On one hand, these conditions are generally fulfilled in arcs and thermal plasmas characterized by temperatures above 8000 K and electron number densities higher than  $10^{21} \text{ m}^{-3}$  (Cram et al., 1988), and are, therefore, generally considered to be at or close to LTE. An important parameter to achieve LTE is  $E/p$  that has to be low enough for electrons and heavy species to reach kinetic equilibrium. This is particularly the case of the arc column where the electron-atomic collisions are numerous and the temperature gradients are low enough to be compensated by the energy exchange between electrons and heavy species. The electric arc plasma torches work in pressure higher than 10 kPa and usually around one atmosphere, which makes the collision frequency inside the arc high enough to equilibrate the temperature between all the plasma particles. But for pressure below 10 kPa the kinetic equilibrium is not feasible (Boulos et al., 1994).

On the other hand, in the peripheral zones of the arc and plasma jet, where the gradients can be very high, the equilibrium can be maintained by the collisions only on the degrees of freedom easiest to excite. The notion of partial local thermodynamic equilibrium (PLTE), where different temperatures characterize the statistical distribution of this or that population (Eddy, 1985; Eddy et al., 1973) is introduced. If the velocity distribution of the species is supposed Maxwellian and the heavy particles are supposed to have all the same temperature because of the efficiency of the elastic collisions on the kinetic energy transfer, this local partial equilibrium is characterized by a temperature for the electrons,  $T_e$ , and a temperature for the heavy particles  $T_h$ . Indeed, the electrons, with their low mass, are very sensitive to the electric field and "store" the energy yielded by the external source. It is only through collisions that they redistribute this energy over the degrees of freedom of the heavy particles, such as the translation or the excitation of the electronic levels.

In regions close to the electrodes characterized by very high electron number density and temperature gradients ( $> 10^6 \text{ K/m}$ ), thermal, electrical and chemical imbalances occur. The latter can, for example, occur when the diffusion and convection rates become higher than the chemical reaction rates, including those involving charged species (ionization, recombination).

Usually the equality of electrons and heavy species temperatures, i.e. local thermal equilibrium (LTE), is justified inside the arc column where the temperature gradient is relatively low. On the contrary, in the areas with steep temperatures gradients, e.g., arc fringes, intense flow of

cold gas, electrode arc attachments, LTE is often violated (Boulos et al., 1994). This is because the collision frequency between electrons and heavy species is not high enough in the periphery of the arc (thermal non equilibrium) along with significant different diffusion rates leading to chemical non equilibrium.

#### I.4.2. Electromagnetic aspect

The electric arc, similarly to all the current-conducting channels, has a self-induced azimuthal magnetic field  $\vec{B}$ . This magnetic field combined with the electric current density gives the Lorentz force (1.4), which exerts only constricting action on the straight part of the arc. However, in case of a constriction of the arc near the electrodes, as illustrated in Figure 5, the electric current density has a nonzero radial component in the electrode attachment area. Thus, the Lorentz force acquires also the uncompensated nonzero axial component, which acts as a "magnetic thrust" and accelerates the plasma near the electrode. The constricting action of Lorentz force is balanced by an increase in the radial pressure gradient and, therefore, the pressure increases inside the arc with the highest values close to the cathode (Maecker, 1955). The pressure gradient additionally accelerates the plasma flow. As a result of axial action of the Lorentz force, pressure gradient and intensive plasma expansion near the electrodes, the obtained electrode plasma jet appears to be the location of the maximum velocity (Kelkar and Heberlein, 2000). Such plasma acceleration near the electrode is called Maecker effect, which gives rise to the cathodic or anodic jet. The velocity of this jet is proportional to  $(I \cdot j)^{0.5}$  where  $I$  is the arc current and  $j$  is the current density. The jet entrains a part of the cold plasma-forming gas, favoring the development of the arc column (Maecker, 2009, 1955).

$$\vec{F}_L = [\vec{j} \times \vec{B}] \quad (1.4)$$

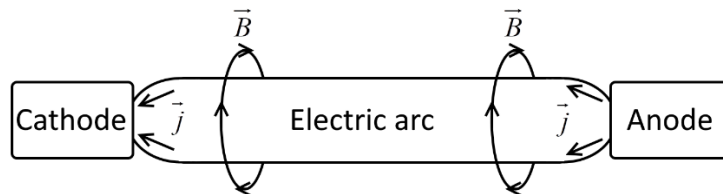


Figure 5: The simplest electric arc: straight discharge between two pin-type electrodes

Self-induced magnetic field may also be a source of magnetic instability as it was shown in (Hülsmann and Mentel, 1987; Mentel, 1977). A hydrogen arc in a long cylindrical channel after exceeding a critical value of current exhibits a uniform periodical helical shape but may be stabilized by an external axial magnetic field. Without external magnetic field further increase of electric current leads to additional disturbances and eventually formation of turbulent discharge (Maecker, 2009).

Electric discharge produces ions and electrons from the neutral particles. Generally speaking, in some individual volumes the total charge of one sign might differ from the opposite one. But the compensating electric force is so powerful that the electric arc should be considered quasi neutral except the thin sheath near the electrodes (Zhukov and Zasytkin, 2007). The voltage drop for the cathode sheath changes in wide range for low current density, but above some limit it retains almost the same value around 10 V for argon (Cayla et al., 2008; Khrabry et al., 2018; Neumann, 1977).

### I.4.3. Arc electrodes interaction: near cathode and near anode area

#### I.4.3.1. Near cathode area

Electrode arc attachment is the area of the cathode surface, which acts as an interface between the electric arc and electrode. Cathode arc attachment can have constricted and diffuse form. In case of constricted arc attachment, the electric current is concentrated at the small part of the cathode surface, which makes the distribution of interface electric current significantly uneven. Diffuse attachment has rather uniform distribution of electric current density over a large area of the electrode. Both constricted and diffuse modes were described in (Benilov et al., 2006; Goodfellow and Polk, 1993) and numerically investigated for electric current ranging from 20 to 200 A in (Mitrofanov and Shkol'nik, 2007): the plasma temperature in front of the cathode for both modes was rather high (above 34 kK). However, in most of the cases for high currents, the cathode arc attachment was constricted (Benilov and Marotta, 1995) and the constricted attachments have a complex dynamic behavior and requires a great effort for proper description.

For low currents the cathode arc attachment may be diffuse. Such attachments were studied in (Benilov et al., 1995; Kovbasyuk et al., 1986). Due to the uniformity of the electric current density, the diffuse cathode arc attachment may be described by one-dimensional model. It is characterized by severe violation of local thermal equilibrium: the heavy species temperature may be two orders of magnitude lower than the electron temperature; cathode voltage drop may be in the order of hundreds of volts and steep gradient of electron number density may prevail. The electrical resistance of the near-cathode layer in diffuse arc attachment is several orders of magnitude higher than the corresponding value on the anode.

The total current through the near-cathode layer consists of emitted electrons, plasma ions heading to the cathode and back diffused electrons from the arc.

$$j = e(\zeta J_i + J_{em} - J_{abd}) \quad (1.5)$$

Where  $\zeta$  is the ion charge,  $e$  the electron charge,  $J_i$  the ion flux,  $J_{em}$  the flux of emitted electrons,  $J_{abd}$  the flux of back diffused electrons.

The electrons leaving the cathode may come from photoelectric effect, Townsend avalanche, secondary emission and thermionic emission. Photoelectric effect source is negligible in gas discharges (Kovbasyuk et al., 1986). Townsend avalanche and secondary emission are essential for glow discharge (Neumann, 1977), but for the arc discharges the major contribution comes from the thermionic emission (Benilov et al., 1995; Neumann, 1977).

The interface between the cathode tip and LTE plasma may be divided into three subdomains:

1. Space charge sheath. It is a collision-free layer of violation of quasineutrality. The corresponding sheath voltage drop is the most significant part of the whole near-cathode voltage drop (Benilov et al., 1995). This layer accelerates the electrons which are emitted from the cathode. In addition, the layer accelerates the substantial amount of plasma gas ions that enter the space charge sheath and head to the cathode surface. The emitted electrons carry away energy from the cathode, while ions bring energy to the cathode and heat it up. The space charge sheath is characterized by the Debye radius. For electric arcs in argon plasma, the Debye radius is around 0.02  $\mu\text{m}$  (Benilov and Marotta, 1995). In (Benilov et al., 1995) it was shown that the space charge near the cathode is mainly formed by the ions.

2. Ionization layer. It is a layer of violation of ionization equilibrium, e.g., the plasma composition cannot be described by the Saha equation (Chen and Han, 1999; Gleizes et al., 1999; Gomes, 1983). It provides the majority of ions to the space charge layer. The ions are produced from the gas atoms after collisions with the electrons emitted from the cathode and accelerated by the space charge layer. The ion current in the arc root is below 1%, while in order to heat up the cathode the ion current share must be from 10% up to 50% (Neumann, 1977). That is why the production of ions in the ionization layer is essential for cathode heating and further thermal emission. The ionization layer voltage drop is usually smaller than the sheath voltage drop. The ionization layer is characterized by the recombination length, which is the scale on which the rate of variation of the charged particle density due to ambipolar diffusion is comparable to the recombination or ionization rates. For electric arcs in argon plasma, the recombination length is around 10  $\mu\text{m}$  (Benilov and Marotta, 1995).
3. The thermal non-equilibrium layer is the layer of deviation of electron and heavy species temperatures. In this case, the plasma composition can be described by the Saha equation, but the plasma composition is different for different combinations of electron and heavy species temperatures. The Potapov formulation was used in (Chen et al., 1981; Kannappan and Bose, 1977). However, van de Sanden formulation (van de Sanden et al., 1989; van de Sanden and Schram, 1991) of the Saha equation is often considered (Chen and Han, 1999; Girard et al., 1999) more suitable than the Potapov formulation (Potapov, 1966) when the electron temperature is not equal to the heavy species temperature. The thermal non-equilibrium layer is characterized by the length of electron energy relaxation. The latter is the length scale on which the electron thermal conduction and heating by the ambipolar electric field are comparable to the electron energy exchange in collisions with heavy particles (Benilov and Marotta, 1995).

A substantial part of the heat flux to the cathode is related to the electric current, i.e. kinetic energy of the plasma ions accelerated by the space charge sheath and ionization energy released after the plasma ions neutralization. At the same time, the heat flux to the cathode from plasma itself, conditioned only by the convection and heat diffusion, is not prevailing. The heat flux to the cathode increases the cathode temperature, clearing the way for thermionic emission from the cathode material. The heat flux to the cathode can even cause melting at the attachment spot. The maximum local value of the heat flux is realized at the spot edge where the temperature is lower than in the spot center, but the electric current density is still high enough (Benilov and Marotta, 1995). The heat flux to the cathode strictly increases with an increase of the total electric current (Zhukov, 1972). The accommodation coefficient, which is usually defined in this context as the portion of the ion kinetic energy transferred to the cathode after collision with its surface, is usually assumed to be equal to one, while the real value might be different (Neumann, 1977).

The plasma temperature at the edge of the near-cathode layer, where LTE holds, should be high enough to maintain the ionization degree in the order of unity, that is, around 15-20 kK.

(Neumann, 1977, 1969) showed that the gas pressure is an important parameter for the cathode heating up to the thermal emission temperature since it defines the supremum of ion current. The absolute value of ion current density in front of the cathode, which defines the cathode temperature and space charge sheath electric field, must be at least  $10^6 \text{ A/m}^2$  in order

to maintain the thermal emission. For pressure below  $6.6 \cdot 10^6$  Pa, the ion flux is too low and thermal emission is negligible. That is why in that case the secondary emission becomes essential for the discharge. Another mechanism of electric conduction through the cathode-plasma interface is the field electron emission, which appears in case of high electric current density and high electric field.

All the cathode processes described above deal with smooth cathode surface. The interaction of electric arc with bulges on rough cathode surface were described in (Ecker, 1977, 1976). The cathode surface protrusion with tip temperature around boiling point and size bigger than the thickness of the space charge sheath is subjected to two competing effects: electric field and surface tension. The electric field attempts to tear apart the liquid surface and destroy the protrusion, while the surface tension attempts to compress the liquid and suppress the protrusion. Another effect is the evaporation of the liquid part of the protrusion. The balance between these two effects defines the destiny of the cathode protrusion: collapsing or evaporation. The metal vapor of the cathode material, due to lower ionization potential, contributes to the electrical conductivity of plasma and can affect the electric current and temperature distribution (Murphy and Park, 2017).

#### **I.4.3.2. Near anode area**

The anode arc attachment has a little more variability than the cathode one. The near-anode region was studied in (Nemchinskii and Peretts, 1977). The study divides the region into four sublayers:

1. The space charge sheath which is characterized by the Debye radius,
2. The ionization layer which is characterized by the recombination length,
3. The thermal non-equilibrium layer,
4. The isothermal layer with disproportion of Joule power and radiation in which the convection has a significant contribution in the thermal balance. This layer is distinguished in free-burning arcs (Baksht et al., 1997), but in constricted arcs with additional gas flow the convection becomes a significant thermal contribution almost in the whole area.

The near-anode region is cooled by the anode material resulting in a decrease in the charge carriers' number density. Additional mechanisms are required to conduct the electric current through the near-anode region. The major part of the electric current to the anode consists of electrons, while the ions drift in the electric field from the anode surface. A lack of ions results in a negative space charge and may be compensated by additional ionization of neutral particles in the near-anode region. Ionization can happen as a result of collisions with electrons in strong electric field (direct ionization) or high temperatures (thermal ionization). The direct ionization prevails in low current arcs and requires high anode voltage drop up to tens of volts, while the thermal ionization prevails in high current arcs and decreases the anode voltage drop (Neumann, 1977).

The charge balance strongly depends on the plasma flow near the anode. In case of an intensive plasma flow directed to the anode, the positive ions brought by the flow compensate the ions drift in the electric field that may lead to a negative value of the anode voltage drop (Yershow and Panevin, 1973). The opposite plasma flow, called anodic jet, leads to an increase of the anode voltage drop up to a positive value (Finkelnburg and Maecker, 1956). A

cross flow which leads to intense arc cooling may have an additional effect on the anode arc attachment and arc behavior (Kelkar and Heberlein, 2000; Maecker and Stablein, 1986).

The two essential modes of anode arc attachment are the diffuse and constricted attachment. The diffuse attachment has a rather uniform distribution of electric current density and electric current and can take up a large part of the anode surface. The constricted attachment occurs on a much smaller spot with a higher electric current density and a pronounced boundary of the spot.

Single constricted anode arc attachments, multiple constriction and diffuse anode arc attachments are studied in (Baksht et al., 1997; Dyuzhev et al., 1997) for xenon and argon free-burning arcs, various electric currents and electrode spacing. The authors also drew attention to the difference between constricted anode and cathode arc attachments. In (Baksht et al., 1997) constricted anode arc attachment is considered as a result of overheating instability between Joule power and radiation near the anode. An increase of the arc current led to an increase of the number of multiple anode attachments and eventually to diffuse anode arc attachment.

Diffuse anode arc attachment was studied in (Benilov et al., 1995) in a one-dimensional model for low intensity electric arcs. Benilov found that the near-anode layer voltage drop is up to hundreds of volts; it heavily depends on the anode surface and arc plasma temperatures and can be increased by an external magnetic field.

In case of diffuse attachment, the mean electric current density at the anode surface in atmospheric pressure has an order of magnitude around  $10^6$  A/m<sup>2</sup> and may be different from the mean electric current density in the arc root: arcs with  $|\vec{j}_{arc\_root}| < 10^6$  A/m<sup>2</sup> and diffuse attachment are narrower near the anode, while high intensity arc with  $|\vec{j}_{arc\_root}| \gg 10^6$  A/m<sup>2</sup> are wider near the anode.

The value of the electric current density in the diffuse anode arc attachment is defined by the conservation of energy and electric charge. In order to get  $|\vec{j}_{attachment}| < 10^6$  A/m<sup>2</sup>, a low gas pressure below  $2.64 \cdot 10^4$  Pa or hot surface of anode above 2000 K are necessary. While values of  $|\vec{j}_{attachment}| > 10^7$  A/m<sup>2</sup> in the diffuse attachment may be found for high intensity arcs with a pressure above  $10^6$  Pa. The constricted anode arc attachment has values of  $|\vec{j}_{attachment}|$  between  $10^7$  and  $10^9$  A/m<sup>2</sup>, it is accompanied with anode erosion and arc instabilities (Neumann, 1977).

In the study of vacuum arcs (Kimblin, 1971) it was found that the transition of anode arc attachment from the diffuse mode to constricted mode coincides in time with the anode melting and is followed by a significant decrease of anode voltage drop. It is worth noting that the threshold current for anode arc attachment transition in vacuum depends on the anode size: 400 A for an anode diameter of 1.3 cm and 2100 A for an anode diameter of 5 cm. In other words, a larger anode requires a higher current for the anode spot formation in vacuum. In addition, the threshold current is affected by the electrode spacing: the higher electrode spacing, the lower current necessary for anode spot formation. While the study of the transition of vacuum arc to atmospheric pressure (Kimblin, 1974) showed for current 350 A that with an increase of helium pressure, the anode spot formation required less and less electrode

spacing. Eventually for pressure around half an atmosphere the anode attachment was constricted for any electrode spacing.

Thus, large electrode spacing and small anode surface area lead to the formation of constricted intensively evaporating anode spot. Intense cathodic jet may prevent the anode spot formation (Kimblin, 1974).

An additional factor affecting the anode arc attachment transition is the cathodic jet. In (Barrault et al., 1971) it was found that the strong cathodic jet of high pressure arc with a truncated conic cathode prevents the constriction of anode arc attachment for currents up to 10 kA. An intense cathodic jet may also result in very high heat transfer to the anode: up to 80% of the whole arc power (Bowman, 1972).

The transition from diffuse anode arc attachment to constricted one was studied in (Hartmann and Heberlein, 2001; Yang and Heberlein, 2007b) in the context of straight axisymmetric transferred arc with rod-type cathode with conical tip and flat anode. The arc was surrounded by the gas flow from the cathode to the anode and confined by an electrically insulated constrictor. The authors showed that for an electric current of 100 A, a decrease of the gas flow rate leads to a weakening of the cathode jet and finally to the constriction of the anode arc attachment. In (Yang and Heberlein, 2007b) it was also shown that a decrease of the arc current results in a weaker magnetic constriction of the cathode arc attachment and, therefore, a weaker cathode jet. For low gas flow rate and currents below 200 A, the anode arc attachment was always constricted. The diffuse mode was obtained for high gas flow rate and was accompanied by a negative anode voltage drop. The electric current density was at most  $10^6$  A/m<sup>2</sup>, which is in good agreement with the data provided in (Neumann, 1977). With a diffuse anode arc attachment, the arc expands towards the anode and exhibits a bell-shape. The transition from diffuse anode arc attachment to constricted attachment occurs through two transition modes: the lift-up mode and multiple-attachment mode. The constricted anode arc attachment with strong anode jet was obtained for low gas flow rate; it had significantly higher maximum electric current density around  $5 \cdot 10^6$  A/m<sup>2</sup> and positive anode voltage drop. The constricted anode arc attachment is cooled down by the ambient gas, which is sucked inside the arc and enhances the arc constriction (Hartmann and Heberlein, 2001; Yang and Heberlein, 2007b). Positive and negative anode voltage drops were experimentally observed in (Tanaka and Ushio, 1999) and numerically found in (Amakawa et al., 1998; Jenista et al., 1997; Tanaka et al., 1999). In (Tanaka and Ushio, 1999) the positive anode voltage drop was observed for 50 A with the anode boundary layer remarkably deviated from LTE, while the negative anode voltage drop was observed for 150 A with the anode boundary layer much closer to LTE. Also a negative anode voltage drop was demonstrated in (Sanders and Pfender, 1984). (Yang and Heberlein, 2007b) showed the possibility to simulate the transition of the anode arc attachment by a two-dimensional second order finite difference method. The study (Hartmann and Heberlein, 2001) shows that the transition of a diffuse to a constricted anode arc attachment is followed by a significant increase of the arc voltage due to the increase of the near-anode layer resistance. A further constriction of the arc attachment results in a higher electric current density, intense anode jet and decrease of the arc voltage.

The study of (Yang et al., 2006) describes the transferred arc attachment to a flat anode in a cross flow for different gas flow rates. It shows the transition from a diffuse to constricted attachment under the cross flow. With further increase of the cross flow the constricted attachment deflected and exhibited the restriking motion with reattachments. A strong cross flow led to a significant arc constriction and increase in the electron temperature near the

anode. Therefore, the arc attachment may be constricted because of external reasons, and not only because of the arc parameters.

#### 1.4.4. Energy balance at the electrodes

The erosion of electrode is a major challenge in plasma torch operation. It limits the electrode lifetime and affects the cost of the produced coating. The electrode erosion mainly depends on the electric current density at the electrode arc attachment and the plasma temperature near the electrode surface. The arc attachment through a small spot with high current intensity leads to a significant heat flow to the electrode at the attachment spot. If the arc residence time at a certain location through a small spot is long enough it results in melting and erosion of the electrode.

##### 1.4.4.1. Cathode

At the cathode, the electric current is essentially transported by the electrons emitted by the cathode spot. Each emitted electron carries a quantity of energy equal to the work of extraction of the metal. The electron emission has a cooling effect on the cathode. Therefore, to maintain the surface of the cathode at a temperature sufficient for the thermoelectronic emission to occur, this cooling must be compensated for by the heat flux supplied by the accelerated ions in the space charge region and possibly backscattered electrons from the ionization zone to the cathode. As the cathode spot reaches high temperatures, it can also be cooled by radiation and evaporation. However the cathode radiation is usually assumed negligible due to the small area of the cathode arc attachment. The energy balance at the cathode tip surface is generally given by the following formula (1.6).

$$-\lambda_{cathode} \left. \frac{\partial T_{cathode}}{\partial n} \right|_{interface} = -\lambda_{plasma} \left. \frac{\partial T_{plasma}}{\partial n} \right|_{interface} + Q_{ions} - Q_{electrons} + Q_{radiation} - Q_{evaporation} \quad (1.6)$$

Where  $Q_{ions}$  is the heat flux brought by the ions,  $Q_{electrons}$  the heat flux carried away by electron emission,  $Q_{radiation}$  the radiation from the plasma and  $Q_{evaporation}$  the heat flux extracted by material evaporation.

##### 1.4.4.2. Anode

At the anode, the energy gains are balanced by the conduction in the metal electrode; the other modes of dissipation are either very difficult to evaluate like evaporation or negligible like the anode material radiation. In fact, the evaporation of the anode material plays a vital role on the total balance, but more by the modification of the properties of the anodic plasma than by the cooling of the anode (Bouaziz, 1996). The power  $Q_{anode}$  collected by the anode is generally limited to three terms given in the formula (1.7).

$$Q_{anode} = Q_{convection} + Q_{electrons} (I) + Q_{radiation} \quad (1.7)$$

Where  $Q_{convection}$  is the heat flow from the hot gas and plasma in the immediate vicinity to the anode,  $Q_{electrons}$  is the anode heating due to the electrons collected from the arc, and  $Q_{radiation}$  is the plasma radiation absorbed by the whole surface of the anode. The absorbed radiation is more significant for the anode due to a larger surface area exposed to the arc luminosity.





The arc breakdown (2) is called “restrike”. It happens between the arc column (1) and torch chamber wall. The restrike is followed by a significant drop of the arc voltage. When the arc near the anode attachment curves too much, a fine-scale arc-arc shunting (3) can happen. In addition the arc may undergo a fine-scale arc-anode shunting (4) downstream from its primary attachment since the cold boundary layer becomes thinner and hotter downstream from the cathode. A fine scale shunting results in a low amplitude voltage pulsation (Zhukov and Zasytkin, 2007). The electric arc may also have several anode attachments, but most of them have a very short lifetime, that is why most of the time a single anode arc attachment dominates (Duan and Heberlein, 2002).

It is worth mentioning that during the restrike or fine-scale shunting the arc itself does not move upstream as a solid body, since the whole fluid in the torch channel continues flowing downstream towards the nozzle exit. Instead of the upstream bulk motion of the radial part of the arc, the arc acquires a new part which appears to be energetically favorable (Chazelas et al., 2017). The new modified arc attachment gets closer to the cathode; the arc column gradually shortens which results in a decrease of the arc voltage. Such arc dynamics resembles an oscillating process and repeats itself again and again.

The arc column is separated from the anode surface by the cold gas, which is not electrically conductive. In case of a laminar flow and straight arc column, the electric potential in the arc column far from the cathode tip changes according to a linear law along the torch axis, which results in an almost constant electric field in the axial part of the arc (Zhukov et al., 1981), while the electric potential of the anode surface remains almost the same due to the significantly-high electrical conductivity of the anode metal. Therefore, in the cold gas gap between the arc column and anode surface a voltage drop appears. The voltage drop between the arc column and the anode changes gradually: near the cathode tip it is the highest and comparable with the whole arc voltage, while getting close to the anode arc attachment it decreases down to the voltage of the electric bridge between the arc column and anode surface.

A strong anodic jet may also result in a restrike on the opposite side of the anode (Duan and Heberlein, 2002). If the electric arc near the anode is inclined downstream to the nozzle exit, as it is shown in Figure 6, additional contribution is made by the Lorentz force conditioned by self-magnetic field of the electric arc (Wutzke et al., 1968). In some cases the Lorentz force is even capable of counterbalancing the viscous gas dynamic force.

For the reasons given above the arc voltage in the plasma torch keeps changing during the torch operation which results in a variation in heat production, even if the oscillations of the direct current supplied to the torch are negligible. Such variation in the arc voltage and anode arc attachment position leads to fluctuations in the temperature and direction of the plasma jet issuing from the torch. It affects the coating reproducibility and technology reliability.

### **I.5.2. Arc instabilities. Steady, take-over and restrike modes**

The thickness and velocity of the cold boundary layer can significantly affect the arc voltage fluctuations. A rapid and dense cold boundary flow makes the radial part of the arc thinner and increases the mean arc voltage and its fluctuations. A significant cold boundary layer creates an unstable balance of viscous forces, pressure gradient and self-induced Lorentz force which results in a complex behavior of the whole arc. Meanwhile, a thin cold boundary layer results in smooth and weak fluctuations of the arc voltage.

Given that the arc voltage depends primarily on the properties of the arc, the time sweep of the arc voltage can be used for analysis of the arc dynamics. From the time-evolution of the arc voltage three arc modes are distinguished: steady, takeover, and restrike (Duan and Heberlein, 2002). These modes illustrated in Figure 7. The studies (Duan and Heberlein, 2002; Wutzke et al., 1967) demonstrated a correlation between the arc modes and the thickness of the cold-gas boundary layer which separates the arc from the anode surface. The thickness of the cold-gas boundary layer depends on the torch geometry and operation parameters (current intensity, plasma forming gas composition and flow rate). It was found that a thin boundary layer is accompanied by a steady mode, while a thicker boundary layer results in a restrike mode. In addition, the arc voltage fluctuations correlate with the pressure fluctuation in the cavity behind the cathode near the gas injection (Delair et al., 2005; Rat et al., 2017; Rat and Coudert, 2010a).

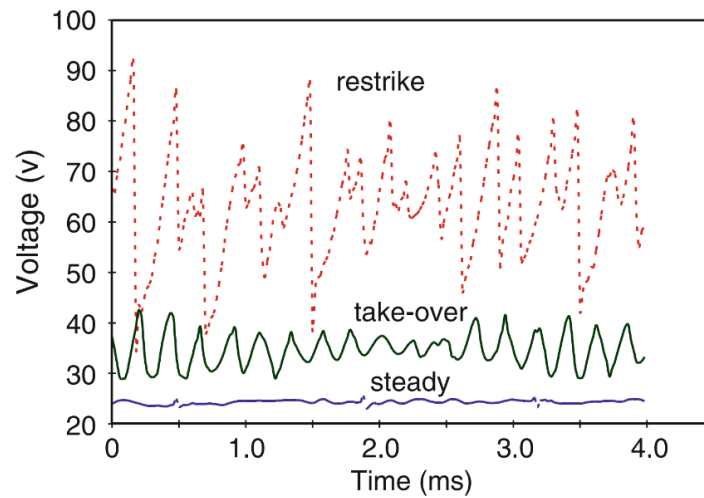


Figure 7 Anode arc attachment modes: restrike mode 100 A, 12/40 slpm of Ar/He; take-over mode 500 A, 40/20 slm of Ar/He; steady mode 900 A, 60 slm of Ar (Duan, 2000)

Figure 7 illustrates the key modes of electric arc instabilities on a short time scale. The electric arc instabilities can be described from the arc voltage and characterized by the ratio of the duration of voltage ascent  $t_{up}$  to the duration of voltage descent  $t_{down}$  given by the formula (1.8) and by the amplitude of voltage fluctuations  $\Delta V$  divided by the voltage itself  $V$  given by the formula (1.9) (Duan and Heberlein, 2002). These coefficients are called “voltage fluctuation shape factor” and “voltage fluctuation amplitude factor”; they are defined by the following formulae:

$$S_{VT} = \frac{t_{up}}{t_{down}} \quad (1.8)$$

$$A_V = \frac{\Delta V}{V} \cdot 100\% \quad (1.9)$$

Using these two formulae, the modes are usually defined as:

**Steady mode**, a rather stable voltage behavior over time with  $A_V < 2\%$ .

**Take-over mode**, with  $A_V \geq 10\%$ , but  $S_{VT} < 1.1$  which corresponds to a smooth and balanced fluctuation. The take-over mode is favored by the arc being close to the anode surface

(Chazelas et al., 2017). The steady and take-over modes can be observed with a high arc current in argon.

Restrike mode, with  $A_v \geq 10\%$  up to 70% and  $S_{VT} \geq 5$  meaning that the voltage decreases much faster than it grows, and the voltage together with its fluctuation amplitude have close orders of magnitude. The restrike mode appears when the cold boundary layer is too thick for being heated up smoothly, and the continuous and smooth voltage oscillating process is hard to implement. The restrike mode requires rather high electric field, but it is still around two orders of magnitude lower than the field necessary for breakdown in the cold gas under atmospheric pressure. The electric field in the cold boundary layer is not high enough for the electron avalanche. The restrike mode may result in a discontinuity of the plasma flow and formation of plasma blobs outside the plasma torch (Coudert et al., 1995).

Between these three distinct modes there are smooth transitions with mixing modes (Duan, 2000).

A decrease in current intensity and admixing of gas with higher thermal conductivity results in a lower arc diameter and eventually in restrike mode. In general, an increase of the cold boundary layer thickness leads to more severe voltage fluctuations and eventually to the restrike mode (Fauchais et al., 2014).

The arc voltage fluctuation amplitude and frequency in the restrike mode depend on the current intensity and gas flow rate (Zhukov and Zasytkin, 2007). An increase of current intensity decreases the voltage fluctuation amplitude and increases its frequency. An increase of gas flow rate with a constant arc current results in higher voltage fluctuations amplitude, but lower fluctuation frequency.

However, a study with a 100 A transferred arc with a lateral gas flow of 0 to 50 SLPM (Yang et al., 2006) showed that after the appearance of the restrike mode at flow rate of 30 SLPM the restrike frequency increased from 300 Hz to 450 Hz in a range of gas flow rate from 30 to 50 SLPM.

As it was described in (Nemchinsky, 2015), the cold gas layer around the arc column upstream from the anode arc attachment has still a substantial electrical conductivity due to the violation of LTE and ionization equilibrium. Such disequilibrium allows the arc, in the restrike mode, to form a new attachment through the gas layer with low-temperature heavy species. In addition, the study (Yang et al., 2006) found some nonzero current through the dark area between the arc parallel to the anode and the anode itself, indicating existence of charge carriers at close range outside of the arc, in the area with low temperature of heavy species. A simplified technique of mimicing the formation of a new arc attachment in the area with critical electric field was used in (Moreau et al., 2006; Trelles, 2007).

The arc reattachment process in dc plasma torch with nitrogen was studied in (Prevosto et al., 2015). It was confirmed that the reattachment mechanism consists in the vibrational thermal instability in the cold boundary layer. It was also demonstrated that the reattachment is a threshold process with duration around 100 microseconds. The reattachment starts with the gas heating by electrons through a vibrational-translational relaxation, which leads to an initial decrease of the gas density, and increase of the reduced electric field  $E/N$ , where  $E$  is the electric field and  $N$  is the number density of neutral particles. The electron temperature in the cold boundary layer increases together with the electron number density, which eventually leads to a new anode arc attachment formation closer to the cathode, which becomes

dominant. The previous arc attachment disappears because it becomes energetically unfavorable.

The presented above arc voltage fluctuation may change on a 50h time scale due to anode erosion and surface unevenness. In (Coudert et al., 1995) it was shown that the anode erosion can affect the arc behavior, switching the arc from a smooth sliding on the new anode to a stagnation of the arc attachment after upstream and downstream restrikes on an eroded anode.

### I.5.3. Pressure-voltage fluctuation correlation

The correlation of gas pressure and arc voltage fluctuations was studied in (Rat and Coudert, 2011). Example of such correlation is illustrated in Figure 8. The study deals with the cathode cavity, which is the space between the injection ring and cathode tip. This space accommodates the cold plasma-forming gas whose pressure is far from being constant. The cold gas in the cathode cavity is presented as an oscillating system affected by motion of plasma and torch instabilities.

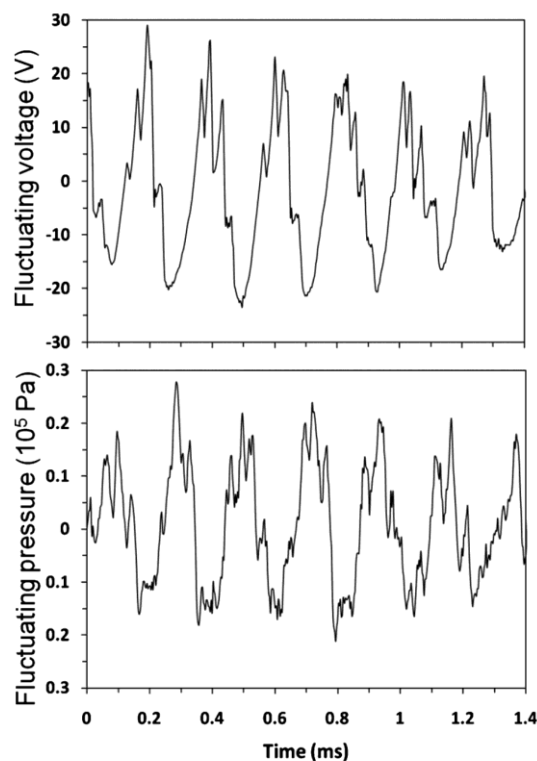


Figure 8 Fluctuations of arc voltage and pressure in the cathode cavity for 600A and Ar-H<sub>2</sub> 45-6 slm (Rat and Coudert, 2010b)

The pressure fluctuations in the cathode cavity together with the arc voltage fluctuations were measured. Both recorded-fluctuations, which, at first glance, looked random, were decomposed by a Wiener filter into several contributions: Helmholtz mode, mode 1, mode 2 and restrike mode as illustrated in Figure 9. The Helmholtz mode is the harmonic main fluctuation and has the lowest frequency. At the same time, the restrike mode is much more random and has the highest frequencies distributed over a wide range. Moreover, the modes 1 and 2 have a distinct harmonic nature but their origin is unclear. The harmonic nature of the Helmholtz mode, mode 1 and mode 2 results in prominent spikes in the fluctuation power spectrum. In addition, the superposition of several harmonic fluctuations with significantly

different frequencies results in a beating phenomenon. However, no spike in the power spectrum corresponds to the restrike mode (Coudert and Rat, 2008).

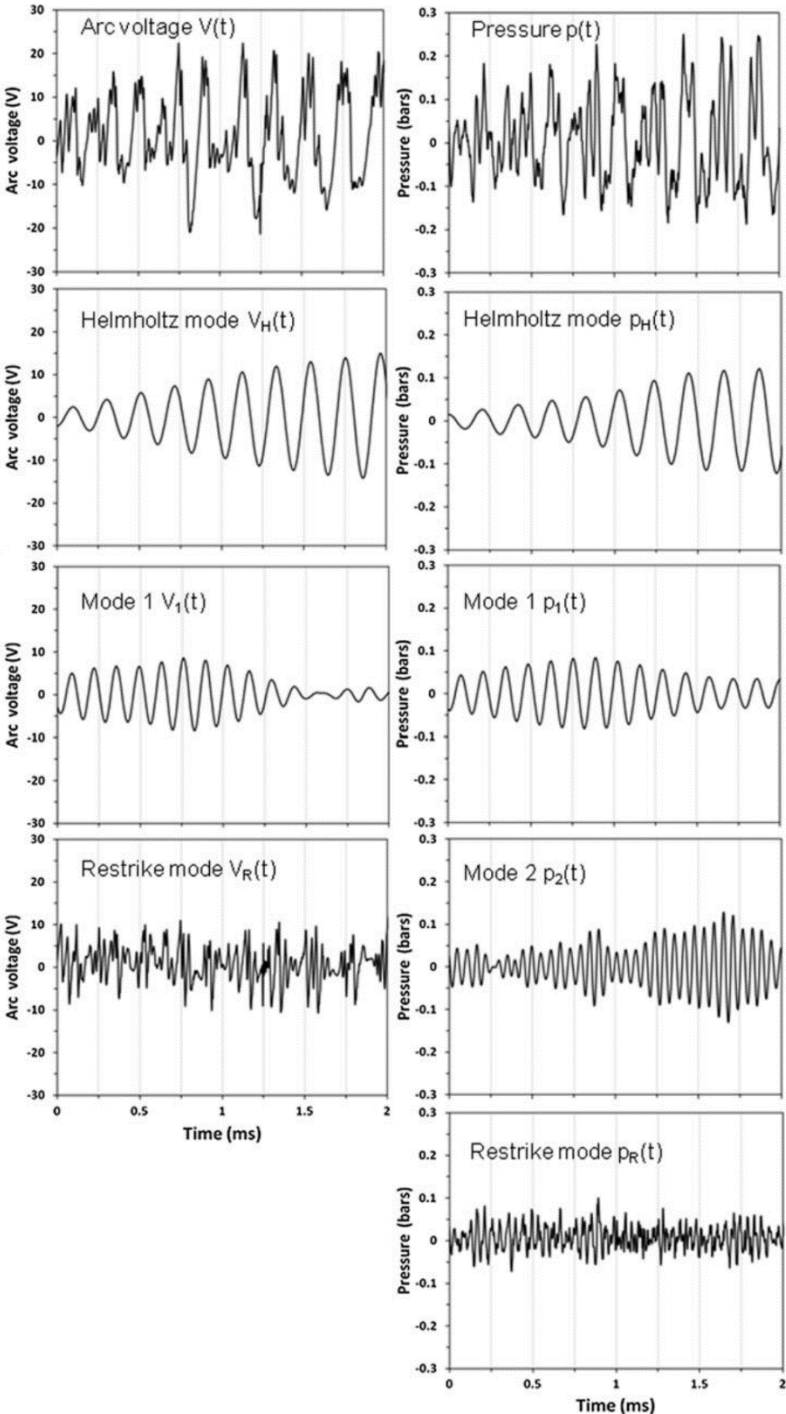


Figure 9 Time sweep of raw signal of pressure and voltage and their decomposition into several components with different frequencies (Rat and Coudert, 2011)

In (Coudert et al., 2007; Coudert and Rat, 2008) it was shown that the Helmholtz mode fluctuations that have the lowest frequency (4-5 kHz and), correspond to the most significant component of the arc voltage fluctuations. A closer comparison of the Helmholtz fluctuations of arc voltage and cathode cavity pressure reveals a time shift between them: the pressure fluctuation is delayed by a constant period for every set of parameters. Such period is called the propagation time in (Rat and Coudert, 2011) and associated to the travel time of a

mechanical wave from the arc to the pressure sensor in the cathode cavity. The mechanical wave is created by the overheating and expansion of the plasma due to a spike of arc voltage. This process repeats due to the Helmholtz resonance in the cathode cavity. Thus, the main voltage fluctuation frequency depends on the cathode cavity volume and sonic speed of the injected cold gas. Therefore, the Helmholtz frequency can be altered by modifying the cathode cavity or the gas composition, i.e. an increase in the hydrogen flow rate leads to a decrease of the mixture molar mass and hence an increase of the sonic speed. That is why with a higher hydrogen content in the plasma-forming gas mixture, the Helmholtz frequency increases.

The study (Rat and Coudert, 2011) shows that, in the plasma torch, there is a coupling of the arc voltage and pressure in the cathode cavity. However, a correlation between the arc voltage and pressure fluctuations does not imply that one fluctuation is the cause of the other.

Due to the Helmholtz resonance the fluctuation can be dumped by an external resonator with a variable volume (Rat and Coudert, 2010a) illustrated in Figure 10. The use of such acoustic stub helps to decrease the Helmholtz peak in the voltage power spectrum and decrease the relative fluctuation of voltage. When the Helmholtz fluctuations are dumped, the arc beating phenomenon is mitigated.

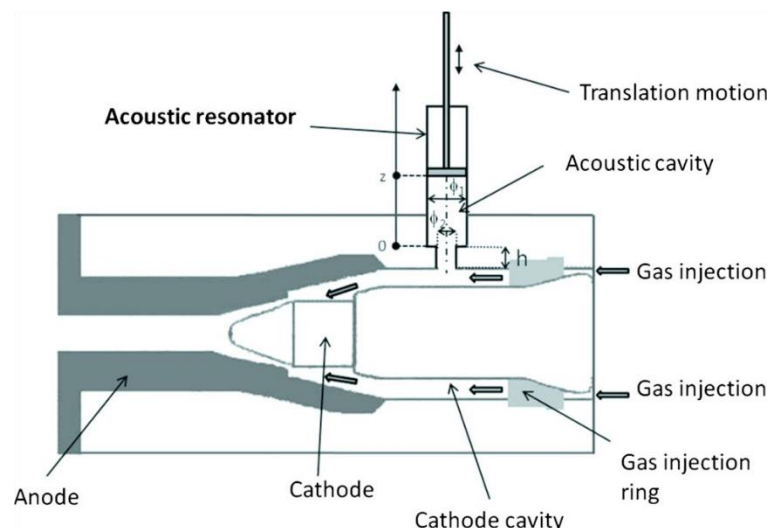


Figure 10 Torch with a mounted acoustic stub (Rat and Coudert, 2010a)

The pressure fluctuations are present in the cathode cavity, but in the feeding line the pressure is almost constant, meaning that the fluctuations are suppressed by the injection ring (Rat and Coudert, 2010b). As a result, the actual gas flow rate entering the cathode cavity must fluctuate. In addition, an increase of the gas flow rate results in an increase of the torch mean voltage due to the arc elongation.

## I.6. Toward more stable plasma torches

Since the arc attachment and its motion affect the electrode lifetime through erosion and the coating reproducibility through the arc fluctuations, it is essential to control the arc shape and behavior. The arc control consists of

- arc length control by using various configurations of the anode;
- anode arc attachment size and mode control, in particular, thanks to the plasma-forming gas type and flow rate;

- anode arc attachment motion control by a swirling gas injection and/ or an axial external magnetic field.

### I.6.1. Types of plasma torches

The plasma torches used in plasma spraying have various geometrical and engineering configuration. The basic model is the conventional plasma torch illustrated in Figure 1: a single cathode with a conic tip and an anode that surrounds the cathode and serves as a nozzle for the issuing plasma jet. The conventional plasma torch has a self-setting arc length which leads to the inherent characteristics of such a torch: severe voltage fluctuations. In conventional plasma torches the coating material is injected a few millimeters upstream or downstream of the anode exit. Deviations from such a concept results in new types of plasma torches.

The combination of two and more electric arcs in one plasma jet with subsequent central injection of the coating material is described in (Marqués et al., 2009). Each electric arc has its own cathode, anode and power supply that makes the arcs to move and fluctuate independently. Three plasma jets converging in one plasma jet have lower relative fluctuations of plasma temperature and velocity than a single arc. Such enhanced plasma jet stability improves the reproducibility of the coating.

In order to mitigate an essential drawback of conventional plasma torches, namely significant fluctuation of the arc length and subsequently arc voltage, torches with a fixed arc length were proposed.

The first type of plasma torch with a fixed arc length is illustrated in Figure 11. The torch presents a sudden expansion of the channel, i.e. a ledge (Zhukov and Zasytkin, 2007). The wider part of the channel plays the role of anode, where the arc attaches. The arc length remains constant in a wide range of current intensity and gas flow rate. In this case the axial part of the arc length is smaller than the one in the conventional plasma torch. At the same time, the radial part of the arc is elongated. Such plasma torches are rather simple and reliable. However due to the short axial part of the arc they produce plasma jets with relatively low specific enthalpy.

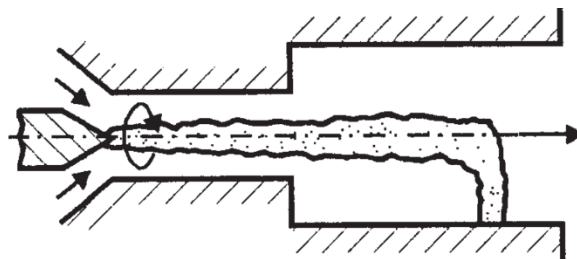


Figure 11 Plasma torch with sudden expansion of the anode diameter and arc length smaller than in the conventional plasma torch. (Zhukov and Zasytkin, 2007)

In order to increase the arc voltage and thus the plasma jet specific enthalpy, torches with cascaded anode were proposed (Bernecki et al., 1988; Zhukov, 1980; Zhukov et al., 1981). Such type of plasma torch is shown in Figure 12. In these plasma torches the electrodes are distanced by one or more electrically-insulated inter-electrode inserts, also called neutrodes, which play the role of channel with wall-stabilization between the button-type cathode and cylindrical liner of the anode.



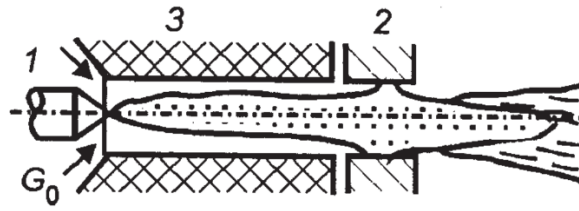


Figure 12 Plasma torch with inter-electrode insert and arc length greater than in the conventional plasma torch. 1: cathode, 2: anode, 3: inter-electrode insert,  $G_0$  is the flow rate of the injected plasma-forming gas. (Zhukov and Zasyplin, 2007)

The neutrodes are usually made of copper and electrically insulated from each other. The neutrodes may have channels or pores for additional counter-directional and co-directional gas injection for additional protection of the plasma torch elements and intensification of plasma energy dissipation (Zhukov et al., 1981). The arc has to pass through the insulated channel and attach to a limited area of the anode. In this case the arc length is rather large and may vary over a small range. Therefore in cascaded-anode plasma torches, the fluctuation of the total heat production in the torch is lowered while the total power is increased due to a greater arc length than in the conventional plasma torch. Cascaded-anodes also help to increase the total power of the plasma torch, while keeping the cooling loss close to the values of the conventional plasma torches.

When the channel of the plasma torch is long enough and the attachment is restricted to the area far from the cathode, the arc column itself can be subjected to radial helical fluctuations and “arc-arc” shunting as illustrated in Figure 13 (Zhukov and Zasyplin, 2007).

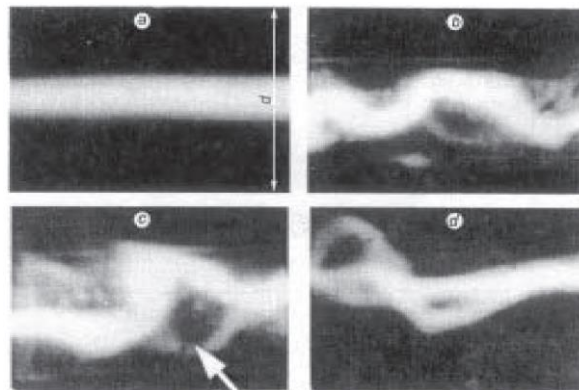


Figure 13 Electric arc photographs in a long cylindrical channel. a) the arc in the initial section of the gas flow; b) random oscillations of the arc in the transition section; c) arc-arc shunting; d) splitting of the arc (Zhukov and Zasyplin, 2007)

During the torch operation the arc induces a uniform electric potential in every insulated neutrode. The potential difference between neighboring neutrodes can cause an electrical breakdown and eventually numerous small arcs may appear between the neutrodes as illustrated in Figure 14. Such multiple arcs are detrimental for the torch. Therefore the neutrodes must have such thickness that the breakdown between them does not happen (Ramakrishnan, 1995; Zhukov et al., 1981). The condition for the thickness  $l$  of the neutrode

to avoid arcing between the neutrodes is  $\int_0^l E dx < U_A + U_C$  where  $E$  is the electric field in the

torch channel,  $U_A$  and  $U_C$  the anode and cathode sheath voltage drop respectively (Vardelle et al., 2015).

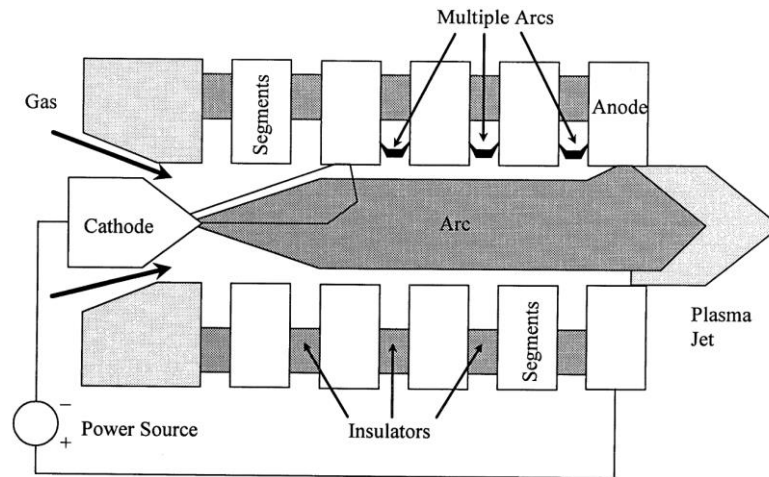


Figure 14 Plasma torch with cascaded anode and arcing between the neutrodes (Ramakrishnan, 1995)

The cascaded-anode plasma torches require additional effort to initiate the arc. For instance in SinplexPro™ and TriplexPro™ of Oerlikon, the arc is ignited by a high voltage ignition pulse between the cathode and the neutrode, and then the arc moves to the anode. After ignition the neutrode is electrically isolated and the arc strikes between the electrodes. Another way suggested in (Bernecki et al., 1988) is moving the cathode towards the anode for ignition and retracting it after the arc has started.

An idea of using a cathode assembly having three smaller pin-shaped cathodes was suggested in (Landes, 1994, 1993). The cathodes are evenly distributed around the torch axis and give rise to three distinct arcs that are found to be separate in the whole channel of the arc. The existence of three distinct arcs that do not unite results in three anode arc attachments, which have fixed location on the inner circumference of the anode surface. A swirling gas injection does not rotate the anode arc attachments, but rather shifts their angular position with respect to their cathodes. Such technology allows to produce a stable plasma flow. In addition the assembly of three cathodes decreases the current density in the arc attachment spots on cathode and anode and, so extends the life time of the electrodes.

Three-part anodes are used in GTV Delta torch, also five-part anodes in the GTV Penta torch in order to compulsory split the arc into several anode attachments (GTV GmbH, n.d.; "GTV Verschleiss-Schutz," 2019; Hawley, 2006). Triple and quintuple anode arc attachments allow to make the plasma jet more axisymmetric which is more reliable and predictable helps for powder injection. In addition the anodic jets from several attachments counterbalance each other making the plasma jet straighter. Such anode reduces the heat load to the anode and thus the anode erosion.

However the drawback of plasma torches with several cathode or anodes is the necessity of the corresponding number of direct-current power supplies, wires and connections.

Another remarkable example of plasma spray torches engineering is the Water Stabilized Plasma (WSP) torch presented in (Ondac et al., 2016). It includes arc stabilization by water flow and an external disk-shaped rotating anode.

### 1.6.2. Swirling gas injection

A swirling plasma forming gas injection is used to stabilize the cathode arc root and rotate the anode arc attachment. The rotation of the anode arc attachment helps to redistribute the heat

load on the anode wall and decrease the anode erosion. However, in (Sun and Heberlein, 2005) it was shown that the swirling gas injection has to have a proper configuration of injection orifices in order to achieve an uniform distribution of the circumferential velocity of the flow and eventually decrease the anode erosion.

The angle of gas injection varies in a wide range: the plasma torches SinplexPro™ and TriplexPro™ use a 25° injection angle, while, for example, in (Zhukov et al., 1981) 30°, 45°, 75° and 90° injection angles were studied in plasma torches with inter-electrode inserts. The swirling gas injection helps also to decrease the heat load to the inter-electrode inserts and anode and stabilize the arc attachment on the large flat cathode (Zhukov et al., 1981). However, the swirling injection increases the turbulence and plasma heat dissipation.

The effect of a gas injection angle from 0° to 60° with a 15° step on plasma torch characteristics was studied in (Cao et al., 2016). An increase of the gas injection angle resulted in an increase in the arc voltage, thermal efficiency and specific enthalpy. However, a too steep injection angle above 45° resulted in a lower axial plasma velocity and shortened plasma jet.

### I.6.3. External magnetic field

External axial magnetic field created by an external solenoid was extensively used to rotate the anode arc attachment and decrease the anode erosion in all kinds of plasma torches with flat, conic-tip, button-type and well-type cathodes (Zhukov, 1980).

If the arc axis corresponds to the spatial variable  $z$  and the external magnetic field created by an external solenoid is perfectly axial and uniform:  $\vec{B}^{ext} = (0; 0; B_z)$ . Then, the Lorentz force created by the axial external magnetic field can be expressed by the formula (1.10). From this formula one can see that the Lorentz force has only those nonzero axial components which are perpendicular to the axis.

$$\vec{F}_L^{ext} = \left[ \vec{j} \times \vec{B}^{ext} \right] = \begin{vmatrix} \vec{e}_x & \vec{e}_y & \vec{e}_z \\ j_x & j_y & j_z \\ 0 & 0 & B_z \end{vmatrix} = (j_y B_z; -j_x B_z; 0) \quad (1.10)$$

Also the Lorentz force depends only on those components of electric current density which are perpendicular to the torch axis. Thus the external magnetic field should mostly affect the anode arc attachment and not the axial part of the arc, as it is shown in Figure 15. However, even an initially straight electric arc can change its shape when an axial external magnetic field is imposed. It was shown in (Allen et al., 1960; Yuen, 1966) that above some threshold value of the axial magnetic field the initially straight electric arc exhibits a helical shape which is explained by minor radial fluctuations of its axial part. The stabilizing mechanisms in the arc are viscous and thermal. At the same time an axial external magnetic field can be used to compensate the spiraling of the arc caused by its own self-induced magnetic field as shown in (Hülsmann and Mentel, 1987). On top of that, the external magnetic field can affect the expanding part of the cathode arc attachment and distort it.

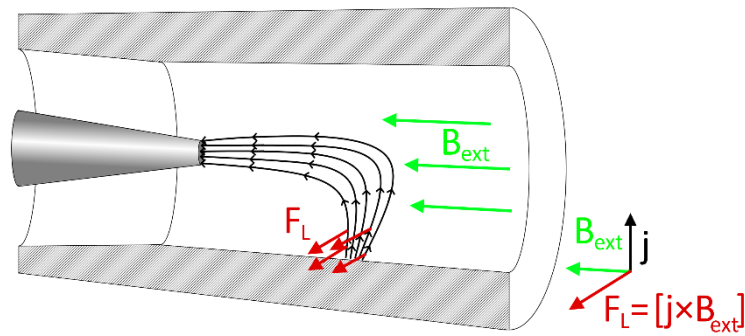


Figure 15 Example of the Lorentz force created by an axial external magnetic field in the arc in a conventional DC plasma torch. Black lines and black arrows represent the electric current lines. Red arrows represent the Lorentz force. The absolute values of electric current density and Lorentz force are not presented.

The effect of an axial external magnetic field varied from 0 T to 0.63 T on an argon electric arc of 160 A with inter-electrode inserts was described in (Zhukov et al., 1981) and demonstrated in Figure 16. The increase of the axial external magnetic field first led to the constriction and spiraling of the arc core (2 in Figure 16) and eventually to a chaotic behavior of the arc (4 in Figure 16). At low values of the external magnetic field, the arc voltage increased and the arc was visible from outside as a luminous ring. At high values above some threshold, the mean arc voltage and arc's behavior almost stopped changing due to the saturation of the arc's fluctuations. The spiraling effect of the external magnetic field on the axial part of the arc could be mitigated by the swirling gas injection. The fluctuations of the axial part of the arc with the external magnetic field decreased the radiative heat flux to the torch while the convective heat flux increased.

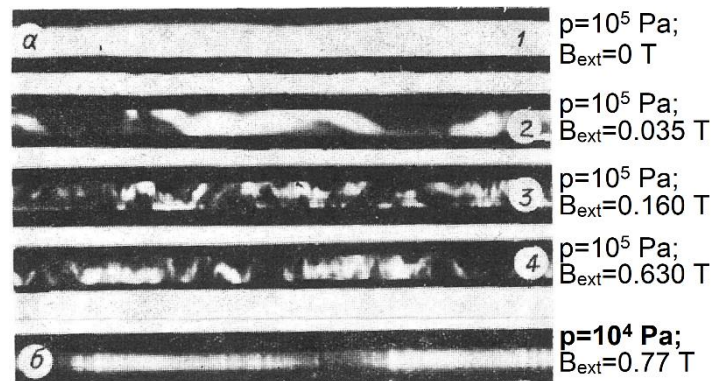


Figure 16 Time sweep of arc luminosity with external magnetic field in the plasma torch with interelectrode inserts. Current intensity of 160 A, pressure of  $10^5$  Pa and  $10^4$  Pa (Zhukov et al., 1981)

The effect of the axial external magnetic field from 0 T to 0.15 T on the anode arc attachment in a plasma torch with a conic-tip rod-type cathode, graphite anode, current up to 120 A was studied in (Wang et al., 2019a). During increase of the external magnetic field the anode arc attachment changed from constricted to diffuse mode. The transition to the diffuse mode was favored by higher external magnetic field or higher current. For example, with arc current of 80 A the transition happened at 0.08 T, while for 100 A at 0.06 T. Thus, for some plasma torches the axial external magnetic field can be used to widen the anode arc attachment and decrease the local maximum of electric current density on the anode surface to decrease anode erosion. The process was simulated in 2D in (Wang et al., 2019b). In (Nemchinsky, 2016) it was suggested to use axial cables with alternating current outside of the anode in order to create

azimuthal magnetic field together with the axial one in order to have the arc rotating and also moving in axial direction.

In addition, a research work (Bobzin et al., 2019) considered two permanent magnets with remanences of  $B = 0.68$  T and  $1.2$  T in order to create an external magnetic field perpendicular to the torch axis to study the general effect of external magnetic field on the anode arc attachment behavior. Permanent magnets helped to shift the anode arc attachment, but rotation was not observed due to lack of axial component of the external magnetic field.

### **I.7. Plasma torch operation model and its validation**

Computer simulation is a safe and relatively cheap way to find out what happens inside the complex devices or apparatuses that are difficult to look inside or too massive to measure all the data at once, for example, engineering structures, atmospheric processes, nuclear reactors, gas turbines, rocket engines. Researchers may simulate the distribution of values or behavior of physical processes, e.g., stress, velocity, temperature or particles motion, condensation, evaporation, interaction of phases. The key elements of computer simulation are the equations that describe the process under predetermined assumptions. Usually the governing equations comprise the terms contributing into the balance of some certain physical quantity. In case of deterministic discrete computer model, the differential equations are employed, which include certain source terms defined by the medium properties, spatial derivatives and, in case of unsteady simulation, the time derivative that helps to predict dynamic characteristics of the simulated device or apparatus.

A transient fluid model consists of a set of general transport equations expressed in a conservative form as a balance of accumulation, net flux by advection and diffusion and net production. In general, the governing equations follow the same pattern (1.11) and they all can be solved by the same methods and iterative solvers.

$$\frac{\partial \psi}{\partial t} + \vec{\nabla} \cdot \psi = \Gamma_{\psi} \quad (1.11)$$

Where  $\psi$  is a conserved property. The first term of the right-hand side in equation (1.11) represents the transient behavior, which is essential in unsteady simulation. The second term of the right-hand side represents the advection and diffusion. Finally, the left-hand side of the equation consists of the production or depletion source terms for each property.

In order to simulate an electric arc plasma torch the computational fluid dynamics (CFD) along with simulation of electric discharge are employed. CFD simulation assumes division of the computational domain into mesh of small volume elements (also called cells) in which the balance of mass, momentum, energy, charge, etc. is computed. The inherent characteristics of electric arc plasma torch are stiff gradients and significant temporal fluctuations of the plasma properties. All the terms comprised into the thermal balance of electric arc and their ratios change in a wide range, which makes the simulation a challenging issue. The aforesaid makes it vital for the simulation to have fine meshes, efficient computation algorithms with a lot of iterations, small time step for unsteady simulation just to reach convergence and get at least some results.

Possible numerical methods to model electric arc are finite volume method (FVM) and finite element method (FEM). FEM considers values at points; it requires inversion of large matrices and is very sensible to the amount of random access memory (RAM). Parallel computing in FEM requires complex algorithms and special efforts (Choporov, 2013; Fu and Zhang, 2006).

FEM is usually used in structural analysis, models of heat transport and electricity. The advantages of FEM are the ability to handle complicated geometries and to provide smooth continuous distributions of solved variables. FEM is rather rare in electric arc simulation and used for example in (Lisnyak, 2018; Trelles, 2007; Trelles and Modirkhazeni, 2014). While FVM considers the balance of solved variables in every single cell one by one and does not require large matrices inversion. FVM is usually used in CFD simulation. Parallel computing in FVM is rather simple and well-established. Another option is the hybrid method proposed in (Abdo, 2018) which uses FEM to solve electromagnetic equations and FVM to solve mass, momentum and energy conservation equations.

### **1.7.1. Individual assumptions of various existing models of free burning arc and electric arc plasma torches**

In the earliest models of electric arcs the researchers did their best to predict and describe the process while having poor computational resources. The initial models were one-dimensional and steady. For example the simple model of high current electric arc in high pressure stabilized by a nozzle was presented in (Lowke, 1974; Lowke and Ludwig, 1975). As the theory of electric arc is too complex and the computational resources were too scarce, a lot of researchers had to employ the Steenbeck principle (Finkelburg and Maecker, 1956; Li et al., 2003; Li and Pfender, 2007; Paik et al., 1993; Peters, 1956; Zhou and Heberlein, 1994), which states that “For a given current intensity the arc column properties are naturally adjusted in such a way that the arc voltage, electric field, and Joule power have the lowest values possible in the given geometrical configuration” (Steenbeck, 1932). A comprehensive review of the principle usage was given in (Ecker, 1977). The Steenbeck’s principle is useful for a significant number of cases, including the channel model of the stationary free-burning arc, and capable of providing reasonable results which are useful for practical purposes (Christen, 2010). Also in some studies a tendency for arc voltage to decrease and become more stable is assumed, which is similar to the idea of the Steenbeck’s principle (Farrall, 1973). However, as it was shown in (Benilov, 2010) the Steenbeck's principle has unclear derivation and relationship with the general theory of electric arc; it can produce uncontrollable errors. In addition, the Steenbeck's principle doesn't account for dynamic arc behavior and multiple possible modes with the same current intensity, which is detrimental for plasma torch simulation. Similarly, as it was shown in (Ecker, 1976) the Steenbeck’s principle is not applicable for the model of strongly non-stationary moving cathode arc attachment. Fortunately, the properties of electric arc discharge can be fully described by the full system of differential equations accompanied by the boundary conditions and initial values for every given physical problem and does not require the Steenbeck’s principle (Elenbaas et al., 1936).

One of the key parameters of the model is the number of dimensions. 2D models were, for a long time, an inevitable compromise between computational cost and solution accuracy. Another key parameter of the model is time dependence. The arc model can be either steady or unsteady. Due to severe temporal fluctuations of plasma properties it is desirable to catch the dynamics of electric arc in unsteady simulation, however it increases the simulation computational cost, since instead of just one state in steady simulation, the unsteady simulation re-computes numerous consequent states with a small time step.

As soon as at least some computational resources became easily accessible for researchers, they started creating 2D axisymmetric steady arc models with thousands of rectangular mesh elements that solved mass, momentum, energy conservation equations along with the current continuity equation (1.12) (Lowke et al., 1997, 1992; Westhoff and Szekely, 1991; Zhu et al.,

1995, 1992). Further development (Sansonnens et al., 2000) of the model by Lowke accounts for effects of ambipolar diffusion due to electron number density gradient on electrical conductivity and electric current.

$$\frac{1}{r} \frac{\partial}{\partial r} \left( r \sigma \frac{\partial \varphi}{\partial r} \right) + \frac{\partial}{\partial z} \left( \sigma \frac{\partial \varphi}{\partial z} \right) = 0 \quad (1.12)$$

Some plasma torch models and their parameters are listed in Table 1 including unsteadiness, number of dimensions, turbulence model, simulated plasma torch, and incorporation of the electrodes into the computational domain.

Table 1: Characteristics of some recent models of plasma torches

Reference	2D/3D	Steady / unsteady	Thermal equilibrium	Electrodes included	Number of cathodes	Plasma forming gas	Torch	Turbulent/ laminar
(Westhoff and Szekely, 1991)	2D	Steady	LTE	No	1	Ar, 0.53 scmh (8.8 SLPM)	simplified geometry of plasma torch used at INEL	Laminar
(Han and Chen, 2001)	2D	Steady	LTE	No	1	Ar, 72.5 SLPM	Unknown	Laminar
(Yuan et al., 2004)	2D	Steady	LTE	No	1	Ar, 50 SLPM and 150 SLPM	Praxair SG-100	Standard K-ε model of turbulence
(Jin Myung Park et al., 2004)	3D	Unsteady	LTE	Only anode	1	Ar + 10% H2 40 LPM	Not mentioned, with external magnetic field	Standard K-ε model of turbulence
(Trelles et al., 2006)	3D	Unsteady	LTE	No	1	Ar, 60 SLPM or Ar-H2(75/25) 60-90 SLPM	F4-MB Sulzer-Metco	Unknown
(Trelles et al., 2007)	3D	Unsteady	2T	No	1	Ar, 60 SLPM	Praxair SG-100 nozzle diameter 8mm	Unknown
(Selvan et al., 2009)	3D	Steady	LTE	No	1	Ar 20-25 SLPM plus N2 3 SLPM	Unknown	Standard K-ε model of turbulence
(Lebouvier et al., 2011)	3D	Unsteady	LTE	No	1	Air 0.32 g/s	Laboratory experimental set-up, nozzle diameter 8mm	Laminar
(Bobzin et al., 2011)	3D, only 120° angle	Steady	LTE	No	3	Ar, 50-70 SLPM	TriplexProTM-200	Laminar
(Baeva and Uhlandt, 2011)	3D	Unsteady	chemical non-equilibrium	No	1	Ar, 8.5 SLPM	typical rod-cathode plasma torch	Standard K-ε model of turbulence
(Bolot et al., 2011)	3D	Steady	LTE	Only anode	1	Ar 35 SLPM plus H2 10 SLPM	ProPlasma HP	Laminar

(Huang et al., 2011)	3D	Unsteady	Improved LTE	No	1	Ar, 50 SLM	Praxair SG-100	Standard K-ε model of turbulence
(Huang et al., 2012)	3D	Unsteady	LTE	No	1	Ar, 50 SLM	Praxair SG-100	Standard K-ε model of turbulence
(Huang et al., 2013)	3D	Unsteady	LTE VS improved LTE	No	1	Ar, 50 SLM	Praxair SG-100	Standard K-ε model of turbulence
(Trelles and Modirkhazeni, 2014)	3D	Unsteady	2T	No	1	Ar, 60 SLPM	Praxair SG-100 nozzle diameter 8mm	No explicit turbulence model
(Guo et al., 2015)	3D	Steady	LTE	No	1	Ar 40 SLPM plus H2 8 SLPM	Sulzer F4	Standard K-ε model of turbulence
(Bobzin and Öte, 2016)	3D, only 120° angle	Steady	LTE	Both	3	Ar, 70 - 180 SLPM	TriplexProTM-200	Shear Stress Transport (SST) turbulence model
(Zhang et al., 2016)	3D	Quasi-steady	LTE	No	1 or 3	Ar, 60 SLPM	Unknown	Laminar
(Liang and Groll, 2018)	3D	Unsteady	2T	Both, specific coupling, simplified sheath model	1	Ar, 60 SLPM	Praxair SG-100	Laminar
(Saifutdinov et al., 2018)	3D	Unsteady	LTE	Both	1	Ar, 2 g/s	Sulzer F4	Unknown
(Modirkhazeni and Trelles, 2018)	3D	Unsteady	2T	No	1	Ar, 40 SLPM	Not mentioned, nozzle diameter 0.0088 m	Unknown

In the majority of the studies which deal with the numerical simulation of electric arc, the mass and momentum conservation equations are the laminar weakly compressible Navier-Stokes equations. However, some models of plasma torches consider the standard K-ε model of turbulence as shown in Table 1 in order to capture the plasma mixing process outside of the torch and in the thick cold boundary layer. The equations will be presented in Chapter II.

Most of the models of electric arcs assume LTE due to a lower computational cost and availability of plasma properties. Increase of available computational resources and further research in plasma properties gave rise to development of models that consider departure from LTE:

- “Improved LTE model”, which considers the electron temperature derived from the LTE temperature and electric field, instead of calculating it in a separate equation (Huang et al., 2013, 2011).
- Models with violated kinetic equilibrium, i.e.  $T_e \neq T_h$ . Such models require solving two separate energy conservation equations for electrons and heavy species coupled by



the energy exchange term. The assumption  $T_e \neq T_h$  is called 2T or PLTE (Boselli et al., 2013; Colombo et al., 2011; Freton et al., 2012; Haidar, 1999; Modirkhazeni and Trelles, 2018; Trelles, 2007; Trelles and Modirkhazeni, 2014). However, in the 2T models assumptions may vary between different authors. The study (Freton et al., 2012) dealt with association of ionization energy, reactive thermal conductivity and volumetric radiative losses to heavy species or electrons.

- Models with violation of chemical and thermal equilibria, for example (Al-Mamun et al., 2010; Baeva and Uhrlandt, 2011). Such models deal with the plasma chemical reactions.

Two specific fields are calculated in electric arc simulation: the electric current density and magnetic field. The computation procedure of these two field varies from one study to another.

The electric current density can be calculated directly through the current continuity equation as in (Yin et al., 2007) or can be a secondary field derived from the solved electric potential as in (Alaya et al., 2016; Felipini and Pimenta, 2015; Freton et al., 2009; Modirkhazeni and Trelles, 2018; Westhoff and Szekely, 1991; Yuan et al., 2004). The boundary condition for the electric current is a significant parameter and has two options: imposed electric current density profile (Neumann boundary condition) and imposed potential on the electrodes boundaries (Dirichlet boundary condition). The boundary condition on the anode surface is usually an uniform zero electric potential, but for example in (Bobzin et al., 2011) the boundary condition on the anode surface is an uniform perpendicular current density, while the cathode boundary condition is zero potential. The problem of an imposed profile of electric current density on the cathode surface is the necessity to first get this profile. Imposed profiles  $j(r)$  at the cathode surface used in various model are:

- Uniform distribution  $j(r) = j_{const} = \frac{I}{\pi R_{cathode\_tip}^2}$  (Westhoff and Szekely, 1991)
- Parabolic profile  $j(r) = j_0 \left( 1 - \left( \frac{r}{R_{arc}} \right)^n \right)$  (Guo et al., 2015; Selvan et al., 2009)
- Exponential profile  $j(r) = j_0 \exp \left( -b \left( \frac{r}{R_{arc}} \right)^n \right)$  (Guo et al., 2015; Jin Myung Park et al., 2004; Trelles et al., 2006; Zhang et al., 2016)

Also, the Dirichlet boundary condition for the electric potential can be used, that is only a value of the electric potential is imposed and recalculated during the unsteady simulation in order to meet the imposed current intensity (Abdo et al., 2017; Baeva and Uhrlandt, 2011; Chemartin et al., 2011; Lebouvier et al., 2011; Zhang et al., 2016).

The self-induced magnetic field can be computed by the Biot & Savart law for magnetic field (1.13). However, this method has a very high computational cost since it requires volume integration throughout the whole domain which has to be done for each mesh element separately (Schlitz et al., 1999a; Speckhofer and Schmidt, 1996).

$$\vec{B}_{self}(\vec{r}) = \frac{\mu_0}{4\pi} \iiint_{domain} \vec{j}(\vec{r}') \times \frac{\vec{r} - \vec{r}'}{|\vec{r} - \vec{r}'|^3} dV \quad (1.13)$$

Where  $\vec{r}$  is the vector from the origin (0,0,0) to the observation point,  $\vec{r}'$  the vector from the origin to the volume element with electric current.

For 3D unsteady simulation of electric arc plasma torch with large detailed mesh the computational cost of such method becomes prohibitively high. That is why it is easier to derive the magnetic field from:

- The electric current density through Ampère's law (1.14) as in (Westhoff and Szekely, 1991) or (1.15) as in (Lowke et al., 1997, 1992; Sansonnens et al., 2000; Zhu et al., 1995, 1992) for axisymmetric 2D models or (1.16) as in (Lisnyak et al., 2017) for 3D models

$$B_\theta(R) = \frac{\mu_0}{R} \int_0^R j_z(r) r dr \quad (1.14)$$

$$\frac{1}{r} \frac{\partial}{\partial r} (r B_\theta(r)) = \mu_0 j_z(r) \quad (1.15)$$

$$\nabla \times \frac{1}{\mu_0} \vec{B}(\vec{r}) = \vec{j}(\vec{r}) \quad (1.16)$$

- The magnetic vector potential (1.17) which is used to deduce the magnetic field distribution. The advantage of using the magnetic vector potential is its ability to be solved by the same algorithms as the other variables of CFD simulation. It is used for sophisticated 3D models with fine meshes.

$$\begin{aligned} \text{div}(\nabla \vec{A}(\vec{r})) &= -\mu_0 \vec{j}(\vec{r}) \\ \vec{B}_{self}(\vec{r}) &= \nabla \times \vec{A}(\vec{r}) \end{aligned} \quad (1.17)$$

In the latter case the magnetic vector potential is a solved variable and requires some boundary conditions which are not consensus among the researchers. The two main methods to set the boundary conditions for the magnetic vector potential are:

- A zero value of the magnetic vector potential at the boundaries distant from the electric arc since the magnetic vector potential should be zero at infinity. At all the other boundaries that are close to the arc, a zero flux of magnetic vector potential is imposed (Liang and Groll, 2018). Referred to as PVNF in (Freton et al., 2011).
- The Biot & Savart formulation for the magnetic vector potential. The boundary value is calculated by the formula (1.18) (Jin Myung Park et al., 2004; Zhang et al., 2016). Referred to as BS.

$$\vec{A}_{boundary}(\vec{r}) = \frac{\mu_0}{4\pi} \iiint_{domain} \frac{\vec{j}(\vec{r}')}{|\vec{r} - \vec{r}'|} dV \quad (1.18)$$

Where  $\vec{r}$  is the vector from the origin (0,0,0) to the observation point,  $\vec{r}'$  the vector from the origin to the volume element with electric current.

A comparison of these two approaches was described in details in (Freton et al., 2011). Freton et al. showed that, when the finite volume method (FVM) is used, the Biot & Savart (BS) approach provides more reasonable results and allows using smaller domains while retaining good accuracy, while the PVNF approach tends to have numerical distortion and lead to an overestimation of the magnetic field at the corners of the domain. However, (Abdo, 2018) showed that in finite element method (FEM) the PVNF approach is enough for reasonable prediction of the magnetic field. In addition, (Baeva, 2017) stated that the model developed in the computational platform COMSOL Multiphysics (COMSOL Inc., 2019), which applies the FEM, even with the PVNF approach provides results in perfect agreement with the analytical solution. The BS approach is also used in some models of circuit breakers electric arc; for example in (Piqueras et al., 2008).

Another way to make the predictions more realistic is the inclusion of electrodes in the computational domain. It requires a special treatment of the plasma-metal coupling but removes the problem of choosing some electric current density profile at the cathode surface. On the contrary, the included cathode helps to predict the proper electric current density profile at the cathode surface (Liang and Groll, 2018). In addition, the inclusion of electrodes into the computational domain improves the prediction of the self-induced magnetic field (Freton et al., 2011) and makes it possible to predict the electrode temperature (Alaya et al., 2016; Lisnyak, 2018; Lowke and Tanaka, 2006). The first steps of cathode-arc coupling were done in (Lowke et al., 1992; Zhu et al., 1992). Comprehensive improvements of the cathode-arc coupling theory was latter suggested in (Benilov and Marotta, 1995). The anode-arc coupling in order to predict the anode temperature was considered in (Zhu et al., 1995). The study with an optimized model (Lowke et al., 1997) described the thermal fluxes to the electrodes for electrode temperature prediction. However the researchers simplified the non-equilibrium sheaths which are a significant part of any arc discharge and might have a significant contribution to voltage and thermal flux to electrodes (Benilov, 2008).

The coupling of the metal electrode and plasma through the continuity of temperature in LTE simulation gives rise to the problem of too low electrical conductivity of the plasma-forming gas at the temperature of metal surface. Several solutions have been proposed to overcome this problem:

- Large enough (around diffusion length of electrons in the arc) cells adjacent to the electrode surface to include the effect of ambipolar diffusion and thus have a high enough temperature for sufficient electrical conductivity in the plasma cells (Lowke et al., 1997; Lowke and Tanaka, 2006). At the same time the cells should be not too large in order to capture the high temperature gradient near the electrode surface. For example, 20 to 100 $\mu$ m if the temperature near the electrode is around 10 to 20 kK. The higher temperature near the electrode is, the smaller the cells adjacent to the electrode can be in an LTE model.
- Take into account the ambipolar diffusion effects on the electrical conductivity and electric current (Lowke and Tanaka, 2006; Sansonnens et al., 2000)
- An artificially high electrical conductivity imposed in the first layer of cells adjacent to the electrode surface (Alaya et al., 2016; Liang and Groll, 2018; Trelles et al., 2006)

- A model of the non-equilibrium sheath combined with an LTE model of the arc (Lisnyak, 2018)

An important part of the electric arc dynamics simulation is the prediction of the take-over and restrike modes. The arc rolling back or restriking is a highly non-equilibrium process including deviation of kinetic and ionization equilibria. Even though the temperature behind the arc attachment is rather low, the electrical conductivity there remains at a very substantial level (Nemchinsky, 2015). A simplified simulation of this process was presented in (Moreau et al., 2006; Trelles, 2007).

## **I.7.2. Models dealing with control of anode arc attachment rotation**

These models tackle either a swirling gas injection and/or the use of an external magnetic field to control the movement of the arc on the anode wall.

### **I.7.2.1. Swirling gas injection**

In order to estimate the degree of swirling inside the plasma torch, the concept of swirl number given by formula (1.19) was presented in (Westhoff and Szekely, 1991).

$$Sw = \frac{\int_S \rho u w r dS}{R_0 \int_S \rho u^2 dS} \quad (1.19)$$

Where  $\rho$  is the plasma density;  $u$  is the axial velocity component;  $w$  is the azimuthal velocity component;  $S$  is the cross section area where the swirl number is calculated;  $r$  is the radial coordinate of the surface element  $dS$ ;  $R_0$  is a characteristic radius of the channel, used for normalization.

The swirl number is a ratio of axial flux of azimuthal momentum to the axial flux of axial momentum (Felipini and Pimenta, 2015). Felipini and Pimenta showed that the swirling gas injection has an effect on the plasma temperature and axial velocity distributions. However, this effect is not linearly dependent on the swirl number. In particular, in the low range of  $Sw$ , an increase of flow swirling barely has any effect, while for high values of  $Sw$ , the intensification of swirling yields significant change in the flow temperature distribution. For the plasma torch simulated in (Felipini and Pimenta, 2015) it was predicted that the swirl number should be above 3 in order to have any impact. However, this certain threshold value of the swirl number should depend on the torch geometrical configuration.

### **I.7.2.2. External magnetic field**

The simulation of free-burning electric arc behavior in transverse external magnetic field was presented in (Abdo et al., 2017; Schlitz et al., 1999b). The simulation of the arc rotation in well-type cathode plasma torch was presented in (Freton et al., 2009; Jin Myung Park et al., 2004) and in plasma torch with conic-tip rod-type cathode in (Baeva and Uhrlandt, 2011; Jin Myung Park et al., 2004). However to the best of author's knowledge, the simulation of arc rotation in an axial external magnetic field in commercial thermal spray plasma torch is not implemented yet.

### **I.7.3. Models validation**

The predictions of plasma torch models can be validated through comparison with experimental measurements of mean voltage along with its fluctuations, plasma torch thermal efficiency, and plasma jet temperature and velocity. The torch voltage and its fluctuations are important parameters of plasma torch operation and stability since they directly affect the total power input to the plasma gas. However, the voltage is an integral parameter of the whole torch and does not reflect local phenomena in the different parts of the torch.

The temperature distributions are generally measured by using optical diagnostics as emission spectroscopy, Thomson and Rayleigh scattering or coherent anti-Stokes Raman spectroscopy. Tomographic methods make it possible to get a spatially-resolved temperature distribution (Coudert et al., 2002; Landes, 2006; Mauer et al., 2011). Also, enthalpy probes can be used in the plume of the plasma jet (Fincke et al., 1993; Rahmane et al., 1995). The velocity of the plasma jet can be determined from the plasma jet luminosity fluctuations time of flight (Planche et al., 1998), drawn from the velocity of small particles seeding the plasma jet (Pfender et al., 1991) or by using Pitot tube (Capetti and Pfender, 1989) if the plasma density is known. Also, high-speed cameras can be used to capture the anode arc attachment behavior (Bobzin et al., 2019; Duan and Heberlein, 2002; Wang et al., 2019a) or the arc behavior inside the torch through a glass gap between the electrodes (Zhukov et al., 1981).

Finally, the predicted arc attachment shape and behavior can be compared with the erosion traces on the used hardware of the corresponding plasma torch operated with one set of conditions similar to that used in the numerical simulations.

### **I.8. Approach of this study: Selection of the plasma torch and numerical model**

The non-exhaustive survey of the literature presented above shows that the numerical simulation of the operation of a DC plasma spray torch has made much progress since the 90's and can be a useful tool to better understand the effect of the operating parameters and even torch geometry on the plasma jet issuing from the torch. The most common approach to predict the processes inside the plasma torch is the simulation of electric arc under Local Thermal Equilibrium (LTE), which means equality of electron and heavy species temperature. Such approach has a lot of examples and comprehensive accumulated experience among various laboratories.

Further development of the plasma torch model is intended to encompass the thermal disequilibrium between electrons which obtain energy from Joule heating and heavy species which obtain energy from exchange with electrons. The developed LTE model is fully valid only inside the arc core, while consideration of departure from thermal equilibrium is aimed to better describe the distribution of plasma properties also at the areas with high gradient of temperature, namely arc fringes and in some space around the electrode arc attachments.

Departure from the thermal equilibrium is conditioned by unbalance between heat diffusion and heat exchange between electrons and heavy species. Electrons have higher thermal conductivity and thus high temperature electrons diffuse much faster out of the arc than they lose their kinetic energy in collisions with atoms and ions. Thus in the vicinity of the arc there are abundant high temperature electrons which increase electrical conductivity in this area even though the heavy species are cold there. Under the LTE assumption the plasma with temperature below 5000K is assumed to have almost zero electrical conductivity. Meanwhile in the 2T model the intense diffusion of high temperature electrons increases the electrical

conductivity of the space around the electrode arc attachments. Higher electrical conductivity upstream from the anode arc attachment will allow the electric current to pass through the cold boundary layer gas before it arrives to the anode arc attachment itself. Additional Joule power in the cold boundary layer prior to the anode arc attachment will help to simulate the disequilibrium phenomenon described in (Nemchinsky, 2015) and it will help to improve the prediction of the anode arc attachment type, size and shape.

Departure from thermal equilibrium requires solving two separate thermal variables for electrons and heavy species, e.g. two temperatures or two enthalpies, hence the name of the 2T model. Consideration of the electrons temperature separately from the heavy species gives rise to another problem: inability to predict the electron temperature far from the arc where there is no electric field, the gas is cold and not ionized. Due to almost zero number density of electron in the cold gas far from the arc, the continuum hypothesis is not valid anymore, the concept of electron temperature becomes irrelevant, and it is clear that the model will not be able to describe the degree of thermal disequilibrium in the periphery of the outlet tank and in the cathode cavity near the gas inlet.

Despite the growing interest in cascaded-anode plasma torches, the majority of existing models concern conventional plasma spray torches with the self-setting arc length but very few models consider the actual geometry of commercial plasma torches and, to the best of author's knowledge, very few, if any, deal with the Helmholtz fluctuations.

### **I.8.1. Plasma torch**

The selected torch is the SinplexPro™ torch manufactured by Oerlikon Metco. It has a cascaded anode and one cathode.

This torch was chosen because:

- The cascaded anode yields a more stable operation than that of self-setting plasma torches. In conjunction with a single cathode, this configuration makes it possible to focus on the physics simulation rather than on complex geometry.
- Till now, very few numerical studies deal with plasma spray torches with cascaded anode and essentially for TriplexPro™ (Bobzin et al., 2011; Bobzin and Öte, 2016; Molz et al., 2007; Muggli et al., 2007). Also, very few measurements have been performed on the plasma jet issuing from the SinplexPro™ plasma torch. Getting an insight into the arc and plasma jet formation inside this plasma torch would provide useful ground for torch operation.
- Finally, the IRCER laboratory is going to use the SinplexPro™ torch to develop multifunctional coatings for aerospace industrial applications. This development requires a deep knowledge of the time and space-variation of the characteristics of the fine particles processed in the plasma jet. This begins with the temperature and velocity fields of this plasma jet as a function of the operating parameters.

### **I.8.2. Plasma torch operation model**

The idea is to gather the best and well-established features from the existing models and apply them to the commercial plasma torch SinplexPro™. The developed model will be used for the analysis of the arc behavior and, eventually, improvements of the plasma torch design to increase the process reproducibility and extend the lifetime of the plasma torch parts.

This model should have the following features:

- Use an open-source software in order to have scalability and flexibility. Free software allows using cloud computing without buying specific license. The access to the source code allows implementing further improvements faster than it could be done by the private companies. The chosen software is Code\_Saturne developed by EDF; it has embedded robust and customizable parallelism.
- For a given torch geometry, provide stable and smooth simulation for various torch operating parameters. This requires, in particular, advanced boundary conditions for the magnetic vector potential in order to predict a reliable magnetic field, and also a fine mesh with a large number of cells.
- Be able to predict the arc dynamics inside the plasma torch and simulate various methods to reduce anode erosion. This goal will be achieved through the gas swirling injection and external magnetic field created by a coil.
- Include the electrodes into the computational domain. This makes it possible to take into account the electric current inside the electrodes, its effect on the magnetic field and eventually improve the prediction of velocity distribution near the cathode. Including the electrodes will allow later to try new geometry configurations of the torch.
- Estimate the effect of departure from LTE on arc simulation. For that a 2T model with separate thermal equations for electrons and heavy species will be developed.
- Further development of the plasma torch model is intended to encompass the thermal disequilibrium between electrons, which obtain energy from Joule heating and heavy species which obtain energy from exchange with electrons.

The model will deal with argon as plasma-forming gas as the computational algorithm for calculating its thermodynamic and transport properties at LTE and with a high degree of disequilibrium between the electrons and heavy species is available at IRCER.

# Chapter II. LTE and 2T models of plasma torch operation

---





## II.1. Introduction

The purpose of plasma torch simulation is the prediction of plasma temperature and velocity fields. They are both essential in plasma spraying since they condition the processing of the coating particles. The plasma temperature also determines the plasma composition, namely the number densities of electrons, atoms and ions. In the hottest zones of electric arc plasma torches, the plasma is almost fully ionized and the number density of neutral atom is negligible (Colombo et al., 2008; Freton et al., 2012; Trelles et al., 2007). The ions may have charges up to +4.

The heavy species, e.g. atoms and ions, reach the Maxwellian distribution of thermal energy and the same temperature quickly due to their close mass which makes collisions very efficient way of kinetic energy exchange (Boulos et al., 1994). Also, the heavy species have a sufficiently high number density in the whole considered temperature range, whereas the electron number density is practically zero at low temperature and their temperature may deviate significantly from that of the heavy species. This imposes limitations on the electron temperature computation and requires special treatment in the areas far from the arc where the gas is usually cold and has low degree of ionization.

Most of known models of plasma torch deal with argon as a plasma-forming gas. Consequently, simulation with this gas is well established, plasma properties are available and their computation is verified (Chazelas et al., 2017). The present study is intended to elaborate a flexible model which will function correctly with SinplexPro™, take into account its detailed geometry and be able to describe more complex physics: departure from LTE. Therefore the developed model deals with argon as initial step in study of various plasma-forming gases. Additional advantage of argon as a plasma forming gas for the model is presence of the computational algorithm for argon properties. Other gases can be studied after the model is verified with argon.

Nowadays, the magnetohydrodynamic (MHD) approach is generally used to predict the complex dynamic behavior of the electric in a DC plasma spray torch. This chapter deals with the two models developed in this study. The first assumed LTE in the whole gas phase; the second considers two different temperatures for the electrons and heavy species.

The chapter first presents the main assumptions used for the arc models. It then describes the LTE and 2T arc models used in this study. As the behavior of the plasma is influenced by the electromagnetic field and, at the same time, its behavior changes the electromagnetic field, these models consist in coupling the equations of fluid mechanics with equations of electromagnetism for an anisothermic fluid. The set of equations is solved by using the open-source CFD software Code-Saturne which imposes to express the energy conservation equation in enthalpy and therefore requires some additional effort to implement the 2T model. Finally, the chapter includes the numerical features necessary for the simulation: mesh, boundary conditions, initialization and fluid-electrode coupling.

## II.2. Model assumptions

The main assumptions of the arc models are the following:

- Continuum hypothesis is valid for the simulated flow. The temperatures of the different species are not necessarily equal. However the idea of temperature and bulk plasma velocity implies the continuum hypothesis that is the association of bulk macroscopic properties (e.g. temperature, velocity, etc.) to infinitesimal nonzero volume. The

continuum hypothesis requires the number of particles in the element of volume to be sufficient for averaging in the bulk properties computation (McDonough, 2009). The order of magnitude of the total number density of plasma particles in the 300 - 35000 K temperature range extends from  $10^{22}$  to  $10^{25} \text{ m}^{-3}$  which allows to consider the flow on microscales. In other words, a volume element of about  $1 \mu\text{m}^3 = 10^{-18} \text{ m}^3$  is suitable for the plasma generated inside the plasma torch. At the same time, averaging on nanoscales would produce unreliable results.

- The plasma flow is subsonic. The speed of sound in argon, computed by Professor Pascal André using the methods presented in (André et al., 2016), is 3117.6 m/s for 20000 K, 3191.7 for 22000 K, 3563.9 for 25000 K and 4430 m/s for 30000 K. Thus the plasma flow, whose predicted velocity is around 2500 m/s and temperature at the nozzle exit is around 22000 K, is subsonic.
- The plasma is dilatible but weakly compressible. In other words, plasma properties depend on temperature but not on pressure. The time derivative of pressure in the energy conservation equations is neglected. The criterion for incompressibility is that the flow speed should be much less than the sound speed. Specifically, the Mach number  $Ma$  (flow speed/ sound speed) must obey  $Ma^2 \ll 1$ . The maximum value of  $Ma^2$  in the model is around 0.6 in the plasma flow issuing from the torch, meanwhile inside the torch the value of  $Ma^2$  is below 0.3. Thus, the incompressibility of the medium is verified in most of the gas phase.
- The plasma flow is laminar. In an arc plasma, the fluctuations may result more from the interaction between the gas flow and magnetic force than from shear stress (Delalandre et al., 1994; Gonzalez, 1992). In addition, the arc itself has a very viscous outside layer which tend to suppress the turbulence. As a rough approximation, the channel of the plasma torch used in this work has a diameter of 9 mm and the cold boundary layer between the arc and the wall is around 1 mm (Duan and Heberlein, 2002), the velocity of the cold gas in the boundary layer ranges between 0 and 200 m/s, its density between 1 and  $0.08 \text{ kg/m}^3$  and dynamic viscosity between  $5 \cdot 10^{-5}$  and  $2 \cdot 10^{-4} \text{ kg/m}\cdot\text{s}$ . For such parameters the Reynolds number of the boundary layer gas is less than 300, while the transition to turbulent boundary flow happens around  $Re=5 \cdot 10^5$  (Incropera and DeWitt, 1990). That is why the plasma flow inside the plasma torch is usually considered laminar. In addition, the plasma torch selected for this study has a cascaded anode which stabilizes the arc length, the arc and voltage fluctuations are relatively low compared to the conventional plasma torches. Some models, however, consider  $K-\varepsilon$  turbulence model due to specificities of the task and severe arc fluctuations (Baeva and Uhrlandt, 2011; Guo et al., 2015; Jin Myung Park et al., 2004; Selvan et al., 2009). Also, high-power plasma torches with large channels (Zhukov et al., 1981) may require turbulent simulations.
- The modelled plasma is assumed to be either in LTE or in ionization equilibrium in the 2T model.
- The plasma is optically thin;
- Gravitation is negligible;
- Viscous dissipation is negligible;
- The simulated plasma is assumed to be electrically neutral;

- Temporal changes of magnetic and electric field are considered slow. In other words, the derivatives of magnetic and electric fields are cancelled within the Maxwell equations;
- The magnetic permittivity of electrodes is the same as the permittivity of vacuum.

### II.3. LTE Model governing equations

The governing equations of an anisothermic fluid involve the mass, momentum and energy conservation equations. For an electric arc, they can be written as (2.1), (2.2) and (2.7).

$$\underbrace{\frac{\partial \rho}{\partial t}}_{\text{transient term}} + \underbrace{\text{div}(\rho \vec{u})}_{\text{advection}} = 0 \quad (2.1)$$

$$\underbrace{\frac{\partial}{\partial t}(\rho \vec{u})}_{\text{transient term}} + \underbrace{\text{div}(\rho \vec{u} \otimes \vec{u})}_{\text{advective terms}} = -\nabla p + \underbrace{\text{div}(\vec{\tau})}_{\text{viscous forces}} + \underbrace{(\vec{\Gamma}_{\text{expl}} + \vec{\Gamma}_{\text{impl}} \vec{u})}_{\text{user imposed source term}} + \underbrace{\vec{j} \times \vec{B}}_{\text{Lorentz force}} \quad (2.2)$$

Where  $\rho$  is the plasma density;  $\vec{u}$  the plasma velocity;  $p$  the plasma pressure;  $\mu$  the dynamic viscosity, which is dependent on the plasma temperature;  $\vec{\tau}$  the viscous stress tensor given by the formula (2.3);  $\vec{j}$  the electric current density;  $\vec{B}$  the magnetic field.

$$\vec{\tau} = \mu \left( \vec{\nabla} \vec{u} + \vec{\nabla} \vec{u}^T - \frac{2}{3} \text{tr}(\vec{\nabla} \vec{u}) \vec{Id} \right) \quad (2.3)$$

The last term of the equation (2.2) is the Lorentz force, an inherent source term in the momentum conservation equation for electric arc models. In the current model it depends only on the electric current density and magnetic field, but not on the plasma velocity. The contribution of plasma velocity into electric current and thus into the Lorentz force is assumed to be negligible, but was included for example in (Baeva and Uhrlandt, 2011).

The LTE model utilizes the plasma composition as described in the Annex A. The LTE assumption implies that a single enthalpy  $h$  includes all the particles. The plasma enthalpy  $h$  and density  $\rho$  are computed by the formulae (2.4) and (2.5) for this plasma composition. The plot of the plasma density is given in Annex B. The argon plasma specific heat  $C_p$  is computed by the formula (2.6).

$$h = \frac{5}{2} \frac{k_B}{\rho} n_e T + \frac{5}{2} \frac{k_B}{\rho} \sum_{\zeta=0}^N n_h^{\zeta+} T + \frac{1}{\rho} \sum_{\zeta=0}^N n_h^{\zeta+} E_{\zeta} \quad (2.4)$$

$$\rho = n_e m_e + \sum_{\zeta=0}^N n_h^{\zeta+} m_h^{\zeta+} \quad (2.5)$$

$$C_p = \frac{\partial h}{\partial T} \quad (2.6)$$

Where  $n_e$  and  $m_e$  are the electron number density and mass respectively;  $n_h^{\zeta+}$  and  $m_h^{\zeta+}$  the number density and mass of the ion  $Ar^{\zeta+}$ ;  $E_\zeta$  the ionization energy of the particle  $Ar^{(\zeta-1)+}$  to  $Ar^{\zeta+}$ ;  $k_B$  the Boltzmann constant;  $N$  the maximum ion charge in the plasma composition.

The computed enthalpy as a function of temperature is illustrated in Figure 17.

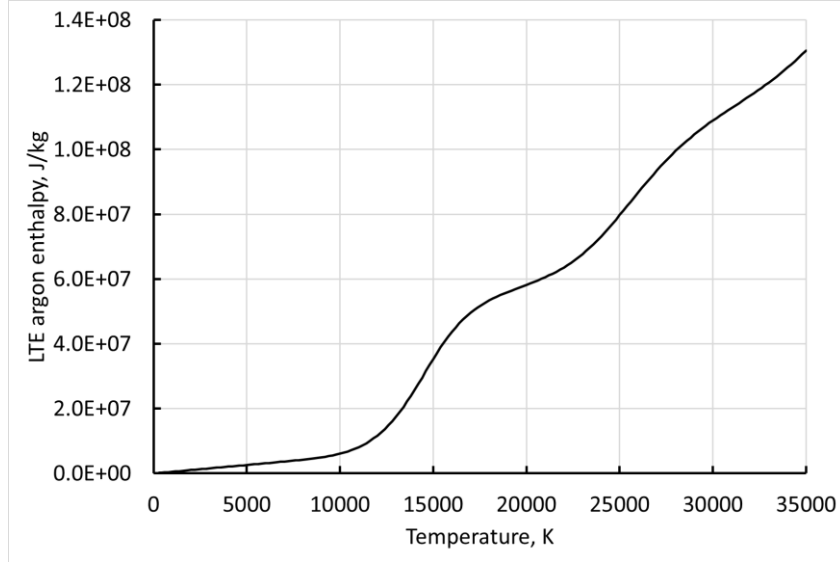


Figure 17 LTE argon plasma enthalpy as a function of temperature

The energy conservation equation (2.7) is expressed in terms of enthalpy  $h$ .

$$\frac{\partial(\rho h)}{\partial t} + \text{div}(\rho \vec{u} h) = \text{div}\left(\frac{\lambda}{C_p} \vec{\nabla} h\right) + Q_J - Q_R \quad (2.7)$$

Where  $\lambda = \lambda_e^{tr} + \lambda_h^{tr} + \lambda_r$  is the plasma thermal conductivity which consist of the electron and heavy species translational thermal conductivity and reactive thermal conductivity;  $Q_J = \vec{j} \cdot \vec{E}$  the Joule power;  $Q_R$  the volumetric net radiation energy losses computed by a simplified formula taken from (Beulens et al., 1991). Some arc models (Douce et al., 2003; Lago et al., 2004) also take into account the absorption of plasma by considering a few wavelength bands.

The predicted enthalpy is then translated to a single LTE temperature using the lookup table with the values presented in Figure 17. The plasma properties, i.e. depend on the temperature, their computation is given in Annex B.

A lookup table contains the data depending on a single parameter (in this case LTE temperature  $T$ ) with a given step. In the present model the data are  $h(T)$ ,  $\rho(T)$ ,  $C_p(T)$ ,  $\lambda(T)$ ,  $\mu(T)$ ,  $\sigma(T)$ ,  $Q_R(T)$ . The temperature step is 200 K. For every single cell each property is interpolated to the temperature of the cell.

The plasma properties computation is given in Annex B, given that  $T_e = T_h$ , in other words the same temperature for all the particles.

The equation used to calculate the electric potential  $\varphi$  is the electric current continuity equation (2.8) written in terms of electric potential under the assumption of electric neutrality.

$$\text{div}(\sigma \nabla \varphi) = 0 \quad (2.8)$$

The values derived from the solved electric potential are the electric field  $\vec{E}$  (2.9), electric current  $\vec{j}$  (2.10), and Joule power  $Q_J$  (2.11).

$$\vec{E} = -\nabla \varphi \quad (2.9)$$

$$\vec{j} = \sigma \vec{E} = -\sigma \nabla \varphi \quad (2.10)$$

$$Q_J = \vec{j} \cdot \vec{E} = \sigma \nabla \varphi \cdot \nabla \varphi \quad (2.11)$$

Where  $\sigma$  is the electrical conductivity of the plasma gas.

The general equation that couples the electric current and the magnetic field is the Ampère's circuital law which is presented by the equation (2.12).

$$\nabla \times \vec{B}(\vec{r}) = \mu_0 \left( \vec{j}(\vec{r}) + \varepsilon_0 \frac{\partial \vec{E}(\vec{r}, t)}{\partial t} \right) \quad (2.12)$$

Where  $\mu_0$  is the magnetic permeability;  $\varepsilon_0$  the vacuum permittivity.

In this study, the magnetic field is derived from the magnetic vector potential  $\vec{A}$  which is introduced as (2.13).

$$\vec{B}(\vec{r}) = \nabla \times \vec{A}(\vec{r}) \quad (2.13)$$

Thus the Ampère's circuital law can be rewritten in terms of magnetic vector potential as follows:

$$\nabla \times \nabla \times \vec{A}(\vec{r}) = \mu_0 \left( \vec{j}(\vec{r}) + \varepsilon_0 \frac{\partial \vec{E}(\vec{r}, t)}{\partial t} \right)$$

Reformulating the curl of a curl of a vector field yields the following formula:

$$\nabla \left( \nabla \cdot \vec{A}(\vec{r}) \right) - \nabla^2 \vec{A}(\vec{r}) = \mu_0 \left( \vec{j}(\vec{r}) + \varepsilon_0 \frac{\partial \vec{E}(\vec{r}, t)}{\partial t} \right)$$

Taking into account the Coulomb gauge (2.27) and the assumption of slow changes in the electric field, the equation for the magnetic vector potential can be written as (2.14).

$$\text{div} \left( \nabla \vec{A}(\vec{r}) \right) = -\mu_0 \vec{j}(\vec{r}) \quad (2.14)$$

This approach was used in the majority of the recent unsteady 3D models of electric arcs. Also it was shown in (Freton et al., 2011) that such magnetic field simulation along with the electrodes included in the computational domain and correct boundary conditions for the magnetic vector potential provides quite accurate predictions of the magnetic field.

All the plasma transport properties used in this study, i.e. thermal and electrical conductivities, viscosity, volumetric net radiation losses, are given in the Annex B.

#### II.4. Modification of the enthalpy equations for 2T model

As the energy conservation equation in this study is expressed in enthalpy, the governing energy equations of the 2T model have to be written in terms of enthalpy of electrons and heavy species. Then the two temperatures  $T_e$  and  $T_h$  are drawn from the solved enthalpies  $h_e$  and  $h_h$  and the temperature-dependent plasma properties can be calculated. These plasma properties are then used for the following time step.

The enthalpy of the argon plasma including electrons and heavy species is expressed in the formula (2.15). It is logical to assume that the first term on the right hand side of the equation, which includes the kinetic energy of the heavy species can be attributed to their enthalpy. Similarly, the third term includes the kinetic energy of electrons and can be attributed to their enthalpy. The last term is related to the internal degree of freedom associated with the atomic structure of atoms and is negligible in the considered temperature range from 300 to 35000 K. The attribution of the second term on the right hand side of the equation (2.15), which includes the ionization energy of plasma to the heavy species or electrons is still debatable. (Freton et al., 2012) showed that for a free burning transferred arc the association of the ionization energy to electrons is physically correct and based on the Boltzmann equation. However several 2T models of plasma torches, e.g. (Liang and Groll, 2018; Modirkhazeni and Trelles, 2018; Trelles, 2007) consider the opposite formulation: the ionization term is associated to the heavy species.

$$\begin{aligned}
 h_h(T_h) + h_e(T_e) = & \\
 = & \underbrace{\frac{5 k_B}{2 \rho} \sum_{\zeta=0}^N n_h^{\zeta+} T_h}_{\text{kinetic energy of heavy species}} + \underbrace{\frac{1}{\rho} \sum_{\zeta=0}^N n_h^{\zeta+} E_{\zeta}}_{\text{ionization energy}} + \underbrace{\frac{5 k_B}{2 \rho} n_e T_e}_{\text{kinetic energy of electrons}} + \underbrace{\frac{k_B}{\rho} \sum_{\zeta=0}^N n_h^{\zeta+} T_e^2 \frac{\partial \ln Q_{\zeta}^{\text{int}}(T_e)}{\partial T_e}}_{\text{negligible term related to the internal degrees of freedom}}
 \end{aligned} \quad (2.15)$$

Where  $n_e$  and  $m_e$  are the electron number density and mass respectively;  $n_h^{\zeta+}$  and  $m_h^{\zeta+}$  the number density and mass of the ion  $Ar^{\zeta+}$ ;  $E_{\zeta}$  the ionization energy of the particle  $Ar^{(\zeta-1)+}$  to  $Ar^{\zeta+}$ ;  $k_B$  the Boltzmann constant;  $Q_{\zeta}^{\text{int}}(T_e)$  the internal partition function for the ion  $Ar^{\zeta+}$ ;  $\rho$  the plasma density;  $N$  the maximum ion charge in the plasma composition.

In the present study both formulations are studied. The first one is referred to as 2T(I) and considers the ionization term as a part of the heavy species enthalpy similarly to (Colombo et al., 2011; Modirkhazeni and Trelles, 2018; Trelles, 2007; Trelles and Modirkhazeni, 2014). The enthalpies of heavy species and electrons in the 2T(I) model are then expressed by the formulas (2.16) and (2.17), respectively.

$$2T(I): \quad h_h = \frac{5 k_B}{2 \rho} \sum_{\zeta=0}^N n_h^{\zeta+} T_h + \frac{1}{\rho} \sum_{\zeta=0}^N n_h^{\zeta+} E_{\zeta} \quad (2.16)$$

$$2T(I): \quad h_e = \frac{5 k_B}{2 \rho} n_e T_e \quad (2.17)$$

The second formulation according to (Freton et al., 2012) considers the ionization term as a part of the electron enthalpy similarly to (Al-Mamun et al., 2010; Boselli et al., 2013; Haidar, 1999) and is referred to as 2T(II). The heavy species and electron enthalpies in the 2T(II) model are then expressed by the formulas (2.18) and (2.19), respectively.

$$2T(\text{II}): \quad h_h = \frac{5}{2} \frac{k_B}{\rho} \sum_{\zeta=0}^N n_h^{\zeta+} T_h \quad (2.18)$$

$$2T(\text{II}): \quad h_e = \frac{5}{2} \frac{k_B}{\rho} n_e T_e + \frac{1}{\rho} \sum_{\zeta=0}^N n_h^{\zeta+} E_{\zeta} \quad (2.19)$$

The plasma composition is given in Annex A. The plasma properties computation is given in Annex B.

The dependencies of the 2T(I) enthalpies  $h_h$  and  $h_e$  on temperature for various values of  $\theta = T_e / T_h$  are illustrated in Figure 18. The dependencies of the 2T(II) enthalpies  $h_h$  and  $h_e$  on temperature for various values of  $\theta = T_e / T_h$  are illustrated in Figure 19. All the computed data for the values of  $\theta$  are stored in the lookup tables and later used to determine the temperatures  $T_e$  and  $T_h$  and disequilibrium degree  $\theta: h_e, h_h \rightarrow T_e, T_h, \theta$ .

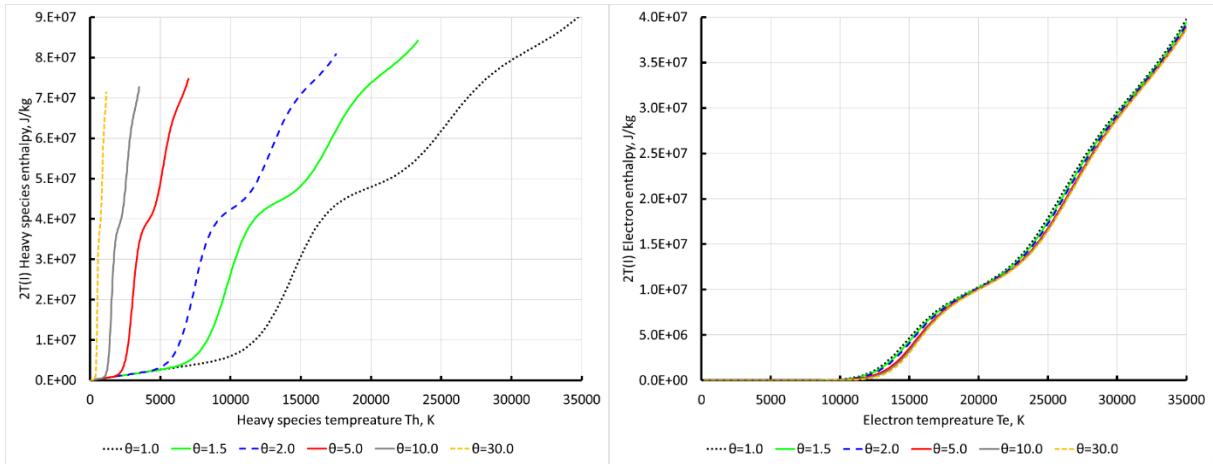


Figure 18 Computed heavy species and electron enthalpy in the **2T(I)** model

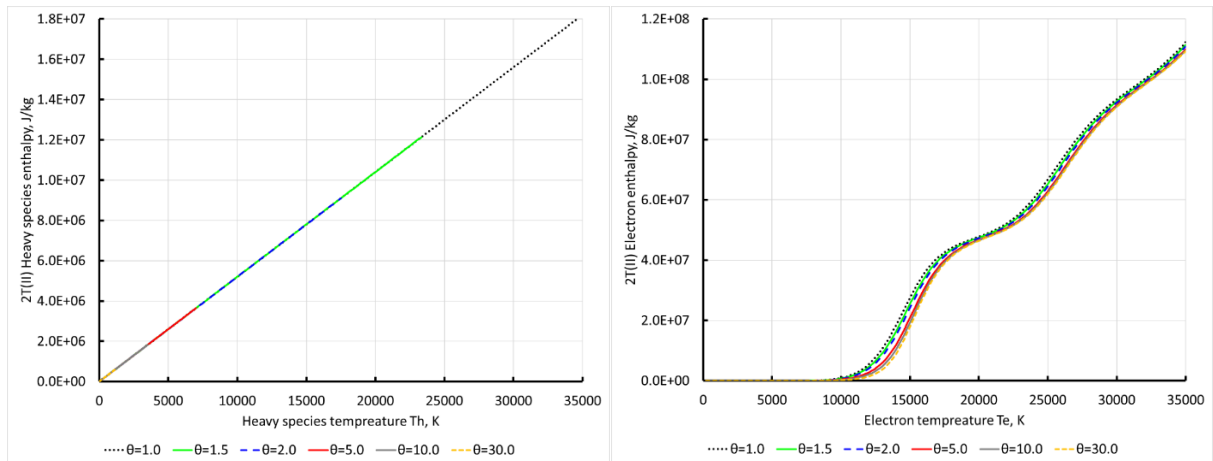


Figure 19 Computed heavy species and electron enthalpy in the **2T(II)** model



The energy conservation equation for electrons is given by the formula (2.20). The source of energy for electrons is the Joule heating  $Q_J = \vec{j} \cdot \vec{E}$  while the losses are the energy exchange with the heavy species  $Q_{exchange}$  and continuum radiation  $\delta_e Q_R$ .

$$\frac{\partial}{\partial t}(\rho h_e) + \text{div}(\rho \vec{u} h_e) = \text{div}\left(\frac{\lambda_e}{C_p^e} \nabla h_e\right) + Q_J - \delta_e Q_R - Q_{exchange} \quad (2.20)$$

The energy conservation equation for heavy species is given by the formula (2.21). The source of energy for heavy species is the energy exchange with electrons  $Q_{exchange}$  while the loss is the line radiation  $(1 - \delta_e) Q_R$ .

$$\frac{\partial}{\partial t}(\rho h_h) + \text{div}(\rho \vec{u} h_h) = \text{div}\left(\frac{\lambda_h + \lambda_r}{C_p^h} \nabla h_h\right) - (1 - \delta_e) Q_R + Q_{exchange} \quad (2.21)$$

The total volumetric net radiation loss  $Q_R$  is the same as in the LTE model but in the 2T model it is distributed between the equations (2.20) and (2.21) as it was suggested in (Freton et al., 2012). The continuum contribution of radiation is assigned to electrons, its share is  $\delta_e$  which depends on electron temperature with the values taken from (Erraki, 1999). The rest of the volumetric net radiation losses is due the absorbed and non-absorbed lines and assigned to the heavy species as an energy loss term. The values of  $\delta_e$  from the continuum contribution (black line) and  $(1 - \delta_e)$  from both line contributions (green and red lines) are given in Figure 20.

In the present model, the coefficient  $\delta_e$  and volumetric net radiation loss depend on the electron temperature for both electron and heavy species enthalpies. The use of  $T_e$  as a parameter for these values is acceptable since in the areas with significant volumetric net radiation losses  $T_e \approx T_h$ ;  $\theta = T_e / T_h \approx 1$ , i.e. the electric arc itself and plasma jet where both electron and heavy species temperature are above 10000 K.

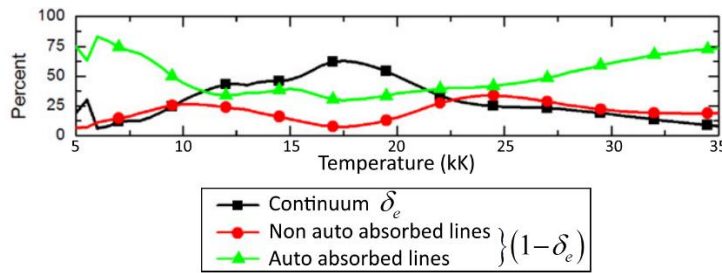


Figure 20 Lines and continuum radiation shares in argon plasma (Erraki, 1999)

An important issue of 2T arc modelling addressed in (Freton et al., 2012) about the association of reactive thermal conductivity to electrons or to heavy species is beyond the scope of the present study. However, up to now no acceptable results with reactive thermal conductivity associated to the electrons were obtained for the model of SimplexPro™ plasma torch. Thus, in this study the idea presented in (Trelles, 2007) was followed: the reactive thermal conductivity is associated to the heavy species.

The reactive thermal conductivity is defined with respect to the gradient of the electron temperature. Thus, in general, the reactive thermal conductivity, if assigned to the heavy species temperature gradient, should be multiplied by  $\theta = T_e / T_h$ . However, in the temperature range in which  $\lambda_r$  has significant values, the plasma is close to LTE, therefore  $\theta = T_e / T_h$  is usually close to 1. Hence, in the current study multiplication of  $\lambda_r$  by  $\theta$  does not change the simulation result.

The formulation of the 2T(I) model is close to that of (Trelles, 2007) in terms of enthalpies and thermal conductivities, while the formulation of the 2T(II) model is similar to that of (Haidar, 1999).

The time derivative of pressure is not taken into account, since the pressure computation algorithm in the present model is weakly compressible and its time derivative has nonphysical fluctuations. The enthalpy diffusion term due to electric current  $\frac{5}{2} \frac{k}{|e|} (\vec{j} \cdot \nabla T_e)$ , which was taken into account in (Boselli et al., 2013; Freton et al., 2012; Haidar, 1999), is considered negligible in this study because almost in the whole domain the vectors  $\vec{j}$  and  $\nabla T$  are mostly perpendicular. However, in the very vicinity of the cathode tip this term is comparable with the Joule power and may have some effect on the electron temperature.

The contribution of the electron pressure gradient into the electric field  $\frac{\nabla(n_e k_B T_e)}{en_e}$  is neglected.

The main difference compared to the single thermal equation of the LTE model is that the Joule power is assigned only to electrons, while the heavy species gain energy through the collisions with electrons. The last term on the right hand side of the equations (2.20) and (2.21) is the exchange term given by the formula (2.22) which consists of the energy transfer from electrons to heavy species in elastic collisions.

$$Q_{exchange} = K_{exchange} (T_e - T_h) \quad (2.22)$$

Computation of the exchange coefficient  $K_{exchange}$  and its plots for several  $\theta = T_e / T_h$  are given in Annex B. The exchange term is considered to be zero when  $T_e < T_h$ .

After solution of both thermal equations the two predicted enthalpies are translated into  $T_e$  and  $T_h$  and the disequilibrium degree  $\theta = T_e / T_h$  is calculated. The algorithm of translation  $h_e, h_h \rightarrow T_e, T_h$  implemented in the model and performed for every cell of the mesh is as follows:

1. For each value of  $\theta_{table}$  a lookup table is filled with values of  $h_e(T_e)$  and  $h_h(T_h)$ .
2. After solving both thermal equations,  $h_e$  and  $h_h$  are translated into  $T_e$  and  $T_h$  for each available value of  $\theta_{table}$ .

3. For each  $\theta = T_e / T_h$  from the previous step, the initial  $\theta_{table}$  is compared with the resulting ratio  $T_e / T_h$ .
4. The closest value of  $T_e / T_h$  to the initial  $\theta_{table}$  is selected as the most accurate from those which are available.
5. The chosen  $\theta_{table}$  together with  $T_e$  and  $T_h$  are assigned to the cell under consideration and later used for computation (interpolation) of  $\lambda, \sigma, \mu, Q_{exchange}$  from the lookup tables.
6. Finally, the computed  $\lambda, \sigma, \mu, Q_{exchange}$  are used in the next time step of calculation.

A brief example of such translation in the 2T(I) model with only six values of  $\theta_{table}$  is illustrated in Figure 21 and Figure 22. Let us assume that in some cell the computed enthalpies are  $h_e = 4 \cdot 10^6$  and  $h_h = 2.5 \cdot 10^7$ . The algorithm goes through all the  $\theta_{table}$ , and for each  $\theta_{table}$  it takes the temperatures which correspond to the computed enthalpies. For those  $\theta_{table}$  which are shown in Figure 21 and Figure 22 the corresponding temperatures and recomputed  $\theta$  have the following values:

$$\begin{aligned} \text{From } \theta_{table} = 1.0 : T_e = 14600; T_h = 14400; \theta_{recomputed} = T_e / T_h = 1.0139; \delta_\theta = \theta_{recomputed} / \theta_{table} - 1 = 1.4\% \\ \text{From } \theta_{table} = 1.5 : T_e = 14800; T_h = 9900K; \theta_{recomputed} = T_e / T_h = 1.4949; \delta_\theta = \theta_{recomputed} / \theta_{table} - 1 = -0.34\% \\ \text{From } \theta_{table} = 2.0 : T_e = 14940; T_h = 7600; \theta_{recomputed} = T_e / T_h = 1.9658; \delta_\theta = \theta_{recomputed} / \theta_{table} - 1 = -1.7\% \\ \text{From } \theta_{table} = 5.0 : T_e = 15250; T_h = 3160K; \theta_{recomputed} = T_e / T_h = 4.8259; \delta_\theta = \theta_{recomputed} / \theta_{table} - 1 = -3.5\% \\ \text{From } \theta_{table} = 10.0 : T_e = 15360; T_h = 1620K; \theta_{recomputed} = T_e / T_h = 9.5; \delta_\theta = \theta_{recomputed} / \theta_{table} - 1 = -5.2\% \\ \text{From } \theta_{table} = 30.0 : T_e = 15500K; T_h = 540K; \theta_{recomputed} = T_e / T_h = 28.7; \delta_\theta = \theta_{recomputed} / \theta_{table} - 1 = -4.3\% \end{aligned}$$

As it can be seen from the presented values, the closest fit of  $T_e / T_h$  to the  $\theta_{table}$  is for  $\theta_{table} = 1.5$ . Thus it is the selected  $\theta_{table}$  for which the other plasma properties are assigned to the cell under consideration. In this illustration only six values of  $\theta_{table}$  were shown, while in the model the set of  $\theta_{table}$  available for translation is [1.0; 1.1; 1.2; 1.3; 1.4; 1.5; 1.6; 1.7; 1.8; 2.0; 2.5; 3.0; 4.0; 5.0; 6.0; 7.0; 8.0; 9.0; 10.0; 12.0; 15.0; 17.0; 19.0; 21.0; 23.0; 25.0; 30.0], thus the actual translation is done with a much smaller step in  $\theta = T_e / T_h$  and is more accurate.

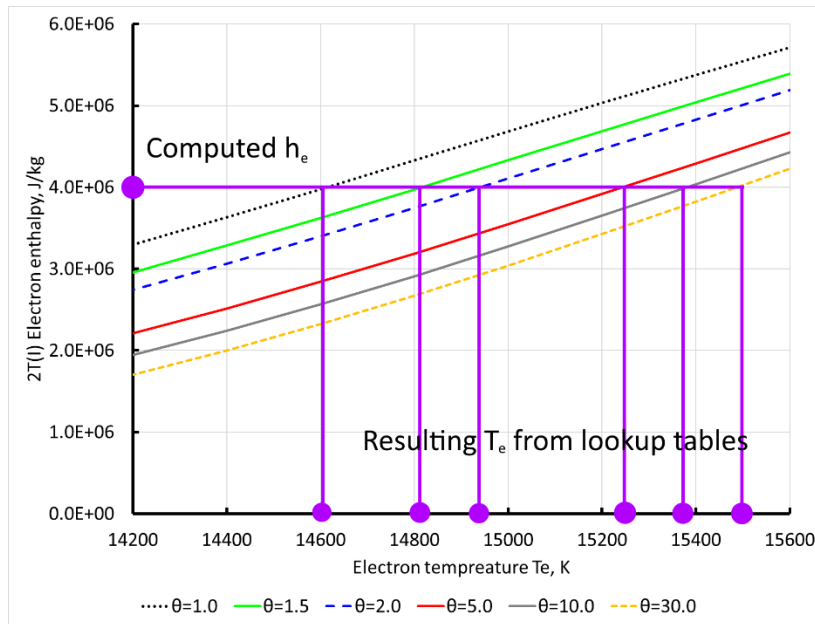


Figure 21 Translation of electron enthalpy to electron temperature in the 2T(I) model

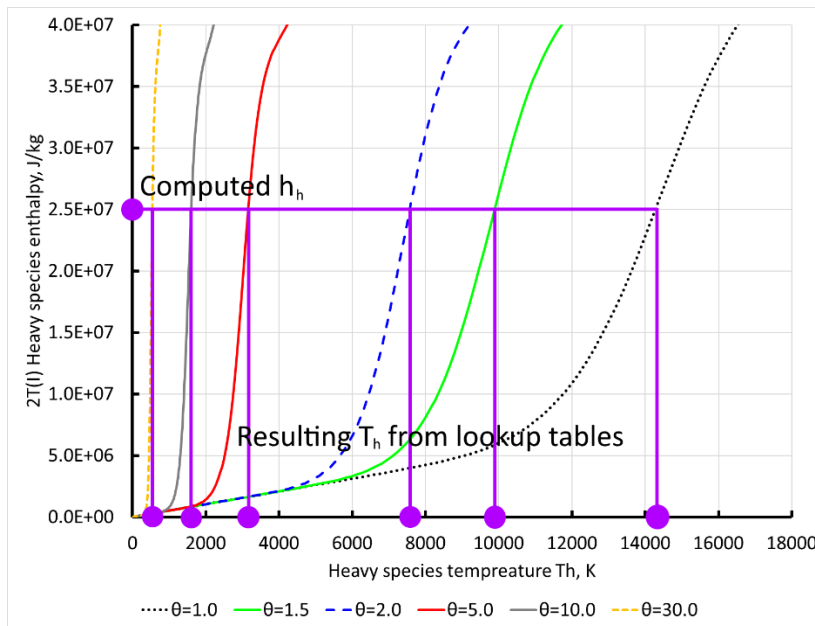


Figure 22 Translation of heavy species enthalpy to heavy species temperature in the 2T(I) model

The translation  $h_e, h_h \rightarrow T_e, T_h$ , in the 2T(II) model follows the same algorithm, except that the values of enthalpies in the lookup tables are different.

During the translation, the parameter  $\theta_{table}$  is kept in the range  $[1.0; 30.0]$ , since it is the range of data in the used lookup tables with plasma properties. In case when the electron enthalpy is too low and heavy species enthalpy too high to fit any lookup table, the parameter  $\theta_{table}$  is assumed to be 1.0. In the opposite case of too high electron enthalpy the parameter  $\theta_{table}$  is assumed to be 30.0. The lower bound of  $\theta$  is related to the physical inconsistency of the case  $\theta = T_e / T_h < 1.0$ . However, such effect should be considered as a simulation artefact. This artefact was discussed in (Freton et al., 2012). The upper bound of  $\theta$  was defined in a series

of simulations and occasionally reached in a few cells. The high enough upper bound of  $\theta$  available in the properties lookup tables is essential for initialization of the unsteady simulation and faster convergence.

The rest of governing equation for the 2T model are the same as in the LTE model, except that all the transport properties in the 2T model, namely thermal conductivity, viscosity and electrical conductivity, are dependent on both temperatures.

## II.5. Modelling of a cascaded-anode plasma torch with Code\_Saturne

### II.5.1. Operating Conditions of the plasma torch

The plasma torch under consideration is the SinplexPro™ of Oerlikon Metco. Its inner geometry is illustrated in Figure 23. It has a neutrode stack assembly between the two electrode to increasing the arc length and decreasing its fluctuation. The neutrode stack assembly consists of copper and ceramic rings and forms a channel in which the arc is burning. The simulated cathode is in tungsten and the anode is lined with tungsten cylinder.

The plasma forming gas is argon. According to the operating parameter windows given by the torch manufacturer, the gas flow rate is varied between 60 and 120 NLPM and arc current is set at 100 A, 200 A and 500 A, respectively.

Experimental values of arc voltage and torch thermal efficiency as well as used electrodes are provided by the torch manufacturer.

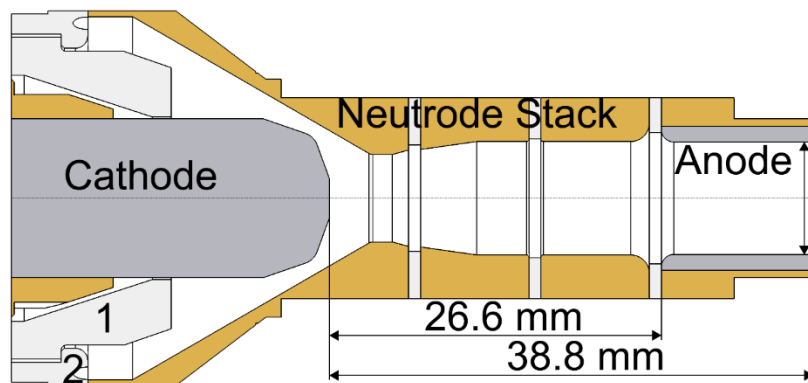


Figure 23 Simulated plasma torch SinplexPro™ manufactured by Oerlikon Metco. 1 is a ceramic electrode insulator. 2 is a gas injector ring.

### II.5.2. Numerical features

The chosen software for simulation is the free open-source Code\_Saturne developed by EDF (Code\_Saturne, EDF R&D, 2019). It has considerable customization, free support and well-established online community with annual meetings. It is realized for Windows and Linux and wields a scalable parallel solver for multi-processor systems. The pressure-based solver SIMPLEC is employed for velocity-pressure coupling (EDF R&D, 2017).

Code\_Saturne has several embedded iterative solvers and only two of them are able to compute electric potential in the geometry under investigation: preconditioned conjugate gradient (Straeter, 1971) and preconditioned GMRES (Saad and Schultz, 1986). Often both of them provide very close simulation results in Code\_Saturne. The default iterative solver for electric potential in Code\_Saturne is the preconditioned conjugate gradient. However, in some mesh configurations this solver is not stable and convergence is difficult to reach.

Consequently the GMRES method has to be used as in (Trelles, 2007; Trelles et al., 2007; Trelles and Modirkhazeni, 2014). The iterative solver GMRES is more robust but in some cases may be slower by several orders of magnitude; in that situation the conjugate gradient method can be a response to the challenge.

In this work, the processor used for the simulation is the dual Intel® Xeon® Gold 6152 with 88 threads in total. The used software is very sensible to the available memory bandwidth above all and has the highest efficiency with approximately 50k cells per single parallel subdomain. Consequently, during the simulation the computational domain was divided into 44 parallel subdomains for the best performance. Further increase of number of threads decreases the simulation performance. Two and more simultaneously running simulation instances become obstacles to each other in terms of memory bandwidth, and the performance of every instance plummets.

The time step of the simulation is  $0.1 \mu\text{s}$  which enables the simulation for characteristic times of 1 to 10 ms. The simulation of 1 ms of physical time, i.e. 10000 time steps, takes approximately twenty hours of “wall clock” time. Larger time steps would require much larger axial size of the cell in order to respect the requirement (2.23) but the accuracy would become much lower. Smaller time steps make the computational cost very high but can be used to check the validity of the main step, as it is illustrated in Figure 24. Also lower time steps can be used for the simulation of highly unsteady cases. As it can be seen from Figure 24 the voltage fluctuations and mean voltage are very close for time step of 0.1 and  $0.01 \mu\text{s}$ .

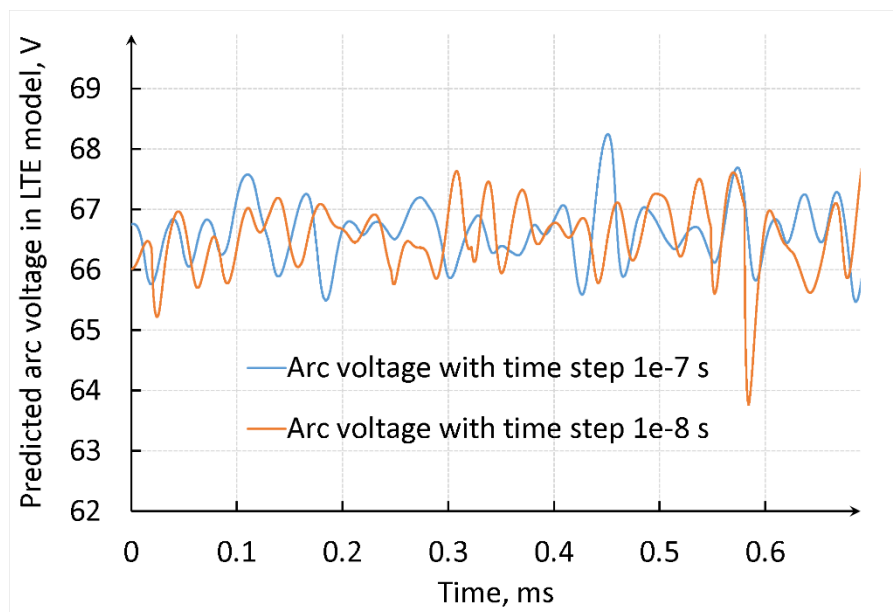


Figure 24 Comparison of the arc voltage time sweeps in the LTE model for time steps of  $1 \cdot 10^{-7}$  s and  $1 \cdot 10^{-8}$  s. Arc current of 500 A, gas flow rate of 60 NLPM. The anode and cathode sheath voltage drops are not taken into account.

The software Code\_Saturne chosen for simulation initially was not adapted for the 2T arc simulation, however it allows the user to add more solved variables with their own diffusivity. The added custom solved variables can have additional source terms and have the same advection term as the main thermal variable. The thermal variable for electric arc simulation in Code\_Saturne is enthalpy, thus all the thermal energy conservation equations are written in terms of enthalpy.

## II.5.3. Basic features of model

### II.5.3.1. Computational domain of model

The computational domain of this study consists of the fluid domain inside the torch, outlet tank and both electrodes: cathode and anode. The outlet tank is necessary for the prediction of plasma jet stability. The computational domain is shown in Figure 25.

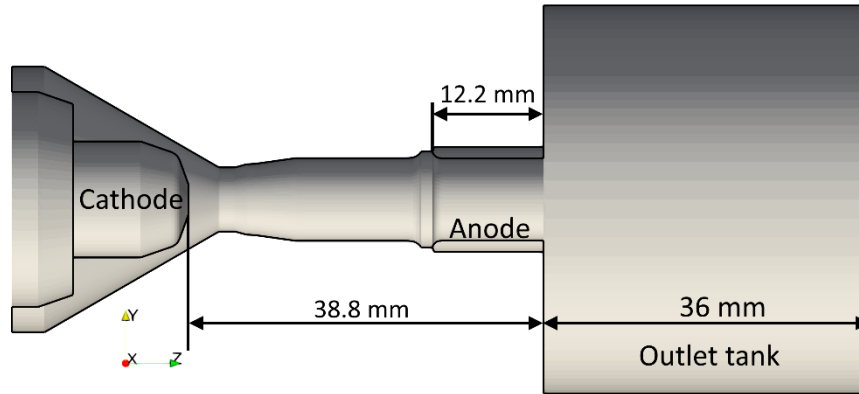


Figure 25 Computational domain of the model

### II.5.3.2. Mesh size limitations

The high velocity of the plasma flow imposes some limitation on the mesh used in plasma torch simulation: the plasma flow in every direction in every given point should not travel more than one mesh spacing in the corresponding direction (Courant et al., 1928). This limitation is called Courant–Friedrichs–Lewy (CFL) condition; it can be expressed by the Courant number  $C$  which should not exceed some critical value usually taken as 1. The Courant number is given in equation (2.23).

$$C = \Delta t \sum_{i=1}^3 \frac{u_{x_i}}{\Delta x_i} \leq C_{\max} \sim 1 \quad (2.23)$$

Where  $\Delta t$  is the time step,  $\Delta x_i$  the mesh element size in direction  $x_i$ ,  $u_{x_i}$  the plasma velocity size in direction  $x_i$ .

As a result of this limitation and high values of axial component of plasma velocity, a compromise has to be reached for the axial cell size in order to have an accurate spatial resolution with not too small cells in order to respect the CFL condition. A too low Courant number  $C$  in areas with low velocity, large cells of hexahedral mesh combined with small time step can also cause checkerboard order oscillations of pressure and velocity (Rhie and Chow, 1983; Zang et al., 1994). Example of such checkerboard order oscillations of pressure and velocity in the outlet tank with large cells and low velocity magnitude around the plasma jet is shown for the model of transferred arc with the geometry configuration illustrated in Figure 26. The distributions of velocity and pressure from the cross section highlighted in red are given in Figure 27.

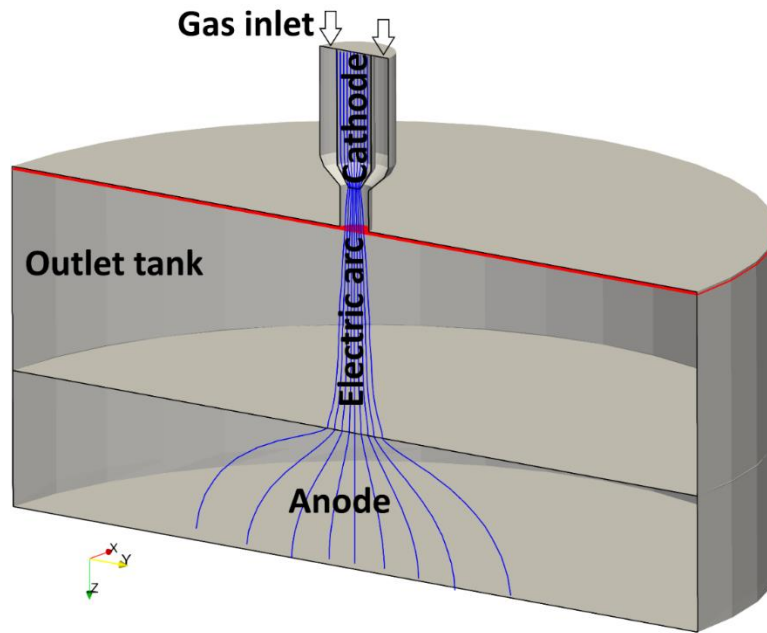


Figure 26 Example of model of constricted transferred arc for which the checkerboard order oscillations may appear in the outlet tank. The distributions below are given for the red cross section.

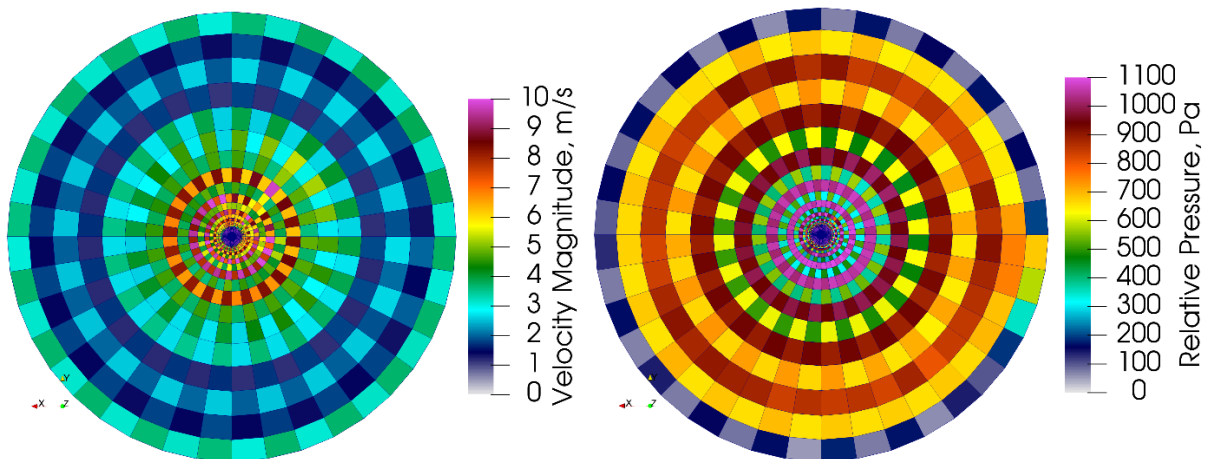


Figure 27 Example of checkerboard order oscillations of plasma and velocity

These solution oscillations are inherent to various CFD solvers which work with hexahedral meshes and necessitate the use of fine meshes even at the periphery of the computational domain. However, the periphery of the computational domain is usually a large area which significantly increases the computational cost. The checkerboard order oscillations often can be suppressed by artificial correction filter, but it alters the physics of the problem.

### II.5.3.3. Mesh configuration

The hexahedral mesh used in the simulation of the plasma torch consists of 2M cells including 70k cells in the anode, 330k cells in the cathode and 1.6M cells in the fluid phase. The thickness of the first layer of cells at the plasma-cathode interface is 25  $\mu\text{m}$ , this part of the mesh is illustrated in Figure 28. The thickness of the first layer of cells at the plasma-anode interface is 50  $\mu\text{m}$ , this part of the mesh is illustrated in Figure 29. The circumference of the mesh is divided into 128 circular sectors, which allows to catch even a minor motion of the anode arc attachment.



Most of the computational domain is the cylindrical volumes. Thus, the O-grid type topology is necessary for the mesh construction. It consists in the combination of a square pattern in the center and a ring-radial pattern in the outside part as shown in Figure 29. Such mesh is low in skewness and has an orthogonal structure on the outside boundary (ANSYS, Inc., 2016).

The mesh in the outlet tank is shown in Figure 30. It has to be fine enough even at the periphery in order to mitigate the checkerboard order fluctuations illustrated in Figure 27. In the current study the cell size in the periphery of the outlet tank is around 0.8 mm. This size was selected after tests with different cell sizes. For instance, 4 mm cells in the periphery bring about fluctuations of pressure in the whole domain and eventually violation of the mass flow rate stability. Assuming that the model does not consider compressible effects, the fluctuations of the mean spatial pressure have no physical sense and correspond merely to a numerical noise. The comparison of the fluctuations of the mean spatial pressure and mass flow rate through the nozzle for grids with 4mm and 0.8 mm cells at the periphery is shown in Figure 31 and Figure 32, respectively. The rough mesh in the periphery increases the fluctuations of mean pressure and mass flow rate tenfold and eventually brings about a significant disturbance of the total heat balance by around 10%.

In the fluid domain close to the cathode tip, the convergence of computations is very difficult to achieve. Thus, the cells near the cathode have to be as rectangular as possible. Acute corners and needle-shaped cells in the mesh near the cathode tip can induce severe numerical effects on the electric potential distribution, which causes loops of parasitic electric current and unphysically high Joule power in these cells.

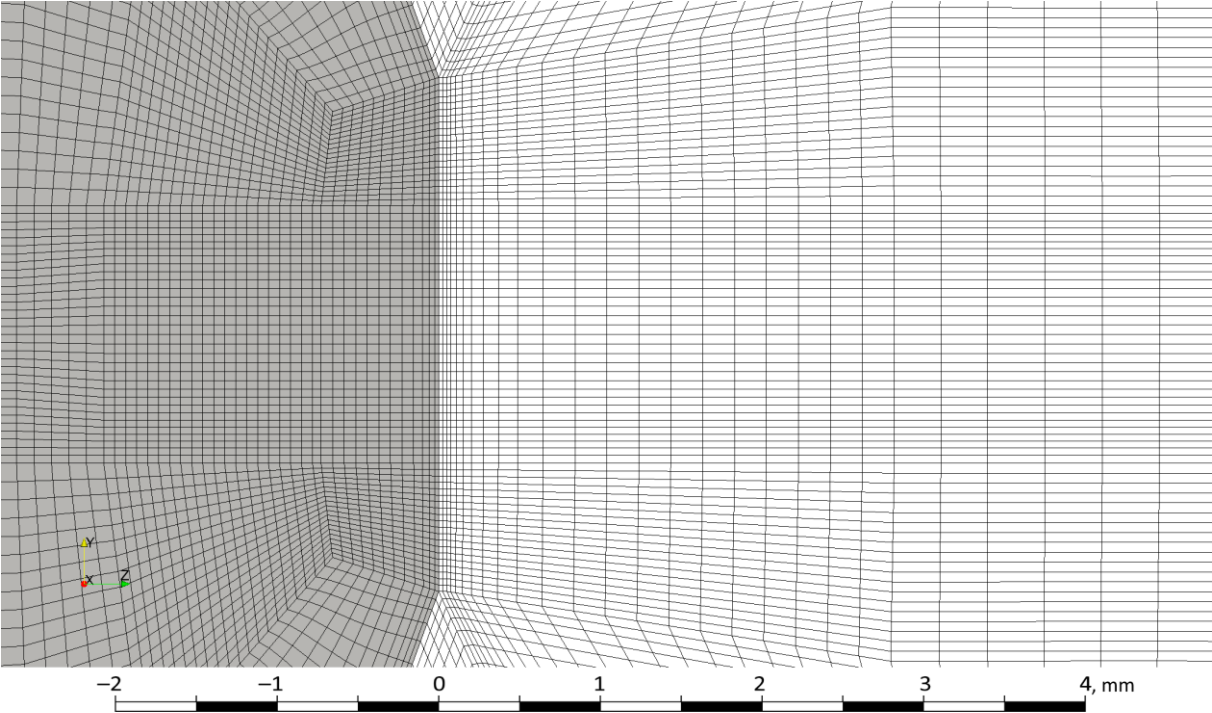


Figure 28 Mesh near the cathode tip. Cells in grey are a part of the cathode.

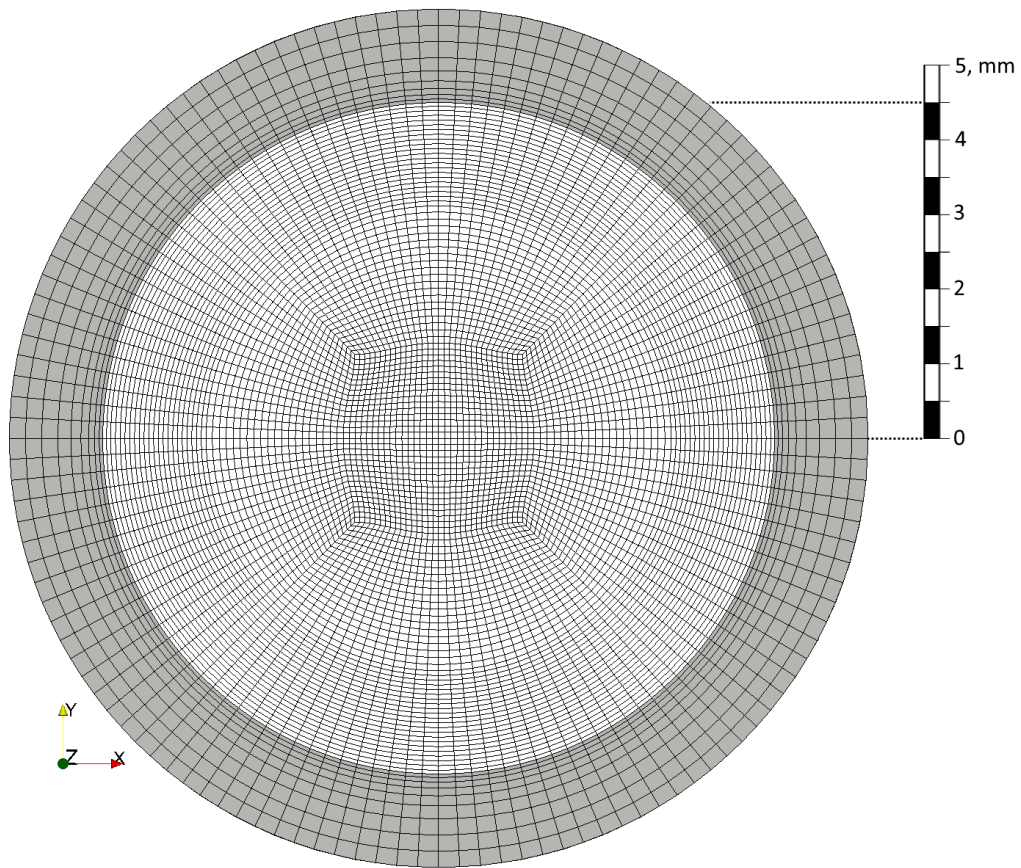


Figure 29 Mesh at the torch nozzle exit. Cells in grey are a part of the anode.

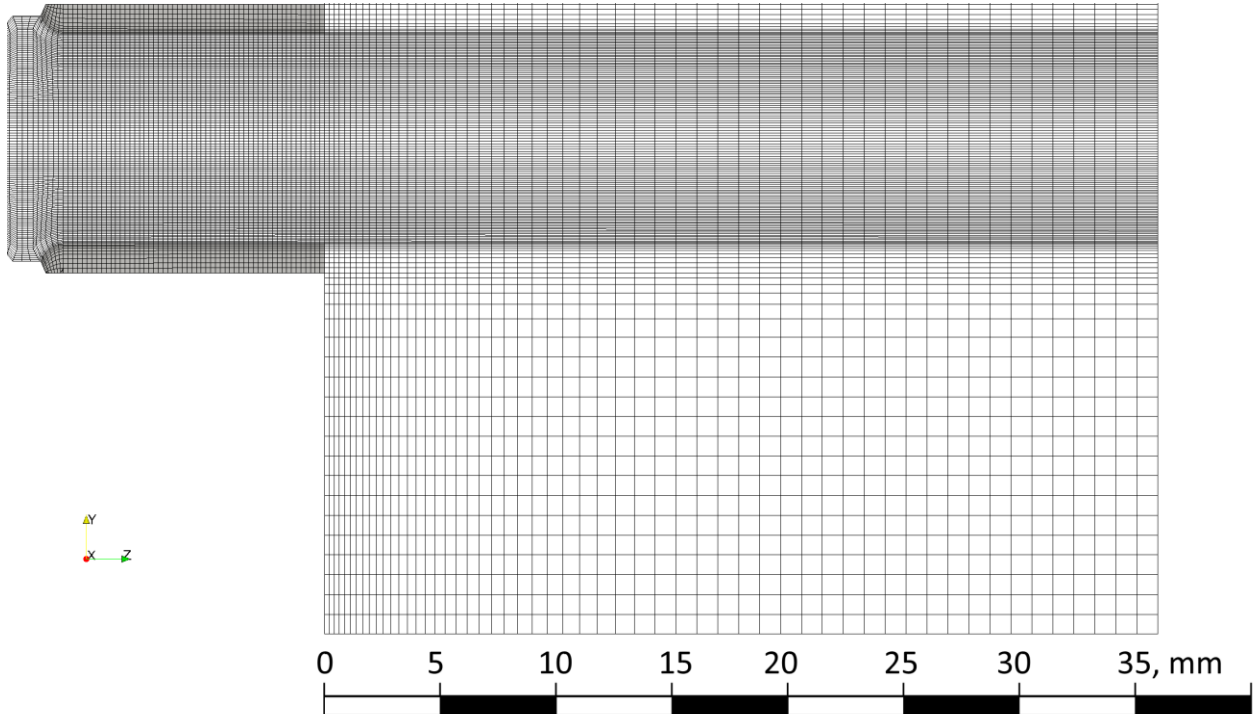


Figure 30 Mesh at the outlet tank. Size of the cells in the periphery of the outlet tank is 0.8 mm.

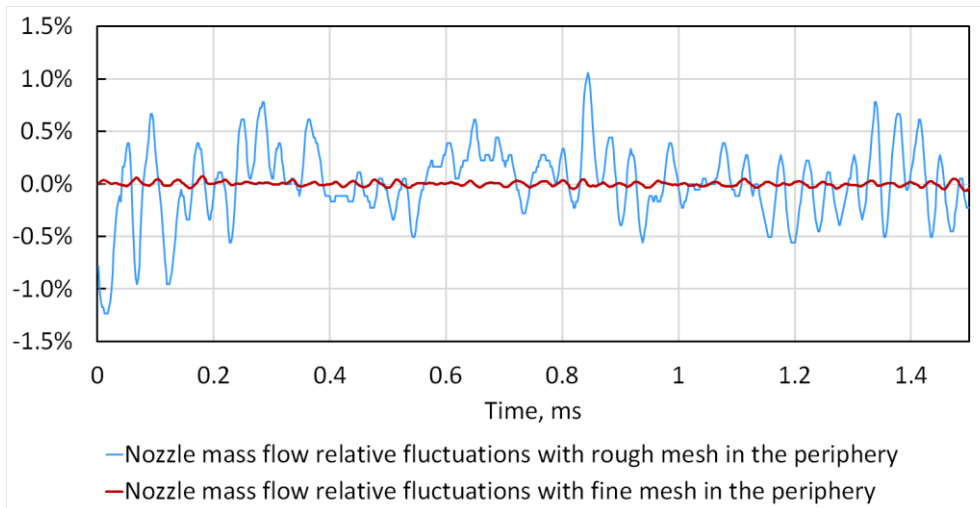


Figure 31 Relative fluctuations of the input mass flow rate. The rough mesh has a cell size of 4 mm in the periphery; the fine mesh has a cell size of 0.8 mm.

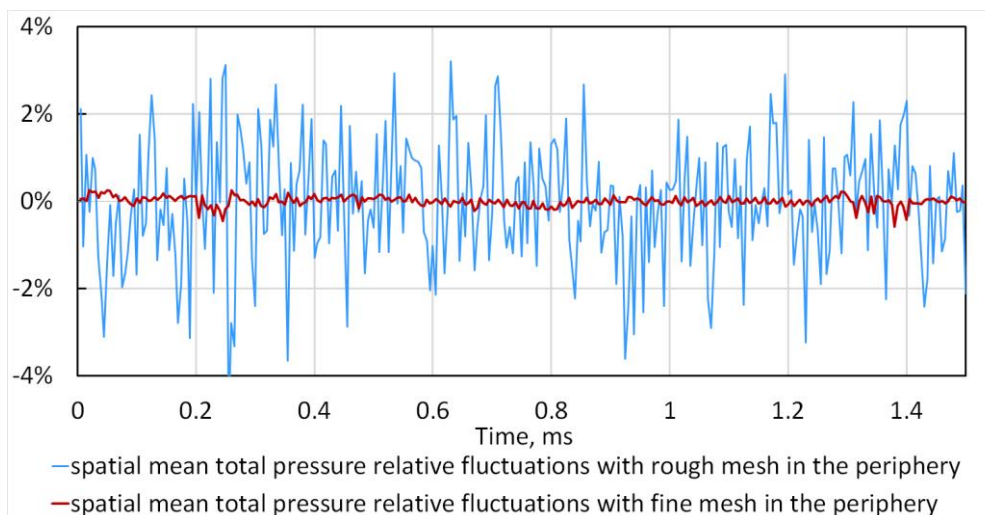


Figure 32 Relative fluctuations of the spatial mean total pressure. The rough mesh has a cell size of 4 mm in the periphery; the fine mesh has a cell size of 0.8 mm.

#### II.5.3.4. Boundary conditions

##### Velocity

The free outlet boundary condition that is a zero-flux condition is set for the velocity component normal to the face, which means that  $u_n$  has to be constant in space. Thus the free outlet boundary condition tends to stabilize the normal velocity and sometime even attract the flow passing parallel to the outlet boundary surface. Hence, the outlet has to be far from the nozzle exit and the plasma normal velocity component has to be nearly asymptotic. Therefore, the outgoing plasma flow has to be either perpendicular to the outlet or zero, otherwise the velocity stream lines may deflect and stick to the incorrectly located outlet surface. Unfortunately it is very hard to have zero velocity at the periphery with relatively large cells while keeping a low time step. Due to the checkerboard order velocity fluctuations at the periphery of the outlet tank the corner cells will always have some non-zero velocity. Meanwhile, this velocity has to be perpendicular to the outlet boundary and cannot be perpendicular to two different face simultaneously. Thus every single boundary cell should have at most one outlet face.

Otherwise the cells with two and more outlet faces will suffer pressure and velocity fluctuations. Therefore, the free outlet boundary condition is assigned to only one surface: far right flat disk side which is opposite to the nozzle exit. The cylindrical boundary surface of the outlet tank is considered as a wall in order to stabilize the velocity in the corner cells.

At the inlet boundary surface the velocity in each boundary cell is perpendicular to the boundary face. The swirling injection angle is achieved through a momentum source in the cylindrical cavity in the proximity of the inlet boundary right in front of the gas-injection ring. The right angles and almost cubic cells near the inlet boundary allow to have more stable volume flow rate and a proper control of it.

Internal walls of the plasma torch are considered as a cold smooth solid wall face, impermeable and with friction.

### Enthalpy: LTE model

The boundary condition for enthalpy  $h$  in the LTE model corresponds to the  $T = 300\text{ K}$  almost in the whole plasma torch except the outside surface of the anode, where it corresponds to  $T = 400\text{ K}$ . The outlet surface has zero gradient as the boundary condition. The boundary conditions for enthalpy  $h$  on the other surfaces of the outlet tank (outside plane surface and outside cylindrical surface) correspond to  $T = 300\text{ K}$ .

The enthalpies imposed on the fluid boundaries are taken from the function  $h(T)$  for argon. The boundary enthalpies on the electrode boundaries are taken from the function  $h(T)$  for tungsten.

The boundary conditions of the LTE model are shown in Figure 33.

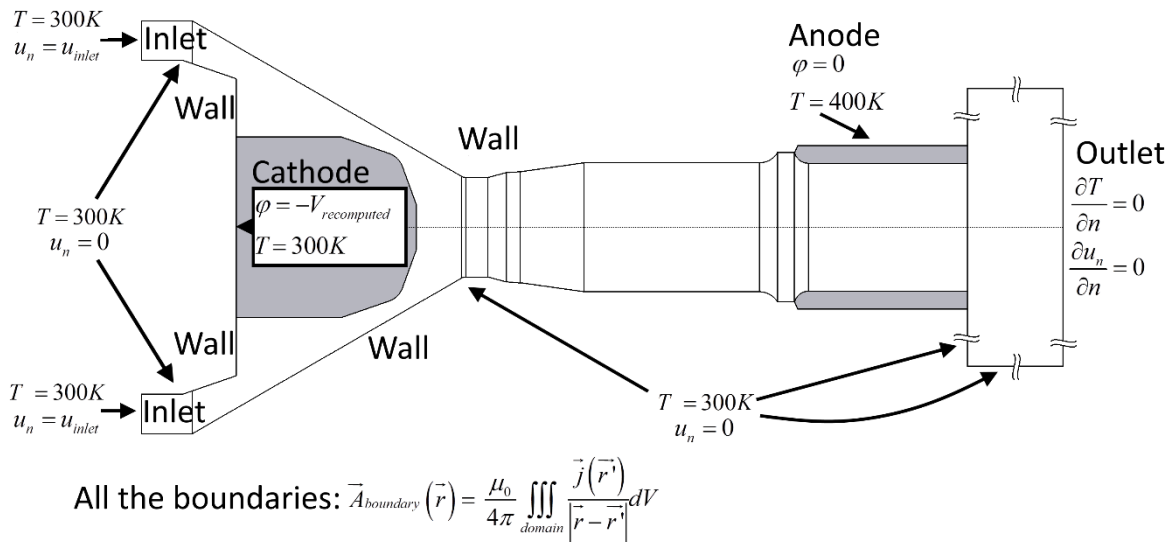


Figure 33 Boundary conditions of the LTE model

In Figure 33,  $\vec{r}$  is the location of the face at which the boundary condition is computed,  $\vec{r}'$  the location of the cell which is taken into account during the computation,  $dV$  is the volume of the cell,  $\vec{j}(\vec{r}', t)$  is the electric current density in the cell.

### Enthalpy: 2T model

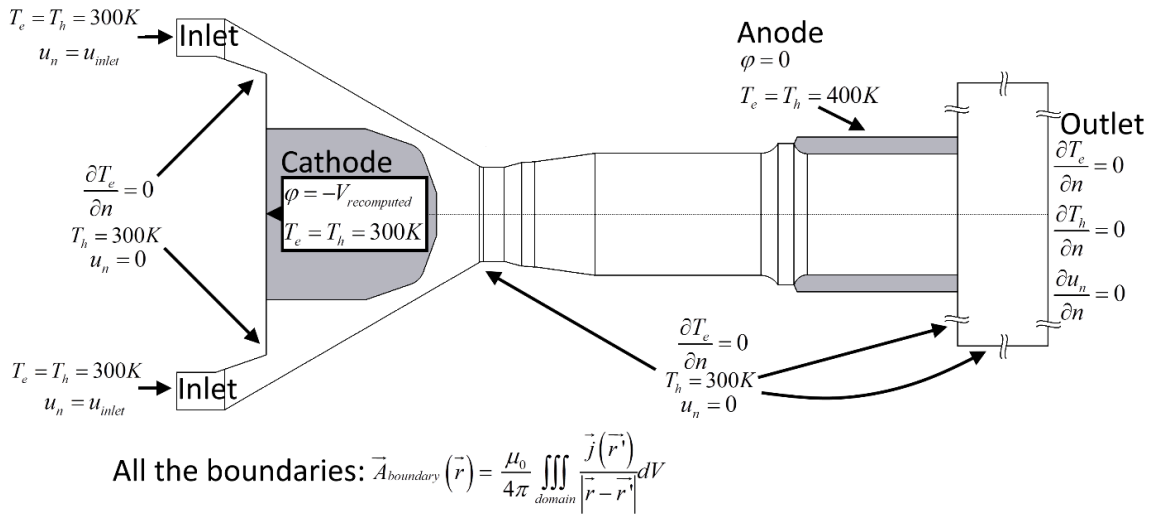


Figure 34 Boundary conditions of **2T(I)** and **2T(II)** models

The 2T model has the same geometry configuration of the torch, the same mesh and boundary conditions than the LTE model except for the electrons enthalpy. At the gas inlet, the electron enthalpy boundary condition at the gas inlet corresponds to 300 K and  $\theta = T_e / T_h = 1$ , while at all the other boundaries have zero flux boundary conditions for the electron enthalpy. The boundary conditions are summarized in Figure 34. Inside the electrodes both fields  $h_e$  and  $h_h$  are the same with the same source terms and boundary conditions.

#### II.5.3.5. Boundary condition for electric potential: Arc voltage scaling algorithm

In this model, an imposed potential on the electrodes boundaries (Dirichlet boundary condition) is used. It makes the simulation with the electrodes included in the computational domain easier to initialize and more stable.

To maintain the target current intensity in the computational domain in unsteady simulation, a voltage scaling algorithm which readjusts the imposed value of voltage in the boundary conditions (EDF R&D, 2017). is used. Such algorithm allows to use the Dirichlet boundary condition for electric potential.

The voltage scaling algorithm computes the total Joule effect in the computational domain  $\int_{domain} Q_J(\vec{r}) dV$  and compares it with the product of the target current intensity and voltage imposed on the previous time step  $I_{imposed} \cdot V_{prev}$ . The comparison of these two values leads to a voltage correction coefficient expressed in equation (2.24). Using this coefficient the voltage for the next time step is corrected as shown in (2.25).

$$K_{correction} = \frac{I_{imposed}}{I_{computed}} = \frac{I_{imposed} \cdot V_{prev}}{\int_{domain} Q_J(\vec{r}) dV} \quad (2.24)$$

$$V_{new} = V_{prev} \cdot K_{correction} \quad (2.25)$$

The arc voltage scaling algorithm allows to predict the arc voltage dynamically rather than impose it.

However, one of the drawbacks of the voltage scaling algorithm is its instability in case of an arc with a complex shape or low-quality meshes with needle-shaped cells. A numerical effect in needle-shaped cells cause unphysical fluctuations of the electric potential distribution, which results in sudden severe increase of total Joule power in the simulation domain. The voltage scaling algorithm in such situation is trying to lower the Joule power by decreasing the voltage but instead either produces significant voltage fluctuations or extinguishes the arc.

### II.5.3.6. Boundary conditions for magnetic vector potential

The boundary conditions for the magnetic vector potential are essential in plasma torch model for the arc stability and model reliability.

In order to look at the problem of the boundary condition from a different angle, let's first compare the mathematical concepts of the magnetic field and magnetic vector potential.

The basic restrictions for the magnetic field simulation are:

- The Gauss's law for magnetism (2.26). The physical meaning of this law is the non-existence of magnetic monopoles and the total flux through a closed surface must be zero.

$$\nabla \cdot \vec{B}(\vec{r}) = \frac{\partial B_x}{\partial x} + \frac{\partial B_y}{\partial y} + \frac{\partial B_z}{\partial z} = 0 \quad (2.26)$$

- The Coulomb gauge (2.27). This restriction is devoted to the elimination of excessive unphysical degrees of freedom.

$$\nabla \cdot \vec{A}(\vec{r}) = \frac{\partial A_x}{\partial x} + \frac{\partial A_y}{\partial y} + \frac{\partial A_z}{\partial z} = 0 \quad (2.27)$$

Thus the magnetic vector potential and the magnetic field should follow the same basic rule: zero divergence. The lines of the magnetic vector potential should either form a closed loop or come from infinity and go to infinity.

Numerically, the magnetic vector potential is the source of the magnetic field:  $\vec{B}(\vec{r}) = \nabla \times \vec{A}(\vec{r})$

However, the physical source of the magnetic field of the electric arc is the electric current density. The relation between the electric current density and magnetic field can be drawn from equation (2.12), assuming that the temporal derivative of the electric field is low, into the equation (2.28).

$$\nabla \times \vec{B}(\vec{r}) = \mu_0 \vec{j}(\vec{r}) \quad (2.28)$$

In addition, outside of the power source with assumption of electrical neutrality we have a similar restriction for the electric current density can be written:  $\nabla \cdot \vec{j}(\vec{r}) = 0$

Thus in our model outside of the power source the electric current density and magnetic vector potential have similar properties:

- Zero divergence;
- They are the source of the magnetic field:  $\vec{A}$  is the numerical source in the model and  $\vec{j}$  is a physical source in reality.

Hence, the electric current density and magnetic vector potential exhibit a common pattern: the stream lines of both fields should come from the ground (or anode) with null electric potential and head to the source of electrical energy with negative potential (or cathode) as shown in Figure 35 and Figure 36.

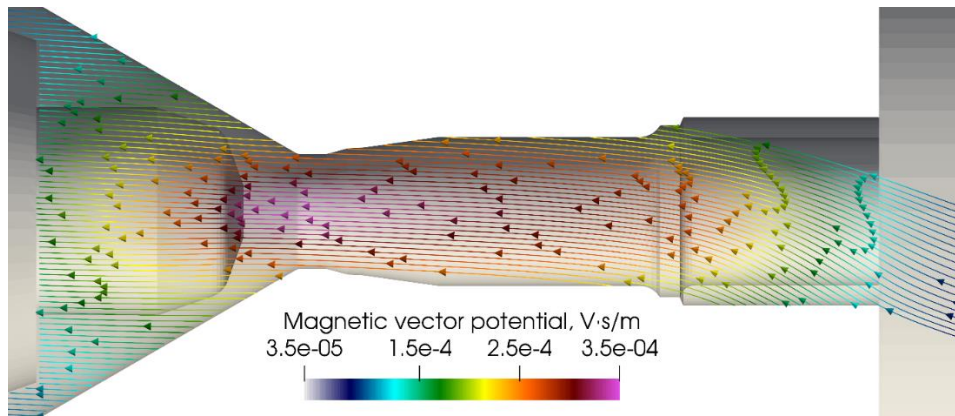


Figure 35 Magnetic vector potential stream lines inside the plasma torch in the LTE model

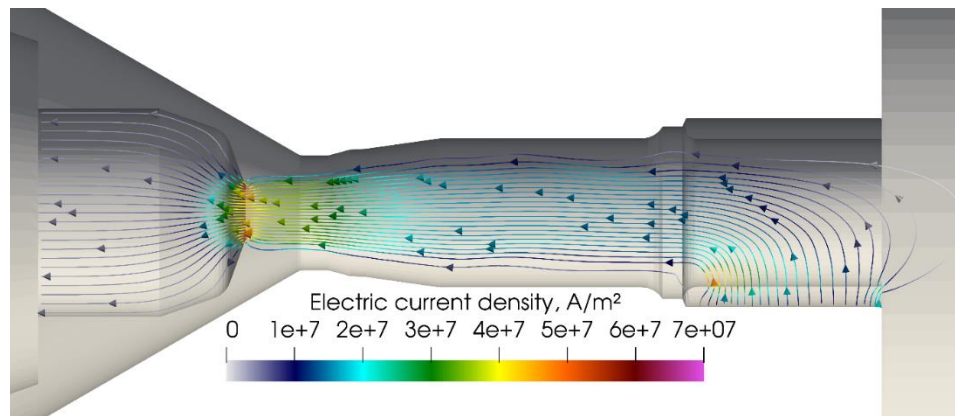


Figure 36 Electric current density stream lines inside the plasma torch in the LTE model

The magnetic vector potential is an essential variable in an electric arc model. A correct computation of magnetic vector potential is required for a correct prediction of the magnetic field and, especially, at the electrodes surface. If the electrodes are not included in the computational domain, the streamlines of the magnetic vector potential and electric current density will disappear at the electrodes surface and the current density inside the electrode is neglected. This could lead to an underestimated of the magnetic field by about 50% at the electrodes surface and therefore to an underestimation of the Lorentz force.

If we consider an infinite electrically conductive cylinder (axial symmetry), the distributions of magnetic vector potential and electric current density will only depend on the radius, while the axial components will be constant along the cylinder. If we cut one half of this cylinder and impose the electrical boundary condition on the new boundary, the electric current beyond this boundary will be neglected and the streamlines of electric current density will simply disappear at the boundary. This has no physical sense, but is rather an approximation of the model. As a consequence, the magnetic vector potential defined by the electric current density distribution at this new boundary will be poorly predicted along with the magnetic field. That is why it can be concluded that the boundary condition that imposes a nonzero electric current or electric potential yields a poor prediction of the magnetic vector potential and an

underestimation of the magnetic field, therefore such boundary condition should be imposed far away from the areas important for the study.

Another problem that arises near the electric boundaries like anode or cathode when an electric potential or non-zero electric current density are imposed, is the violation of the Coulomb gauge (2.27). The distribution of divergence of the magnetic vector potential is illustrated in Figure 37. The violation of the Coulomb gauge (2.27) is more significant near the electric boundaries. Therefore, such boundaries should be distant from the sensitive areas of the model.

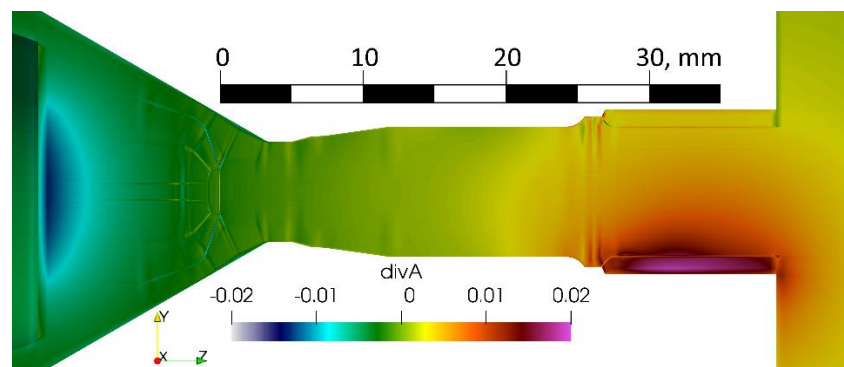


Figure 37 Divergence of magnetic vector potential

There are two general options for the choice of the boundary condition for the magnetic vector potential:

1. A Dirichlet boundary condition or imposed value. It is usually either zero for the distant outlet surface or a computed value.
2. A Neumann boundary condition or imposed flux. It is usually a zero flux boundary condition:  $\frac{\partial A_i}{\partial n} = 0; i = x, y, z$

The two main approaches as discussed in section I.7.1 are:

1. The Biot&Savart approach for the magnetic vector potential boundary condition (referred to as BS).
2. Combined zero flux at close boundaries and zero value at distant boundaries (referred to as PVNF).

The null flux boundary condition for the magnetic vector potential implies that the component of magnetic vector potential perpendicular to the boundary is constant. However, this is not true at the domain boundary close to the electric arc, and especially at the conic “bottleneck” of the domain near the cathode tip as shown in Figure 38.



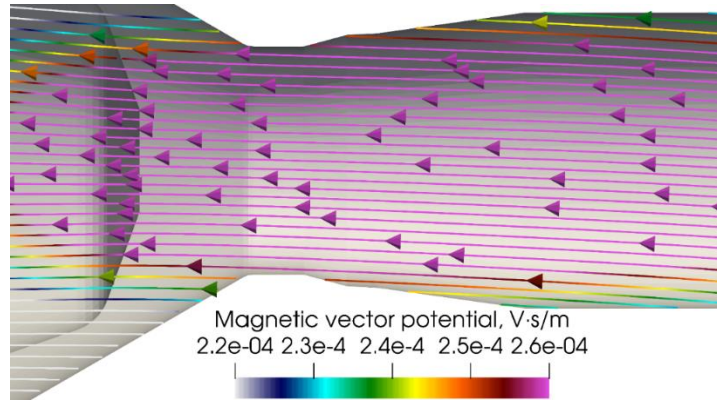


Figure 38 Magnetic vector potential stream lines at the “bottleneck” of the computational domain where the magnetic vector potential is far from being constant

If the boundary is close to the electric arc in a location sensitive for the study, the boundary condition for the magnetic vector potential should be carefully chosen. In this study, the boundary condition is expressed as (2.29).

$$\vec{A}_{boundary}^{new}(\vec{r}, t) = \frac{\mu_0}{4\pi} \iiint_{domain} \frac{\vec{j}(\vec{r}', t)}{|\vec{r} - \vec{r}'|} dV \quad (2.29)$$

Where  $\vec{r}$  is the location of the face at which the boundary condition is computed,  $\vec{r}'$  is the location of the cell which is taken into account during the computation,  $dV$  is the volume of the cell, and  $\vec{j}(\vec{r}', t)$  is the electric current density in the cell.

In the computed distribution of the spatial derivatives of the magnetic vector potential it can be seen that the normal derivatives at the boundary surfaces near the electric arc are far from being zero: for example, the derivative  $\frac{\partial A_y}{\partial y}$  at the bottleneck of the channel inside the torch as shown in Figure 39, or the derivative  $\frac{\partial A_z}{\partial z}$  at the vertical boundary around the nozzle exit as shown in Figure 40.

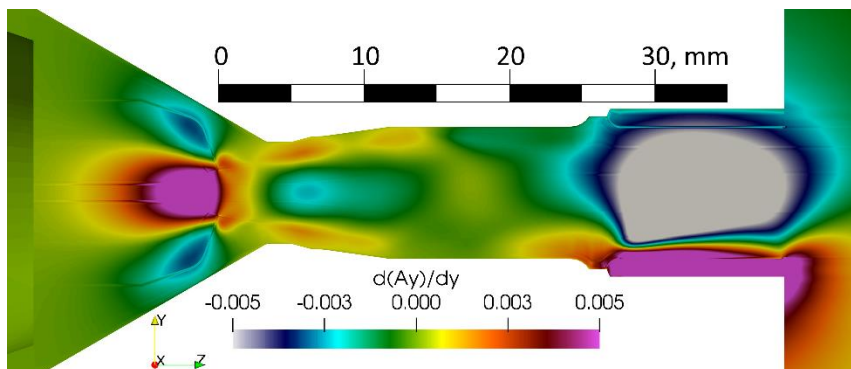


Figure 39 Derivative of magnetic vector potential  $\frac{\partial A_y}{\partial y}$

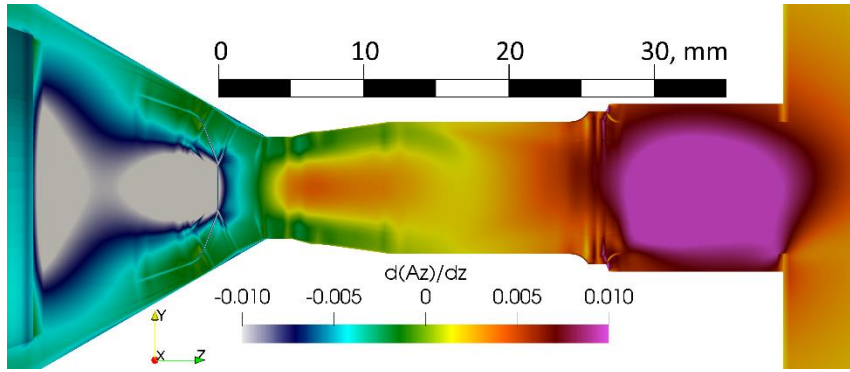


Figure 40 Derivative of magnetic vector potential  $\frac{\partial A_z}{\partial z}$

The integral (2.29) is computed throughout the whole computational domain, which includes all the parallel subdomains. In order to get the information about other parallel subdomains for every given subdomain the standard functions of Code\_Saturne for Message Passing Interface (MPI) are employed.

The boundary condition for the vector potential must be recalculated at the beginning of the simulation in order to get faster convergence of the magnetic vector potential calculation and swiftly get smoother magnetic field distribution. The relaxation of the boundary condition is also very important due to a rapid change in the electric current density field at the beginning. The relaxation of the boundary condition for magnetic vector potential is expressed by the formula (2.30).

$$\vec{A}_{boundary}^{imposed}(\vec{r}, t) = \omega \cdot \vec{A}_{boundary}^{old}(\vec{r}, t) + (1 - \omega) \cdot \vec{A}_{boundary}^{new}(\vec{r}, t) \quad (2.30)$$

where  $\omega$  is the relaxation coefficient. Normally during the simulation this coefficient is around 0.99. In addition, the boundary condition is recomputed every 100 time steps.

However, at the beginning of the simulation the boundary condition for the magnetic vector potential has to be recalculated more often, for example every 10 or even 2 time steps. The relaxation coefficient  $\omega$  at the beginning should be lower than usually, e.g. 0.9 instead of normal 0.99.

One computation of the boundary condition for magnetic vector potential takes as much time as the computation of 23 time steps without recomputed boundary condition. Therefore, when the boundary condition is recomputed only once per 100 time step, the computation of the integral (2.29) constitutes only around 23% of the whole computational cost. However, when the boundary condition is recomputed once per two time step, the whole computational cost increases about twelvefold.

Without proper recalculation of the magnetic vector potential boundary condition, the cathode arc attachment may exhibit the cross shape as illustrated in Figure 41, which is merely a numerical effect and its special orientation is defined by the mesh O-grid. The cross shape of the cathode arc attachment may also affect the convergence of the whole arc because of the Lorentz force effect on the arc. It is therefore essential to have the smoothest, stable and accurate magnetic field distribution as far as possible.

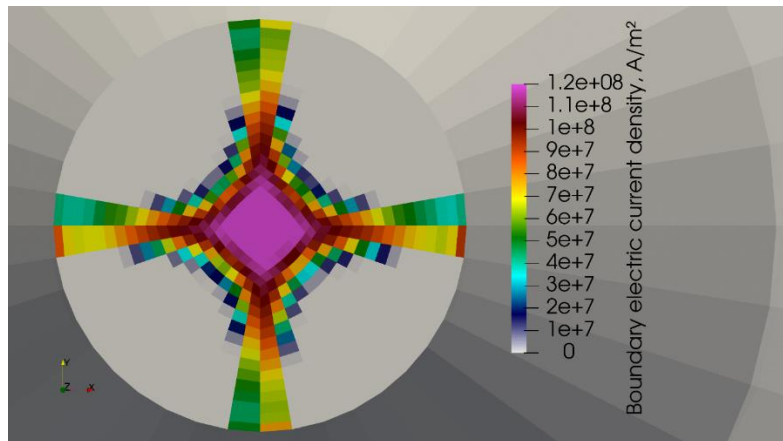


Figure 41 Example of a cross shape of the cathode arc attachment that appears in case of improper initialization of the boundary condition for magnetic vector potential

The resulting computed boundary values of magnetic vector potential on all the boundaries is illustrated in Figure 42.

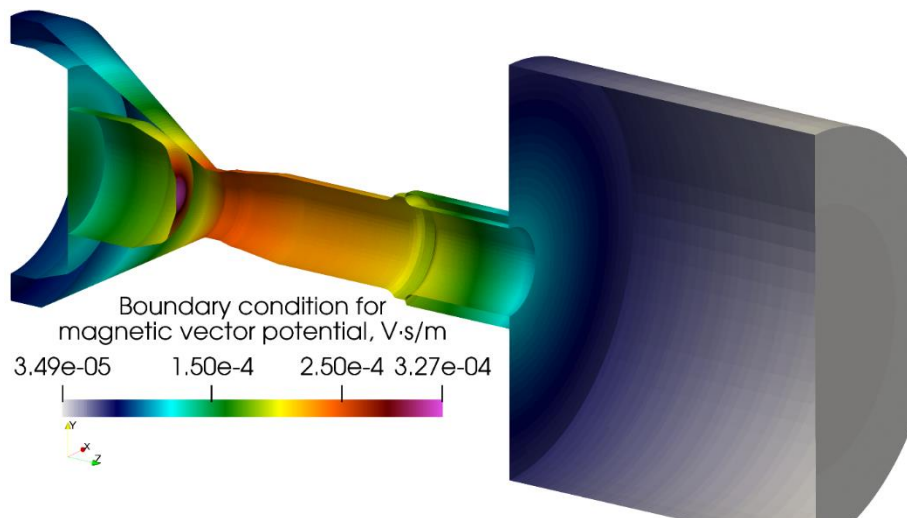


Figure 42 Computed distribution of magnitude of the boundary condition for the magnetic vector potential

### II.5.3.7. Initialization

The model is unsteady and initialized with a hot (8000 K) bridge between the anode and the cathode. The hot column should have the optimal radius and temperature. A too large radius results in a drop of recomputed voltage and the arc fades away in several time steps. The same effect is produced by too high temperature of the arc. Therefore, the hot column between the electrodes for initialization has a temperature of 8000 K and radius of 2 mm.

The initial arc voltage imposed at the first time step is rather arbitrary, but has to be high enough to heat the initial hot column up to the normal temperature during the first several time steps. The initial voltage chosen in the present work is 300 V. During the arc initialization, the voltage imposed as the electric potential boundary condition has to be readjusted. Thus during the first steps the voltage scaling algorithm can be unstable, and the ratio of imposed current to the computed one (2.24) can vary from one time step to another over a large range, e.g. [0.001;1000]. Such numerical fluctuations of voltage are detrimental to the model and as a result the arc fades away. Therefore, in order to smoothly initialize the simulated arc the voltage

correction coefficient has to be limited within the range [0.9; 1.1]. In addition, such range of voltage correction in the time scale around 0.1  $\mu\text{s}$  in the process of the direct current control approximately corresponds to the performance of the real source of direct current, according to the private communication with Hartmut Koschnitzke, the Senior Electrical Engineer from Oerlikon Metco.

The initialization process of the 2T(I) model is more complex than in the LTE model. A simulation start with 500 A is too unstable, and the temperature fluctuations are too abrupt from one time step to another. Thus, it is necessary to start the simulation with a lower current intensity, e.g. 50 A and then gradually increase it up to 500 A.

However, the initialization of the 2T(II) model is more stable and smooth. The higher stability of the 2T(II) model is conditioned by the fact that a larger amount of energy is stored in the electron enthalpy. The Joule power and exchange term have lower relative share in the electron enthalpy equation, which dampens the fluctuations. Thus, the 2T(II) model can be started directly with 500 A.

### II.5.3.8. Inclusion of electrodes

The present model includes both anode and the cathode inside the computational domain for better prediction of magnetic field in the vicinity of the electrodes and thus for accurate prediction of plasma acceleration by the magnetic pressure in the Maecker jet. Another profit of included electrodes is prediction of temperature distribution on the electrode surface.

Simulation of solid cathode and anode requires zero momentum inside the corresponding domain. The desired velocity  $\vec{u}^{desired}$  inside the solid parts is zero, thus here we follow the technique suggested in (Patankar, 1980). That is to say, the zero momentum is achieved through an additional momentum source in the momentum conservation equation (2.2). The momentum source used in the solid phase is given by the formula (2.31). The physical meaning of such source is rapid deceleration of any flow. It allows to reach velocity with order of magnitude around  $10^{-15}$  from the very beginning of the simulation, thus having only thermal diffusion and not advection. Such method is often referred to as the penalty method.

$$\begin{aligned} \bar{\Gamma}_{expl} + \bar{\Gamma}_{impl} \vec{u} &= 10^{30} (\vec{u}^{desired} - \vec{u}^{computed}) = -10^{30} \cdot \vec{u} = \\ &= \left\{ -10^{30} \cdot u_x^{computed}; \quad -10^{30} \cdot u_y^{computed}; \quad -10^{30} \cdot u_z^{computed} \right\} \end{aligned} \quad (2.31)$$

Both the cathode and anode liner are in tungsten. Analytical expressions of the temperature-variation of tungsten properties are taken from (Tolias, 2017). The tungsten properties include density, electrical conductivity, thermal conductivity, enthalpy and specific heat. The analytical expressions for the properties are used to recompute the values before each time step. The magnetic permeability of tungsten is supposed equal to the permeability of free space.

### II.5.4. Fluid-electrode coupling

The thermal variable for electric arc simulation in Code\_Saturne is enthalpy, which requires the continuity and integrability of enthalpy throughout the whole simulation domain. However, the temperature-variation of enthalpy for tungsten and argon,  $h_{Ar}(T)$  and  $h_W(T)$ , are different, that is for the same enthalpy the tungsten and argon temperatures are different. The same problem exist for the thermal and electrical conductivities. However, Code\_Saturne is not adapted for such abrupt changes in medium diffusivities.

Therefore, the treatment of the solid electrodes together with the gas phase without any artificial intervention gives unphysical results: the argon cell between the molten cathode tip (3695K) and a plasma cell (~10000) has temperature about 2000K as illustrated in Figure 43.

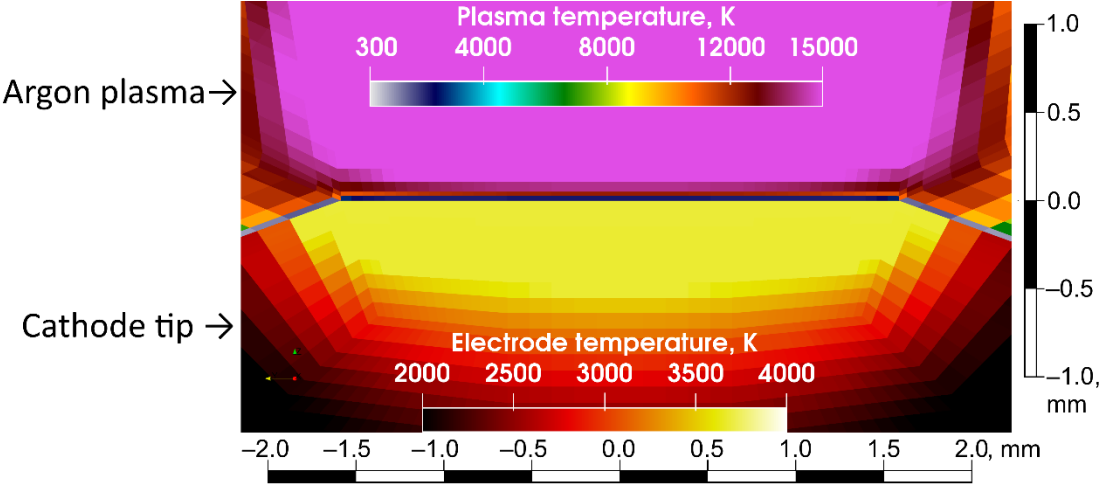


Figure 43 Temperature discontinuity in LTE model in the case without the custom fluid-electrodes coupling

The solution consists in dividing the domain into electrodes and fluid and couple them through a custom coupling algorithm. It consist in imposing the continuity of temperature and thermal flux, electric current and electric potential. It makes it possible to decouple the electrode and fluid enthalpy while retaining rather continuous temperature. The significant difference in thermal and electrical conductivities of tungsten and argon can also be taken into account in the calculation of the electric current and thermal flux.

To do that the computational domain is divided into three subdomains: cathode, fluid, and anode. The division is done with the standard function of Code\_Saturne. As a result two internal boundary surfaces appear on the anode and cathode as illustrated in Figure 44.

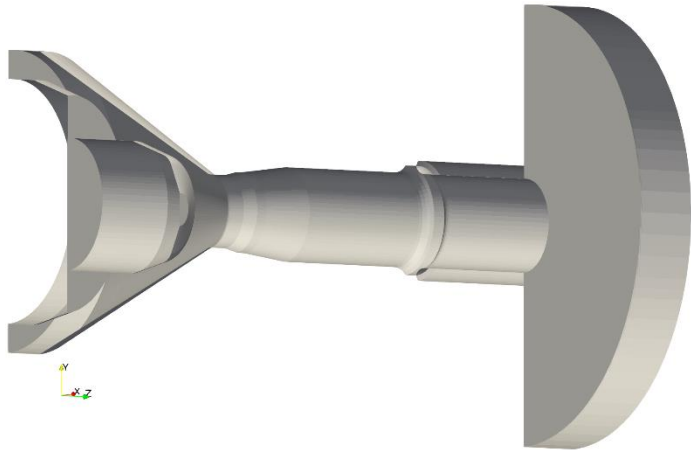


Figure 44 External and internal boundaries of the computational domain. The internal boundaries are used in the fluid-electrode coupling

With the custom fluid electrode coupling the problem of the unphysically low temperature in the first layer of cells near the cathode tip is mitigated. The new temperature distribution after the coupling is presented in Figure 45. As it can be seen from the figure, the temperature in the fluid cells adjacent to the cathode tip at the arc attachment is higher than the cathode tip temperature.

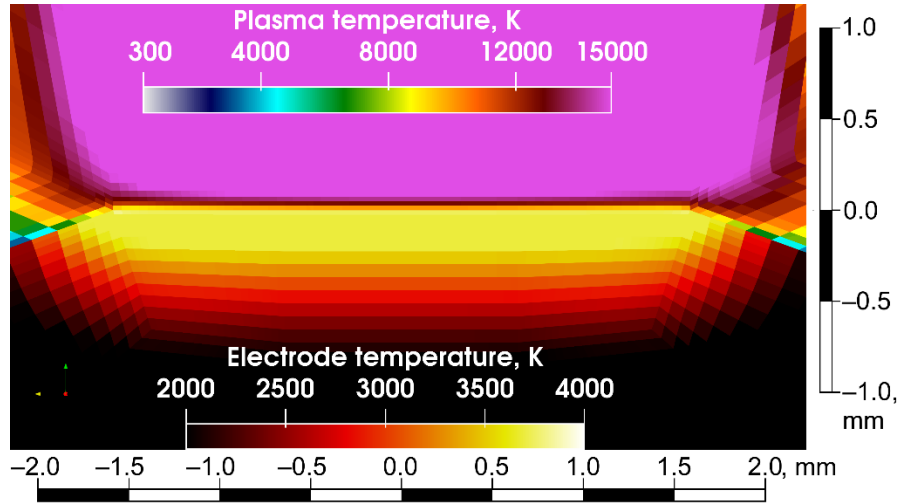


Figure 45 Temperature distribution at the cathode tip in LTE model in the case with the custom fluid-electrodes coupling

### II.5.4.1. Coupling of solved variables

The coupling of the solved variables is implemented through the continuity of electric current, electric potential, temperature and thermal flux. The anode and cathode sheaths are treated separately as additional heat source at the interface electrode cells and additional contribution into the total torch voltage.

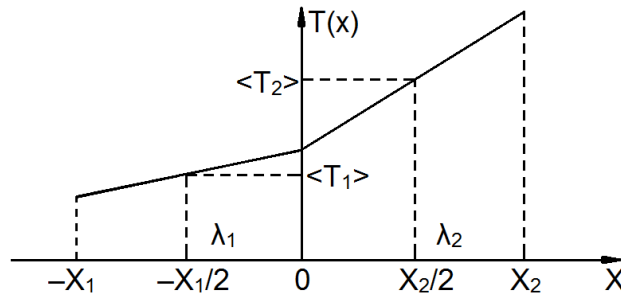


Figure 46 Two-cell case considered at every face of the electrode-fluid interface

For every interface face between the electrode and fluid, a two-cell case is considered as in Figure 46 with a linear approximation of temperature and electric potential inside both boundary cells (2.32). At the interface face, the continuity of temperature, thermal flux, electric potential and electric current is assumed, which is expressed by the set of equations (2.33).

$$\left\{ \begin{array}{l} T_1(x) = \langle T_1 \rangle + a_1 \left( x + \frac{X_1}{2} \right) \\ T_2(x) = \langle T_2 \rangle + a_2 \left( x + \frac{X_2}{2} \right) \\ \varphi_1(x) = \langle \varphi_1 \rangle + b_1 \left( x + \frac{X_1}{2} \right) \\ \varphi_2(x) = \langle \varphi_2 \rangle + b_2 \left( x + \frac{X_2}{2} \right) \end{array} \right. \quad (2.32)$$

$$\begin{cases} T_1(0) = T_2(0) \\ \lambda_1 \left. \frac{dT_1(x)}{dx} \right|_{x=0} = \lambda_2 \left. \frac{dT_2(x)}{dx} \right|_{x=0} \\ \varphi_1(0) = \varphi_2(0) \\ \sigma_1 \left. \frac{d\varphi_1(x)}{dx} \right|_{x=0} = \sigma_2 \left. \frac{d\varphi_2(x)}{dx} \right|_{x=0} \end{cases} \quad (2.33)$$

Where  $\lambda_1, \lambda_2$  are the thermal conductivities of the cells and  $\sigma_1, \sigma_2$  the electrical conductivities.

Inserting (2.32) into the equation set (2.33), the following values of temperature and electric potential at the interface between two cells are obtained:

$$\begin{aligned} T_1(0) = T_2(0) &= \frac{\lambda_1 X_2 \langle T_1 \rangle + \lambda_2 X_1 \langle T_2 \rangle}{\lambda_1 X_2 + \lambda_2 X_1} \\ \varphi_1(0) = \varphi_2(0) &= \frac{\sigma_1 X_2 \langle \varphi_1 \rangle + \sigma_2 X_1 \langle \varphi_2 \rangle}{\sigma_1 X_2 + \sigma_2 X_1} \end{aligned} \quad (2.34)$$

$$\phi_{diff}^{heat}(0) = -\frac{2\lambda_1\lambda_2}{\lambda_1 X_2 + \lambda_2 X_1} (\langle T_2 \rangle - \langle T_1 \rangle) \quad (2.35)$$

If the interacting cells have the same size,  $X_1$  and  $X_2$  can be omitted in (2.34).

The computed interface temperatures are then translated into enthalpies and imposed as a boundary condition. In the LTE model the computed enthalpy is a boundary condition for the whole plasma enthalpy while in the 2T model the computed enthalpy is a boundary condition for the heavy species enthalpy. The electron enthalpy in the 2T model has zero flux boundary condition on the electrode surface.

The formula (2.35) represents the thermal fluxes to the anode and cathode due to thermal conduction.

A non-zero electrical boundary condition in Code\_Saturne should be the Dirichlet boundary condition because it:

- has a lower computational cost;
- allows to get a continuous electric potential in model with included electrodes;
- retains the standard for Code\_Saturne electric scaling function;
- allows to have a dynamic coupling of the fluid and electrodes. Usually the fluid-electrode coupling through unsteady Neumann boundary condition is unstable in time and hard to converge.
- allows to get a smooth and monotonous distribution of electric potential inside the electrodes, whereas the fluid-electrode coupling through a Neumann boundary condition produces an unphysical distribution of the electric potential inside the electrode with unstable local minima and maxima.
- allows to get rid of any artificial profile for the boundary condition.

During the initialization, over stage around 10 to 20 time steps, the shape and absolute value of the electric potential distribution inside the electrodes change a lot, which has no physical meaning. Thus, during the arc initialization the electric potential coupling at the electrode surface should be tightly-controlled. The fluid has to be coupled with both electrodes through a certain fixed spot at the surface of each electrode. At every time step on the initial coupling spots, a certain recomputed value of the electric potential proportional to the arc voltage has to be imposed. Outside of this coupling spot on the electrode surface, an electrical insulation is imposed. The coupling spot on the cathode surface should have a smaller radius than the flat cathode tip; otherwise some numerical effects during the initialization stage will cause an unphysical overwhelming Joule power in corner cells and instant “melting” of the cathode tip edge. After the initial 10 to 20 time steps, the fluid-electrode coupling can be executed normally.

A possible numerical issue of the fluid-electrode coupling is when the interface cells of fluid and metal appear in different parallel subdomains as illustrated in Figure 47. Normally parallel subdomains are handled as separate tasks and coupled through an internal mechanism of Code\_Saturne when they belong to the same phase, e.g. only metal or only fluid. Also, the coupling of metal and fluid interface cells can be easily done in user subroutines when these cells belong to the same parallel subdomain. When the interface cells appear in different phases and different parallel subdomains at the same time, additional effort is needed for coupling. More specifically, the broadcasting of data about the interface cells has to be implemented in order to exchange the information and establish the relation between the cells. Such broadcasting is realized through the standard functions of Code\_Saturne for Message Passing Interface (MPI). The use of MPI functions for the coupling does not increase the computational cost much, but allows to use multiple processors with automatic parallel partitioning of the computational domain.

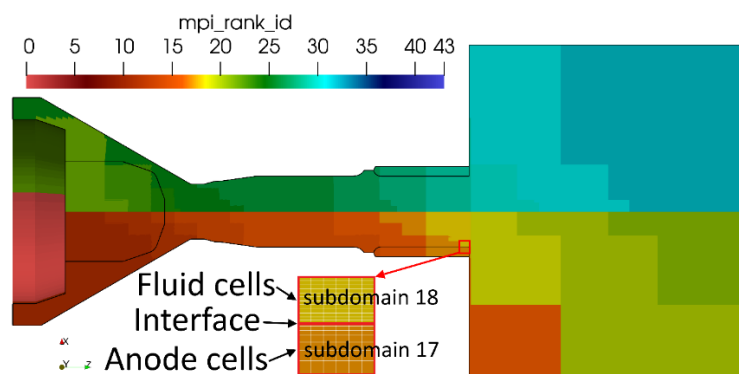


Figure 47 Distribution of the MPI rank of parallel subdomains. Discontinuity of the parallel subdomain at the fluid-electrode interface which raises the problem of the fluid-electrode coupling in multiple-processor computation

#### II.5.4.2. Heat transfer to electrodes dues to electric current

In addition to the diffusive thermal flux (2.35), the thermal flux to electrodes due to ion and electron fluxes has to be taken into account. The heat transfer to the electrodes due to the electric charge carriers is a separate process and is not a part of the boundary condition for the fluid-electrode coupling. This process happens in the 3D area which includes the cathode cells, the interface surface and the plasma cells, not only on the interface surface itself. It is a heat source for the cells of the computational domain and has its own contribution through the source term in the energy conservation equation.



The electric current at the cathode surface consists of the ion flux and electric flux. The electric current due to the electron flux is calculated through the Richardson-Dushman emission law supplemented with Schottky correction given by the formula (1.1). The Schottky reduction  $\Delta W$  of the work function of tungsten is 0.2 eV for 500 A, 0.1 eV for 200 A and 0 eV for 100 A. These values are taken from (Benilov and Marotta, 1995) and correspond to the prediction of the electron temperature in the vicinity of the cathode tip around 15000 K, 12000 K and 11000 K for 500 A, 200 A and 100 A respectively. The predicted cathode tip temperature is around 3850 K for 500 A and decreases to 3400 for 100 Amp. In the study (Benilov and Marotta, 1995) carried out for a wide range of cathode temperature up to 5000 K and  $T_e$  up to 40 000 K, the maximum predicted electric field was around  $4 \cdot 10^8$  V/m which confirms the validity of the Richardson-Dushman emission law with Schottky reduction.

Another option for the emission current calculation is the Murphy-Good equation, which makes significant difference compared to the Richardson-Dushman emission law in case of high enough cathode surface electric field (more than  $10^8$  V/m) and low temperature (lower than 3000K) (Javidi Shirvan et al., 2018). However, in the presented model the cathode surface temperature is around the tungsten melting point. Even for a non-equilibrium cathode sheath with a space charge sheath of  $0.02 \mu\text{m}$  (Benilov and Marotta, 1995) and voltage drop of 10 Volts (Benilov et al., 2016; Cayla et al., 2008; Khrabry et al., 2018; Neumann, 1977), the resulting surface electric field is quite high, approximately  $5 \cdot 10^8$  V/m, but the cathode surface temperature will eliminate the difference between the Richardson-Dushman and the Murphy-Good equations. Subsequently the effect of the Murphy-Good equation compared to the Richardson-Dushman law is negligible.

In (Cayla et al., 2008) it was shown that for an electric current density above  $10^6$  A/m<sup>2</sup>, the effect of the secondary electron emission is negligible and the main source of electrons in electric arc plasma torches is the thermal electron emission.

The ion current is calculated from the balance of the electrons emission and the calculated electric current (2.36).

$$j_{emis}(T_{cath}) + j_{ions} = j_{calc} \quad (2.36)$$

The heat source at the cathode surface due to the electric current consists of the cathode cooling by electrons emission and ions collected and neutralized by the cathode:

$$Q_{cath}(j_{emis}, j_{ions}) = -j_{emis} \cdot \left( \frac{2k_B}{|e|} T_{cath} + W \right) + j_{ions} \cdot \left( \frac{5k_B}{2|e|} (T_{plasma}^h - T_{cath}) + U_C + \Phi_i \right) \quad (2.37)$$

The cathode voltage drop  $U_C$  is taken from (Cayla et al., 2008; Khrabry et al., 2018; Neumann, 1977) and for the electric current density predicted in the present study it is equal to 10 V.  $\Phi_i = 15.76$  eV is the first ionization potential of argon. Only the first ionization is considered since the ion  $\text{Ar}^{1+}$  is prevailing under 20000 K, and the predicted electron temperature  $T_e$  in 2T models and predicted LTE temperature  $T$  in the first layer of cells are always lower than 20000 K.

The heat source at the anode surface due to the electric current consists of the anode heating electrons which bring the thermal energy from plasma, kinetic energy obtained from the anode sheath voltage drop and work function of the cathode material:

$$Q_{anode}(j_e) = j_e \cdot \left( \frac{5k_B}{2|e|} (T_{plasma}^e - T_{cath}) + U_A + W \right) \quad (2.38)$$

The thermal flux to the anode due to the back diffused ions flux is assumed to be negligible, meaning  $Q_{anode}(j_{ions}) \approx 0$ . The anode voltage drop  $U_A$  is assumed to be 4 V (Neumann, 1977; Tanaka and Ushio, 1999).

In the LTE model  $T_e$  is assumed to be equal to  $T_h$  during the computation of the heat flow to the electrodes.

The proper model of the electrode sheath is beyond the scope of present study, but could be developed as it was done for example in (Gonzalez et al., 2009) to make the model more self-sufficient.

### II.5.4.3. Mimicking disequilibrium effects at the electrode arc attachment in LTE model

Even with the custom fluid-electrode coupling the computed temperature of the electrode surface corresponds to almost zero electrical conductivity under the LTE assumption. It is thus necessary to use an additional artificially high electrical conductivity in the first layer of cells adjacent to the whole anode surface and a part of the cathode tip wider than the arc attachment. Without such an artificial conductivity  $\sigma_{attachment}$ , the electrode arc attachment can be unstable for low current intensity, since the Joule power is not high enough in the electrode vicinity, and as a result the electric current density distribution in the vicinity of the electrodes is unstable. The value of  $\sigma_{attachment}$  used in this model is 5000 S/m which allows to get rid of the numerical fluctuations and instabilities of the Joule power in the vicinity of the electrodes, which could induce additional unphysical fluctuations in the whole plasma flow.

Another disequilibrium issue that cannot be reflected by the LTE model of a non-transferred arc is the violation of LTE behind the anode arc attachment that was described by (Nemchinsky, 2015). The specific detail of the non-transferred arc is the fact that it is not straight but embowed and the arc attached to two perpendicular surfaces. Thus in the plasma torch with a cascaded anode the arc has the most curved part near the anode attachment. In the center of this arc curvature the departure from LTE is prominent. However the LTE model is not capable of reflecting it. As a result in the LTE model of the SinplexPro™ without any additional treatment the arc cannot move back on the anode surface or restrike due to non-equilibrium overheating behind the attachment. Eventually in such model the arc attaches to the anode outside of the torch and cannot get inside because the boundary gas layer is too cold to conduct any electricity.

Therefore a small domain with an artificial electrical conductivity that allows the flow to gain some heat from Joule heating prior to the main anode arc attachment is required. This trick is intended to only mimic the disequilibrium effect behind the anode arc attachment and not to predict it. The suggested domain of the artificial  $\sigma_{take-over}$  behind the anode arc attachment and the used values of  $\sigma_{take-over}$  are illustrated in Figure 48. The value of  $\sigma_{take-over}$  imposed in the central part of the domain is 195 S/m, it corresponds to the disequilibrium value for  $T_e = 7000K$  and  $T_h = 1000K$ . The artificial conductivity linearly decreases from the central part to the periphery. The width of the  $\sigma_{take-over}$  domain is 1.4 mm. The angular position of the artificial

electrical conductivity domain corresponds to the angular position of the circular sector with the highest electric current.

The validity of the chosen temperatures for the artificial electrical conductivity will be later verified with the 2T simulation.

The value of  $\sigma_{take-over}$  imposed in the domain behind the anode arc attachment is significantly lower than the value  $\sigma_{attachment}$  imposed in the vicinity of both electrodes, because they have different purpose:  $\sigma_{take-over}$  is responsible for the dynamics of the anode arc attachment, while  $\sigma_{attachment}$  is responsible for the stability and existence of the whole arc. Without the domain with  $\sigma_{take-over}$  the arc would still exist but it would attach to the outside surface of the anode.

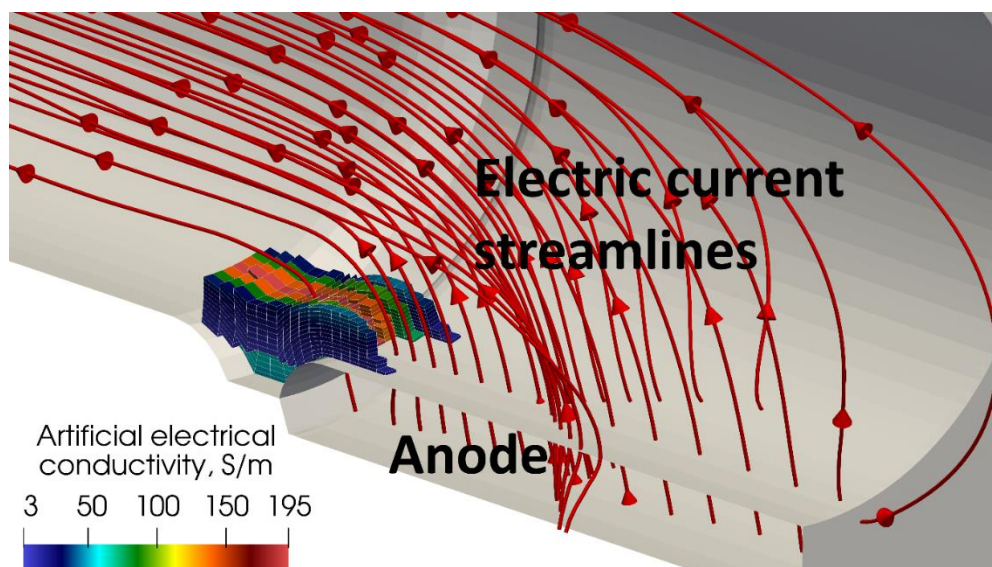


Figure 48 Artificial electrical conductivity (0-195-0 S/m) domain behind the anode arc attachment intended to mimic the disequilibrium effect

Both 2T models are intended to get rid of the described above numerical tricks and do not any artificial electrical conductivity domains for existence and stability of the arc.

## II.6. Conclusion

This chapter was dedicated to the presentation of the two models of DC plasma spray torch developed in this study: LTE model and 2T model. The models take into account the most important features of plasma torch simulation currently present in the plasma torch models found in the literature.

The two models are 3D and unsteady; they allow to predict the 3D and transient effects of arc behavior on plasma jet development and anode arc attachment. They use improved boundary conditions for the magnetic vector potential and, thus, should predict a more accurate self-induced magnetic field and velocity field.

The electrodes are included in the computational domain and coupled with the fluid. This will make it possible to analyze the thermal impact of the arc on the electrodes and the time-variation of the electrode temperature.

All these features will allow to investigate possible ways to control the arc anode attachment motion and, thus, decrease the anode erosion.

The developed 2T model is intended to estimate the departure from the local thermal equilibrium in the simulated plasma torch and its effect on the predicted plasma fields. Two enthalpy formulations for the 2T model are presented: they differ in the association of ionization energy to the electrons or heavy species.

The next chapter will present the LTE and 2T predictions for commercial mono-cathode cascaded-anode plasma torch.



# Chapter III. Simulation results

---



### III.1. Introduction

The current chapter presents the main results of the LTE model and both 2T models. The first two sections deal with two important features of these models: the boundary conditions for the magnetic vector potential and the inclusion of electrodes in the computational domain. Then, the following sections describe the results obtained with the LTE model for a given set of plasma torch operating parameters. Since the LTE model predicts a constricted anode arc attachment, two ways to rotate such attachment and, so, mitigate the anode erosion are tested: swirling gas injection and external magnetic field. The chapter ends with the comparison of the results obtained with the two 2T models developed in this work that differ in the formulation of the electron and heavy species enthalpies, and finally with the validation of predictions against experimental data provided by the torch manufacturer: arc voltage and plasma torch thermal efficiency.

### III.2. LTE model

#### III.2.1. Effect of boundary condition for magnetic vector potential

The most often used boundary condition for the magnetic vector potential is a null flux imposed to the components of the magnetic vector potential at the physical limits of the domains or a value equal to zero if these limits are far from the arc. Freton *et al.* showed that this approach can result in a wrong predicted self-magnetic fields and, thus, velocity fields for free burning or constricted transferred arcs when the finite volume scheme is used (Freton et al., 2011).

In this work, dealing with a non-transferred constricted arc, two types of boundary condition for the magnetic vector potential were compared:

- Null flux at the boundaries close to the arc and null value at the distant boundaries. It is referred as PVNF according to the notation used in the paper (Freton et al., 2011).
- Values of the magnetic vector potential calculated by the Biot&Savart law. It is referred as BS.

A specific detail in this study is a narrow bottleneck around the arc inside the torch channel. Such geometry configuration does not allow to have the boundaries of the computational domain far from the arc. In addition, the channel has a complex geometry which results in many corners in the mesh. The latter appeared to be detrimental for the simulation with the PVNF boundary condition for the magnetic vector potential at the boundaries close to the arc (see section II.5.3.6).

The magnetic field predicted with both types of boundary conditions are shown in Figure 49 and Figure 50. For these simulations, the arc current was 500 A and the gas flow rate of 60 NLPM of argon. It can be seen that the magnetic field is significantly overestimated in the corners with the PVNF boundary condition compared to the BS boundary condition. The same observation was made in (Freton et al., 2011) for transferred arcs and free burning arcs.

The corner effect in the magnetic field calculated with the PVNF boundary condition causes severe fluctuations of the arc: the anode arc attachment becomes unstable; it jumps and moves rapidly and the flow becomes stochastic. Eventually, the model fails to predict any plasma jet issuing from the torch as the flow velocity and temperature are low inside the torch as shown in Figure 51 and Figure 52.



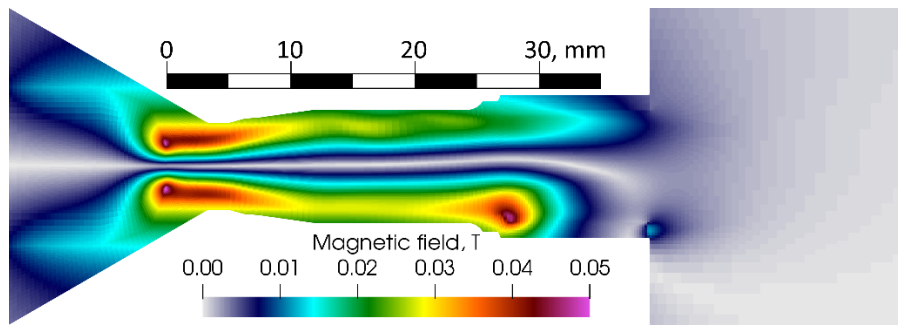


Figure 49 Computed magnetic field with the **BS** boundary condition for magnetic vector potential. 500 A and 60 NLPM of argon

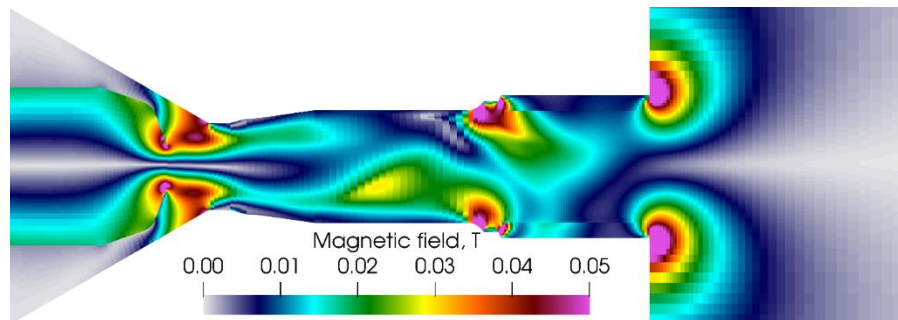


Figure 50 Computed magnetic field with the **PVNF** boundary condition for magnetic vector potential. 500 A and 60 NLPM of argon

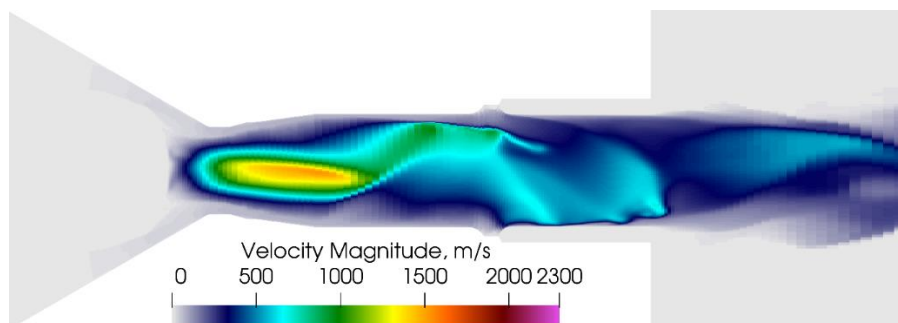


Figure 51 Computed velocity distribution with the **PVNF** boundary condition for magnetic vector potential. 500 A and 60 NLPM of argon

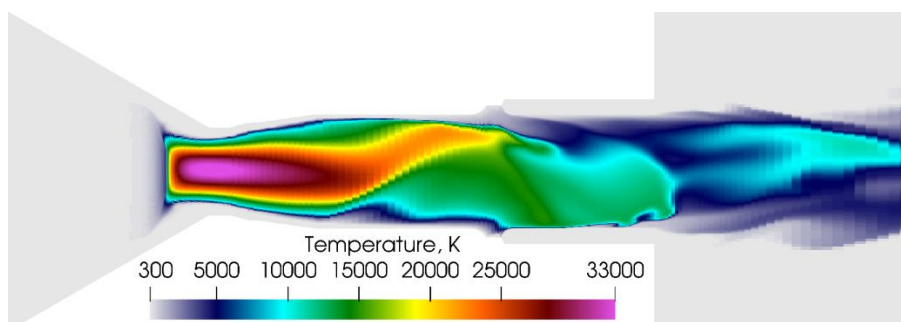


Figure 52 Computed temperature distribution with the **PVNF** boundary condition for magnetic vector potential. 500 A and 60 NLPM of argon

The discrepancy in the heat balance (3.1) between the total Joule power and energy of the plasma flow with the PVNF boundary condition is subject to severe disturbances up to 50%. The predicted voltage fluctuation is high and abrupt as illustrated in Figure 53 which is not expected for a plasma torch operated with a high current intensity and pure argon. Meanwhile

with the BS boundary condition, the plasma jet is much more stable as it can be seen in Figure 75 and the heat balance violation is only about 1%. The predicted voltage corresponds to the take-over mode which is commonly observed for plasma torches operated with argon at high current.

$$I \cdot (V_{arc} + U_C + U_A) = \dot{h} + E_{kin}^{nozzle} + Q_R^{torch} + Q_{anode} + Q_{cathode} \quad (3.1)$$

Where  $I$  is the arc current intensity,  $V_{arc}$  the computed arc voltage in the model,  $U_C$  and  $U_A$  the cathode and anode sheath voltage drops,  $\dot{h}$  the enthalpy flow through the nozzle exit given by the formula (3.2),  $E_{kin}^{nozzle}$  the kinetic energy of the plasma flow through the nozzle,  $Q_R^{torch}$  the radiation losses inside the torch,  $Q_{anode}$  and  $Q_{cathode}$  the heat flow to the anode and cathode respectively.

$$\dot{h} = \int_{nozzle\ exit} \rho h \vec{u} \cdot \vec{n} dS \quad (3.2)$$

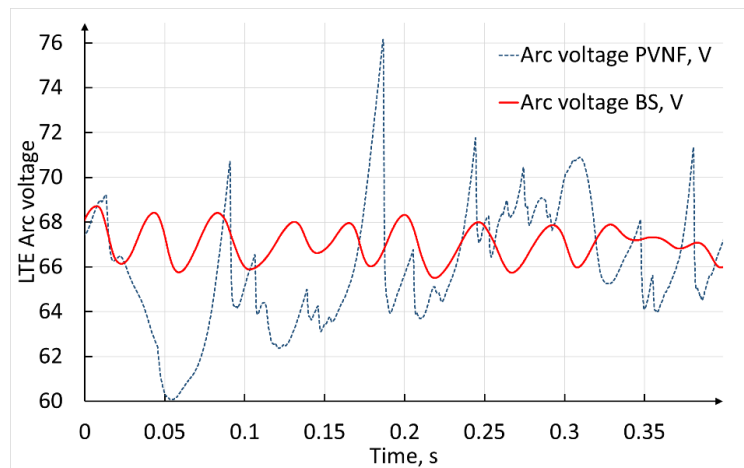


Figure 53 LTE arc voltage fluctuations for the BS and PVNF boundary conditions for the magnetic vector potential. 500 A and 60 NLPM of argon. Sheath voltage drops are not included in the predicted arc voltage

The more stable and continuous prediction of the magnetic field with the BS boundary condition makes the arc behavior much more stable. This results in a more plausible distribution of the electric current density in the torch, which does not exhibit unphysical gradients as shown in Figure 54, while with the PVNF boundary condition, it presents unphysical shape and even may exhibit discontinuities as shown in Figure 55.

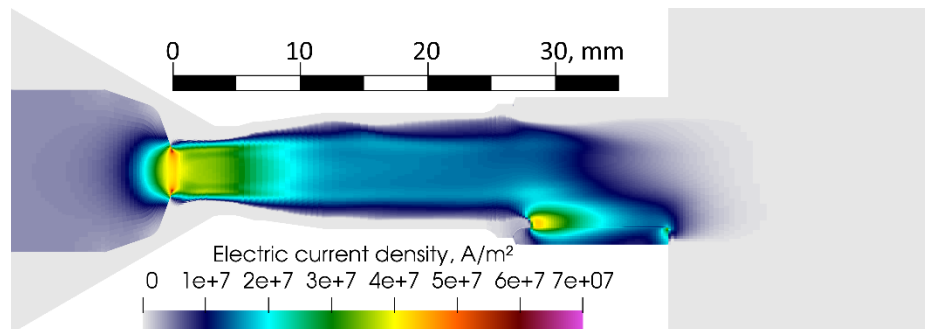


Figure 54 Computed electric current density with the BS boundary condition for magnetic vector potential. 500 A and 60 NLPM of argon

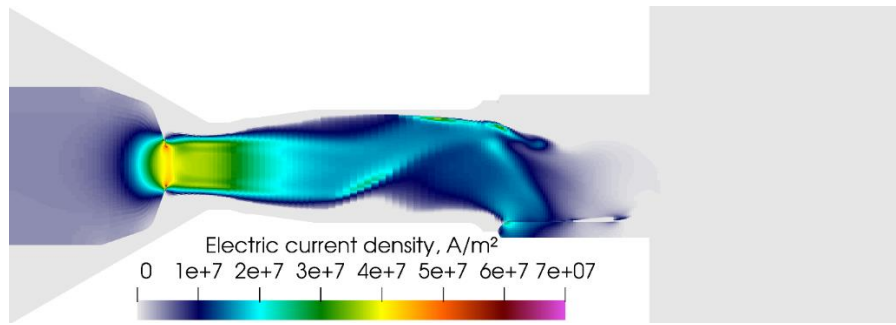


Figure 55 Computed electric current density with the **PVNF** boundary condition for magnetic vector potential. 500 A and 60 NLPM of argon

Therefore, for the simulations of the electric arc inside the plasma torch SinplexPro™, the BS boundary condition for magnetic vector potential was chosen as the most suitable for the geometry configuration under consideration, even if it consumes more computational resources.

### III.2.2. Effect of inclusion of electrodes into computational domain

The majority of the models of plasma torch operation do not include the electrodes into the computational domain. The drawback of such approach is the necessity to impose an electric current density profile at the cathode tip while with the electrodes in the computational domain, the electric current density distribution at the cathode tip is a result of the simulation.

The predicted profile of the electric current density at the cathode tip computed with the model involving the electrodes is presented in Figure 56 for an arc current of 500 A and argon gas flow rate of 60 NLPM. This profile exhibits a prominent spike at the edge between the flat tip of the cathode and conic surface around it. This spike results in a ring of molten tungsten on the cathode tip which is visible in Figure 57. Such profile is difficult to express by a simple formula or derive analytically prior to the simulation as it is generally done for the models dealing with more conventional cathode shapes.

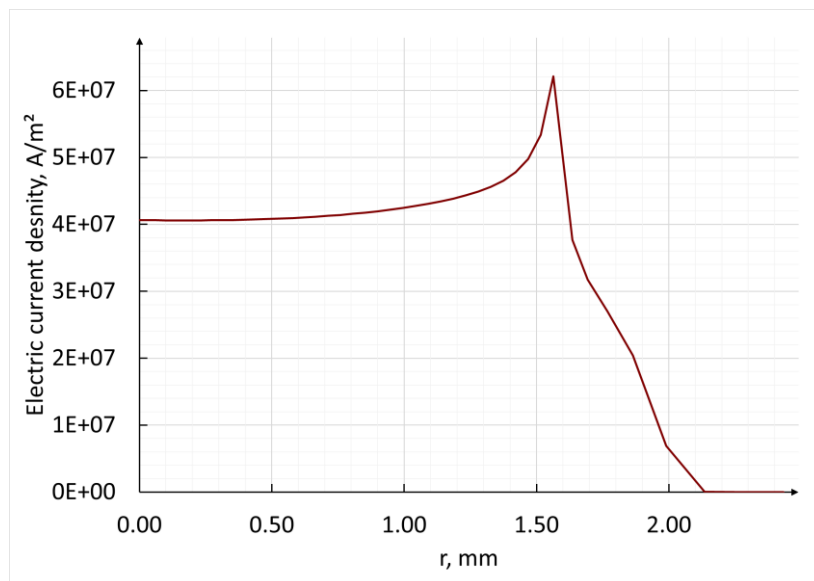


Figure 56 Electric current density profile predicted by the LTE model with electrodes. 500 A and 60 NLPM of argon

The predicted cathode temperature for the same operating conditions is shown in Figure 57. The cathode tip starts melting after about 10 ms. The hot area on the cathode tip forms a distinctive pattern: hot area in the center surrounded by a hot ring. The latter corresponds to the spike of the electric current density profile seen in Figure 56. A similar pattern can be seen on the photo of worn cathodes (Figure 58) and on the photo of tested cathodes (Figure 59) of the SinplexPro™ plasma torch.

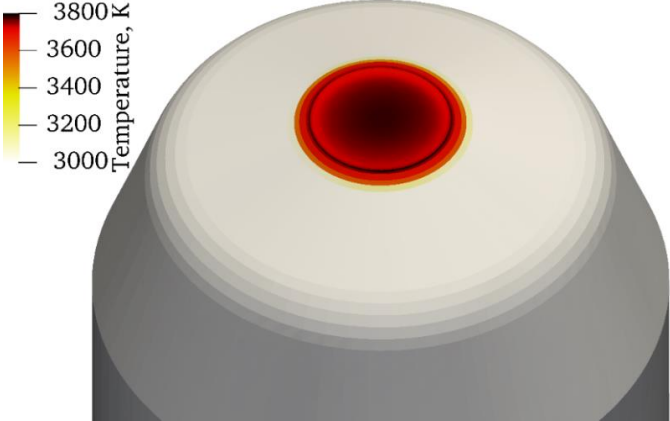


Figure 57 Predicted temperature distribution on the cathode tip with the LTE model. 500 A and 60 NLPM of argon



Figure 58 Photos of worn cathodes of the of the SinplexPro™ plasma torch with molten patterns on the top surface. The cathodes were used for extended period of time with various parameters (courtesy of Oerlikon Metco (US) Inc.)

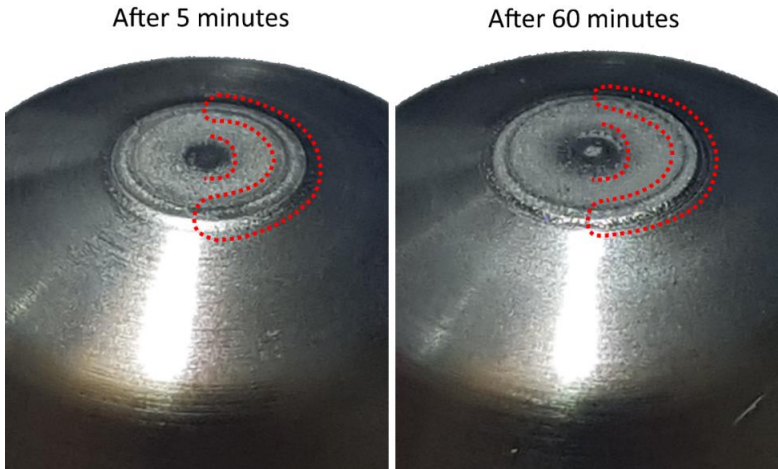


Figure 59 SinplexPro™ cathodes erosion after 5 minutes and 60 minutes of operation with 500 A and 60 NLPM of argon (courtesy of Oerlikon Metco (US) Inc.)

On the anode, if the arc attachment does not move for at least 10 ms the temperature of the tungsten anode liner can reach values close to the material melting point. The temperature distribution on the anode surface and inside is illustrated in Figure 60.

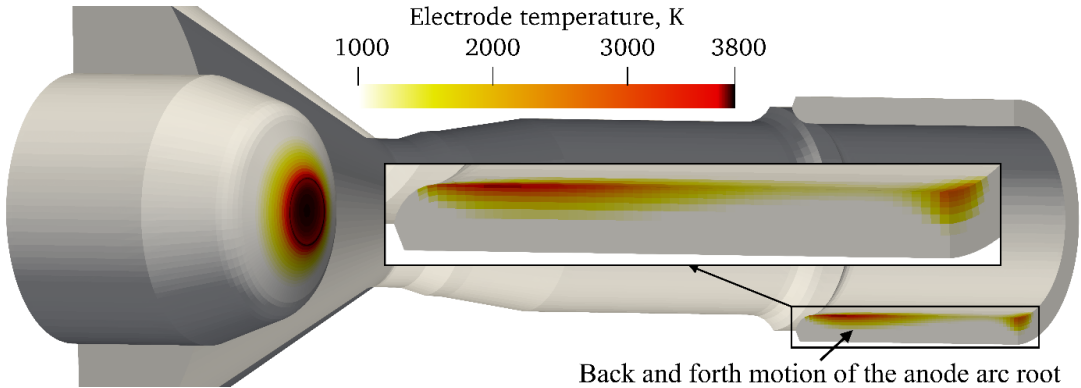


Figure 60 Cathode and anode electrode temperature predicted by the LTE model after 10 ms of operation with a stable angular position of the anode arc attachment. 500 A and 60 NLPM of argon

In this study a model without the electrodes in the computational domain was also developed to compare the predictions with that of the model with the electrodes. In the model without electrodes, the profile of the electric current density, imposed on the cathode tip, was the profile predicted by the model with the electrodes included into the computational domain.

Figure 61, Figure 62, Figure 63 and Figure 65 show the fields predicted by the model limited to the gas phase. The comparison of Figure 49 and Figure 61 shows that the magnetic field is underestimated in the vicinity of the electrodes compared to that predicted by the model with the electrodes because the electric current flow is neglected inside the bulk of the electrodes.

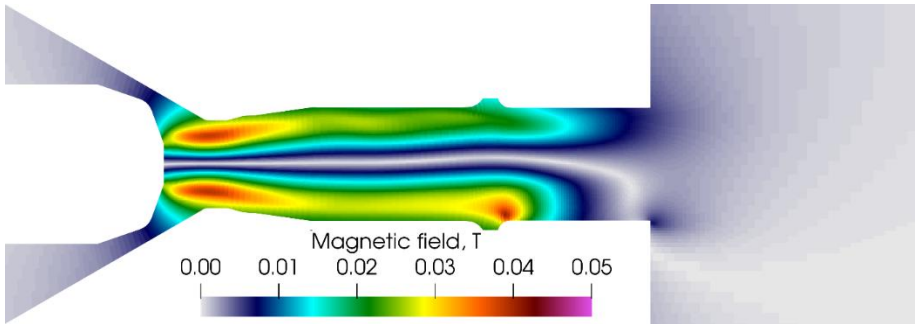


Figure 61 Computed magnetic field without electrodes with the BS boundary condition for the magnetic vector potential and without the electrodes in the computational domain

However, it is possible to obtain nearly the same distribution of electric current density in the fluid domain with both models as shown in Figure 62 and Figure 54 when the proper boundary condition of electric current density is imposed at the cathode tip in the model without electrodes.

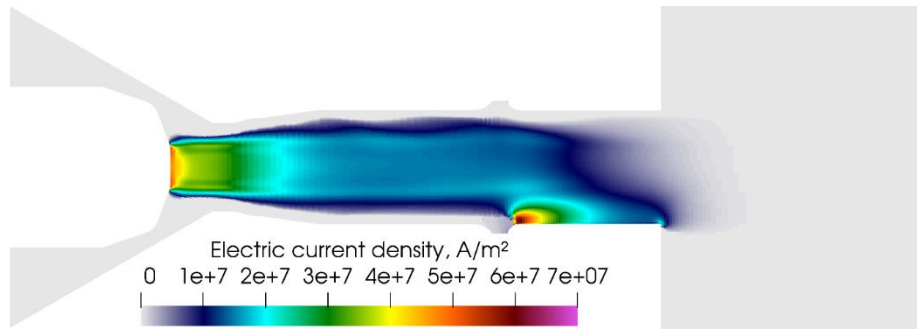


Figure 62 Computed electric current density with the BS boundary condition for the magnetic vector potential and without the electrodes in the computational domain

The plasma velocity computed without the electrodes in the computational domain (Figure 63) is slightly lower than the velocity computed with the electrodes (Figure 64). The difference is especially visible near the cathode tip because of the underestimation of the magnetic field near the cathode tip as explained above. On the contrary, the predicted plasma temperature field (Figure 66) is slightly higher than that predicted with the electrodes in the computational domain (Figure 65). The plasma temperature has its maximum in front of the cathode tip. Thus in the case without the electrodes in the computational domain, the velocity in front of the cathode tip is lower. Therefore, the plasma residence time is higher and the plasma gains more energy from Joule heating, and the temperature in front of the cathode tip is higher.

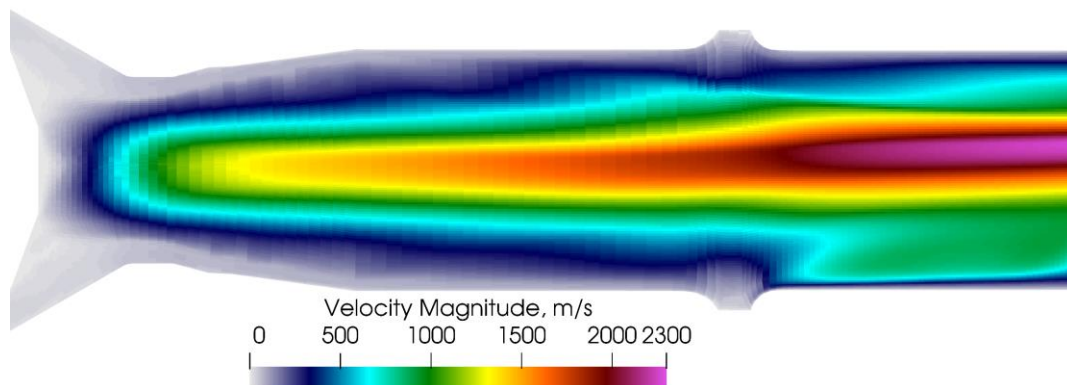


Figure 63 Computed velocity distribution inside the plasma torch with the BS boundary condition for the magnetic vector potential. **Without** the electrodes in the computational domain. 500 A and 60 NLPM of argon

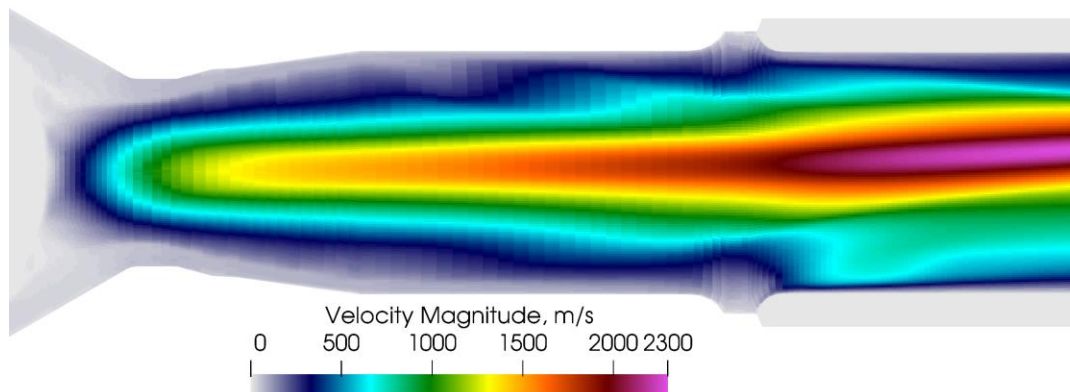


Figure 64 Computed velocity distribution inside the plasma torch with the BS boundary condition for the magnetic vector potential. **With** the electrodes in the computational domain. 500 A and 60 NLPM of argon

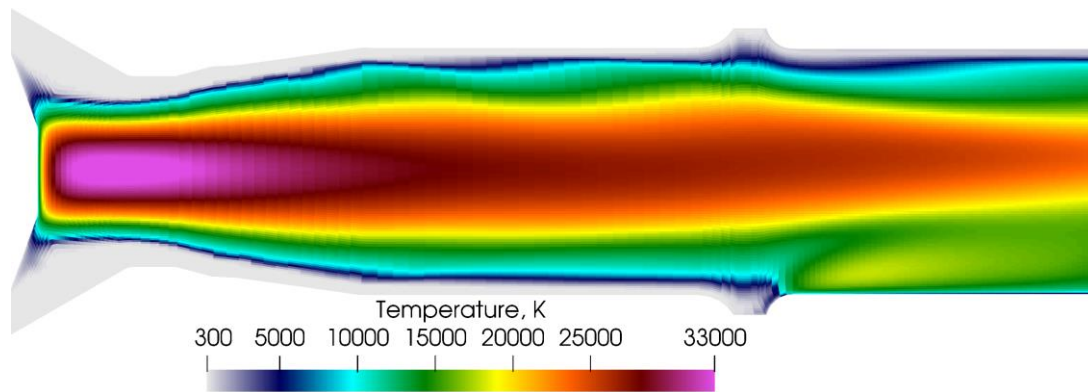


Figure 65 Computed temperature distribution inside the plasma torch with the BS boundary condition for the magnetic vector potential. **Without** electrodes in the computational domain. 500 A and 60 NLPM of argon

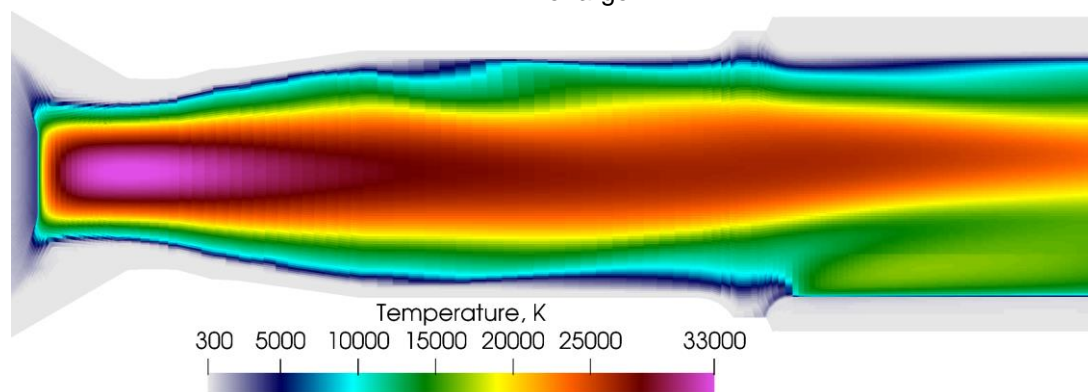


Figure 66 Computed temperature distribution inside the plasma torch with the BS boundary condition for the magnetic vector potential. **With** electrodes in the computational domain. 500 A and 60 NLPM of argon

Therefore, if the proper electric current density profile is imposed at the cathode tip, very similar results in terms of plasma velocity and temperature can be obtained. However, when the cathode has a specific shape as the cathode of the SimplexPro torch, this profile cannot be easily “guessed” and a model with the electrodes in the computational domain is required to determine it

One of the advantages of the model with the electrodes is that the electric current profile at the cathode tip is not needed. In addition, the model allows to investigate the heating of the electrodes by the electric current and predict possible the effect of some change in the electrode design on their erosion. It should be noted that the computational cost of the inclusion of electrodes into the domain is rather low, as both contain a low number of cells and the convergence of the solved variable in the electrodes is quite easy due to the high electrical and thermal conductivities of the materials and velocity equal to zero in the whole solid domains.

### III.2.3. Case study

This section presents a detailed analysis of the predictions obtained with the LTE model with the electrodes in the computational domain and the BS boundary condition for the magnetic vector potential. The operating conditions of the plasma torch are: an anode diameter of 9 mm; arc current of 500 A and argon gas flowrate of 60 NLPM.

One of the essential results of the electric arc simulation inside the plasma torch is the electric current field, since it defines the plasma jet behavior and distribution of velocity and

temperature at the nozzle exit. The predicted electric current streamlines for this case study are illustrated in Figure 67. The LTE model predicts a single constricted anode arc attachment, as illustrated in Figure 68. The value of electric current density in the anode arc attachment is around  $6 \cdot 10^7 \text{ A/m}^2$  which agrees with the data for constricted anode arc attachment presented in (Neumann, 1977). Indeed, the electric arc has to find its way through the cold boundary layer that has a nearly zero electrical conductivity. The intense cooling of the tiny column that links the arc column to the anode by the cold gas flow in the anode boundary layer has to be compensated by the Joule heating. This makes the anode arc attachment to shrink and, eventually, to exhibit a rather high value of electric current density compared to that in the arc column. The highest value of the electric current density at the anode arc attachment is located in the zone of interaction of the cold boundary flow and radial part of the current lines where the constriction is the tightest as seen in Figure 67.

The cathode arc attachment is shown in Figure 69. The curvature of the electric current streamlines near the cathode tip is well predicted by the model. The highest value of the electric current density is at the edge of the cathode between the flat center and conic surface around it.

The arc column is mostly straight in the torch channel. It has a much lower electric current density than in both cathode and anode arc attachments. The electric current density in the arc column ranges from  $1 \cdot 10^7$  to  $3 \cdot 10^7 \text{ A/m}^2$  against  $7 \cdot 10^7 \text{ A/m}^2$  at the electrode arc attachments.

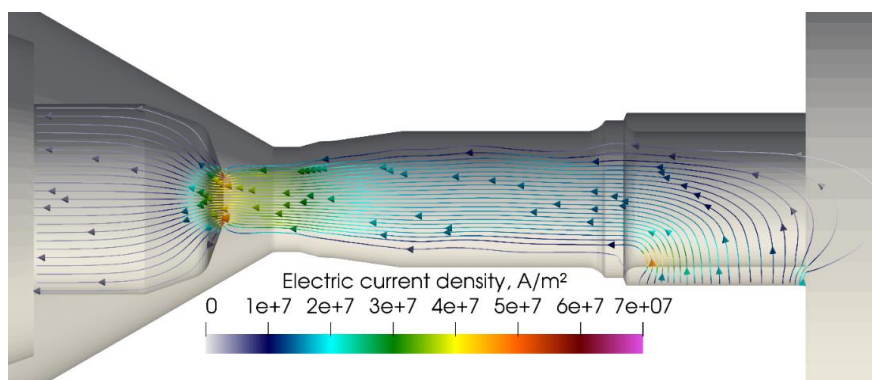


Figure 67 Instantaneous electric current streamlines in the LTE model for 500 A, 60 NLPM of argon and BS boundary condition for the magnetic vector potential

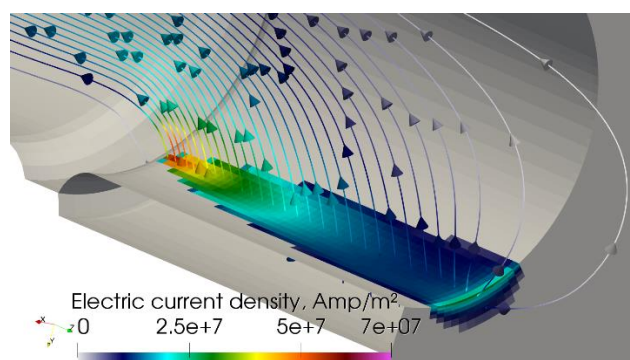


Figure 68 Instantaneous electric current streamlines and distribution on the anode surface for 500 A, 60 NLPM of argon and BS boundary condition for the magnetic vector potential



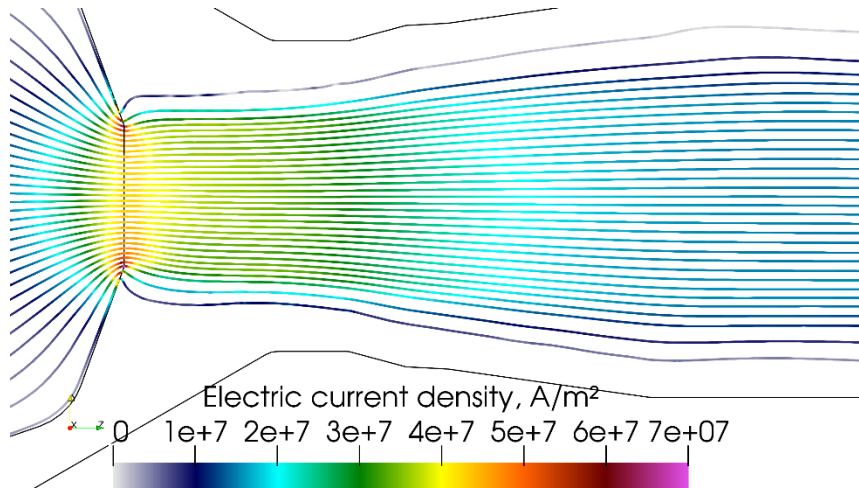


Figure 69 Electric current streamlines at the cathode tip for 500 A, 60 NLPM of argon and BS boundary condition for the magnetic vector potential

The Joule power distribution is illustrated in Figure 70. The areas with the highest Joule power are the electrode arc attachments. The maximum value of the Joule power, around  $10^{12}$  J/m<sup>3</sup>, is located in the vicinity of the cathode tip, where it creates a stiff temperature gradient. The maximum temperature in the whole torch is around 33000 K and located around 1 mm from the cathode tip as illustrated in Figure 71. Downstream, near the anode, the plasma jet becomes wider and consequently the maximum temperature at the nozzle exit is lower. The location of the temperature maximum is conditioned by the value of Joule power and constriction of the cathode arc attachment.

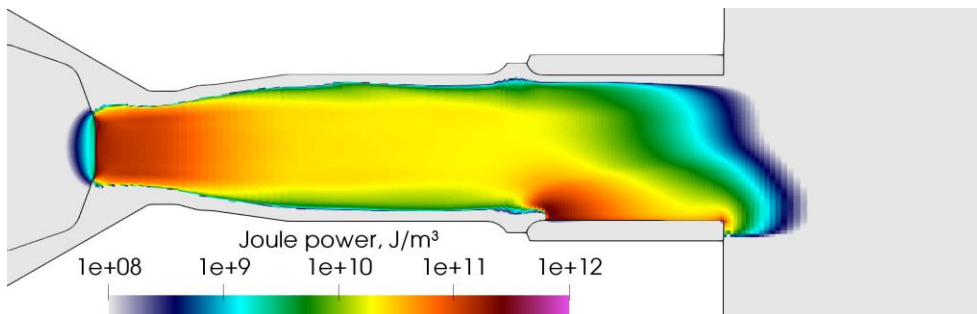


Figure 70 Joule power distribution for 500 A, 60 NLPM of argon and BS boundary condition for the magnetic vector potential

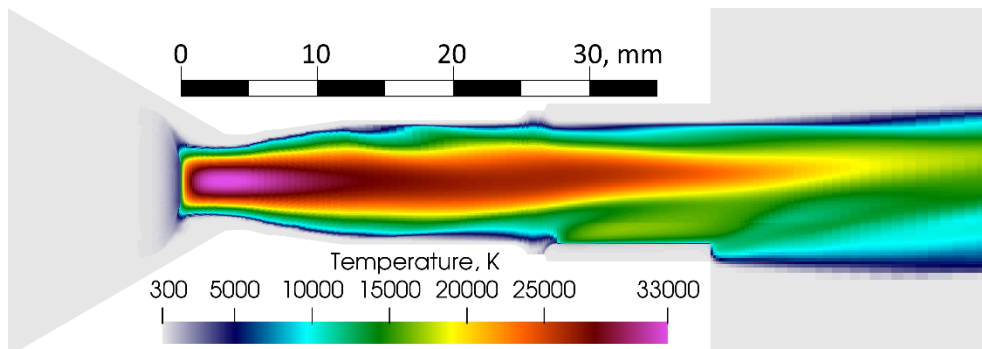


Figure 71 Instantaneous computed temperature distribution in LTE model for 500 A, 60 NLPM of argon and BS boundary condition for the magnetic vector potential

In the plasma torch, the plasma jet originates close to the cathode surface where the self-induced magnetic field associated to the arc produces a compressive force inwards on the arc

$[\vec{j} \times \vec{B}]$ . This force is balanced by an increase in the radial pressure gradient and, therefore, the pressure increases inside the arc with the highest values close to the cathode. The pressure gradient accelerates the plasma flow and induces the cathode jet.

In the vicinity of the cathode tip the Lorentz force has some axial component due to the current streamlines curvature as illustrated in Figure 72, which emphasizes the Maecker jet.

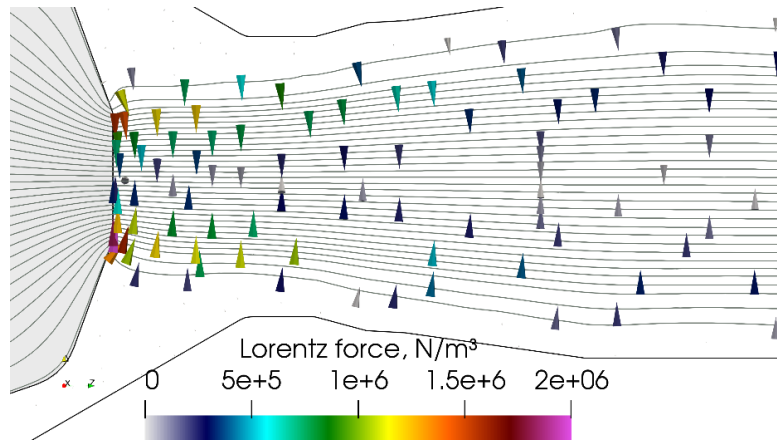


Figure 72 Electric current streamlines and constricting Lorentz force vectors near the cathode tip.

The constricting Lorentz force and expanding pressure gradient in the direction perpendicular to the torch axis are shown in Figure 73 and Figure 74. The computation of the pressure and its gradient is less smooth and stable than the computed Lorentz force, because the latter is a cross product of the previously computed continuous electric current density and magnetic field, while the pressure itself is a weak point in a weakly compressible model, which does not properly include the fluid compressibility. The pressure in this case is rather an auxiliary field of the velocity computation. Thus, some artefacts and checkerboard-order fluctuations are visible in Figure 73.

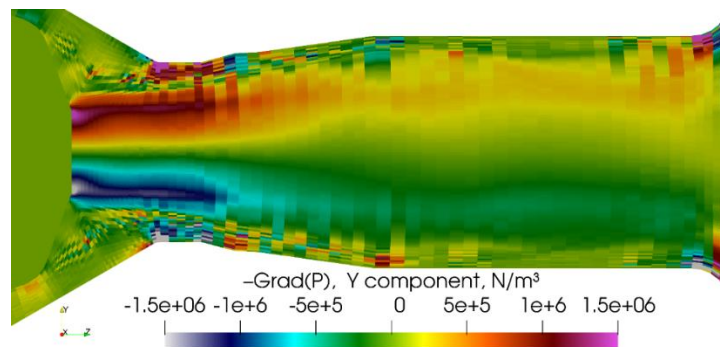


Figure 73 Pressure gradient near the cathode tip in the direction perpendicular to the torch axis.

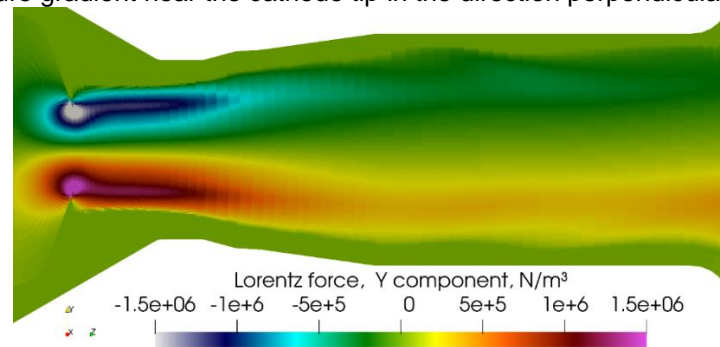


Figure 74 Lorentz force near the cathode tip in the direction perpendicular to the torch axis.

The simulation predicts a gradual acceleration of the plasma flow all the way from the cathode tip to the nozzle exit. An essential contribution into the plasma acceleration is located in front of the cathode tip and conditioned by the magnetic pressure and constriction of the cathodic jet. Then, the plasma flow continue to accelerate because of the increase in its volume as its temperature increases and density decreases. The maximum velocity is located at the nozzle exit as it is illustrated in Figure 75. The plasma velocity streamlines (Figure 76) are mostly straight and smooth as expected for a laminar flow in the plasma torch with a cascaded-anode operating with argon, low gas flow rate and high current intensity.

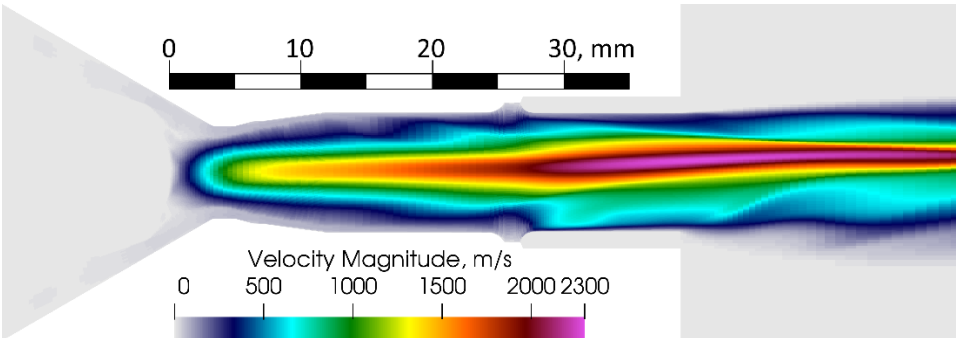


Figure 75 Instantaneous computed plasma velocity in the LTE model for 500 A, 60 NLPM of argon and BS boundary condition for the magnetic vector potential

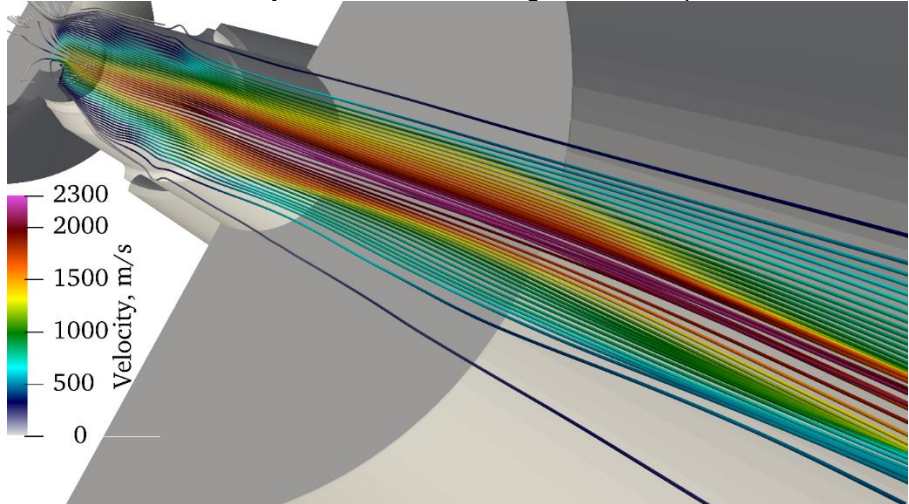


Figure 76 Velocity streamlines in the LTE model for 500 A, 60 NLPM of argon and BS boundary condition for the magnetic vector potential

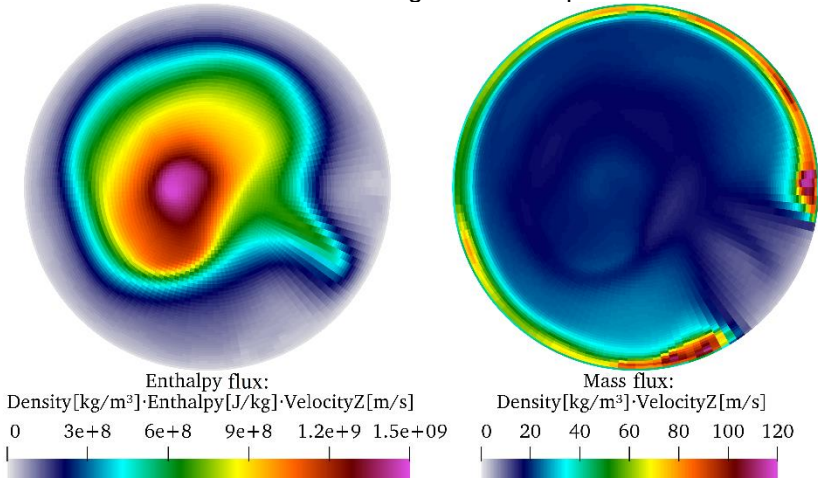


Figure 77 Instantaneous distributions of the enthalpy flux [J/m<sup>2</sup>/s] and mass flux [kg/m<sup>2</sup>/s] at the nozzle exit

The combination of the predicted plasma velocity and temperature make it possible to calculate the energy and mass flow through the nozzle exit. The instantaneous distributions of the enthalpy flow and mass flow in the exit plane of the nozzle are given in Figure 77.

The trace of the constricted anode arc attachment on both distribution is noticeable; it has a significant impact on the asymmetry of the enthalpy and mass flow. The distributions of enthalpy and mass flow smoothly change from one time step to another due to the arc motion back and forth on the anode surface. However, for any time step they keep axial asymmetry, the plasma jet keeps its central core with high enthalpy flow and the mass flow keeps its dense cold boundary flow, which is also affected by the anode arc attachment.

The motion of the anode arc attachment, mostly back and forth on the anode surface, brings about fluctuations of the arc length and voltage. The time-evolution of the arc voltage is illustrated in Figure 78. The presented voltage includes the anode and cathode sheath voltage drops. The voltage fluctuations are smooth with a relatively low amplitude. The voltage fluctuation shape factor  $S_{VT}$  defined by the formula (1.8) is around 1 and the voltage fluctuation amplitude factor  $A_V$  defined by the formula (1.9) is around 6%, which means that the LTE model predicts a mixing mode between the steady and take-over modes. Such characteristics of the arc fluctuations additionally confirms that the back and forth motion of the anode arc attachment is prevailing in the LTE model (Duan and Heberlein, 2002) as it was already numerically observed by (Dalir et al., 2019).

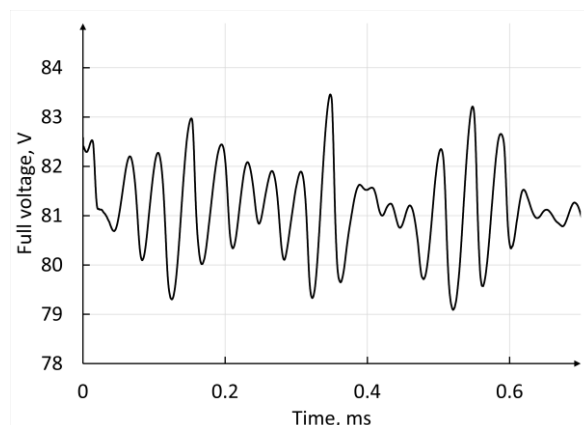


Figure 78 Full arc voltage time sweep in the LTE model with anode and cathode sheath voltage drops. The experimental voltage is  $76.5 \pm 4$  V.

To capture the possible effect of the arc voltage fluctuations on the plasma jet behavior, the simulations have to be unsteady. In addition, unsteady simulations allow to investigate the possible ways to rotate the anode arc attachment in order to limit the anode erosion.

In this study, two approaches are studied for an arc current of 500 A and gas flow rate of 60 NLPM of argon.

- Swirling injection of the plasma-forming gas. It is supposed to stabilize the arc column, drive the cold gas toward the nozzle wall and force a circumferential motion of the arc attachment.
- Externally-applied magnetic field.

If the first approach is commonly used in most of the commercial plasma spray torches, the second, to the best of the author's knowledge, has not been used in commercial plasma spray torches yet.

### III.3. Swirling gas injection in LTE model

#### III.3.1. Modelling of the gas injection

The swirling gas injection angle is modeled through a momentum source in the azimuthal component of the fluid velocity in the cylindrical cavity near the inlet boundary. The azimuthal component of the fluid velocity  $\vec{u}_{azim}$  in Cartesian coordinates is calculated according to the formula (3.3). The momentum source is computed on the basis that the computed azimuthal velocity  $\vec{u}_{azim}$  has to be equal to the imposed azimuthal velocity  $\vec{u}_{azim}^{target}$ ;  $|\vec{u}_{azim}^{target}| = u_z \cdot \tan(\alpha_{inj})$ .

The resulting momentum source is then expressed by the following formula (3.4).

$$\begin{aligned} \vec{u}_{azim} = \vec{u} - \vec{u}_z - \vec{u}_{rad} = \{u_x; u_y; u_z\} - \{0; 0; u_z\} - \frac{(x \cdot u_x + y \cdot u_y)}{x^2 + y^2} \cdot \{x; y; 0\} = \\ = \left\{ y \cdot \frac{y \cdot u_x - x \cdot u_y}{x^2 + y^2}; x \cdot \frac{x \cdot u_y - y \cdot u_x}{x^2 + y^2}; 0 \right\} \end{aligned} \quad (3.3)$$

$$\bar{\Gamma}_{expl} + \bar{\Gamma}_{impl} \vec{u} = K_{numerical} \left( \vec{u}_{azim} - \vec{u}_{azim}^{target} \right) \quad (3.4)$$

Where  $\vec{u} = \{u_x; u_y; u_z\}$  is the fluid velocity;  $\vec{u}_{azim}^{target}$  the target azimuthal velocity which is defined by the axial velocity and gas injection angle;  $x; y; z$  the Cartesian coordinates;

$\bar{\Gamma}_{expl}; \bar{\Gamma}_{impl}$  the user imposed explicit and implicit source terms. The coefficient  $K_{numerical}$  is selected in such a way that the target azimuthal velocity is achieved smoothly and without further fluctuations.

The standard gas injection angle in SinplexPro™ is 25°, but in order to study the effect of this angle on the constricted anode arc attachment, injection angles of 0°, 10°, 25° and 45° are considered in this work.

#### III.3.2. Results

The simulated plasma velocity streamlines for gas injection angles of 10, 25 and 45° are presented in Figure 79, Figure 80 and Figure 81, respectively. For injection angles of 10° and 25°, the swirling of the flow in the anode part of the torch is barely visible and can be easily suppressed by the strong plasma jet originating at the cathode tip. The effect of the swirling gas injection on the flow in the anode part becomes visible for an injection angle of 45° (Figure 81).

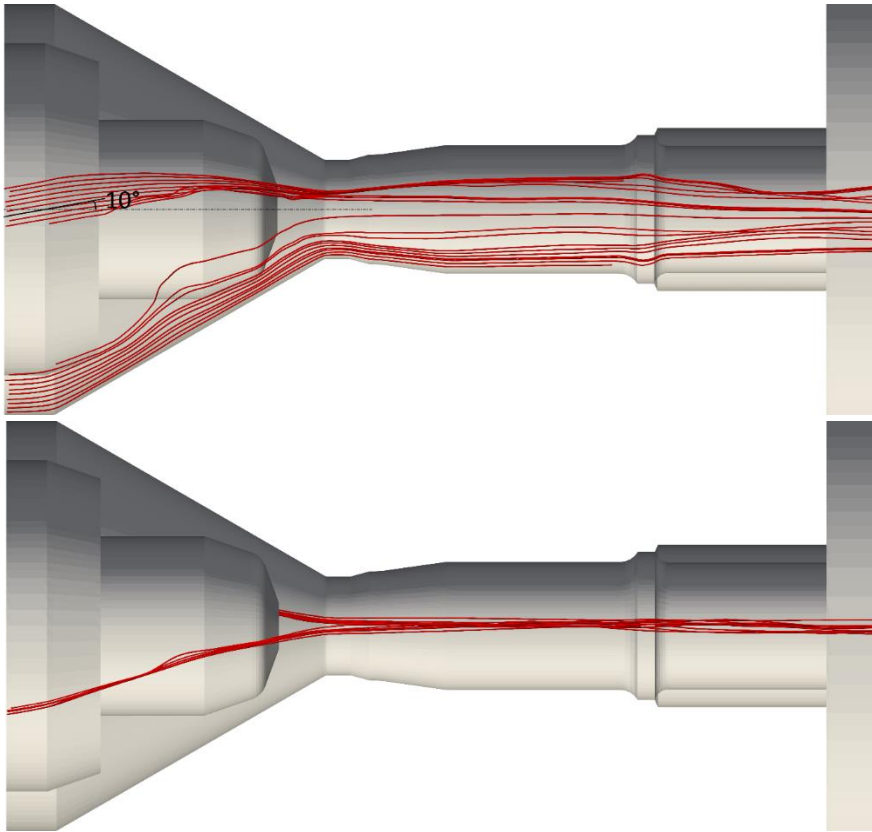


Figure 79 Velocity streamlines with a gas injection angle of 10°

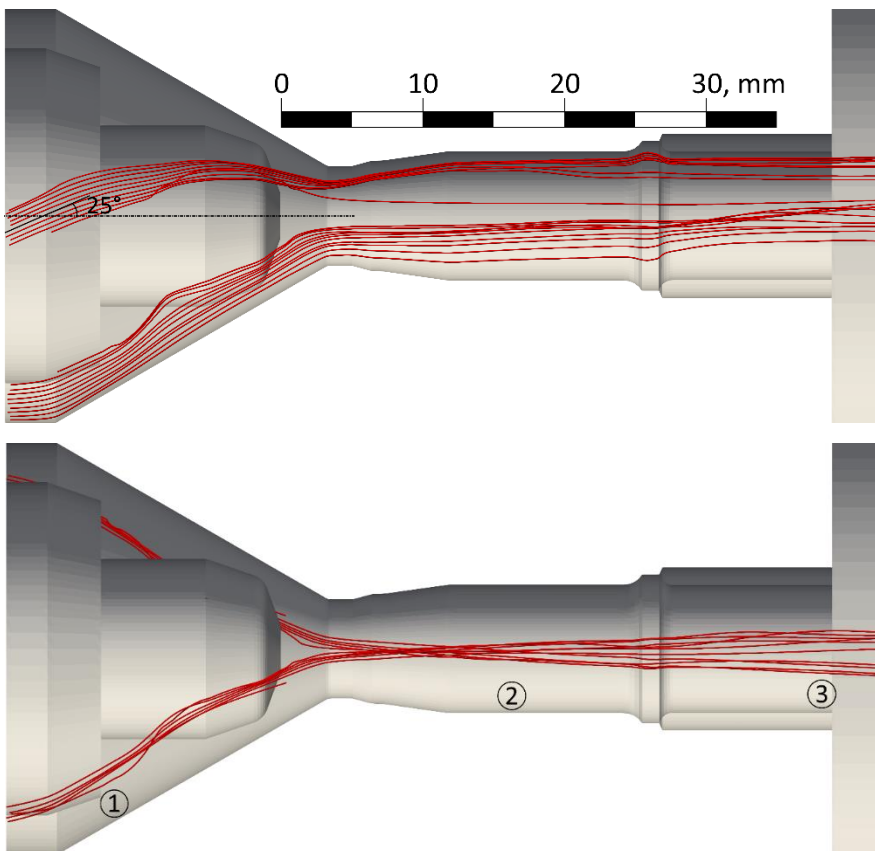


Figure 80 Velocity streamlines with a gas injection angle of 25°

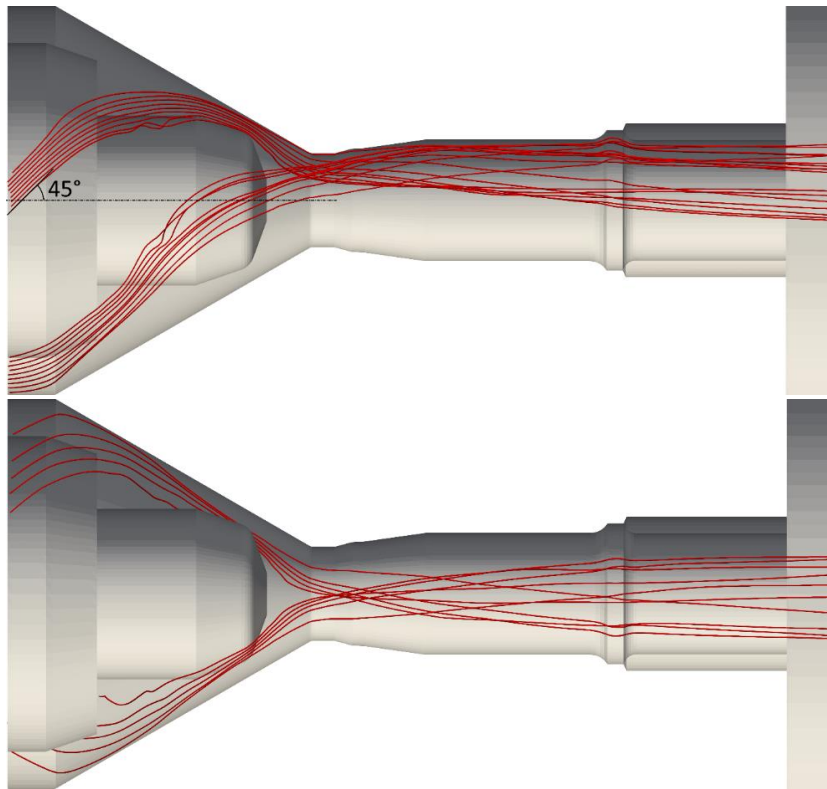


Figure 81 Velocity streamlines with a gas injection angle of 45°

The time-azimuthal distribution of the electric current density without swirling gas injection is presented in Figure 82. The values presented in the figure correspond to the total current in Amperes through one of the 128 azimuthal sectors on the anode surface. In the figure a slight random drift of the arc can be seen. It is conditioned by the numerical fluctuations in the flow streamlines and perfectly smooth surface of the anode. As soon as the arc stays at the same angular position for around 10 ms, the anode temperature at the arc attachment spot reaches the melting temperature of the tungsten liner (3695 K).

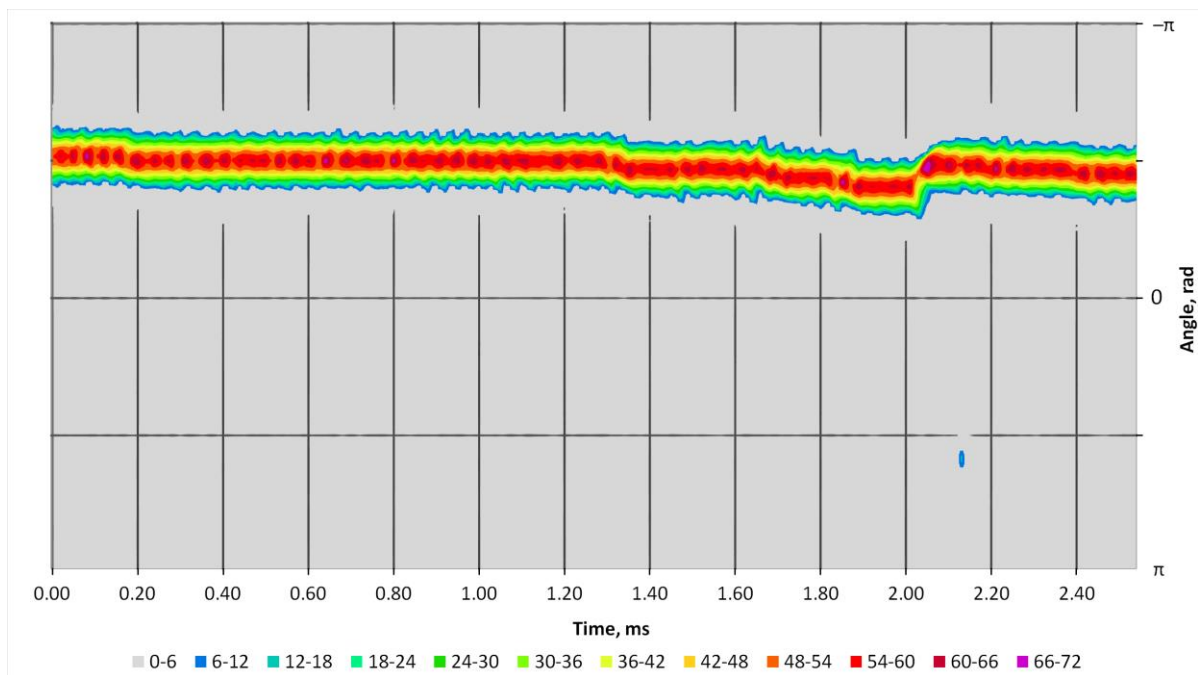


Figure 82 Time-azimuthal distribution of the electric current density on the anode surface plotted over time. Without swirling gas injection and without external magnetic field.

When a swirling injection of  $10^\circ$  is used, the behavior of the anode arc attachment is similar to the result without swirling injection. A slow arc movement at about 0.7 m/s may appear, but not a continuous arc rotation as seen in Figure 83. The anode temperature at the arc attachment spot can reach a temperature close to the tungsten melting temperature as without swirling gas injection.

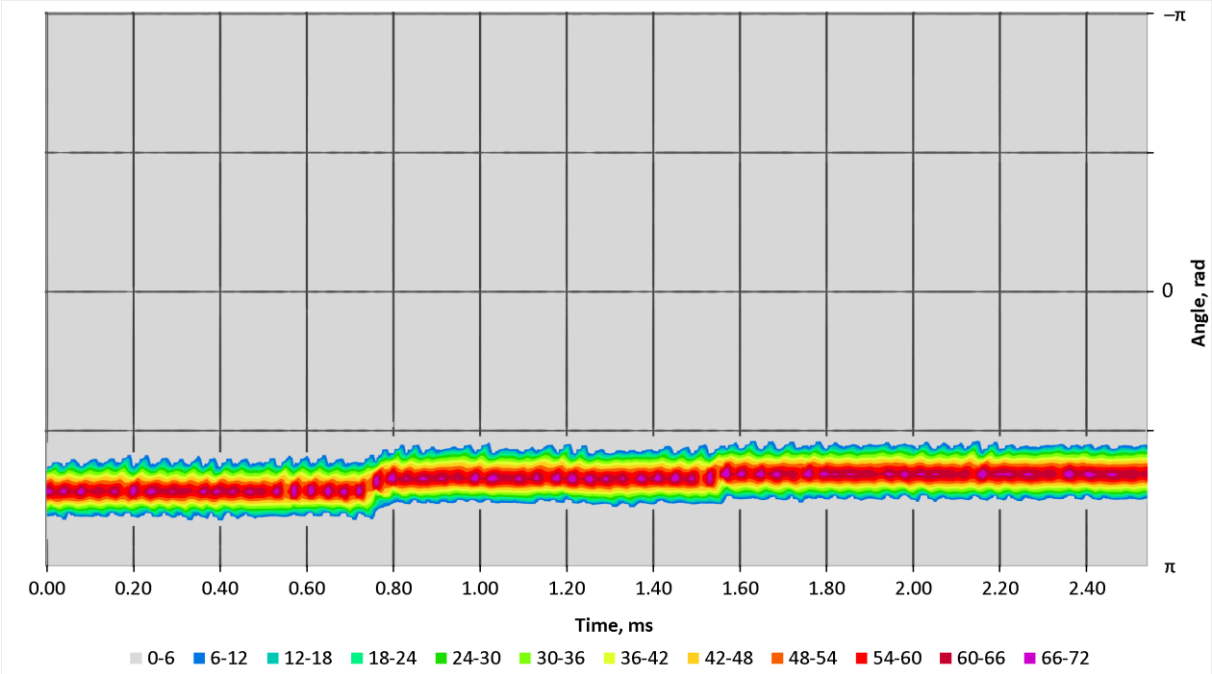


Figure 83 Time-azimuthal distribution of the electric current density on the anode surface. The swirling gas injection angle is  $10^\circ$ .

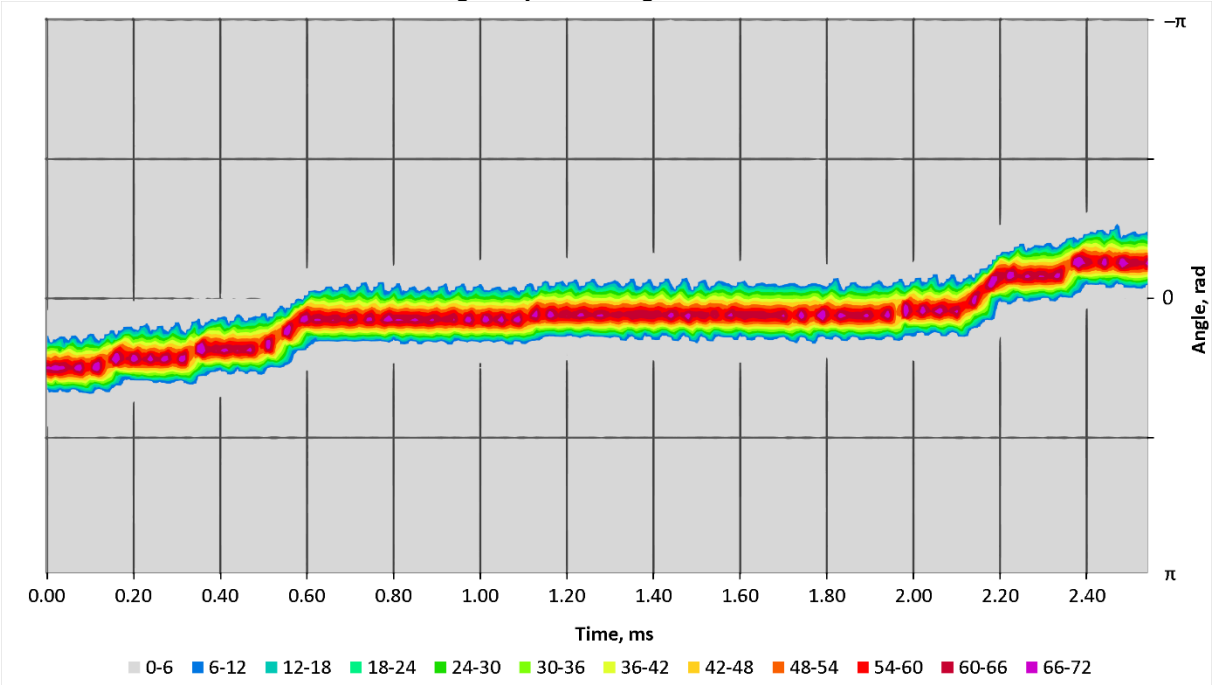


Figure 84 Time-azimuthal distribution of the electric current density on the anode surface. The swirling gas injection angle is  $25^\circ$ .

The torch simulation with the standard swirling injection angle of  $25^\circ$  shows an intermittent slow arc rotation with a circumferential velocity varying from 2 to 4 m/s. The time-sweep of the azimuthal distribution of the current on the anode surface is presented in Figure 84. An illustration of the arc rotation at different times is shown in Figure 86. In this case the maximum



predicted anode temperature is around 2000 K. However, the results for the standard gas injection angle seem very sensible to minor fluctuations and numerical disturbances. Therefore, in the experiments the constricted anode arc attachment may not feel the weak swirling of the flow at the nozzle while attracted to a small unevenness of the surface. On the photos of worn anodes shown in Figure 85, it can be seen that the arc traces and molten tungsten splashes are mostly parallel to the torch axis and the arc motion on the anode is far from being helical.



Figure 85 Photos of worn anodes with the arc traces parallel to the torch axis. The anode were used for extended period of time with various parameters (courtesy of Oerlikon Metco (US) Inc.)

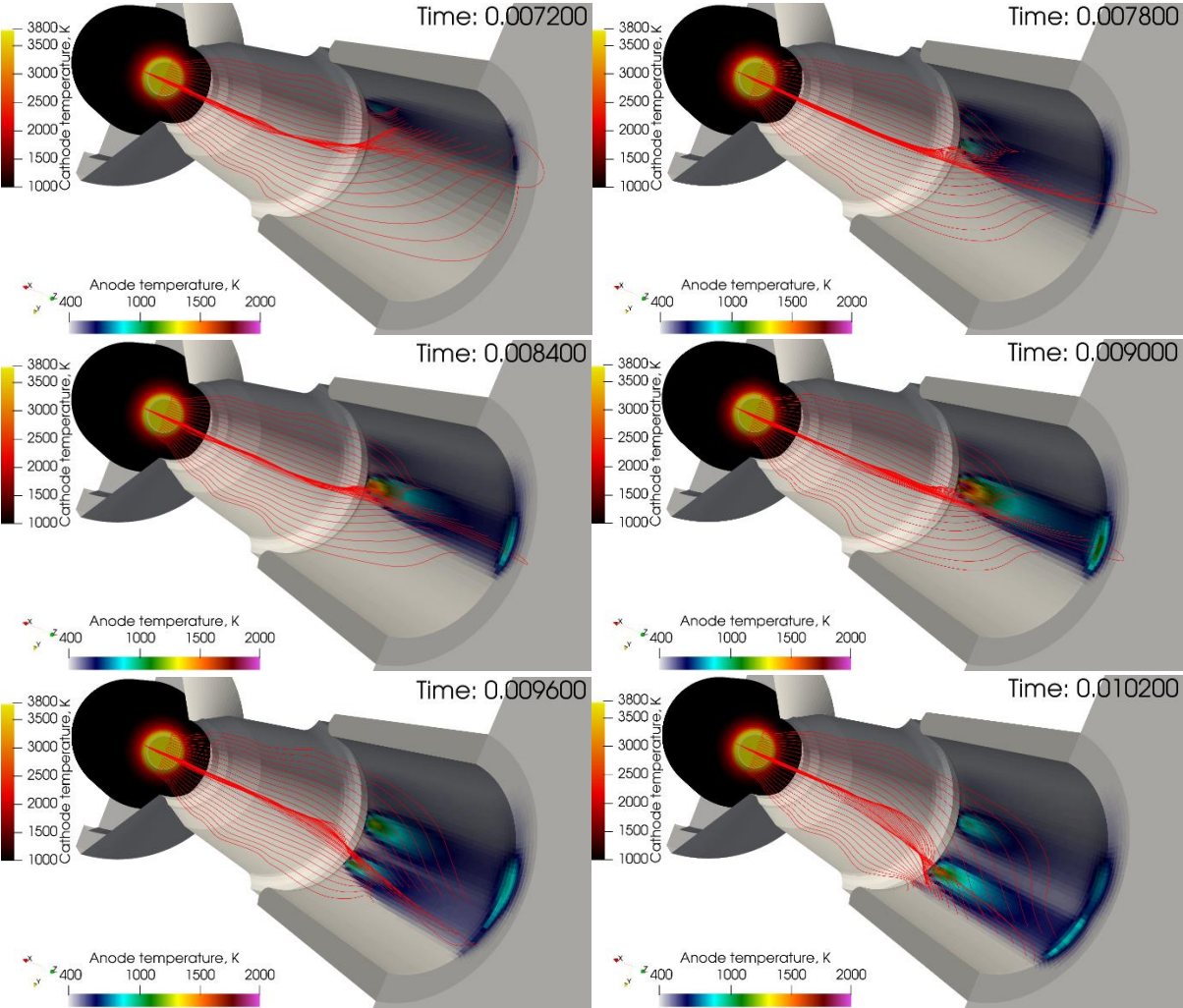


Figure 86 Electric current lines and temperature distribution on surface of anode and cathode at several times with a 25° swirling gas injection.

A gas injection of 45° significantly increases the circumferential velocity of the anode arc attachment as it is illustrated in Figure 87 that shows the azimuthal distribution of current over time. The anode arc attachment velocity reaches 14 m/s and the maximum anode temperature during the simulation is around 600 K which is much lower than the temperature predicted with both the 10° and 25° injection angles. With the 45° injection angle, the predicted arc voltage and its fluctuations are slightly higher: 67.3±2 V against 66.9±1.5 V for the 25° injection angle.

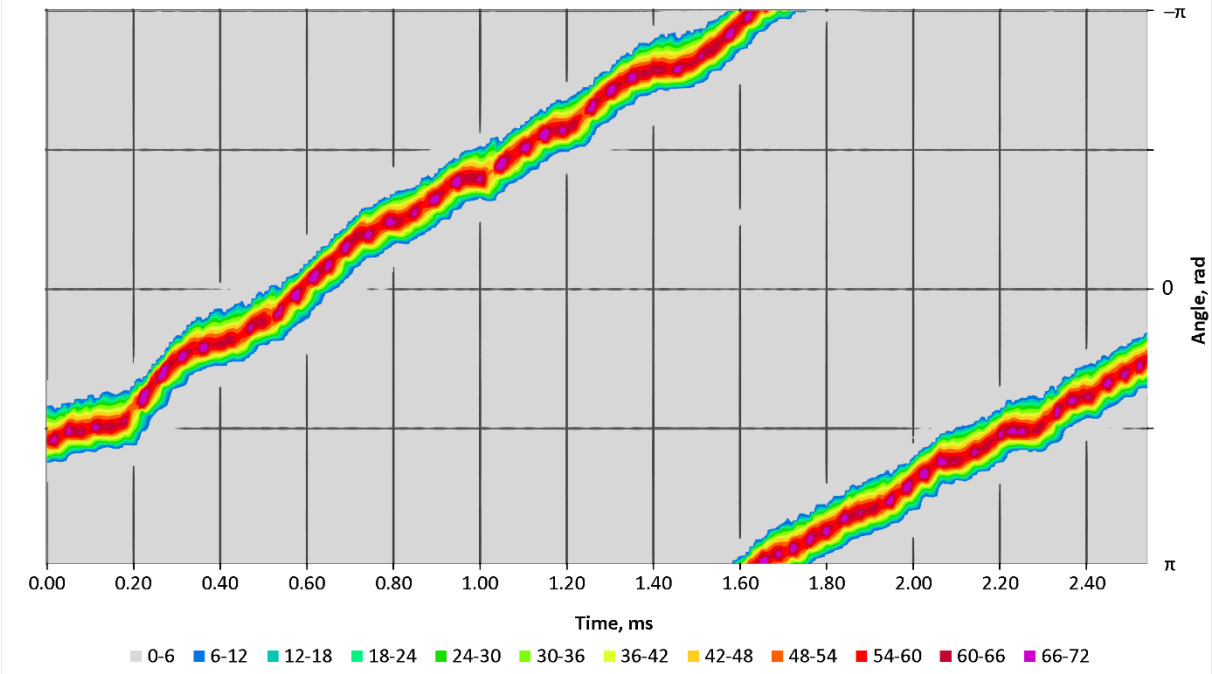


Figure 87 Time-azimuthal distribution of the electric current density on the anode surface. The swirling gas injection angle is 45°.

The swirl number (given by formula (1.19)) for various gas injection angles are given in Table 2. The cross-sections for which the swirl numbers are computed are shown in Figure 80. In general, the swirl number tends to decrease by several times on the way from the gas inlet to the nozzle exit for all the injection angles as the flow swirling is substantially suppressed by the intense axial acceleration of the flow: the azimuthal momentum at the nozzle exit is barely noticeable compared to the axial momentum. The azimuthal momentum exerts some rotating effect on the anode arc attachment but still the characteristic time of such rotation is much longer than the characteristic time of the arc fluctuations and time of plasma residence in the torch.

Table 2: Swirl numbers in different parts of the torch for various gas injection angles

Injection angle	Inlet (1)	Middle of the channel (2)	Nozzle exit (3)
0°	0	0	0
10°	0.33	0.0102	0.0060
25°	0.84	0.023	0.0122
45°	1.92	0.051	0.023

As it can be seen from the predicted circumferential velocity of the anode arc attachment and maximum anode temperature in Figure 88 and Figure 89, the gas injection angle has a very significant effect on the anode arc attachment behavior in the simulation. The maximum anode

temperature corresponds to the maximum value in the whole set of the anode cells over the whole simulated time. From the drastic change in the circumferential velocity, it can be concluded that an increase in the gas injection angle used in the SinplexPro™ plasma torch up to 45° could help to increase the arc rotation velocity and, thus, extend the lifetime of the anodes.

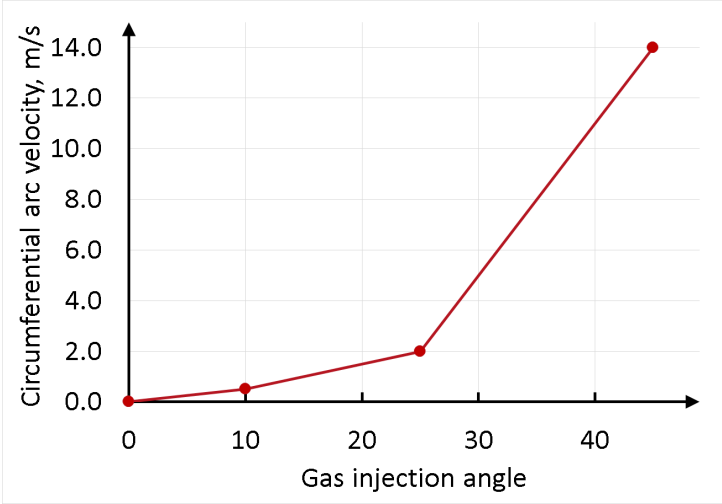


Figure 88 Circumferential velocity of the anode arc attachment as a function of the gas injection angle

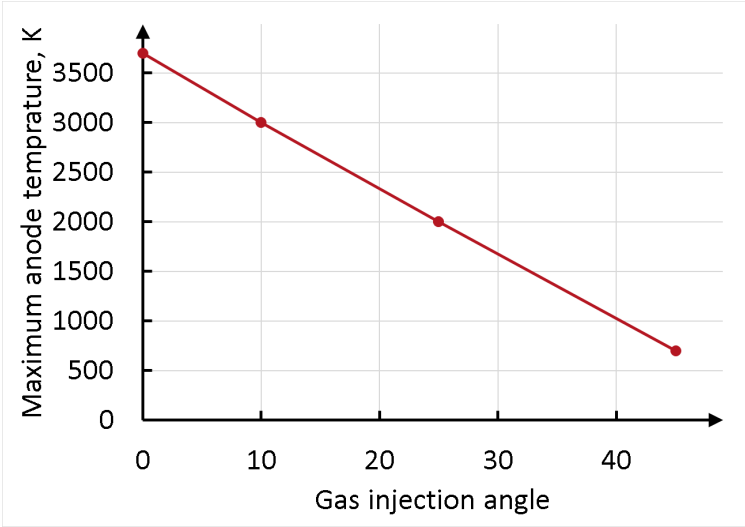


Figure 89 Maximum anode temperature as a function of the gas injection angle

**III.4. Use of external magnetic field in LTE model**

**III.4.1. Predicted flow field**

A magnetic field outside of the plasma torch can be created by a coil mounted around the torch. If this coil does not have an active cooling system, it has to be made of a rather thick copper wire. To create an external magnetic field of about 0.1 T, the coil must have 18 layer of wire, five turns each. The current in each turn has to be 85 A and 170 A for a magnetic field of 0.05 T and 0.1 T, respectively. The wire has to be around 6 mm in diameter plus 1 mm of electrical insulation. Thus the distance between the turn centers is around 8.5 mm. A coil with an active cooling would have less turns, but a design of the coil with such cooling is beyond the scope of the present study.

In the model, the external magnetic field distribution is computed through the Biot&Savart law taking into account the electric current in the coil. The streamlines of the simulated external magnetic field created by the above-described coil with a current of 85 A are shown in Figure 90.

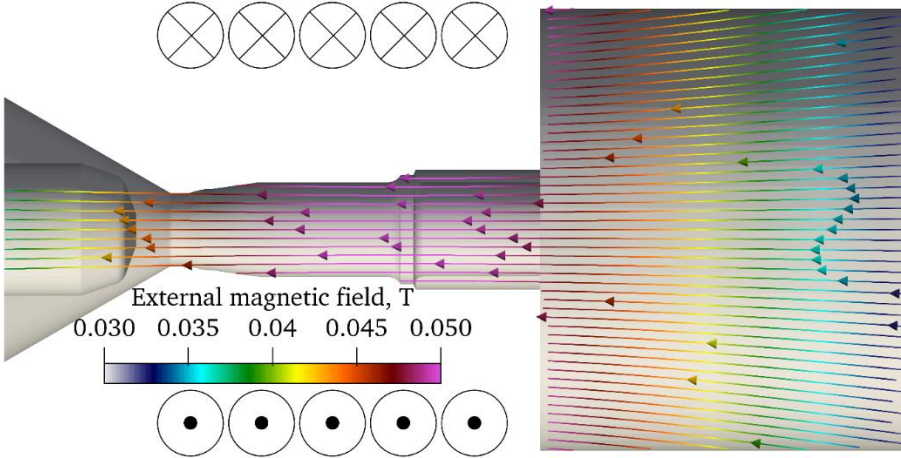


Figure 90 External magnetic field streamlines created by a coil around the torch

The simulation of the plasma filed with the external coil was done for an arc current of 500 A and 60 NLPM of argon with a straight gas injection. The gas injection without swirling was considered in order to only investigate the effect of the external magnetic field.

The time sweep of the azimuthal current distribution without an external magnetic field is illustrated in Figure 82. This time sweep can be used as a reference for 0 T in order to see how the maximum value of current pre azimuthal sector and angular width of the arc change with the application of an external magnetic field. The values presented in Figure 82 correspond to the total current per one azimuthal sector out of all the 128 sectors in the mesh. From the figure it can be seen that without an external magnetic field, the arc is stable and mostly stays at the same angular position, sometimes undergoing a minor drift.

With an external magnetic field, the anode arc attachment rotates but also deforms and splits in parts. An example of the distribution of the electric current lines is illustrated in Figure 91.

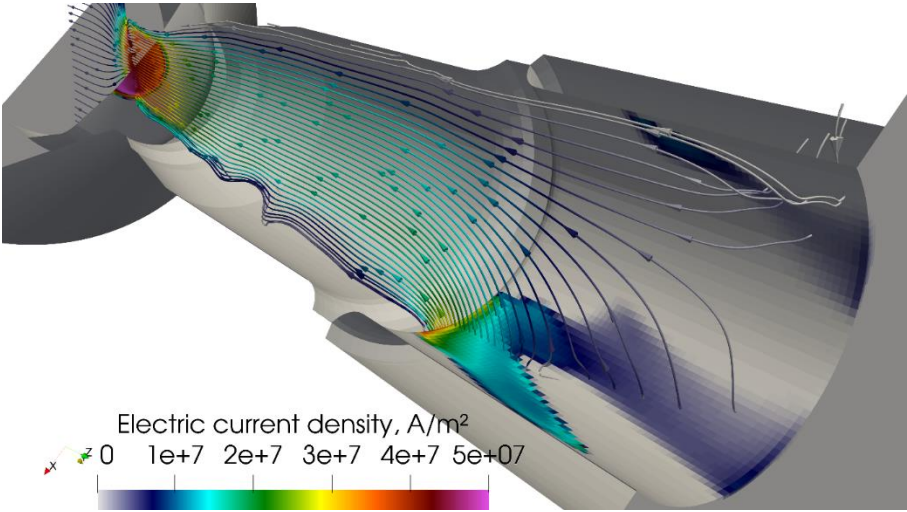


Figure 91 Electric current streamlines in the computational domain and boundary value of electric current density on the electrode surface for an external magnetic field of **0.05 T** and time step of **10<sup>-8</sup> s**

Since the external magnetic field is mostly axial inside the torch, the Lorentz force created by such field is exerted on the areas with nonzero radial component of electric current density, i.e. on the expanding part of the arc near the cathode and anode arc attachment. An example of such Lorentz force exerted on the plasma with a nonzero electric current density in the context of Figure 91 is illustrated in Figure 92.

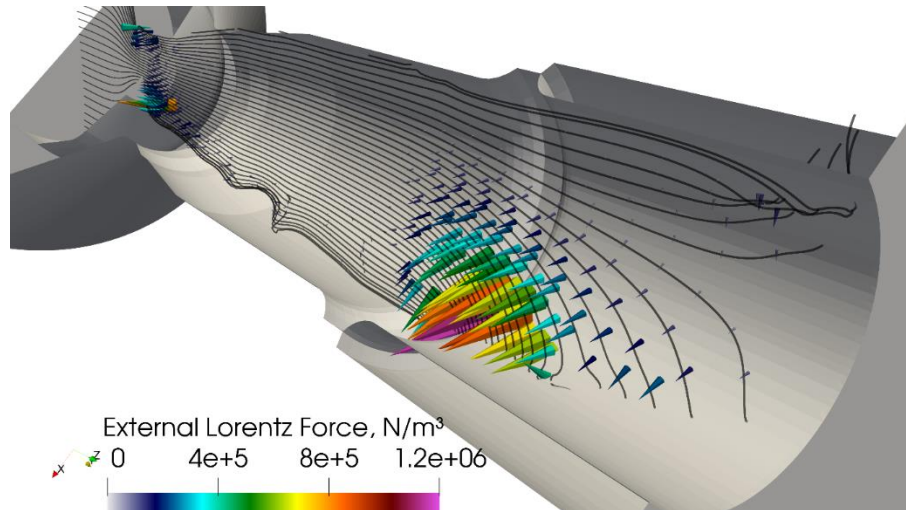


Figure 92 Lorentz force exerted on the plasma shown by the electric current streamlines for an external magnetic field of **0.05 T** and time step of  **$10^{-8}$  s**

### III.4.2. Results

The simulations with an external magnetic field have to major indicators:

1. The circumferential velocity of the anode arc attachment. The arc rotation helps to distribute the heat load of the arc on the anode wall, lower the maximum temperature of the anode surface and make the plasma flow more axisymmetric. However, if the arc circumferential velocity is too high, a second indicator should be also used.
2. The stability and straightness of the plasma flow, convergence of the model, and conservation of energy. A too abrupt behavior of the arc when the characteristic time of the arc dynamics is comparable to the simulation time step is a source of all kinds of numerical effects and disturbances.

An external magnetic field of 0.01 T creates a swirling effect similar to that generated by a  $10^\circ$  injection angle in terms of swirl number and drift of the anode arc attachment that shows nearly no rotation. The azimuthal distribution of the electric current is given in Figure 93.

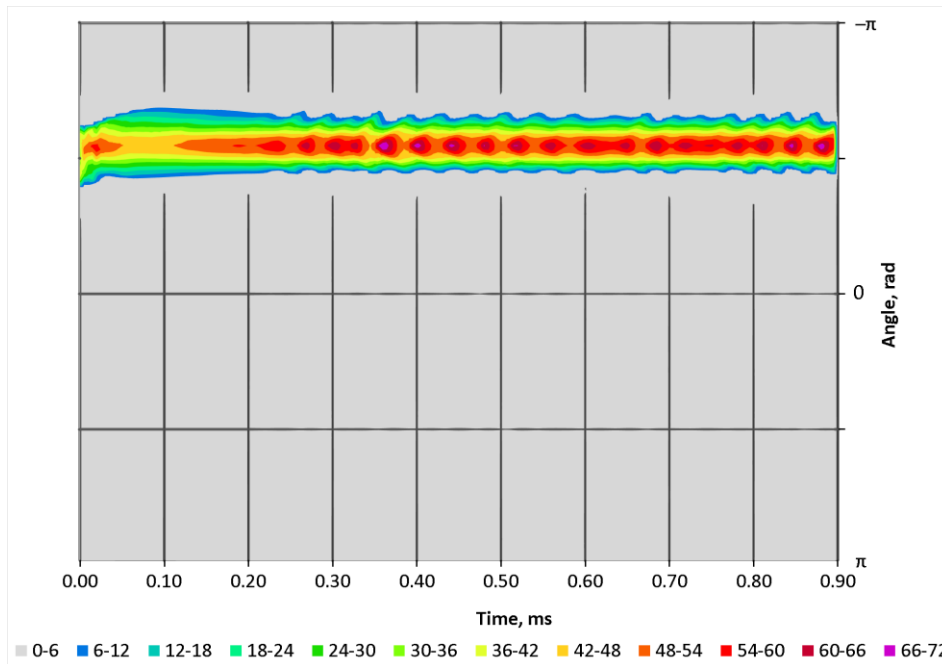


Figure 93 Time-azimuthal distribution of the electric current density on the anode surface for an external magnetic field of **0.01 T** and time step of  **$10^{-7}$  s**

In addition it is worth noting, that with the 0.01 T external magnetic field the flow swirling is mostly concentrated on the torch axis as illustrated in Figure 94 which also explains the stable azimuthal position of the arc. The swirling of the plasma flow along the torch axis originates from the cathode tip where the external Lorentz force caused by the arc expansion is unopposed by any other counterforce and freely rotates the plasma even though the Lorentz force is lower than at the anode arc attachment. At the anode arc attachment, the external Lorentz force with a magnetic field of 0.01 T seems to be suppressed by the forces inherent to the constricted anode arc attachment: the self-induced Lorentz force, viscous force and plasma pressure gradient.

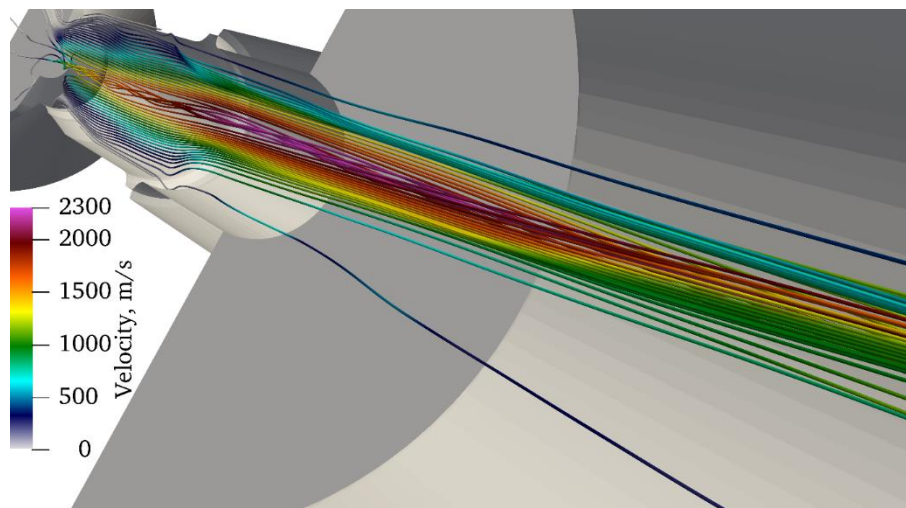


Figure 94 Velocity streamlines for an external magnetic field of **0.01 T** and time step of  **$10^{-7}$  s**

From 0.02 T, the external magnetic field affects the anode arc attachment: the motion of the arc is not continuous; it is, interrupted by some jumps of the arc, but it's the azimuthal position of the arc on the anode changes and so the anode surface is not heated to its melting temperature. The circumferential velocity of the anode arc attachment, when the maximum

current density on the anode surface is around  $10^8$  A/m<sup>2</sup>, can be estimated around 50 m/s. However, to get a continuous motion of the anode arc attachment, further increase in the external magnetic field is necessary.

An increase of the external magnetic field up to 0.03 T leads to a proportional increase of the swirl number in the middle of the channel and at the nozzle exit as is illustrated in Figure 135. The anode arc attachment has a similar expansion-contraction behavior as with a magnetic field of 0.01 T as illustrated in Figure 95. However the azimuthal position of the arc becomes intermittent, that is the arc starts jumping in such configuration of the simulation.

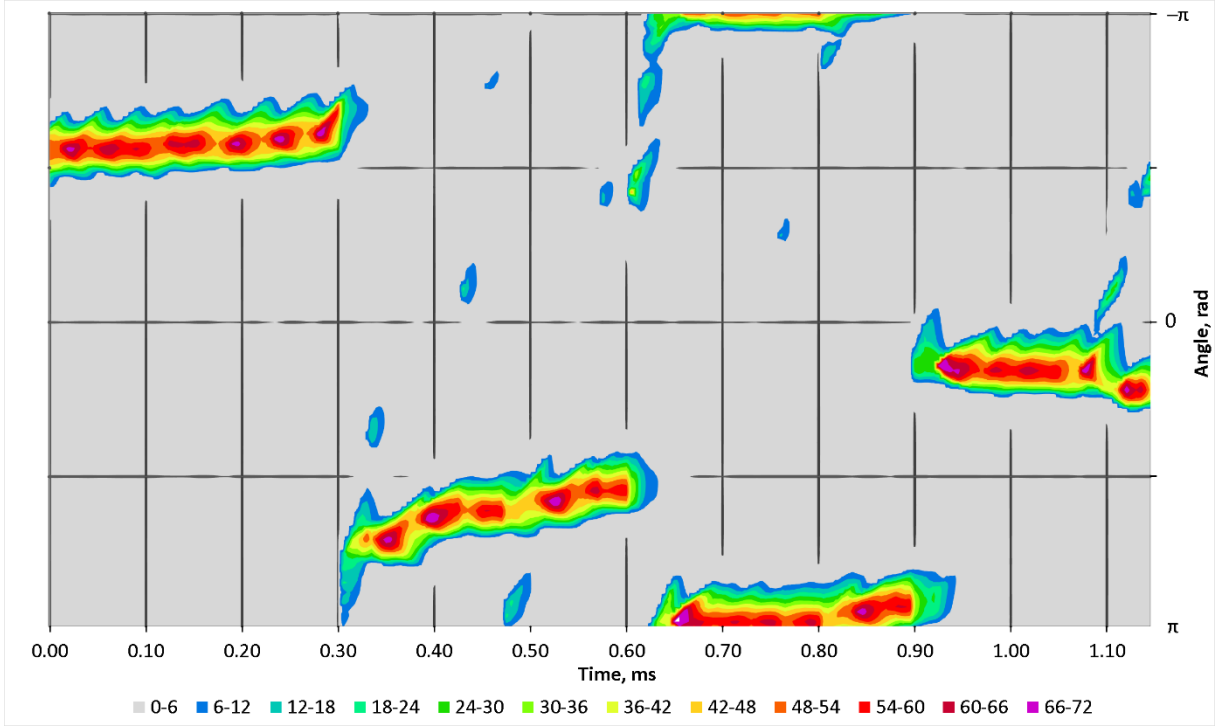


Figure 95 Time-azimuthal distribution of the electric current density on the anode surface for an external magnetic field of **0.03 T** and time step of  **$10^{-7}$  s**

The energy balance expressed in equation (3.5) is violated by around 5%: the total Joule power is significantly higher than the combined energy of the issuing plasma jet, energy transferred to the electrodes and radiation loss inside the torch. The violation of the thermal balance in the model happens due to the too abrupt arc behavior for which the model convergence cannot be reached and therefore some energy gets lost during the unstable simulation.

$$I \cdot (V_{arc} + U_C + U_A) = \dot{h} + E_{kin}^{nozzle} + Q_R^{torch} + Q_{anode} + Q_{cathode} \quad (3.5)$$

Where  $I$  is the arc current intensity,  $V_{arc}$  the computed LTE arc voltage,  $U_C$  and  $U_A$  the cathode and anode sheath voltage drops,  $\dot{h}$  the enthalpy flux through the nozzle exit,  $E_{kin}^{nozzle}$  the kinetic energy of the plasma flow through the nozzle exit,  $Q_R^{torch}$  the radiation losses inside the torch, and  $Q_{anode}$  and  $Q_{cathode}$  the heat flow to the anode and cathode respectively.

The use of a smaller time step makes it possible to understand in the sensitivity of the results to this parameter. The simulation of the arc behavior with an external magnetic field of 0.03 T and a time step of  $10^{-8}$  s produced a more consistent result with a well-pronounced rotation of

the anode arc attachment and better energy balance (3.5) which is violated by only 1%. The circumferential velocity of the anode arc attachment is around 160 m/s, as it can be seen on the azimuthal distribution in Figure 96.

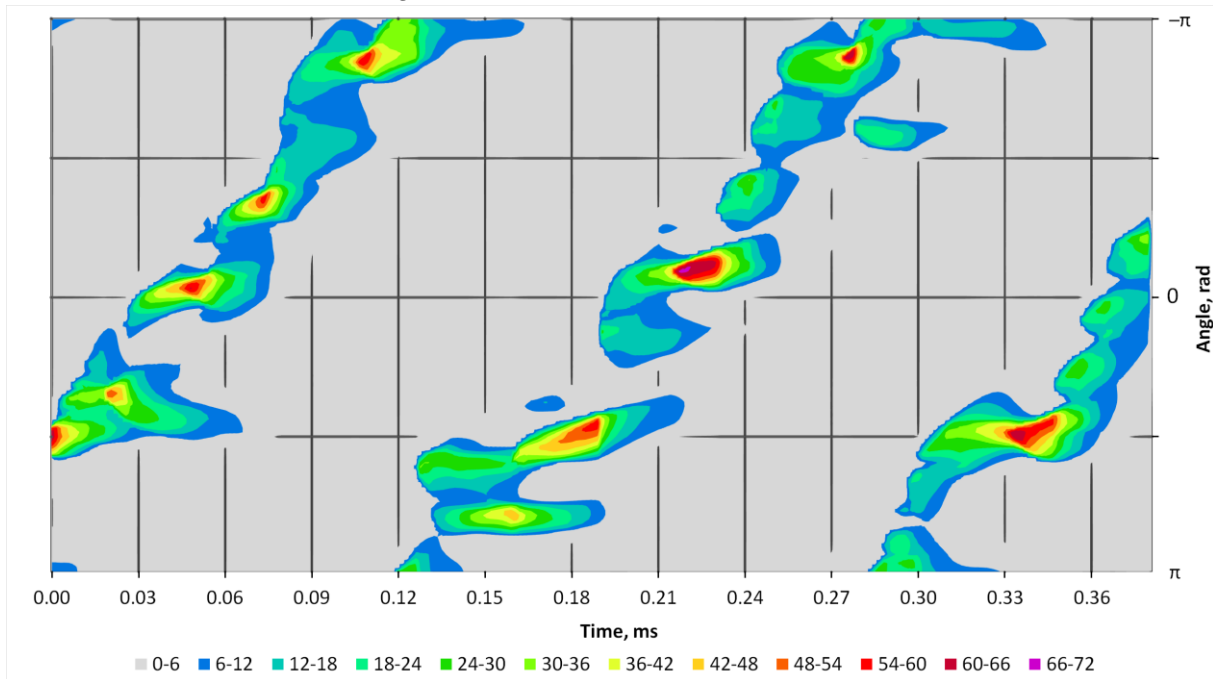


Figure 96 Time-azimuthal distribution of the electric current density on the anode surface for an external magnetic field of **0.03 T** and time step of  **$10^{-8}$  s**

The swirl number is similar to that calculated for an injection angle of  $45^\circ$ . However, the circumferential velocity of the anode arc attachment is much higher with the external magnetic field due to the composition of the plasma flow swirling due to the Lorentz force near the cathode tip and Lorentz force effect on the anode arc attachment rotation. The maximum anode temperature over the whole simulation with the magnetic field of 0.03 T and time step of  $10^{-8}$  s barely reaches 500 K which means an effective protection of the anode from melting.

With an external magnetic field around 0.05 T and time step of  $10^{-7}$  s the arc becomes too dynamic and it is hard to retrieve any circumferential anode arc attachment velocity from the time sweep of the azimuthal distribution of the electric current density in Figure 97. If the arc motion was continuous, the circumferential arc velocity in would be around 30 m/s. However, the continuous motion combined with arc jumps results in a fluctuating circumferential arc velocity around 140 m/s. The velocity streamlines presented in Figure 98 show lower velocity of the plasma jet issuing from the torch compared to that predicted without magnetic field (Figure 76). The whole plasma jet is much less straight and stable in the case with external magnetic field 0.05 T and time step  $10^{-7}$  s. The energy balance (3.5) is violated even more: by around 19%.

Therefore, in this case, the model is not capable to capture the arc dynamics and cannot properly describe the plasma jet issuing from the torch for an external magnetic field of 0.05 T and time step of  $10^{-7}$  s.



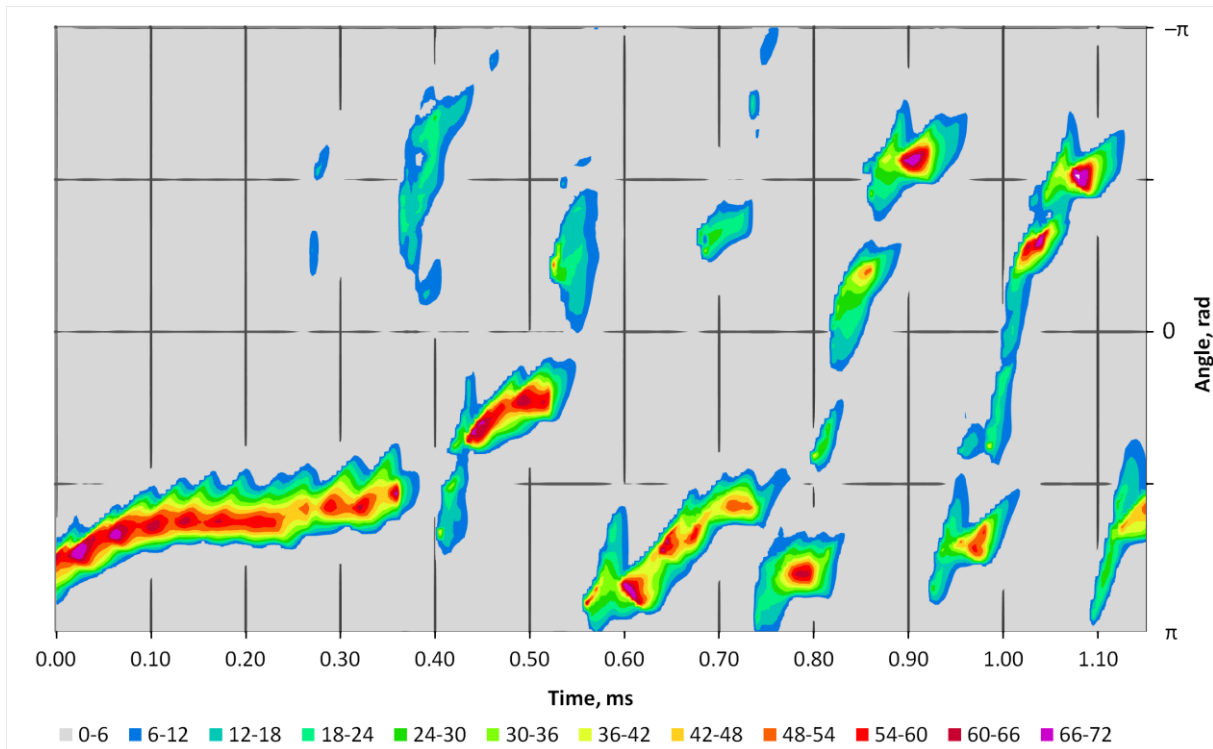


Figure 97 Time-azimuthal distribution of the electric current density on the anode surface for an external magnetic field of **0.05 T** and time step of  **$10^{-7}$  s**

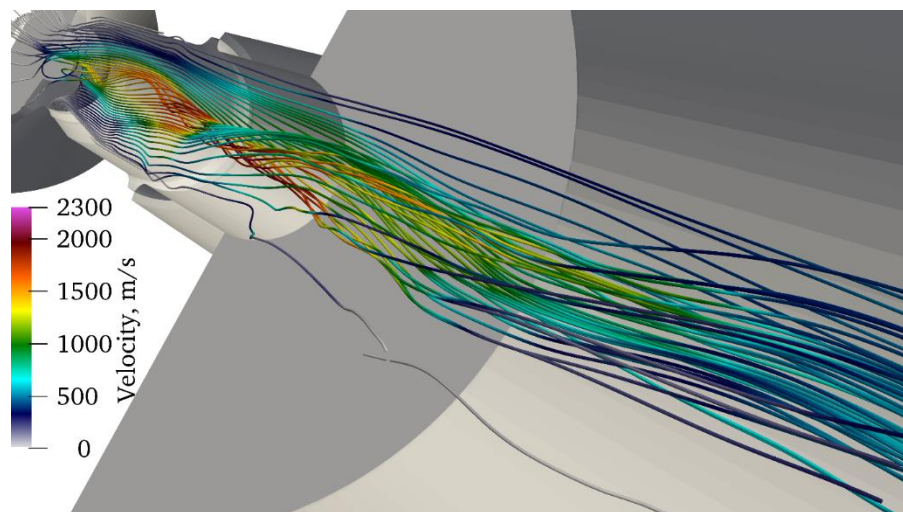


Figure 98 Velocity streamlines for an external magnetic field of **0.05 T** and time step of  **$10^{-7}$  s**

Therefore, it is to decrease the time step down to  $10^{-8}$  s in order to capture the arc behavior. With lower time steps, the arc dynamics is much smoother and easier to analyze. The resulting circumferential velocity of the anode arc attachment retrieved from Figure 99 is around 180 m/s. The plasma jet is much more stable; it retains its momentum downstream from the nozzle exit as it can be seen in Figure 100. The energy balance (3.5) in the torch is violated by less than 1%. Therefore a time step of  $10^{-8}$  s is much more suitable for the plasma torch simulation with an external magnetic field of 0.05 T.

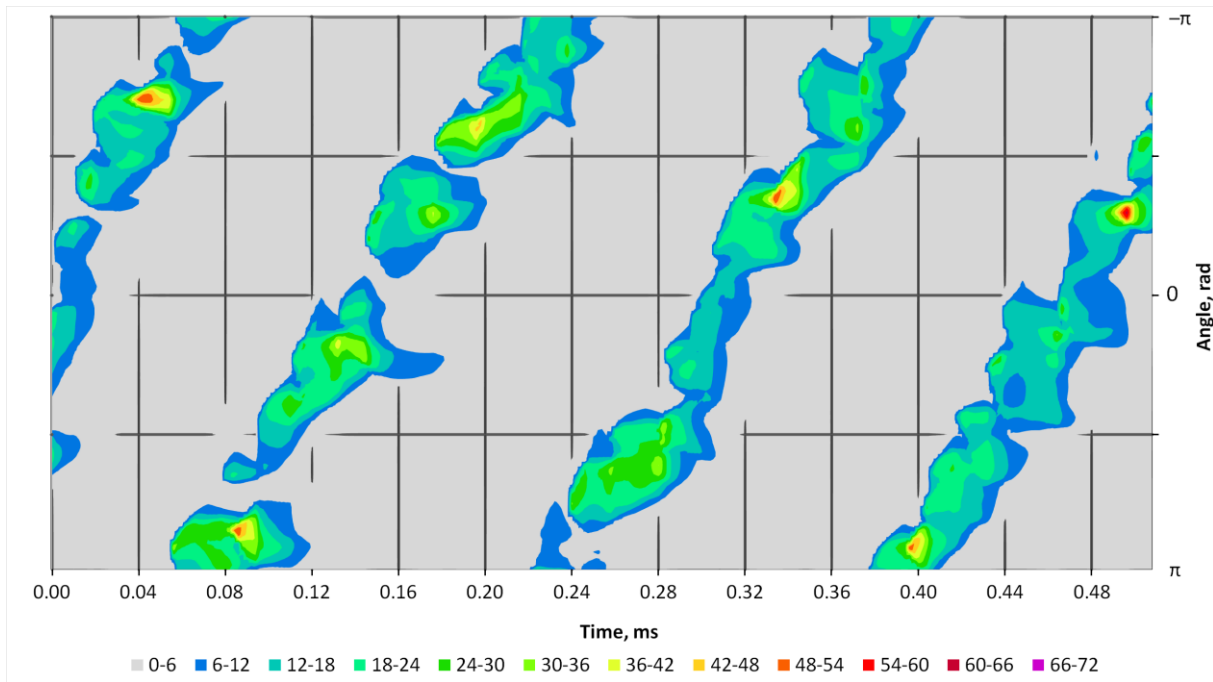


Figure 99 Time-azimuthal distribution of the electric current density on the anode surface for an external magnetic field of **0.05 T** and time step of  **$10^{-8}$  s**

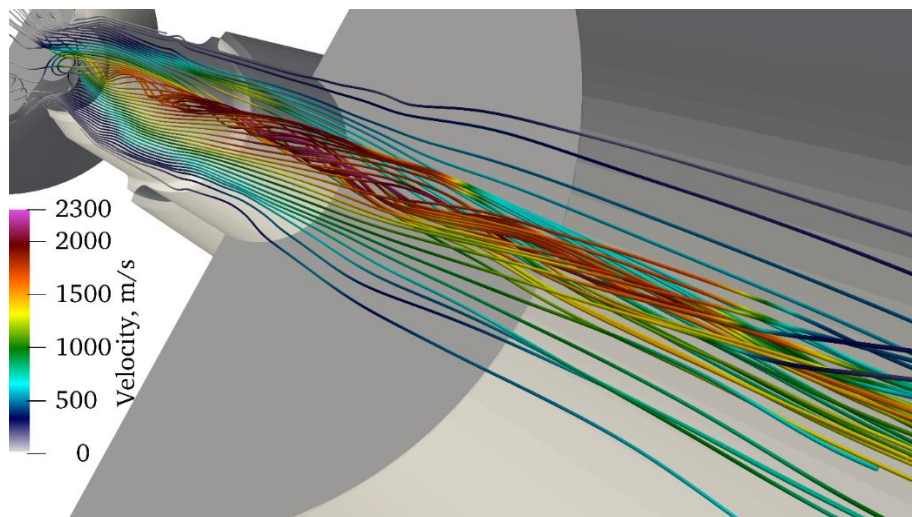


Figure 100 Velocity streamlines for an external magnetic field of **0.05 T** and time step of  **$10^{-8}$  s**

A further increase of the external magnetic field up to 0.1 T leads to a quite chaotic anode arc attachment behavior. The time sweep of the azimuthal distribution of the electric current density on the anode surface is shown in Figure 101. It is hard to retrieve any circumferential velocity of the anode arc attachment from such result. As it is illustrated in Figure 102 even with a time step of  $10^{-8}$  s the plasma jet loses its momentum and the velocity drops by around 50% outside of the torch due to the unstable electric arc behavior. The energy balance is violated by about 15%. Thus the present model cannot predict the plasma jet with an external magnetic field higher than 0.1 T with the predicted type and shape of the anode arc attachment.

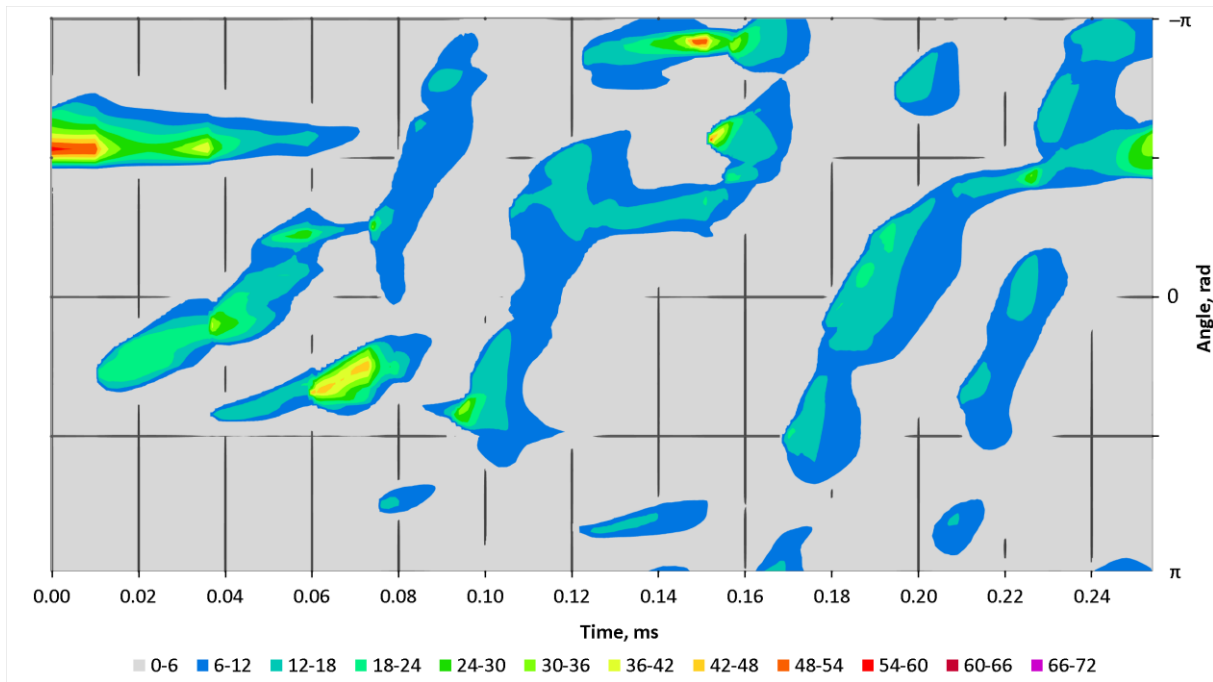


Figure 101 Time-azimuthal distribution of the electric current density on the anode surface for an external magnetic field of **0.1 T** and time step of  **$10^{-8}$  s**

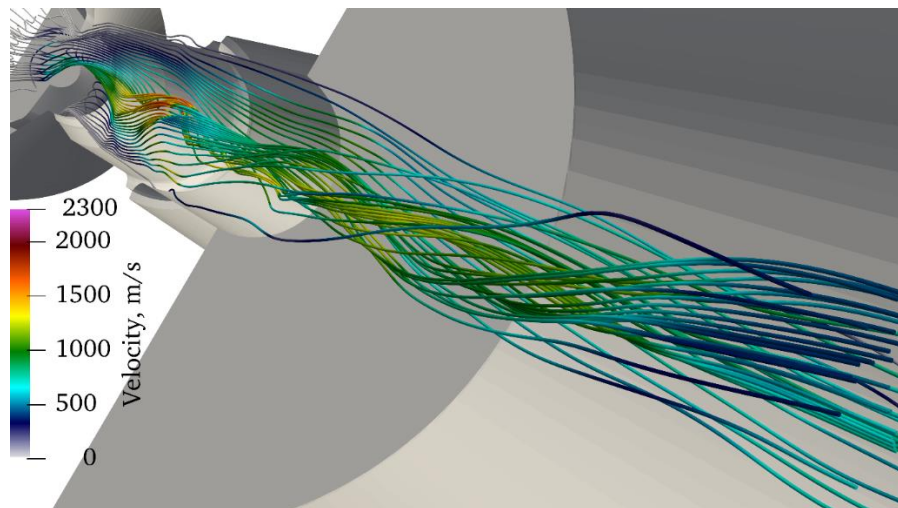


Figure 102 Velocity streamlines for an external magnetic field of **0.1 T** and time step of  **$10^{-8}$  s**

The swirl number for various values of the external magnetic field are given in Table 3. It is significant already in the middle of the torch channel compared to the numbers calculated for the swirling gas injection. It means that the whole plasma flow starts rotating before it reaches the anode. An initial intense rotation appears at the cathode tip where the arc expands and electric current density has a nonzero radial component. The radial component of  $\vec{j}$  combined with the external magnetic field generates a nonzero rotational Lorentz force which makes the plasma inside the torch to swirl. The swirling effect of the external magnetic field on the plasma jet can be seen in Figure 100. At the nozzle exit, an additional contribution to the swirl number arises from the anode arc attachment rotation due to the Lorentz force concentrated at the area with the highest electric current density on the anode surface. From the swirl numbers it can be seen that the swirling contribution of the Lorentz force exerted on the expanding cathode arc attachment is close to the contribution of the Lorentz force exerted on the anode arc

attachment. Thus the anode arc attachment rotates not only because of the Lorentz force applied to it, but also because of the swirling of the whole plasma flow.

In addition, the swirl number dependency on the external magnetic field nearly linear as shown in Figure 103. However, the circumferential velocity of the anode arc attachment has a more complex dependency on the external magnetic field. The circumferential velocity with the fully developed swirling plasma flow is significantly higher than in the beginning of the simulation, when the swirling from the cathode has not reached the anode yet.

Table 3: Swirl numbers in different parts of the torch for various values of the external magnetic field

External magnetic field, T	Inlet (1)	Middle of the channel (2)	Nozzle exit (3)
0.01	0.0	0.0072	0.0109
0.02	0.0	0.0127	0.0217
0.03	0.0	0.021	0.035
0.05	0.0	0.030	0.055
0.1	0.0	0.078	0.11

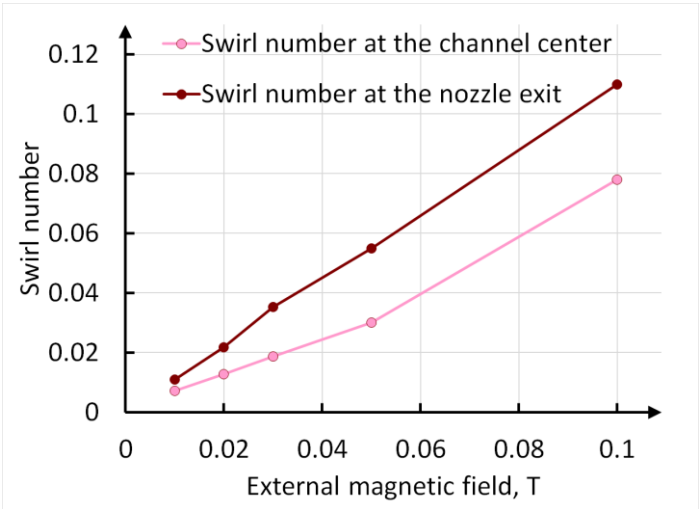


Figure 103 Swirl numbers at the channel center and nozzle exit for various values of the external magnetic field

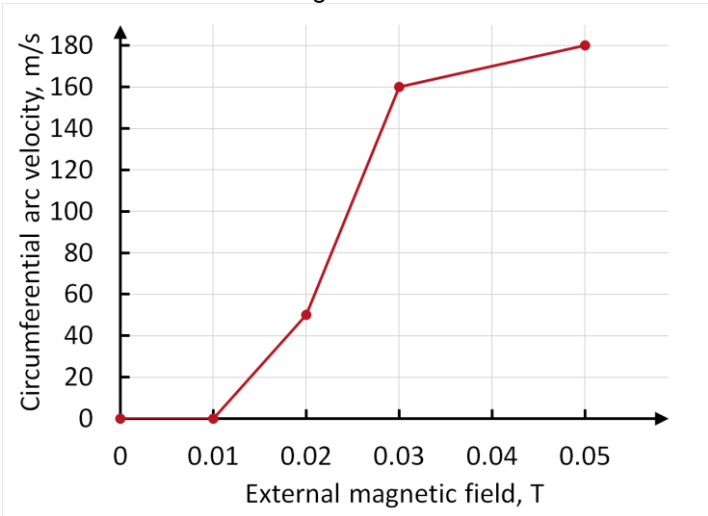


Figure 104 Circumferential velocity of the anode arc attachment as a function of the external magnetic field

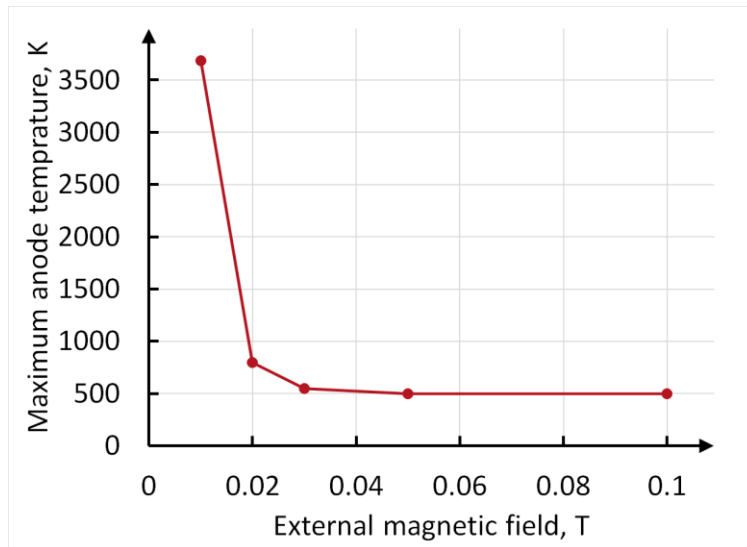


Figure 105 Maximum anode temperature as a function of the external magnetic field

### III.5. 2T simulation results

#### III.5.1. Distribution of electric current density predicted by 2T model

The unsteady 2T simulation was carried out for a current of 500 A and 60 NLPM of argon in order to compare the predictions with those obtained with the LTE model. The time steps used in the 2T(I) and 2T(II) models are  $10^{-8}$  s and  $10^{-7}$  s respectively. The 2T(I) model requires a shorter time step due to the higher fluctuations in heat balance and flow velocity. A significant ripple in all the parameters appears due to the spatiotemporal fluctuations in the energy exchange between electrons and heavy species in the vicinity of the cathode tip with a time step of  $10^{-7}$  s. All the terms of the thermal equations, e.g. Joule power, thermal diffusion of the heavy species cooled by the cathode surface, energy exchange term between electrons and heavy species, have significant values and it is hard to get a perfect thermal convergence in this area. Thus, the solution was to decrease the time step down to  $10^{-8}$  s for the 2T(I) model.

The main difference compared to the LTE model is a different type of the anode arc attachment, which is diffuse and axially symmetric and exhibit a lower value of electric current density on the anode surface. The electric current density streamlines in the 2T(I) and 2T(II) models are practically the same as shown in Figure 106 and Figure 107. The maximum value is around  $8 \cdot 10^6$  A/m<sup>2</sup> as shown in Figure 132 against  $6 \cdot 10^7$  to  $7 \cdot 10^7$  A/m<sup>2</sup> in the LTE model as shown in Figure 68. As the anode arc attachment takes up a larger surface on the anode wall, the latter does not reach the material melting temperature. Both 2T models predict a maximum anode around 1000 K against 3695 K in the LTE model. The value of electric current density in the anode arc attachment agrees with the data for diffuse anode arc attachment presented in (Neumann, 1977).

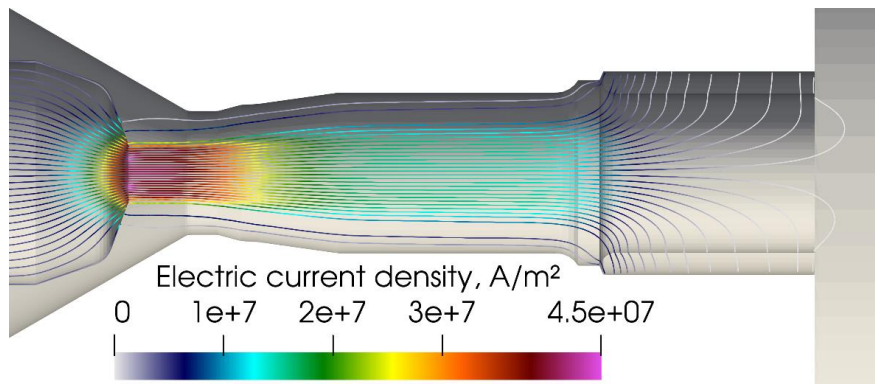


Figure 106 Computed electric current density streamlines in the **2T(I)** model for 500 A and 60 NLPM of argon

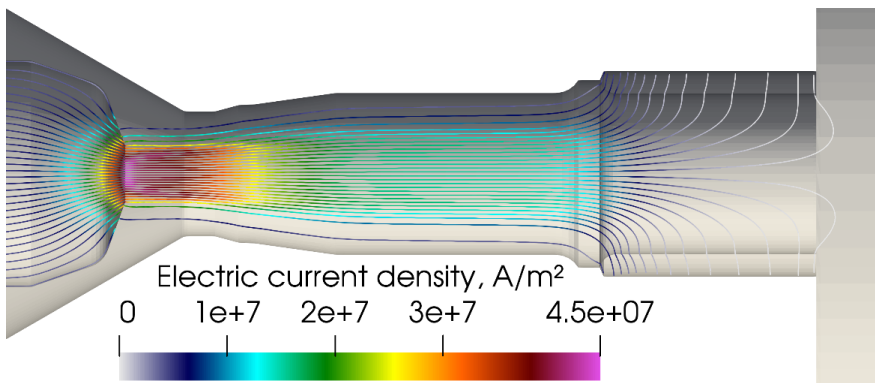


Figure 107 Computed electric current lines in the **2T(II)** model for 500 A and 60 NLPM of argon

The cathode arc attachment in the 2T models is slightly less constricted than in the LTE model due to the faster diffusion of hot electrons and easier heating of the arc fringes because of the much higher thermal conductivity of electrons than heavy species above 15000 K as shown in Annex B. The thermal diffusion of electrons is high enough to yield a higher electrical conductivity in the arc fringes in the 2T model. However, almost the same maximum electric current density is predicted by the LTE and 2T models.

The comparison of the electric current profiles predicted by the 2T and LTE models at the cathode tip is shown in Figure 108. Both 2T(I) and 2T(II) models predict similar current density profiles. However, they are wider, with a higher current density at the center and a lower spike at the edge of the flat part of the cathode tip compared to the profile predicted by the LTE model. The lower spike of  $j(r)$  makes the high temperature ring at the cathode tip less pronounced and the center of the cathode tip melts faster than the edge of the flat cathode tip as shown in Figure 109. However, the pattern of the hot center of the cathode tip and hot ring around it observed on the tested cathodes (Figure 59) is still predicted.

A slight widening of the cathode arc attachment in the 2T model is expectable due to the increased thermal diffusivity of electrons compared to the LTE model that results in a higher electrical conductivity of the plasma layer surrounding the arc in the 2T model.

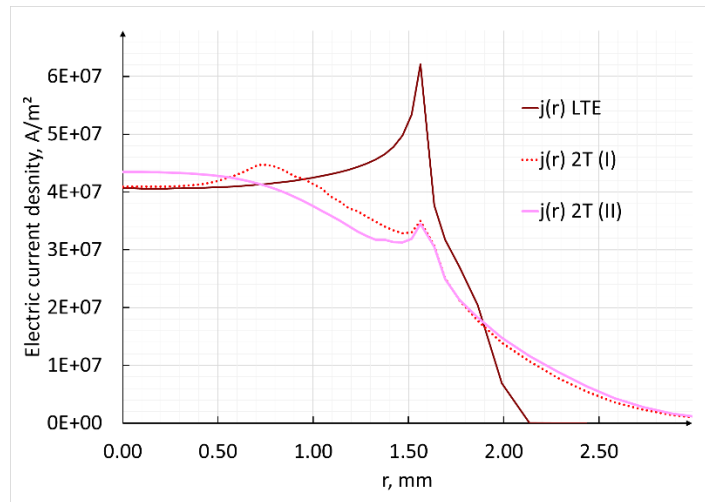


Figure 108 Electric current density profiles at the cathode tip predicted by the 2T(I), 2T(II) and LTE models with 500 A and 60 NLPM of argon

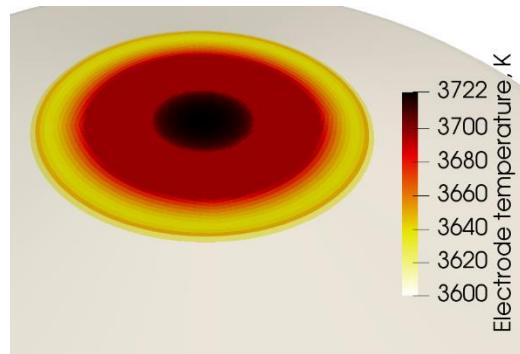


Figure 109 Predicted temperature distribution on the cathode tip in the 2T(II) model with 500 A and 60 NLPM of argon

The Joule power in the 2T(I) and 2T(II) model is the same and shown in Figure 110. The main difference with the Joule power calculated by the LTE model (Figure 70) is a much lower Joule power in the anode arc attachment predicted by the 2T model, since it predicts a much lower electric current density at the anode surface. Also, in the cathode vicinity, the maximum Joule power is 5 times lower in the 2T model than in the LTE model:  $2 \cdot 10^{11} \text{ J/m}^3$  in 2T model against  $10^{12} \text{ J/m}^3$  in the LTE model.

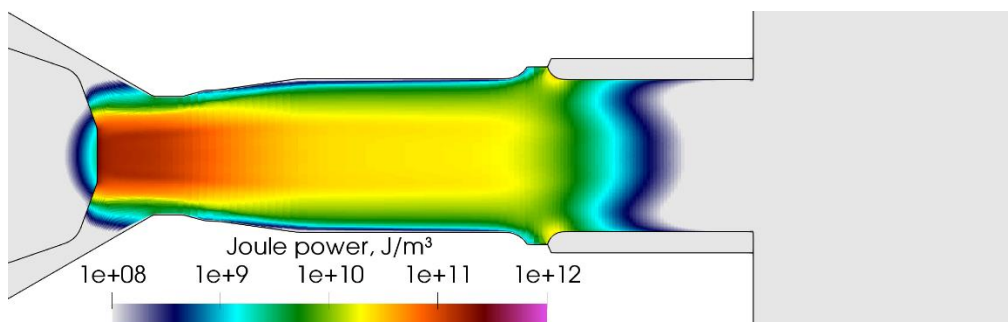


Figure 110 Joule power in the 2T(I) and 2T(II) models for 500 A and 60 NLPM of argon

### III.5.2. Computed plasma flow fields

The maximum value of the electron and heavy species temperatures is located in front of the cathode tip as in the LTE model but this value is lower. Downstream from the cathode tip, the

plasma temperature decreases all the way to the nozzle exit. However, there is a significant difference in the temperatures of the issuing plasma jet predicted by the 2T(I) and 2T(II) models.

The electron and heavy species temperatures predicted by the 2T(I) model are illustrated in Figure 111 and Figure 112. Both the electron and heavy species temperatures have an axial symmetry as shown in Figure 113.

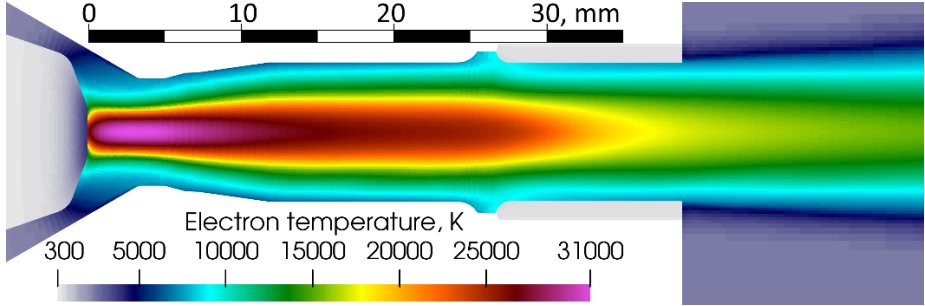


Figure 111 Computed electron temperature  $T_e$  at the axial cross section in **2T(I)** model

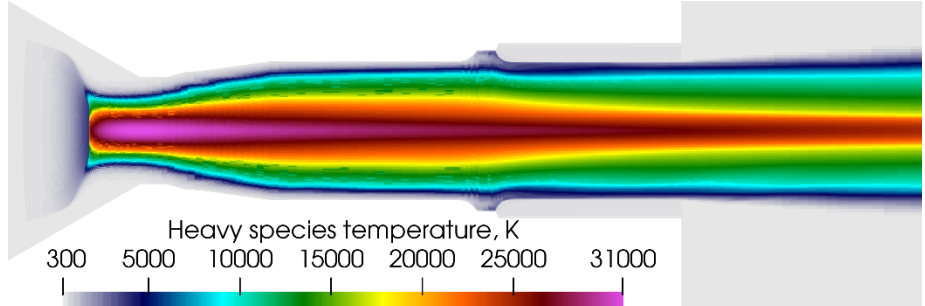


Figure 112 Computed heavy species temperature  $T_h$  at the axial cross section in **2T(I)** model

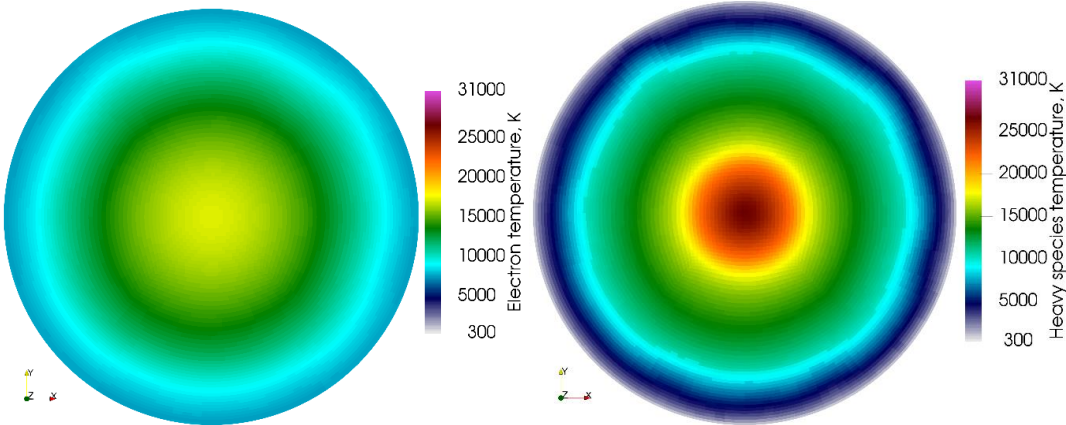


Figure 113 Computed  $T_e$  and  $T_h$  distribution at the nozzle exit in **2T(I)** model

The Figure 113 brings out the major issue of the 2T(I) model: outside of the torch along the central line of the issuing laminar plasma flow with axial symmetry, the electron temperature is lower than the heavy species temperature. As shown in Figure 114, the recomputed  $T_e/T_h$  ratio in the 2T(I) model can be as low as 0.6 at the central line of the issuing plasma jet. This unphysically low  $T_e/T_h$  ratio is preserved until the very outlet. It results from a rather low stored energy assigned to the electrons in the 2T(I) model since the ionization energies are attributed to the heavy species, while its dissipation is rapid.



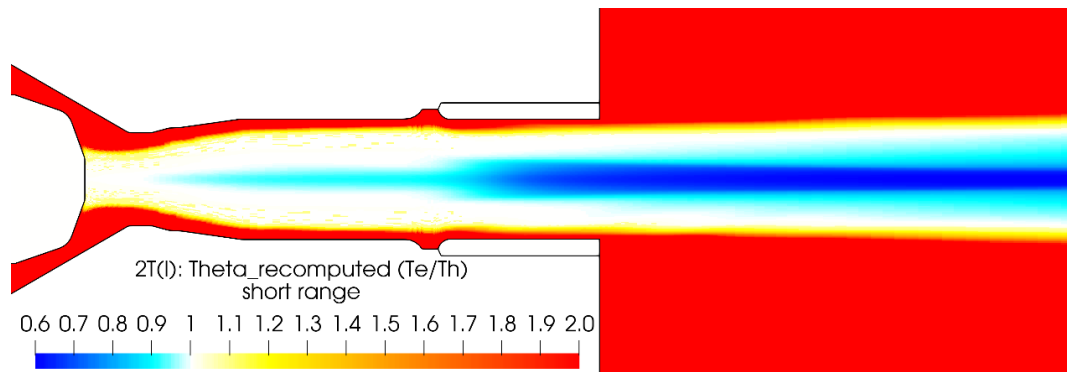


Figure 114 Recomputed  $\theta = T_e/T_h$  in the **2T(I)** model after the governing equations are solved

Figure 115 depicts the axial dependence of the energy terms in the 2T energy equations, namely Joule power exchange term, radiation losses and electron and heavy species thermal diffusion, found in equations (2.20) and (2.21). The dissipation of the electron enthalpy is several orders of magnitude higher than that of the heavy species inside the plasma torch in the 2T(I) model. Outside the plasma torch, the heat dissipation in heavy species takes over the leading position, but the electron temperature is already lower than that of the heavy species. The exchange term becomes null quite close to the cathode tip because the model make the exchange term to vanish when  $T_h$  is lower than  $T_e$ . This means that the artefact with  $T_e/T_h < 1.0$  may appear already 1 mm from the cathode tip in the 2T(I) model as seen in Figure 116.

Thus due to much higher thermal diffusivity and low enthalpy storage of electrons in the 2T(I) model, the electron temperature along the central line decreases rapidly, while the heavy species with lower thermal diffusivity retain their enthalpy along the straight laminar flow.

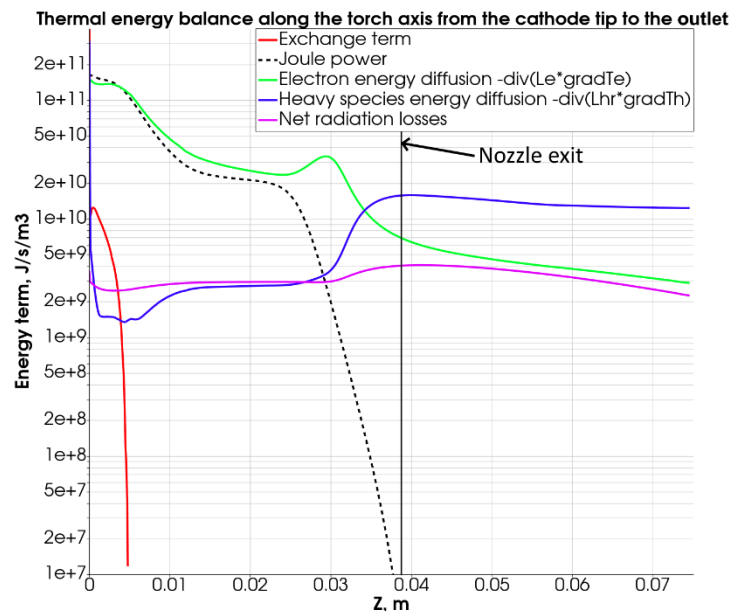


Figure 115 Comparison of the various thermal energy terms in the **2T(I)** model along the torch axis

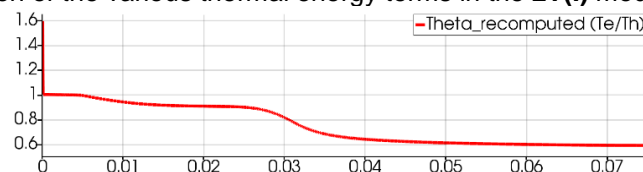


Figure 116 Recomputed  $\theta = T_e/T_h$  in the **2T(I)** model along the torch axis

The 2T(II) model yields more reliable results in terms of temperature ratio in the issuing plasma flow. The distributions of the electron and heavy species temperatures in the axial cross section are shown in Figure 117 and Figure 118, respectively, and their distribution at the nozzle exit in Figure 119. Figure 120 shows the distribution of  $\theta=T_e/T_h$  in the axial cross section and Figure 121 the axial dependence of the energy terms in the 2T(II) energy equations. The latter shows that the electron energy dissipation is slightly higher than in the 2T(I) model, but the energy stored in electrons in the 2T(II) model is much higher due to the ionization energy. Therefore, the electron temperature decreases slower on the torch axis with this model. The heavy species have an opposite story: in the 2T(II) the energy stored in the heavy species is lower and dissipates much faster even if this dissipation is lower than in the 2T(I) model almost along the whole torch axis.

The thermal equilibrium is reached along the axis in 2T(II) model contrarily to the 2T(I) model but, close to the nozzle exit, the unphysical artefact  $T_e < T_h$  is still observed. Both temperatures are closer to each other at the nozzle exit as illustrated in Figure 119. The artefact  $T_e/T_h < 1.0$  still appears in the issuing plasma jet, but in a smaller area and limited to  $T_e/T_h = 0.85$ . This effect disappears 1.5 cm far from the nozzle exit as illustrated in Figure 120. In the arc fringes, the recomputed ratio  $T_e/T_h$  can be less than unity, i.e. around 0.98, but this effect seems to be rather numerical than physical. Another possible source of the low  $T_e/T_h$  ratio can be inaccurate values of the net volumetric radiation losses.

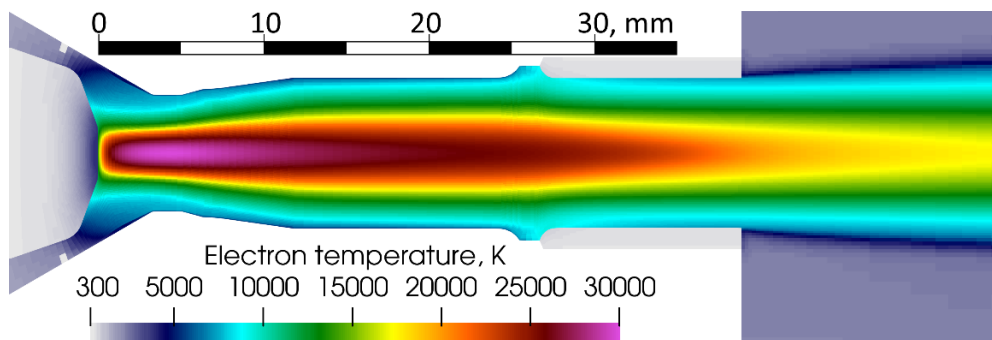


Figure 117 Computed electron temperature  $T_e$  in the axial cross section with the **2T(II)** model

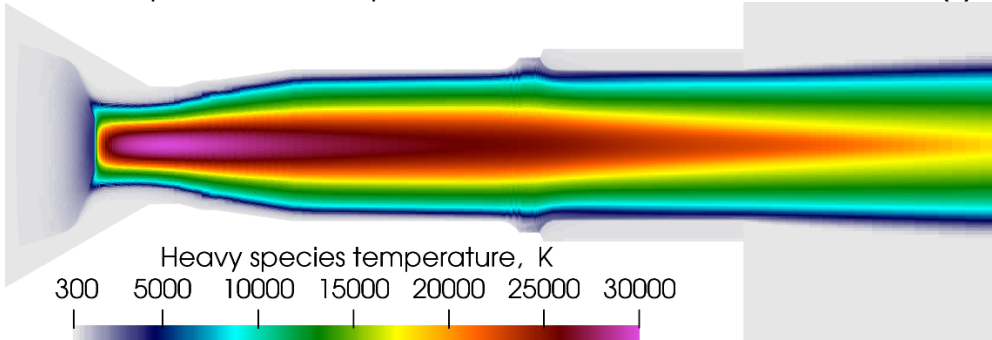


Figure 118 Computed heavy species temperature  $T_h$  in the axial cross section with the **2T(II)** model

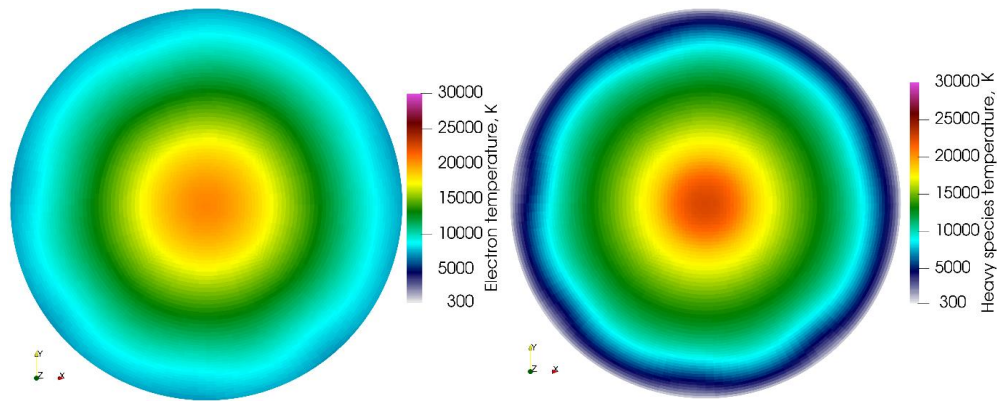


Figure 119 Computed  $T_e$  and  $T_h$  distribution at the nozzle exit with the **2T(II)** model

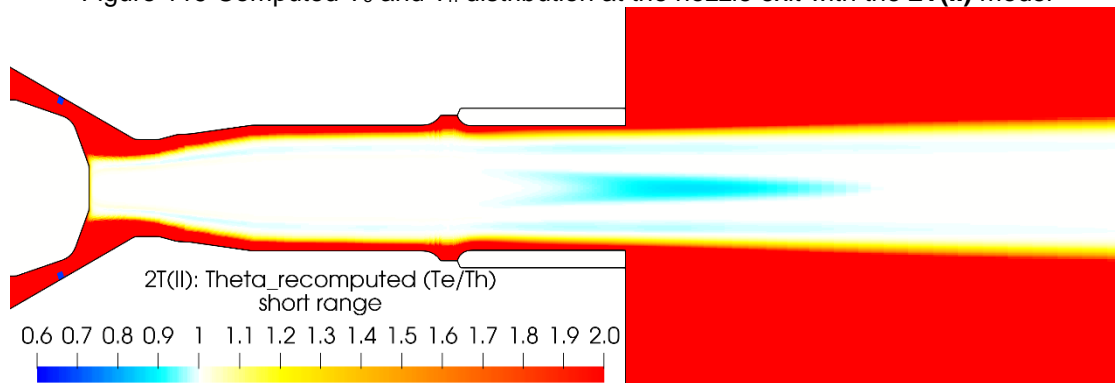


Figure 120 Recomputed  $\theta = T_e/T_h$  in the **2T(II)** model after the governing equations are solved

Figure 121 shows that, in the 2T(II) model, the dissipation of the electron enthalpy is higher than that of the heavy species along the whole axis of the plasma torch. The energy exchange term between the electrons and heavy species is non-zero on a longer distance from the cathode tip compared to the 2T(I) model. Even in the issuing plasma flow, this exchange term can be non-zero, which means that the artefact  $T_e/T_h < 1.0$  is less encountered in the 2T(II) model as seen in Figure 122.

Thus even when distributing the radiation losses to electrons and heavy species and ascribing the ionization energies to electrons as recommended in (Fretton et al., 2012), the artefact  $T_e < T_h$  is still present in the calculations. Consequently, the effect of a decrease in the arc current down to 200 A on the 2T results has been investigated. As shown in Figure 125, the artefact  $T_e/T_h < 1.0$  disappears in the 2T(II) model, while it is still present in the 2T(I) model as shown in Figure 123. Also, it has been found that an increase in gas flow rate does not affect much the artefact  $T_e/T_h < 1.0$ .

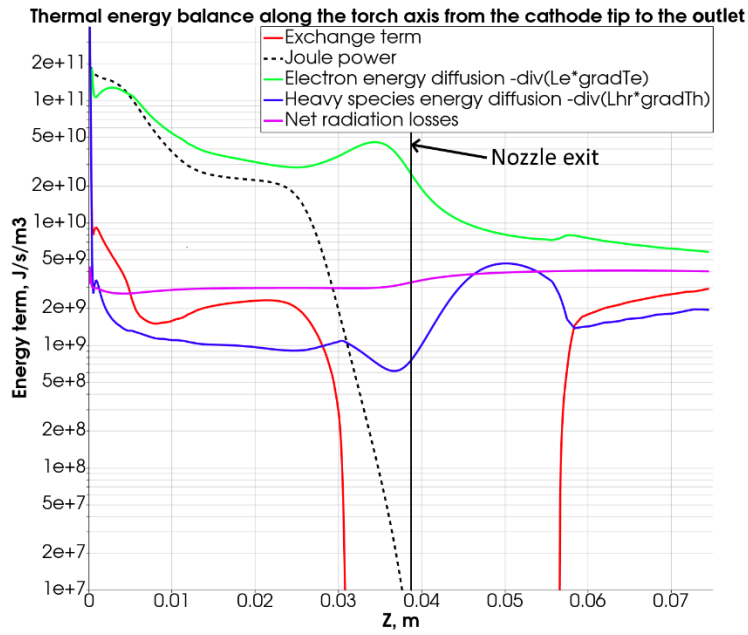


Figure 121 Comparison of the various thermal energy terms in the **2T(II)** model along the torch axis

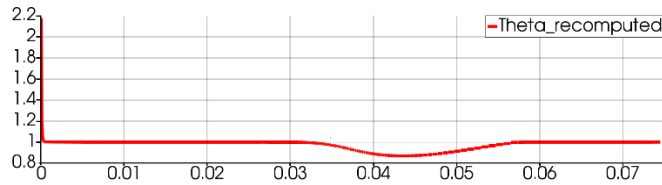


Figure 122 Recomputed  $\theta = T_e/T_h$  in the **2T(II)** model along the torch axis

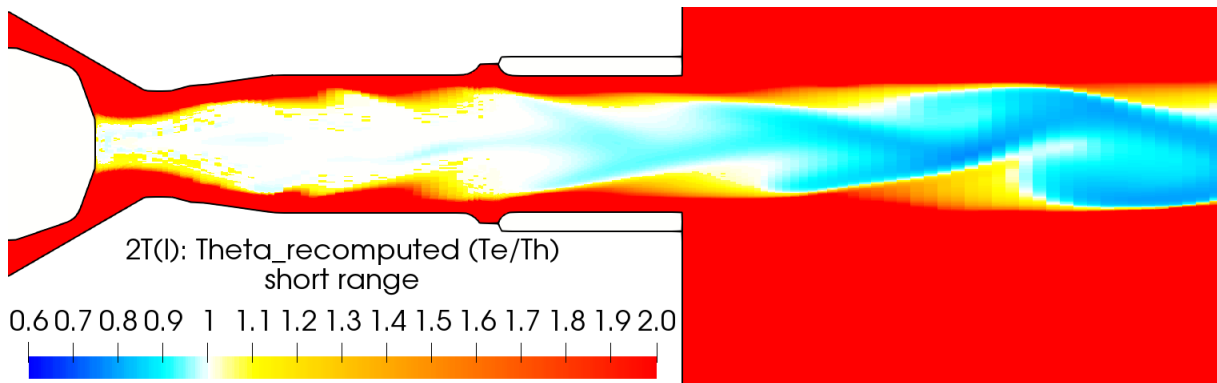


Figure 123 Recomputed  $\theta = T_e/T_h$  in the **2T(I)** model with **200 A** and **60 NLPM** of argon after the governing equations are solved

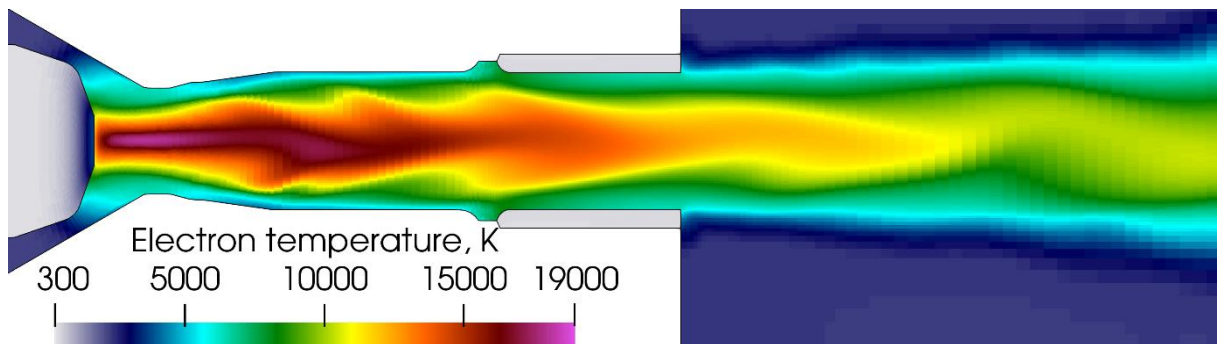


Figure 124 Electron temperature in the **2T(I)** model with **200 A** and **60 NLPM** of argon

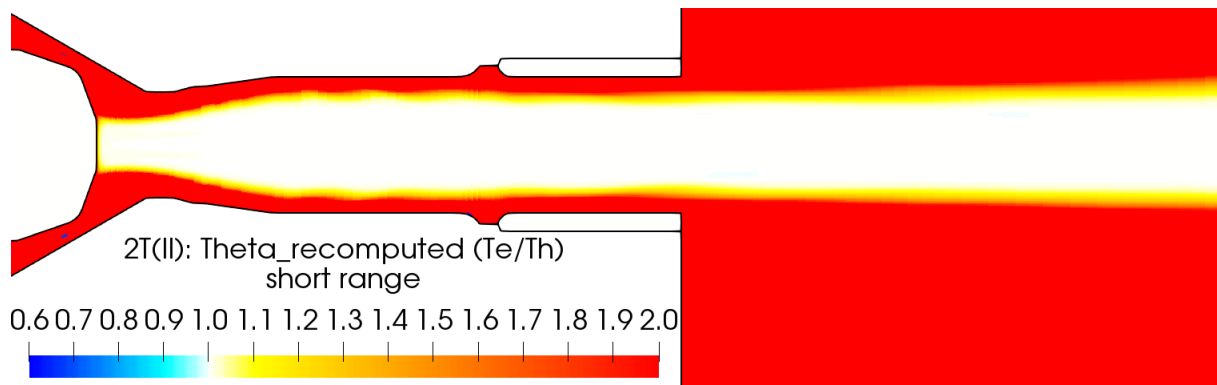


Figure 125 Recomputed  $\theta = T_e/T_h$  in the **2T(II)** model with **200 A** and **60 NLPM** of argon after the governing equations are solved

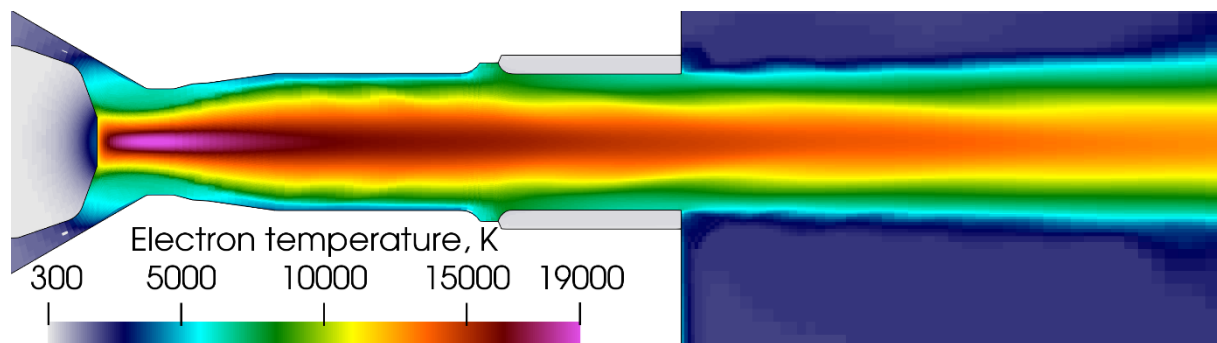


Figure 126 Electron temperature in the **2T(II)** model with **200 A** and **60 NLPM** of argon

The association of the ionization energy to the electrons seems correct not only in terms of equation derivation, but also in terms of the predicted temperature distribution.

The simulation artefact  $T_e/T_h < 1.0$  was also addressed in (Freton et al., 2012). The solution suggested by Freton *et al.* was to redistribute the volumetric net radiation losses between the heavy species and electrons, so that the heavy species lose their enthalpy faster. Unfortunately in the case of a plasma torch with a cascaded anode and a mostly-straight axially symmetric arc and laminar flow, the redistribution of the volumetric net radiation losses is generally not enough to prevent such simulation artefact as electrons colder than atoms and ions. The shares of the radiation losses assigned to the electrons due to continuum  $\delta_e$  and to heavy species due to line contributions  $(1 - \delta_e)$  are around 50% for both cases with current intensity of 200 and 500 A. Therefore the value of  $\delta_e$  is significant and should not be a source of the artefact  $T_e/T_h < 1.0$ .

An opposite heat exchange term from heavy species to electrons seems a possible way to eliminate the simulation artefact but does not have much physical sense.

A possible solution for eliminating the simulation artefact  $T_e/T_h < 1.0$  is to correct the volumetric net radiation losses which seem underestimated above 20000 K. The better results obtained for an arc current of 200 A, where the maximum temperature is around 20000 K as shown in Figure 126, confirms the idea that the term  $Q_r$  is underestimated at high temperatures.

The velocity distributions predicted with the 2T(I) and 2T(II) models are shown in 2T(I) and 2T(II) models are illustrated in Figure 127 and Figure 128. The maximum plasma velocity and its evolution along the torch axis are similar to those obtained with the LTE model. However,

due to the diffuse anode arc attachment that exhibits an axial symmetry, the velocity distribution has the axial symmetry as well, as illustrated in Figure 129.

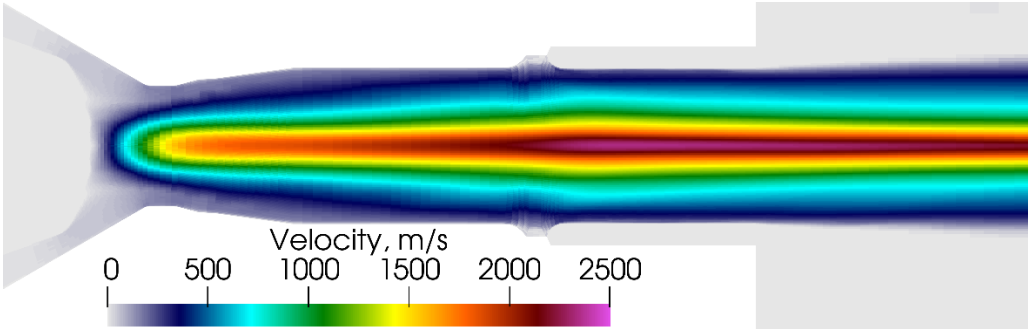


Figure 127 Plasma velocity distribution in the axial cross section predicted by the **2T(I)** model

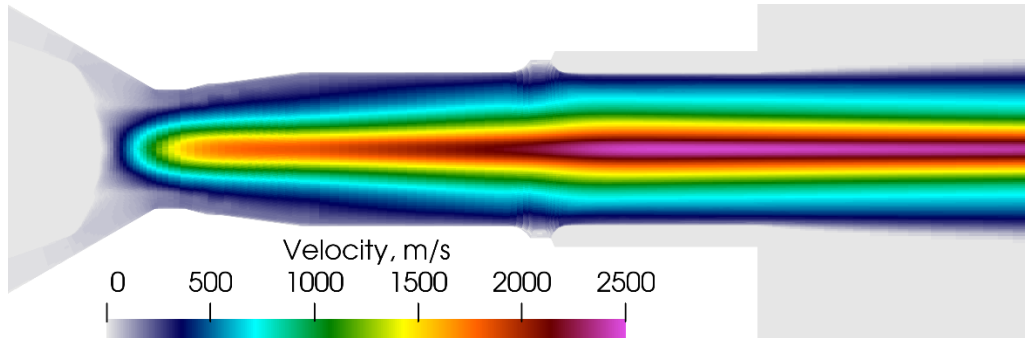


Figure 128 Plasma velocity distribution in the axial cross section predicted by the **2T(II)** model

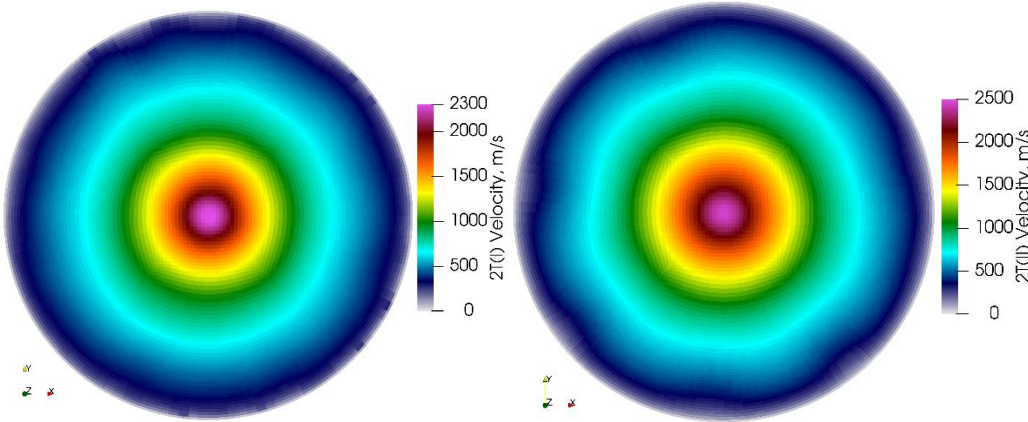


Figure 129 Plasma velocity distribution at the nozzle exit predicted by the 2T(I) and 2T(II) models

**III.6. Validation of the simulation results**

The predicted arc voltage and torch thermal efficiency were validated against the experimental data provided by the torch manufacturer Oerlikon Metco.

The experimental torch efficiency is computed by the formula (3.6).

$$\eta = \frac{IV - Q_{cooling}}{IV} \tag{3.6}$$

Where  $I$  and  $V$  are the arc current and arc voltage, respectively, and  $Q_{cooling}$  the heat rate loss in the torch. It is experimentally measured from the flow rate of the torch cooling water and its temperature increase from the input and output of the water cooling system. The

predicted cooling loss includes the heat transfer to the electrodes due to the electric current and gas thermal conduction to the surface, as well as the radiative heat transfer to the whole torch. The latter is computed assuming that all the radiation emitted by the gas to the solid angle of the torch part is fully absorbed by the surface of the torch parts. In order to compute it, the share of the solid angle of the torch parts in the whole sphere was computed for each cells. This share of the whole radiation in each cell was assumed to be emitted to the torch parts.

The computed full voltage includes the predicted arc voltage plus the cathode and anode sheath voltage drops while the predicted arc voltage is used as a boundary condition (see section II.5.3.5) and does not include the sheath voltage drops.

**III.6.1. LTE model predictions for various arc current intensity and gas flow rate**

In order to validate the developed LTE model and find out the limits to applicability of the model the variation of current intensity and gas flow rate was studied. The core indicators of the model are the full voltage and cooling loss.

The studied values of the electric current are 100, 200 and 500 A, and the values of the argon flow rate 60 and 120 NLPM. The comparison of the predicted and experimental arc voltages and cooling losses is shown in Figure 130 and Figure 131, respectively.

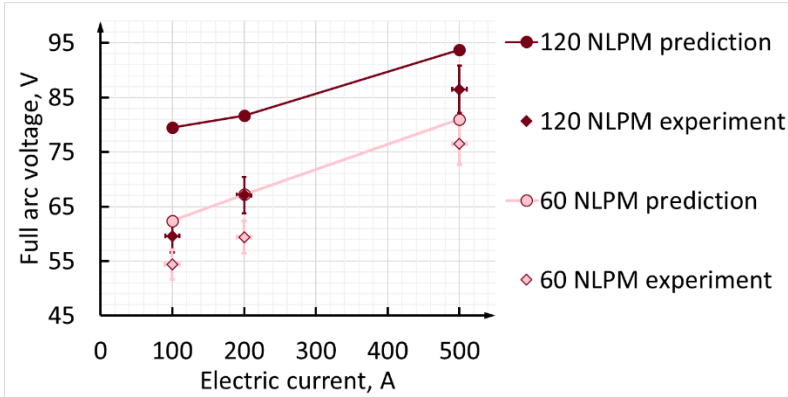


Figure 130 Comparison of the experimental and predicted full arc voltage with the LTE model for various arc current intensity and gas flow rates

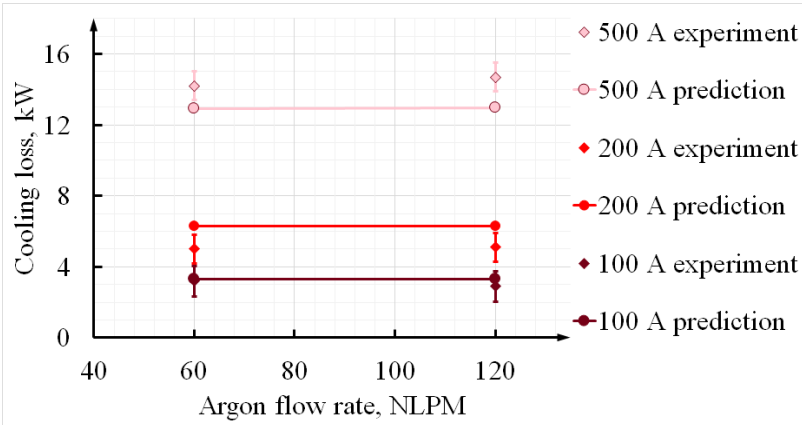


Figure 131 Comparison of the experimental and predicted cooling loss with the LTE model for various arc current intensity and gas flow rates

The comparison of the experimental and predicted cooling loss shows a rather good agreement for all the studied values of arc electric current and gas flow rate. The small

difference can be explained by a non-perfect thermal balance on the electrode surface, not exact values of cathode and anode voltage drops and the chosen values for the volumetric net radiation of the LTE argon plasma.

However, the predicted voltage is close to the experimental value only for a high current and low gas flow rate: 500 A and 60 NLPM. The experimental voltage is 76.5 V, while the predicted full voltage is 80.5 V. Also, the experimental cooling loss is 14.2 kW, while the predicted one is 13.0 kW. This set of operating conditions corresponds to the widest and most stable arc with a thin and slow cold boundary layer, which does not cause the arc to restrike.

From the experimental values of voltage and cooling loss, the specific enthalpy at the nozzle exit can be calculated by the formula (3.7). It represents the energy stored in the issuing plasma jet per unit mass. In the formula (3.7) the kinetic energy of the plasma flow and the energy radiated by the arc through the nozzle are considered negligible.

$$h = \frac{IV - Q_{cooling}}{\dot{m}} \quad (3.7)$$

For the mass flow rate of 60 NLPM of argon corresponding to 1.65786 g/s the experimental value of the specific enthalpy is around 14.51 MJ/kg, which corresponds approximately to an average temperature of 12550 K at nozzle exit. The predicted specific enthalpy, derived from the enthalpy flux through the nozzle exit, is 15.97 MJ/kg, which corresponds to an average temperature of about 12780 K.

The experimental torch efficiency computed by the formula (3.6) is 62.9%, while the predicted torch efficiency is 67.7%.

In conclusion, the LTE model developed in this study is capable of producing reasonable results in terms of full voltage, cooling loss and torch efficiency for low gas flow rate (60 NLPM of argon) and high arc current intensity (500 A). A higher gas flow rate or lower electric current result in a thicker or faster cold boundary layer that favors the arc instability. Under such operating conditions, the validity of the LTE approach is questionable: the arc is too resistive and unstable; the arc voltage fluctuations are too high and arc voltage is overestimated.

Also, in the LTE model a domain with an artificially-high electrical conductivity behind the anode arc attachment is used to get the gas heated enough to become electrically conductive prior to entering the arc region. For a proper prediction of the shape and size of the anode arc attachment, a more complex model of the arc is necessary.

To extend the range of applicability of the arc model, the thermal disequilibrium in the arc fringes has to be considered, which is done in 2T models.

### III.6.2. Validation of the 2T model predictions

To validate the anode arc attachment mode predicted by the 2T model, actual anodes operated with the same operating conditions (500 A and 60 NLPM of Ar) were examined. The predicted electric current distribution on the anode surface is illustrated in Figure 132. The anode erosion after 5 minutes of operation with the aforementioned operating conditions is shown in Figure 133. The arc attachment area can be seen on the tested anode even after such period of time which is much shorter than the normal lifetime of the hardware. The arc mostly attaches at the upstream edge of the anode. The surface of the tested anode changed its color at the arc attachment, but is not molten, similarly to the prediction of the 2T model. In addition, some hair line cracks are visible on the anode surface, which could be caused by the difference in the



thermal expansion of the water-cooled copper and intensively heated tungsten liner. However, the cracks cannot be reflected by the current model. Another tested anode after 60 minutes of operation is shown in Figure 134; it has a similar axisymmetric pattern on the upstream edge. The main difference between the tested anodes used for 5 minutes and 60 minutes is that the latter has less cracks but exhibits one molten spot and axial splash of molten tungsten.

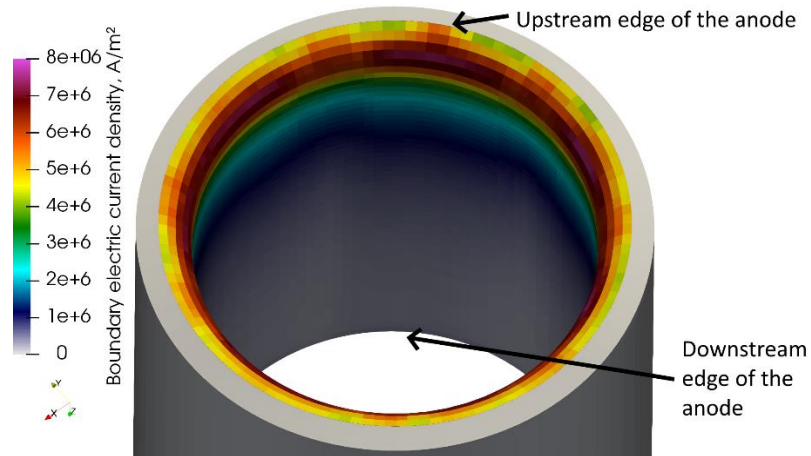


Figure 132 Predicted electric current density on the anode surface with the 2T(II) model. 500 A and 60 NLPM of argon. Most of the electric current density is concentrated on the upstream edge

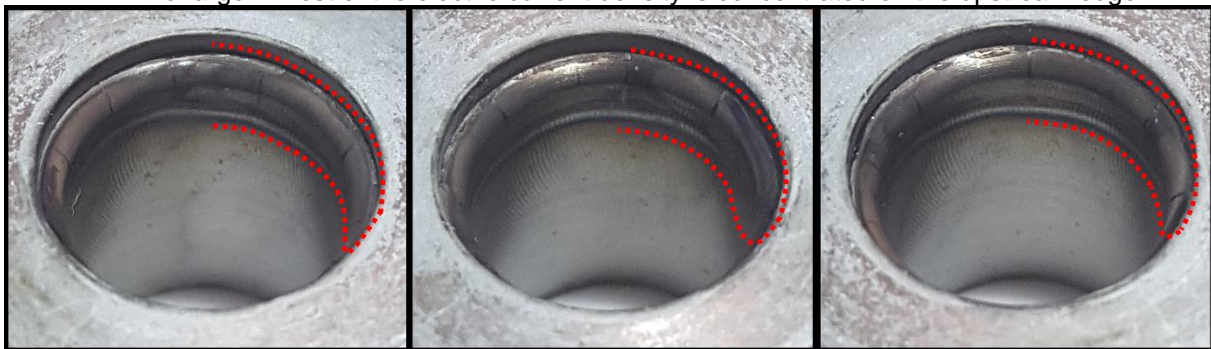


Figure 133 SinplexPro™ anode erosion on the upstream edge **after 5 minutes** of operation with 500 A and 60 NLPM of argon. (courtesy of Oerlikon Metco (US) Inc.)

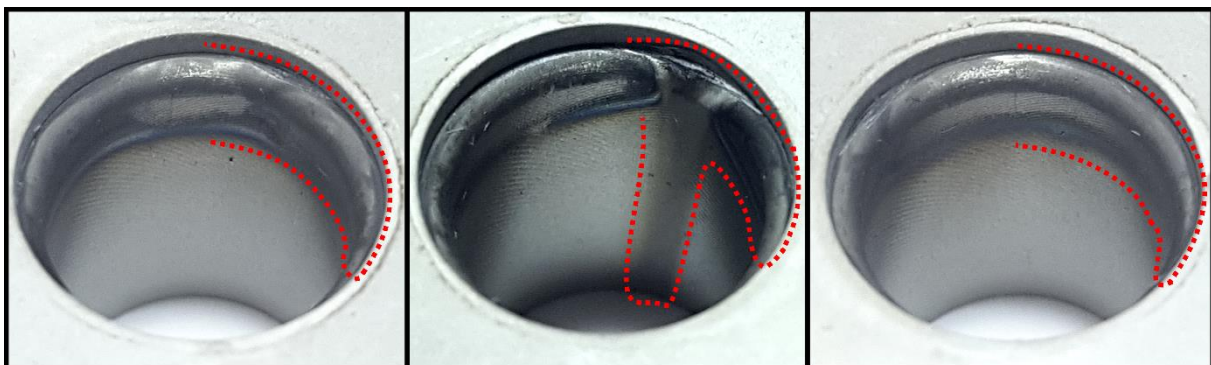


Figure 134 SinplexPro™ anode erosion on the upstream edge **after 60 minutes** of operation with 500 A and 60 NLPM of argon. (courtesy of Oerlikon Metco (US) Inc.)

The 2T models makes it possible to get rid of the area with an imposed artificially-high electrical conductivity behind the anode arc attachment, which was necessary in the LTE model. Without this artificially-high electrical conductivity domain, both 2T models predict a lower mean full voltage and almost negligible voltage fluctuations as illustrated in Figure 135.

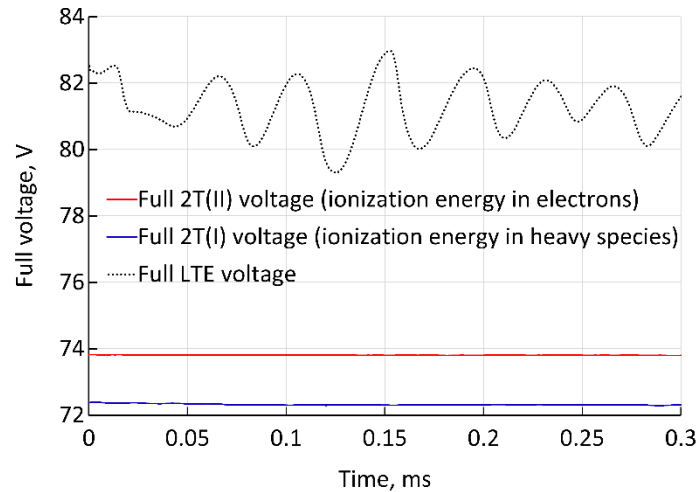


Figure 135 Comparison of the arc voltage time sweeps predicted by the 2T models and LTE model. With anode and cathode sheath voltage drops. The experimental voltage is  $76.5 \pm 4$  V.

The full predicted arc voltage with the 2T(II) model is 74 V while the experimental voltage is  $76.5 \pm 4$  V, which means that the 2T model predicts an arc voltage closer to the experimental value than the LTE model. The relative error of predicted full voltage in the 2T(II) model is 3.3% against 5.2% with the LTE model.

The comparison of the prediction of the full arc voltage with the 2T(I) and LTE models for various current intensities and gas flow rate of 60 NLPM is shown in Figure 136. Both 2T models have close voltage predictions, and they both predict a full arc voltage much closer to the experimental values than the LTE model.

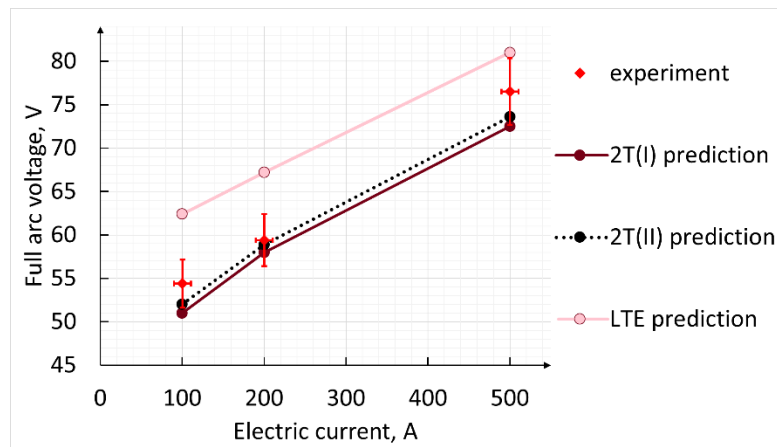


Figure 136 Comparison of the experimental voltage with predicted full voltage with the LTE, 2T(I) and 2T(II) models for various current intensity and **60 NLPM** of argon

The difference in the voltage prediction with the LTE and 2T models is especially visible for low arc current, which is characterized by a thicker cold boundary layer. Under these conditions, the thermal disequilibrium effects are too high and cannot be properly predicted with the LTE model.

The 2T(II) model was also applied to a higher gas flow rate: 120 NLPM. The difference in the predicted full voltage with the LTE and 2T(II) models is further emphasized as illustrated in Figure 137. The predictions of the 2T(II) model are still inside the margins of error for all the current intensities, while the LTE model overestimates the voltage for the whole range of current intensity due to a rapid cold boundary layer. In addition, the experimental and 2T

prediction curves in Figure 137 have a similar slope, while the LTE prediction curve exhibits a different slope and seems to reach an opposite inflection for low currents.

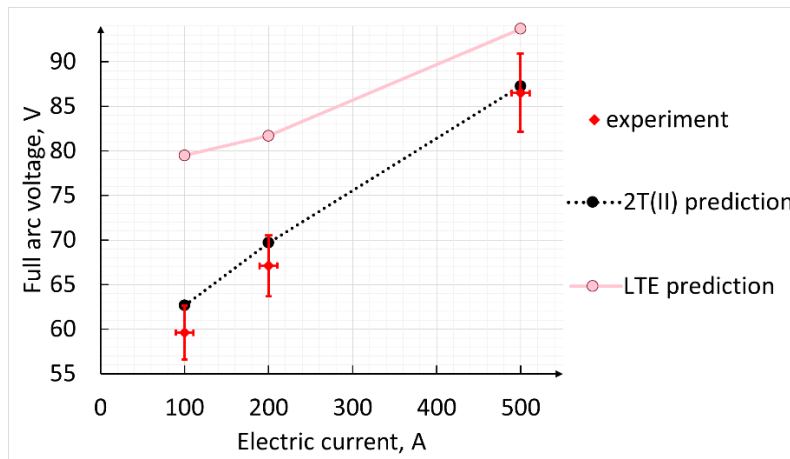


Figure 137 Comparison of the experimental voltage with the predicted full voltage in LTE and 2T(II) models for various arc current intensity and **120 NLPM** of argon

A similar result with a predicted smoother and steadier flow than that of the LTE model was obtained in (Huang et al., 2013) with the so-called “improved LTE” model with an auxiliary electron temperature field defined by the heavy species temperature and electric field. In that study, the arc voltage predicted by the “improved LTE” model was closer to the experimental value and the obtained flow was axisymmetric as well.

### III.7. Conclusion

The predictions of the LTE model developed in this study agree well with the experimental data of full arc voltage and torch cooling loss for high arc current (500 A) and low gas flow rate (60 NLPM) with argon. Under these operating conditions, the maximum temperature, around 33000 K, is found in front of the cathode tip and decreases down to 23000 K at the nozzle exit while the maximum velocity is 2300 m/s and located at the nozzle exit. However, the agreement between the predictions and experimental values of arc voltage and torch cooling losses is not so good when the gas flow rate is increased or arc current decreased. The erosion patterns on the cathode predicted by the LTE model resemble the patterns observed on used hardware. The predicted anode arc attachment is constricted, which makes it possible to use the model to investigate and compare two methods to control the anode arc attachment motion: swirling gas injection and external magnetic field.

In a second step, a 2T model was developed to widen the range of applicability of the model. Two formulations of enthalpy of electrons and heavy species were compared. The first one appears to have higher computational cost and significant unphysical simulation artefact, namely electron temperature significantly lower than the heavy species temperature. The second formulation was found to have lower computational cost and mitigated artefact of  $T_e < T_h$ . The reason of this artefact is assumed to be inaccurate radiation losses used for in the model. The main finding of the 2T model is the diffuse anode arc attachment, which resembles the pattern on the anodes used with argon for 5 and 60 minutes. The plasma flow was found to be axisymmetric and much more stable than in the LTE model. The prediction of full voltage in the 2T model are much closer to the experimental values than in the LTE model in the whole range of studied current intensity (100, 200 and 500 A) and for both studied gas flow rates (60 and 120 NLPM).

# General Conclusion and Perspectives

---



Plasma spraying is now a conventional technique in surface engineering. It makes it possible to coat parts of various shapes and dimensions with coatings whose thickness ranges between around a hundred of micrometers and a few millimeters. The basic tool of the process is the plasma torch that conditions, to a great extent, the treatment of the coating material in the plasma jet and, therefore, the microstructure and properties of the coatings.

The modeling of the operation of a plasma spray torch has been attracting a large body of research since the 90's. Its specificity, compared to the transferred-arc plasma torches used in welding and cutting, is the unstable anode arc attachment whose mode (constricted, diffuse) and location depend on the operating conditions. If many advances have been made in plasma spray torch modeling, still some points need to be better understood or improved; e.g.; the way the electric current is input in the calculation domain, departure from LTE in the arc fringes and close to electrodes, taking into account the actual geometry of the torch, etc.

However, a reliable and comprehensive model would be of great interest to determine the operating window for a given coating powder, help to improve the torch design and lifetime of electrode, and serve as the first brick of the numerical twin of a plasma spray process.

This study engages with this context and its inherent complexity. It intended to develop a reliable model of plasma spray torch operation, which takes into account the 3D transitive processes taking place inside the torch and arc-electrode interaction. It began with a literature review that covered the main components of a plasma spray torch, phenomena specific to electric arc and a non-exhaustive review of DC non-transferred arc plasma torch simulation.

A commercial plasma spray torch with a single cathode and cascaded-anode (SinplexPro™ of Oerlikon Metco) was selected due its stabilized arc length, low voltage fluctuations. This torch is also of strategic relevance for the IRCER laboratory.

## **1. General features of the developed model**

The model is implemented in the free open-source Code\_Saturne developed by EDF, which allows considerable customization and does not restrict the user's control over the computation.

The simulations were carried out with pure argon as plasma gas. The main reasons are i) the thermal and transport properties of argon are available, even for high degree of disequilibrium between electrons and heavy species and ii) many transferred arc and non- transferred arc models published in the literature deal with argon.

The model uses an energy conservation equation written in enthalpy. It includes advanced boundary condition for the magnetic vector potential (Biot&Savart approach) and both electrodes are included in the computational domain. The advanced boundary condition make the predicted magnetic field continuous and plausible, while the arc behavior becomes stable and reasonable. The inclusion of electrodes in the computational domain is necessary for the prediction of their temperature evolution. To couple the electrodes and arc, a special numerical procedure was developed, which was intended to overcome the mathematical problem with the discontinuity of the calculated enthalpy field. Electrode sheath model was not included, but fixed electrode voltage drops drawn from the literature were considered when estimating the heat transfer to electrodes.

The results demonstrated the necessity of an unsteady and three-dimensional model, since the spatiotemporal dynamics of the arc are essential to estimate the effect of arc on the electrodes.

## 2. LTE model

The LTE model was the first step towards a reliable plasma torch model. It predicts a constricted anode arc attachment when the plasma torch is operated with argon. The electric current density reached in the cathode and anode arc attachments is close and high enough to cause the melting of the electrodes that are both in tungsten. The anode starts melting if the arc stays in the same angular position for at least 10 ms.

The LTE predictions were validated against the experimental values of full arc voltage and torch cooling loss provided by the torch manufacturer. The best agreement was reached for a low gas flow rate of 60 NLPM and high electric current of 500 A. Higher gas flow rate or lower current intensity led to a deviation from the experimental voltage due to a neglected thermal disequilibrium effect. Also, the predicted patterns of electric current density and temperature on the cathode tip surface agreed well with the pattern of melting zones on used cathodes.

In addition, the LTE model required a domain with an artificially-high electrical conductivity behind the anode arc attachment to allow the cold boundary layer to gain enough energy and become electrically conductive before interacting with the anode arc attachment. This numerical trick allows the arc to attach to the anode on the internal cylindrical surface. Without this artificial electrical conductivity, the cold boundary layer remains electrically non-conductive and pushes the arc attachment downstream to the outside plain surface of the anode. To overcome this issue, it is necessary to consider the departure from thermal equilibrium in the gas phase and in particular in the arc fringes.

## 3. Arc rotation

Since the LTE model predicts a constricted anode arc attachment, which happens to be the main reason for anode erosion, the LTE model was used to investigate two common ways to control the anode arc attachment rotation: swirling gas injection and axial external magnetic field.

The initial swirling movement was found to undergo a significant decrease in the azimuthal momentum until the nozzle exit. Due to the rapid axial acceleration of plasma gas in the torch channel, the velocity streamlines for the actual gas injection angle of 25° are practically parallel to the torch axis and the effect the plasma swirling on the anode arc attachment is rather low and intermittent. Two other injection angles of 10° and 45°, respectively, were tested. A gas injection angle of 10° yielded almost the same results in terms of anode arc attachment motion as a straight gas injection. On the contrary, a gas injection angle of 45° resulted in a continuous rotation of the anode arc attachment and a significant decrease of the maximum temperature of the anode, which allows concluding that an increase of the gas injection angle from 25° to 45° would help to mitigate the anode erosion during plasma torch operation. In addition, such change only requires the modification of one part of the torch: the gas injection ring. Therefore, the modification of the gas injection angle seems to be a rather affordable way to decrease the anode erosion. However, the effect of this modification on the plasma spraying process deserves a special investigation, in particular for the deposition of suspensions and solutions.

Quite the reverse, an axial external magnetic field requires much higher investments in the torch design with a coil or permanent magnets around it, but it had a much higher effect on the rotation of the anode arc attachment almost in the whole studied range (0.03 T to 0.1 T). The axial external magnetic field, for the configuration of the coil suggested in this work, had two major effects:

- the swirling of the plasma flow near the cathode arc attachment,
- a rotation of the anode arc attachment.

The first effect emphasizes the second and, for an external magnetic field above 0.03 T, the combination of these two effects results in a rather high circumferential velocity of the anode arc attachment, up to 160 m/s. Again, the effect of this fast arc rotation on the plasma spraying process deserves a special investigation.

#### 4. 2T model

The 2T model takes into account the violation of thermal equilibrium and solves the enthalpy equations for the electrons and heavy species separately. First, the non-equilibrium argon plasma properties were computed. Then, because of several interpretation of the 2T model in the literature, two formulations for electron and heavy species enthalpies were considered: the 2T(I) model in which the ionization energy is associated to the heavy species and the 2T(II) model in which the ionization energy is associated to the electrons.

Taking into account the departure from LTE yielded a significant change in the anode arc attachment. Due to the rapid diffusion of electron enthalpy, the cold boundary layer was significantly more electrically conductive close to the anode. Therefore, the anode arc attachment predicted by the 2T(I) and 2T(II) models for the SinplexPro™ plasma torch operated with argon was axisymmetric and diffuse, with a much lower electric current density than in the LTE model. The arc current is mostly concentrated at the upstream edge of the anode. Such predictions agreed with the heating pattern on the tested anodes provided by the company Oerlikon Metco and operated with 500 A and 60 NLPM of argon. After 5 minutes of torch operation, the anode did not show any molten spot, but exhibited some cracks that may be due to the heating by the arc. With both 2T(I) and 2T(II) models, because of the diffuse anode arc attachment and redistributed heat load, the anode liner does not reach the tungsten melting point and its maximum temperature is much lower than in the LTE model. The axisymmetric anode arc attachment results in an axisymmetric distribution of plasma temperature and velocity.

The 2T(I) model, with the ionization energy associated to the heavy species, was found to give unphysical results in the plasma flow related to the disequilibrium degree: in the central part of the flow the heavy species temperature was significantly higher than the electron temperature. The ratio with the 2T(I) formulation could be as low as 0.6. In addition, this model presented numerical instabilities in the heat balance due to the lower energy stored in electrons. The electron energy gain from the Joule power and loss in the collisional exchange with heavy species were comparable with their enthalpy. Thus, the enthalpy of electrons fluctuated and the plasma transport properties significantly changed from one time step to another. It was necessary to decrease tenfold the calculation time step for the 2T(I) model, which significantly increased the computational cost.

Meanwhile, the 2T(II) model considered the ionization energy as a part of the electron enthalpy. It made the heat balance for electrons much more stable as the plasma properties. Because of a larger storage of energy in electrons, their thermal diffusion had a lower impact and their temperatures much closer to that of heavy species. The unphysical artefact of  $T_e / T_h < 1$  was mitigated and appeared in a much smaller area. The minimum value of  $T_e / T_h$  was 0.85 compared to 0.6 in the 2T(I) model. However, a decrease of the current intensity to 200 A led to the disappearance of this artefact: the electron temperature was never lower than the heavy



species temperature. It allows to suppose that the radiation energy loss distributed between the electrons and heavy species was underestimated for high temperatures. For the 2T(I) model, a decrease of the current intensity did not help to get more realistic results.

Both 2T models predicted a total arc voltage closer to the experimental values than the LTE model for 60 NLPM of argon and arc current intensity of 100, 200 and 500 A. In addition, the 2T(II) model was tested with 120 NLPM of argon and different arc current values and predicted a significantly closer voltage to the experimental one than the LTE model.

Thus, the 2T(II) model gave more physical results; it also had a computational cost almost similar to that of the LTE model. This makes this model much more attractive than the 2T(I) model for further developments.

The drawback of the 2T model with enthalpy formulations is the fact that the electron temperature cannot be lower than 2000 K because of a too low electron number density below this temperature and violation of the continuum hypothesis. It may seem a little confusing, but the physical meaning of the electron temperature below 2000 K, when the electron number density is below  $10^6 \text{ m}^{-3}$ , is unclear.

However the developed 2T model still lacks two features that are present in some models in the field (Boselli et al., 2013; Freton et al., 2012; Trelles, 2007; Trelles et al., 2007):

- The contribution of the electron pressure gradient  $\frac{\nabla(n_e k_B T_e)}{en_e}$  into the effective electric field,
- And the contribution of the enthalpy diffusion term  $\frac{5}{2} \frac{k}{|e|} (\vec{j} \cdot \nabla T_e)$  due to electric current and electron temperature gradient into the energy equations for electrons.

## 5. Perspective of the model

If in its stage of development, the LTE and 2T(II) model give the correct trend when an operating parameter is varied, they still need various improvements to ensure more reliable predictions. The main next steps could be the following:

- Inclusion of the electron pressure gradient into the effective electric field;
- Inclusion of the enthalpy diffusion term into the energy equations for electrons;
- Improvement of the computation of the net volumetric radiation energy loss;
- Consideration of a larger outlet tank and taking into account the turbulence of the plasma jet issuing from the plasma torch;
- Development of a mathematical algorithm of the electrode sheath model;
- Use of diatomic gases ( $\text{H}_2$ ,  $\text{N}_2$ ) and mixtures of monoatomic and diatomic gases (e.g.;  $\text{Ar-H}_2$ );
- Injection and processing of the coating powder in the plasma jet.

Some of these improvements are already planned for further development of the model in cooperation with Oerlikon Metco.

## References

---

- Abdo, Y., 2018. Etude du comportement des arcs thermiques soumis à des champs (externes et internes) (Ph.D. dissertation). Université de recherche Paris-Sciences-et-Lettres.
- Abdo, Y., Rohani, V., Cauneau, F., Fulcheri, L., 2017. New perspectives on the dynamics of AC and DC plasma arcs exposed to cross-fields. *J. Phys. D: Appl. Phys.* 50, 065203. <https://doi.org/10.1088/1361-6463/aa540e>
- Alaya, M., Chazelas, C., Vardelle, A., 2016. Parametric Study of Plasma Torch Operation Using a MHD Model Coupling the Arc and Electrodes. *J Therm Spray Tech* 25, 36–43. <https://doi.org/10.1007/s11666-015-0330-3>
- Allen, T.K., Paulikas, G.A., Pyle, R.V., 1960. Instability of a Positive Column in a Magnetic Field. *Phys. Rev. Lett.* 5, 409–411. <https://doi.org/10.1103/PhysRevLett.5.409>
- Al-Mamun, S.A., Tanaka, Y., Uesugi, Y., 2010. Two-Temperature Two-Dimensional Non Chemical Equilibrium Modeling of Ar–CO<sub>2</sub>–H<sub>2</sub> Induction Thermal Plasmas at Atmospheric Pressure. *Plasma Chem Plasma Process* 30, 141–172. <https://doi.org/10.1007/s11090-009-9205-z>
- Amakawa, T., Jenista, J., Heberlein, J., Pfender, E., 1998. Anode-boundary-layer behaviour in a transferred, high-intensity arc. *J. Phys. D: Appl. Phys.* 31, 2826–2834. <https://doi.org/10.1088/0022-3727/31/20/017>
- André, P., Abbaoui, M., Augeard, A., Desprez, P., Singo, T., 2016. Study of Condensed Phases, of Vaporization Temperatures of Aluminum Oxide and Aluminum, of Sublimation Temperature of Aluminum Nitride and Composition in an Air Aluminum Plasma. *Plasma Chem Plasma Process* 36, 1161–1175. <https://doi.org/10.1007/s11090-016-9704-7>
- ANSYS, Inc., 2016. ANSYS ICEM CFD Tutorial Manual.
- Aubreton, J., Fauchais, P., 1983. Influence des potentiels d'interaction sur les propriétés de transport des plasmas thermiques : exemple d'application le plasma argon hydrogène à la pression atmosphérique. *Revue de Physique Appliquée* 18, 51–66. <https://doi.org/10.1051/rphysap:0198300180105100>
- Baeva, M., 2017. Non-equilibrium Modeling of Tungsten-Inert Gas Arcs. *Plasma Chem Plasma Process* 37, 341–370. <https://doi.org/10.1007/s11090-017-9785-y>
- Baeva, M., Uhrlandt, D., 2011. Non-equilibrium simulation of the spatial and temporal behavior of a magnetically rotating arc in argon. *Plasma Sources Sci. Technol.* 20, 035008. <https://doi.org/10.1088/0963-0252/20/3/035008>
- Baksht, F.G., Dyuzhev, G.A., Mitrofanov, N.K., Shkol'nik, S.M., 1997. Experimental investigation of the anode region of a free-burning atmospheric-pressure inert-gas arc. II. Intermediate current regime—multiple anode constriction. *Tech. Phys.* 42, 35–38. <https://doi.org/10.1134/1.1258649>
- Barrault, M.R., Edels, H., Blackburn, T.R., Satyanarayana, P., 1971. Investigation of a Free Burning High Pressure High Current Electric Arc. University of Liverpool, Electr. Eng. Arc. Res. ULAP-T1 (unpublished).
- Benilov, M.S., 2008. Understanding and modelling plasma–electrode interaction in high-pressure arc discharges: a review. *J. Phys. D: Appl. Phys.* 41, 144001. <https://doi.org/10.1088/0022-3727/41/14/144001>
- Benilov, M.S., Almeida, N.A., Baeva, M., Cunha, M.D., Benilova, L.G., Uhrlandt, D., 2016. Account of near-cathode sheath in numerical models of high-pressure arc discharges. *J. Phys. D: Appl. Phys.* 49, 215201. <https://doi.org/10.1088/0022-3727/49/21/215201>

- Benilov, M.S., Bochkarev, G.G., Rogov, B.V., 1995. Modeling of diffuse current transfer in a near-electrode layer of the high-pressure molecular plasma. *IEEE Transactions on Plasma Science* 23, 742–749. <https://doi.org/10.1109/27.467997>
- Benilov, M.S., Carpaij, M., Cunha, M.D., 2006. 3D modelling of heating of thermionic cathodes by high-pressure arc plasmas. *J. Phys. D: Appl. Phys.* 39, 2124–2134. <https://doi.org/10.1088/0022-3727/39/10/024>
- Benilov, M.S., Marotta, A., 1995. A model of the cathode region of atmospheric pressure arcs. *J. Phys. D: Appl. Phys.* 28, 1869–1882. <https://doi.org/10.1088/0022-3727/28/9/015>
- Bernecki, T.F., Varley, K.J., Rusch, W.P., Wlodarczyk, J., Klein, J.F., 1988. Plasma gun with adjustable cathode. US4780591A.
- Beulens, J.J., Milojevic, D., Schram, D.C., Vallinga, P.M., 1991. A two-dimensional nonequilibrium model of cascaded arc plasma flows. *Physics of Fluids B: Plasma Physics* 3, 2548–2557. <https://doi.org/10.1063/1.859967>
- Biagi, S.F., 2004. SCATTERING CROSS SECTIONS. e+Ar. Elastic [WWW Document]. Plasma Data Exchange Project. URL [www.lxcat.net/Biagi-v7.1](http://www.lxcat.net/Biagi-v7.1) (accessed 10.3.19).
- Bobzin, K., Bagcivan, N., Petkovic, I., 2011. Numerical and experimental determination of plasma temperature during air plasma spraying with a multiple cathodes torch. *Journal of Materials Processing Technology* 211, 1620–1628. <https://doi.org/10.1016/j.jmatprotec.2011.05.001>
- Bobzin, K., Öte, M., 2016. Modeling Multi-Arc Spraying Systems. *Journal of Thermal Spray Technology* 25, 920–932. <https://doi.org/10.1007/s11666-016-0407-7>
- Bobzin, K., Öte, M., Knoch, M.A., Heinemann, H., Zimmermann, S., Schein, J., 2019. Influence of external magnetic fields on the coatings of a cascaded plasma generator. *IOP Conf. Ser.: Mater. Sci. Eng.* 480, 012004. <https://doi.org/10.1088/1757-899X/480/1/012004>
- Bobzin, K., Öte, M., Schein, J., Zimmermann, S., Möhwald, K., Lummer, C., 2016. Modelling the Plasma Jet in Multi-Arc Plasma Spraying. *J Therm Spray Tech* 25, 1111–1126. <https://doi.org/10.1007/s11666-016-0438-0>
- Bolot, R., Coddet, C., Allimant, A., Billières, D., 2011. Modeling of the Plasma Flow and Anode Region Inside a Direct Current Plasma Gun. *J Therm Spray Tech* 20, 21–27. <https://doi.org/10.1007/s11666-010-9560-6>
- Bonnefoi, C., Fauchais, P., Université de Limoges, Faculté des sciences et techniques, 1983. Contribution à l'étude des méthodes de résolution de l'équation de Boltzmann dans un plasma à deux températures: exemple le mélange Argon-Hydrogène (Ph.D. dissertation). Université de Limoges, Limoges, France.
- Bora, B., Aomoa, N., Kakati, M., 2010. Characteristics and Temperature Measurement of a Non-Transferred Cascaded DC Plasma Torch. *Plasma Sci. Technol.* 12, 181–187. <https://doi.org/10.1088/1009-0630/12/2/11>
- Boselli, M., Colombo, V., Ghedini, E., Gherardi, M., Sanibondi, P., 2013. Two-temperature modelling and optical emission spectroscopy of a constant current plasma arc welding process. *J. Phys. D: Appl. Phys.* 46, 224009. <https://doi.org/10.1088/0022-3727/46/22/224009>
- Bouaziz, M., 1996. Caractérisation d'un plasma d'arc à la pression atmosphérique au voisinage de l'anode (Ph.D. dissertation). Université Toulouse III - Paul Sabatier, Toulouse, France.
- Boulos, M.I., Fauchais, P., Pfender, E., 1994. *Thermal Plasmas: Fundamentals and Applications*. Springer US.

- Bowman, B., 1972. Convective heat transfer and power balance in high current free-burning arcs. *Electrowarme International* 30, B87–B93.
- Cao, X., Yu, D., Xiang, Y., Yao, J., 2016. Influence of the Gas Injection Angle on the Jet Characteristics of a Non-transferred DC Plasma Torch. *Plasma Chem Plasma Process* 36, 881–889. <https://doi.org/10.1007/s11090-016-9702-9>
- Capetti, A., Pfender, E., 1989. Probe measurements in argon plasma jets operated in ambient argon. *Plasma Chem Plasma Process* 9, 329–341. <https://doi.org/10.1007/BF01054288>
- Cayla, F., Freton, P., Gonzalez, J., 2008. Arc/Cathode Interaction Model. *IEEE Transactions on Plasma Science* 36, 1944–1954. <https://doi.org/10.1109/TPS.2008.927378>
- Chazelas, C., Trelles, J.P., Choquet, I., Vardelle, A., 2017. Main Issues for a Fully Predictive Plasma Spray Torch Model and Numerical Considerations. *Plasma Chem Plasma Process* 37, 627–651. <https://doi.org/10.1007/s11090-017-9808-8>
- Chemartin, L., Lalande, P., Delalandre, C., Cheron, B., Lago, F., 2011. Modelling and simulation of unsteady dc electric arcs and their interactions with electrodes. *J. Phys. D: Appl. Phys.* 44, 194003. <https://doi.org/10.1088/0022-3727/44/19/194003>
- Chen, D.M., Hsu, K.C., Pfender, E., 1981. Two-temperature modeling of an arc plasma reactor. *Plasma Chem Plasma Process* 1, 295–314. <https://doi.org/10.1007/BF00568837>
- Chen, X., Han, P., 1999. On the thermodynamic derivation of the Saha equation modified to a two-temperature plasma. *J. Phys. D: Appl. Phys.* 32, 1711–1718. <https://doi.org/10.1088/0022-3727/32/14/324>
- Choporov, S., 2013. Parallel Computing Technologies in the Finite Element Method. Presented at the Third International Conference “High Performance Computing,” Ukraine, Kyiv, pp. 85–91. <https://doi.org/10.15588/1607-3274-2013-2-15>
- Christen, T., 2010. Comment on ‘What is the mathematical meaning of Steenbeck’s principle of minimum power in gas discharge physics?’. *J. Phys. D: Appl. Phys.* 43, 298001. <https://doi.org/10.1088/0022-3727/43/29/298001>
- Colombo, V., Ghedini, E., Boselli, M., Sanibondi, P., Concetti, A., 2011. 3D static and time-dependent modelling of a dc transferred arc twin torch system. *J. Phys. D: Appl. Phys.* 44, 194005. <https://doi.org/10.1088/0022-3727/44/19/194005>
- Colombo, V., Ghedini, E., Sanibondi, P., 2008. Thermodynamic and transport properties in non-equilibrium argon, oxygen and nitrogen thermal plasmas. *Progress in Nuclear Energy, In Honour of Prof. Bruno Montagnini* 50, 921–933. <https://doi.org/10.1016/j.pnucene.2008.06.002>
- COMSOL Inc., 2019. COMSOL: Multiphysics® [WWW Document]. URL <https://www.comsol.com/> (accessed 11.28.19).
- Cotell, C.M., Sprague, J.A., Smidt, F.A.Jr., 1994. *ASM Handbook, Volume 05*. ASM International.
- Coudert, J.F., Fauchais, P., Vardelle, M., 2002. Diagnostics of Plasma Spray Process and Derived On-Line Control. *HTM* 6. <https://doi.org/10.1615/HighTempMatProc.v6.i2.110>
- Coudert, J.F., Planche, M.P., Fauchais, P., 1995. Characterization of d.c. plasma torch voltage fluctuations. *Plasma Chem Plasma Process* 16, S211–S227. <https://doi.org/10.1007/BF01512636>
- Coudert, J.F., Rat, V., 2008. Influence of configuration and operating conditions on the electric arc instabilities of a plasma spray torch: role of acoustic resonance. *J. Phys. D: Appl. Phys.* 41, 205208. <https://doi.org/10.1088/0022-3727/41/20/205208>

- Coudert, J.F., Rat, V., Rigot, D., 2007. Influence of Helmholtz oscillations on arc voltage fluctuations in a dc plasma spraying torch. *J. Phys. D: Appl. Phys.* 40, 7357–7366. <https://doi.org/10.1088/0022-3727/40/23/016>
- Courant, R., Lewy, H., Friedrichs, K., 1928. Über die partiellen Differenzgleichungen der mathematischen Physik. *Mathematische Annalen* 100, 32–74.
- Cram, L.E., Poladian, L., Roumeliotis, G., 1988. Departures from equilibrium in a free-burning argon arc. *J. Phys. D: Appl. Phys.* 21, 418–425. <https://doi.org/10.1088/0022-3727/21/3/007>
- Cressault, Y., 2001. Propriétés des Plasmas Thermiques dans des Mélanges Argon-Hydrogène-Cuivre (Ph.D. dissertation). Université Toulouse III - Paul Sabatier, Toulouse, France.
- Crowell, C.R., 1965. The Richardson constant for thermionic emission in Schottky barrier diodes. *Solid-State Electronics* 8, 395–399. [https://doi.org/10.1016/0038-1101\(65\)90116-4](https://doi.org/10.1016/0038-1101(65)90116-4)
- Dalir, E., Dolatabadi, A., Mostaghimi, J., 2019. Modeling of Suspension Plasma Spraying Process Including Arc Movement Inside the Torch. *J Therm Spray Tech* 28, 1105–1125. <https://doi.org/10.1007/s11666-019-00883-z>
- Delair, L., Tu, X., Bultel, A., Cheron, B.G., 2005. Helmholtz behavior of a nitrogen plasma arc chamber. *HTM* 9, 583–597. <https://doi.org/10.1615/HighTempMatProc.v9.i4.80>
- Delalondre, C., Zahrai, S., Simonin, O., 1994. Turbulence Modelling in Electric Arc. Presented at the International Symposium on Heat and Mass Transfer under Plasma Conditions, Cesme, Izmir, Turkey.
- Devoto, R.S., 1973. Transport coefficients of ionized argon. *The Physics of Fluids* 16, 616–623. <https://doi.org/10.1063/1.1694396>
- Devoto, R.S., 1967. Transport Coefficients of Partially Ionized Argon. *The Physics of Fluids* 10, 354–364. <https://doi.org/10.1063/1.1762115>
- Devoto, R.S., 1965. The transport properties of a partially ionized monatomic gas. (Ph.D. dissertation). Stanford University, Stanford, CA.
- Douce, A., Delalondre, C., Biausser, H., Guillot, J.-B., 2003. Numerical Modelling of an Anodic Metal Bath Heated with an Argon Transferred Arc. *ISIJ International* 43, 1128–1135. <https://doi.org/10.2355/isijinternational.43.1128>
- Drellishak, K.S., Knopp, C.F., Cambel, A.B., 1963. Partition Functions and Thermodynamic Properties of Argon Plasma. *The Physics of Fluids* 6, 1280–1288. <https://doi.org/10.1063/1.1706896>
- Duan, Z., 2000. Investigations of plasma instabilities in a spray torch (Ph.D. dissertation). University of Minnesota, Minneapolis and Saint Paul, Minnesota, United States.
- Duan, Z., Heberlein, J., 2002. Arc instabilities in a plasma spray torch. *J Therm Spray Tech* 11, 44–51. <https://doi.org/10.1361/105996302770348961>
- Dyuzhev, G.A., Mitrofanov, N.K., Shkol'nik, S.M., 1997. Experimental investigation of the anode region of a free-burning atmospheric-pressure inert-gas arc I. General characteristics of the discharge. Low-current regime. *Tech. Phys.* 42, 30–34. <https://doi.org/10.1134/1.1258648>
- Ecker, G., 1977. Cathode phenomena theory. Experimental studies of plasma torches. Nauka, Siberian Branch, Novosibirsk, in Russian, Ed.by M. F. Zhukov 155–207.
- Ecker, G., 1976. The Vacuum Arc Cathode , - A Phenomenon of Many Aspects. *IEEE Transactions on Plasma Science* 4, 218–227. <https://doi.org/10.1109/TPS.1976.4316971>

- Eddy, T.L., 1985. Electron temperature determination in LTE and non-LTE plasmas. *Journal of Quantitative Spectroscopy and Radiative Transfer* 33, 197–211. [https://doi.org/10.1016/0022-4073\(85\)90149-9](https://doi.org/10.1016/0022-4073(85)90149-9)
- Eddy, T.L., Pfender, E., Eckert, E.R.G., 1973. Spectroscopic Mapping of the Nonequilibrium between Electron and Excitation Temperatures in a 1 ATM Helium ARC. *IEEE Transactions on Plasma Science* 1, 31–42. <https://doi.org/10.1109/TPS.1973.4316111>
- EDF R&D, 2019. Code\_Saturne [WWW Document]. URL <https://www.code-saturne.org/cms/> (accessed 11.28.19).
- EDF R&D, 2017. Code\_Saturne 5.0.0 Theory and Programmer's Guide, In French, Accessed 31 August 2019.
- Elenbaas, W., Kesselring, F., Koppelman, F., 1936. Zur Frage der Berechnung des Minimumprinzips in der Theorie der Bogenentladung (Diskussion). *Elektrotechn. Zeitschr.* 57, 1497.
- Erraki, A., 1999. Etude du transfert radiatif dans les plasmas thermiques : application au SF6 et au mélange argon-fer (Ph.D. dissertation). Université Toulouse III - Paul Sabatier, Toulouse, France.
- Farrall, G.A., 1973. Vacuum arcs and switching, in: *Proceedings of the IEEE*. IEEE, pp. 1113–1136. <https://doi.org/10.1109/PROC.1973.9214>
- Fauchais, P., Etchart-Salas, R., Rat, V., Coudert, J.F., Caron, N., Wittmann-Ténèze, K., 2008. Parameters Controlling Liquid Plasma Spraying: Solutions, Sols, or Suspensions. *J Therm Spray Tech* 17, 31–59. <https://doi.org/10.1007/s11666-007-9152-2>
- Fauchais, P.L., Heberlein, J.V.R., Boulos, M., 2014. *Thermal Spray Fundamentals: From Powder to Part*. Springer US.
- Felipini, C.L., Pimenta, M.M., 2015. Some numerical simulation results of swirling flow in d.c. plasma torch. *J. Phys.: Conf. Ser.* 591, 012038. <https://doi.org/10.1088/1742-6596/591/1/012038>
- Fincke, J.R., Swank, W.D., Snyder, S.C., Haggard, D.C., 1993. Enthalpy probe performance in compressible thermal plasma jets. *Review of Scientific Instruments* 64, 3585–3593. <https://doi.org/10.1063/1.1144285>
- Finkelburg, W., Maecker, H., 1956. Elektrische Bögen und thermisches Plasma. *Handbuch der Physik* 22, 254–444. [https://doi.org/10.1007/978-3-642-45847-7\\_4](https://doi.org/10.1007/978-3-642-45847-7_4)
- Fomenko, V.S., 1981. *Emission Properties of Materials*. Naukova Dumka, in Russian, Kiev.
- Freton, P., Gonzalez, J.-J., Escalier, G., 2009. Prediction of the cathodic arc root behaviour in a hollow cathode thermal plasma torch. *J. Phys. D: Appl. Phys.* 42, 195205. <https://doi.org/10.1088/0022-3727/42/19/195205>
- Freton, P., Gonzalez, J.J., Masquère, M., Reichert, F., 2011. Magnetic field approaches in dc thermal plasma modelling. *J. Phys. D: Appl. Phys.* 44, 345202. <https://doi.org/10.1088/0022-3727/44/34/345202>
- Freton, P., Gonzalez, J.J., Ranarijaona, Z., Mougnot, J., 2012. Energy equation formulations for two-temperature modelling of 'thermal' plasmas. *J. Phys. D: Appl. Phys.* 45, 465206. <https://doi.org/10.1088/0022-3727/45/46/465206>
- Fu, C., Zhang, W., 2006. Parallel computing for finite element structural analysis using conjugate gradient method based on domain decomposition. *J. of Shanghai Univ.* 10, 517–521. <https://doi.org/10.1007/s11741-006-0049-y>
- Girard, R., Belhaouari, J.B., Gonzalez, J.J., Gleizes, A., 1999. A two-temperature kinetic model of SF6 plasma. *J. Phys. D: Appl. Phys.* 32, 2890–2901. <https://doi.org/10.1088/0022-3727/32/22/311>

- Gleizes, A., Chervy, B., Gonzalez, J.J., 1999. Calculation of a two-temperature plasma composition: bases and application to SF<sub>6</sub>. *J. Phys. D: Appl. Phys.* 32, 2060–2067. <https://doi.org/10.1088/0022-3727/32/16/315>
- Gomes, A.M., 1983. Criteria for partial LTE in an argon thermal discharge at atmospheric pressure validity of the spectroscopically measured electronic temperature. *J. Phys. D: Appl. Phys.* 16, 357–378. <https://doi.org/10.1088/0022-3727/16/3/019>
- Gonzalez, J.-J., 1992. Modélisation d'un arc transféré de forte puissance (1 méga-watt) (Ph.D. dissertation). Université Toulouse III - Paul Sabatier, Toulouse, France.
- Gonzalez, J.J., Cayla, F., Freton, P., Teulet, P., 2009. Two-dimensional self-consistent modelling of the arc/cathode interaction. *J. Phys. D: Appl. Phys.* 42, 145204. <https://doi.org/10.1088/0022-3727/42/14/145204>
- Goodfellow, K.D., Polk, J.E., 1993. High Current Cathode Thermal Behavior, Part I: Theory. IEPC-93-030 305–318.
- Griem, H.R., 1964. Plasma spectroscopy. McGraw-Hill, New York.
- Griem, H.R., 1963. Validity of Local Thermal Equilibrium in Plasma Spectroscopy. *Phys. Rev.* 131, 1170–1176. <https://doi.org/10.1103/PhysRev.131.1170>
- GTV GmbH, n.d. GTV DELTA plasma torch. Process optimization by 3 anode / 1 cathode technique [WWW Document]. URL [https://www.gtv-mbh.com/cms/upload/downloads/en/productinformation/GTV\\_Delta\\_Plasmabrenner\\_en.pdf](https://www.gtv-mbh.com/cms/upload/downloads/en/productinformation/GTV_Delta_Plasmabrenner_en.pdf) (accessed 8.6.19).
- GTV Verschleiss-Schutz [WWW Document], 2019. URL [https://www.gtv-mbh.com/\\_old/gtv-mbh-englisch/www.gtv-mbh.de/cms/front\\_content5e33.html?idcat=82](https://www.gtv-mbh.com/_old/gtv-mbh-englisch/www.gtv-mbh.de/cms/front_content5e33.html?idcat=82) (accessed 7.24.19).
- Guo, Z., Yin, S., Qian, Z., Liao, H., Gu, S., 2015. Effect of the deviation of the current density profile center on the three-dimensional non-transferred arc plasma torch. *Computers & Fluids* 114, 163–171. <https://doi.org/10.1016/j.compfluid.2015.03.003>
- Haidar, J., 1999. Non-equilibrium modelling of transferred arcs. *J. Phys. D: Appl. Phys.* 32, 263–272. <https://doi.org/10.1088/0022-3727/32/3/014>
- Han, P., Chen, X., 2001. Modeling of the Subsonic–Supersonic Flow and Heat Transfer in a DC Arc Plasma Torch. *Plasma Chemistry and Plasma Processing* 21, 249–264. <https://doi.org/10.1023/A:1007000431702>
- Harris, W.J., 2002. A study of cathode erosion in high power arcjets (Ph.D. dissertation). Texas Tech University, Lubbock, TX, USA.
- Hartmann, R.M., Heberlein, J.V., 2001. Quantitative investigations on arc-anode attachments in transferred arcs. *J. Phys. D: Appl. Phys.* 34, 2972–2978. <https://doi.org/10.1088/0022-3727/34/19/307>
- Hawley, D., 2006. Method of fixing anodic arc attachments of a multiple arc plasma gun and nozzle device for same. US7030336B1.
- Hingana, H., 2010. Contribution à l'étude des propriétés des plasmas à deux températures : application à l'argon et l'air (Ph.D. dissertation). Université Toulouse III - Paul Sabatier, Toulouse, France.
- Hirschfelder, J.O., Curtiss, C.F., Bird, R.B., 1964. Molecular theory of gases and liquids. Wiley, New York.
- Huang, R., Fukanuma, H., Uesugi, Y., Tanaka, Y., 2013. Comparisons of Two Models for the Simulation of a DC Arc Plasma Torch. *J Therm Spray Tech* 22, 183–191. <https://doi.org/10.1007/s11666-012-9860-0>

- Huang, R., Fukanuma, H., Uesugi, Y., Tanaka, Y., 2012. Simulation of Arc Root Fluctuation in a DC Non-Transferred Plasma Torch with Three Dimensional Modeling. *J Therm Spray Tech* 21, 636–643. <https://doi.org/10.1007/s11666-011-9710-5>
- Huang, R., Fukanuma, H., Uesugi, Y., Tanaka, Y., 2011. An Improved Local Thermal Equilibrium Model of DC Arc Plasma Torch. *IEEE Transactions on Plasma Science* 39, 1974–1982. <https://doi.org/10.1109/TPS.2011.2163828>
- Hülsmann, H.G., Mentel, J., 1987. Experimental investigation of the helical magnetic instability of an arc discharge in an axial magnetic field and comparison with theory. *The Physics of Fluids* 30, 2274–2279. <https://doi.org/10.1063/1.866162>
- Incropera, F.P., DeWitt, D.P., 1990. *Fundamentals of heat and mass transfer*, 3rd ed. ed. New York : Wiley.
- Javidi Shirvan, A., Choquet, I., Nilsson, H., Jasak, H., 2018. Coupling boundary condition for high-intensity electric arc attached on a non-homogeneous refractory cathode. *Computer Physics Communications* 222, 31–45. <https://doi.org/10.1016/j.cpc.2017.09.010>
- Jenista, J., Heberlein, V.R., Pfender, E., 1997. Numerical model of the anode region of high-current electric arcs. *IEEE Transactions on Plasma Science* 25, 883–890. <https://doi.org/10.1109/27.649585>
- Jin Myung Park, Keun Su Kim, Tae Hyung Hwang, Sang Hee Hong, 2004. Three-dimensional modeling of arc root rotation by external magnetic field in nontransferred thermal plasma torches. *IEEE Transactions on Plasma Science* 32, 479–487. <https://doi.org/10.1109/TPS.2004.828125>
- Kannappan, D., Bose, T.K., 1977. Transport properties of a two-temperature argon plasma. *The Physics of Fluids* 20, 1668–1673. <https://doi.org/10.1063/1.861788>
- Kelkar, M., Heberlein, J., 2000. Physics of an arc in cross flow. *J. Phys. D: Appl. Phys.* 33, 2172–2182. <https://doi.org/10.1088/0022-3727/33/17/312>
- Khrabry, A., Kaganovich, I.D., Nemchinsky, V., Khodak, A., 2018. Investigation of the short argon arc with hot anode. I. Numerical simulations of non-equilibrium effects in the near-electrode regions. *Physics of Plasmas* 25, 013521. <https://doi.org/10.1063/1.5007082>
- Kimblin, C.W., 1974. Cathode spot erosion and ionization phenomena in the transition from vacuum to atmospheric pressure arcs. *Journal of Applied Physics* 45, 5235–5244. <https://doi.org/10.1063/1.1663222>
- Kimblin, C.W., 1971. Vacuum arc ion currents and electrode phenomena. *Proceedings of the IEEE* 59, 546–555. <https://doi.org/10.1109/PROC.1971.8215>
- Kiziroglou, M.E., Li, X., Zhukov, A.A., de Groot, P.A.J., de Groot, C.H., 2008. Thermionic field emission at electrodeposited Ni–Si Schottky barriers. *Solid-State Electronics* 52, 1032–1038. <https://doi.org/10.1016/j.sse.2008.03.002>
- Kovbasyuk, V.I., Benilov, M.S., Bochkarev, G.G., Buznikov, A.E., 1986. Analysis of the characteristics of a diffuse discharge in the near-anode boundary-layer of an MHD generator. *Thermophysics of High Temperature*, in Russian 24, 1049–1054.
- Kramida, A., Ralchenko, Y., Reader, J., 2018. NIST: Atomic Spectra Database - Energy Levels Form [WWW Document]. URL [https://physics.nist.gov/PhysRefData/ASD/levels\\_form.html](https://physics.nist.gov/PhysRefData/ASD/levels_form.html) (accessed 9.21.19).
- Lago, F., Gonzalez, J.J., Freton, P., Gleizes, A., 2004. A numerical modelling of an electric arc and its interaction with the anode: Part I. The two-dimensional model. *J. Phys. D: Appl. Phys.* 37, 883–897. <https://doi.org/10.1088/0022-3727/37/6/013>



- Landes, K., 2006. Diagnostics in plasma spraying techniques. *Surface and Coatings Technology*, The 2nd International Meeting on Thermal Spraying 201, 1948–1954. <https://doi.org/10.1016/j.surfcoat.2006.04.036>
- Landes, K., 1994. Plasma spray apparatus for spraying powdery or gaseous material. US5332885A.
- Landes, K., 1993. Plasma spray apparatus for spraying powdery or gaseous material. US5225652A.
- Landes, K.D., Dzulko, M., Theophile, E., Zierhut, J., 2002. NEW DEVELOPMENTS IN DC-PLASMA TORCHES. *HTM* 6. <https://doi.org/10.1615/HighTempMatProc.v6.i3.70>
- Leblanc, L., Moreau, C., 2002. The long-term stability of plasma spraying. *J Therm Spray Tech* 11, 380–386. <https://doi.org/10.1361/105996302770348772>
- Lebouvier, A., Delalondre, C., Fresnet, F., Boch, V., Rohani, V., Cauneau, F., Fulcheri, L., 2011. Three-Dimensional Unsteady MHD Modeling of a Low-Current High-Voltage Nontransferred DC Plasma Torch Operating With Air. *IEEE Transactions on Plasma Science* 39, 1889–1899. <https://doi.org/10.1109/TPS.2011.2160208>
- Li, H.-P., Pfender, E., 2007. Three Dimensional Modeling of the Plasma Spray Process. *J Therm Spray Tech* 16, 245–260. <https://doi.org/10.1007/s11666-007-9023-x>
- Li, H.-P., Pfender, E., Chen, X., 2003. Application of Steenbeck's minimum principle for three-dimensional modelling of DC arc plasma torches. *J. Phys. D: Appl. Phys.* 36, 1084–1096. <https://doi.org/10.1088/0022-3727/36/9/306>
- Liang, P., Groll, R., 2018. Numerical Study of Plasma–Electrode Interaction During Arc Discharge in a DC Plasma Torch. *IEEE Transactions on Plasma Science* 46, 363–372. <https://doi.org/10.1109/TPS.2017.2786079>
- Lisnyak, M., 2018. Theoretical, numerical and experimental study of DC and AC electric arcs (Ph.D. dissertation). Université d'Orléans, Laboratoire GREMI – Groupe de Recherche sur l'Énergétique des Milieux Ionisés, Orléans, France.
- Lisnyak, M., Cunha, M.D., Bauchire, J.-M., Benilov, M.S., 2017. Numerical modelling of high-pressure arc discharges: matching the LTE arc core with the electrodes. *J. Phys. D: Appl. Phys.* 50, 315203. <https://doi.org/10.1088/1361-6463/aa76d3>
- Lowke, J.J., 1974. Predictions of arc temperature profiles using approximate emission coefficients for radiation losses. *Journal of Quantitative Spectroscopy and Radiative Transfer* 14, 111–122. [https://doi.org/10.1016/0022-4073\(74\)90004-1](https://doi.org/10.1016/0022-4073(74)90004-1)
- Lowke, J.J., Kovitya, P., Schmidt, H.P., 1992. Theory of free-burning arc columns including the influence of the cathode. *J. Phys. D: Appl. Phys.* 25, 1600–1606. <https://doi.org/10.1088/0022-3727/25/11/006>
- Lowke, J.J., Ludwig, H.C., 1975. A simple model for high-current arcs stabilized by forced convection. *Journal of Applied Physics* 46, 3352–3360. <https://doi.org/10.1063/1.322239>
- Lowke, J.J., Morrow, R., Haidar, J., 1997. A simplified unified theory of arcs and their electrodes. *J. Phys. D: Appl. Phys.* 30, 2033–2042. <https://doi.org/10.1088/0022-3727/30/14/011>
- Lowke, J.J., Tanaka, M., 2006. 'LTE-diffusion approximation' for arc calculations. *J. Phys. D: Appl. Phys.* 39, 3634–3643. <https://doi.org/10.1088/0022-3727/39/16/017>
- Maecker, H., 2009. *The Electric Arc. The Physics of Stationary Gas Discharges near Thermal Equilibrium*. H Popp Matlab GmbH, D 82335 Berg.
- Maecker, H., 1955. Plasmaströmungen in Lichtbögen infolge eigenmagnetischer Kompression. *Z. Physik* 141, 198–216. <https://doi.org/10.1007/BF01327300>

- Maecker, H.H., Stablein, H.G., 1986. What Keeps an Arc Standing in a Cross Flow? *IEEE Transactions on Plasma Science* 14, 291–299. <https://doi.org/10.1109/TPS.1986.4316554>
- Marqués, J.L., Forster, G., Schein, J., 2009. Multi-Electrode Plasma Torches: Motivation for Development and Current State-of-the-Art. *The Open Plasma Physics Journal* 2. <https://doi.org/10.2174/1876534300902010089>
- Mason, E.A., Munn, R.J., Smith, F.J., 1967. Transport Coefficients of Ionized Gases. *The Physics of Fluids* 10, 1827–1832. <https://doi.org/10.1063/1.1762365>
- Mauer, G., Vaßen, R., Stöver, D., 2011. Plasma and Particle Temperature Measurements in Thermal Spray: Approaches and Applications. *J Therm Spray Tech* 20, 391–406. <https://doi.org/10.1007/s11666-010-9603-z>
- Mentel, J., 1977. Magnetic Instability of Electric Arc. The theory of the electric arc under condition of forced heat exchange. *Nauka, Siberian Branch, Novosibirsk*, in Russian, Ed. by M. F. Zhukov 182–205.
- Mitchner, M., Kruger, C., 1973. Partially ionized gases, 1st ed, Wiley series in plasma physics. New York : Wiley.
- Mitrofanov, N.K., Shkol'nik, S.M., 2007. Two forms of attachment of an atmospheric-pressure direct-current arc in argon to a thermionic cathode. *Tech. Phys.* 52, 711–720. <https://doi.org/10.1134/S1063784207060060>
- Modirkhazeni, S.M., Trelles, J.P., 2018. Non-transferred Arc Torch Simulation by a Non-equilibrium Plasma Laminar-to-Turbulent Flow Model. *J Therm Spray Tech* 27, 1447–1464. <https://doi.org/10.1007/s11666-018-0765-4>
- Molz, R., McCullough, R., Hawley, D., Muggli, F., 2007. Improvement of Plasma Gun Performance Using Comprehensive Fluid Element Modeling II. *J Therm Spray Tech* 16, 684–689. <https://doi.org/10.1007/s11666-007-9100-1>
- Moreau, E., Chazelas, C., Mariaux, G., Vardelle, A., 2006. Modeling the restrike mode operation of a DC plasma spray torch. *J Therm Spray Tech* 15, 524–530. <https://doi.org/10.1361/105996306X147306>
- Mostaghimi, J., Pershin, L., Yugeswaran, S., 2017. Heat Transfer in DC AND RF Plasma Torches, in: Kulacki, F.A. (Ed.), *Handbook of Thermal Science and Engineering*. Springer International Publishing, Cham, pp. 1–76. [https://doi.org/10.1007/978-3-319-32003-8\\_27-1](https://doi.org/10.1007/978-3-319-32003-8_27-1)
- Muckenfuss, C., Curtiss, C.F., 1958. Thermal Conductivity of Multicomponent Gas Mixtures. *J. Chem. Phys.* 29, 1273–1277. <https://doi.org/10.1063/1.1744709>
- Muggli, F.A., Molz, R.J., McCullough, R., Hawley, D., 2007. Improvement of Plasma Gun Performance Using Comprehensive Fluid Element Modeling: Part I. *J Therm Spray Tech* 16, 677–683. <https://doi.org/10.1007/s11666-007-9098-4>
- Murphy, A.B., 2000. Transport Coefficients of Hydrogen and Argon–Hydrogen Plasmas. *Plasma Chemistry and Plasma Processing* 20, 279–297. <https://doi.org/10.1023/A:1007099926249>
- Murphy, A.B., Park, H., 2017. Modeling of Thermal Plasma Processes: The Importance of Two-Way Plasma-Surface Interactions. *Plasma Processes and Polymers* 14, 1600177. <https://doi.org/10.1002/ppap.201600177>
- Nemchinskii, V.A., Peretts, L.N., 1977. Anode sheath in a high-pressure, high-current arc. *Zhurnal Tekhnicheskoi Fiziki*, in Russian 47, 1868–1875.

- Nemchinsky, V., 2016. A Method to Reduce Electrode Erosion in a Magnetically Driven Rotating Arc. *IEEE Transactions on Plasma Science* 44, 3474–3478. <https://doi.org/10.1109/TPS.2016.2628885>
- Nemchinsky, V., 2015. On Conductivity of Cold Gas Layer Separating Arc Column and Nozzle in Nontransferred Plasma Arc (Anode Reattachment Process in Plasma Spray Systems). *IEEE Transactions on Plasma Science* 43, 2715–2720. <https://doi.org/10.1109/TPS.2015.2450012>
- Nemchinsky, V., 2014. Erosion of Thermionic Cathodes in Welding and Plasma Arc Cutting Systems. *Plasma Science, IEEE Transactions on* 42, 199–215. <https://doi.org/10.1109/TPS.2013.2287794>
- Neumann, W., 1987. *The Mechanism of the Thermoemitting Arc Cathode*. Akademie-Verlag, Berlin.
- Neumann, W., 1977. Electrode processes in high pressure gas discharge. Experimental studies of plasma torches. Nauka, Siberian Branch, Novosibirsk, in Russian, Ed.by M. F. Zhukov 253–292.
- Neumann, W., 1976. Influence of Cooling Conditions on Anode Behavior in a Nitrogen Plasma Jet Design. *Beiträge aus der Plasmaphysik* 16, 97–109. <https://doi.org/10.1002/ctpp.19760160204>
- Neumann, W., 1969. Der Katodenmechanismus von Hochdruckbögen. *Beiträge aus der Plasmaphysik* 9, 499–526. <https://doi.org/10.1002/ctpp.19690090607>
- Nottingham, W.B., 1956. Thermionic Emission, in: Nottingham, W.B., Good, R.H., Müller, E.W., Kollath, R., Weissler, G.L., Allis, W.P., Loeb, L.B., von Engel, A., Little, P.F. (Eds.), *Electron-Emission Gas Discharges I / Elektronen-Emission Gasentladungen I*, *Encyclopedia of Physics / Handbuch Der Physik*. Springer, Berlin, Heidelberg, pp. 1–175. [https://doi.org/10.1007/978-3-642-45844-6\\_1](https://doi.org/10.1007/978-3-642-45844-6_1)
- Ondac, P., Maslani, A., Hrabovsky, M., 2016. Investigation of the Arc-Anode Attachment Area by Utilizing a High-Speed Camera. *Plasma Physics and Technology Volume 3*, 1–4.
- Paik, S., Huang, P.C., Heberlein, J., Pfender, E., 1993. Determination of the arc-root position in a DC plasma torch. *Plasma Chem Plasma Process* 13, 379–397. <https://doi.org/10.1007/BF01465872>
- Paschen, P., 1996. Alternatives to thorium additions to tungsten-based materials. *JOM* 48, 45–47. <https://doi.org/10.1007/BF03221362>
- Patankar, S., 1980. *Numerical Heat Transfer and Fluid Flow*. Hemisphere Publishing Corporation, Washington, D.C.
- Peters, Th., 1956. Über den Zusammenhang des Steenbeckschen Minimumprinzips mit dem thermodynamischen Prinzip der minimalen Entropieerzeugung. *Z. Physik* 144, 612–631. <https://doi.org/10.1007/BF01327656>
- Pfender, E., Fincke, J., Spores, R., 1991. Entrainment of cold gas into thermal plasma jets. *Plasma Chem Plasma Process* 11, 529–543. <https://doi.org/10.1007/BF01447164>
- Pfender, E., Heberlein, J., 2007. Heat Transfer Processes and Modeling of Arc Discharges, in: Fridman, A., Cho, Y.I., Greene, G.A., Bar-Cohen, A. (Eds.), *Advances in Heat Transfer*. Elsevier, pp. 345–450. [https://doi.org/10.1016/S0065-2717\(07\)40004-1](https://doi.org/10.1016/S0065-2717(07)40004-1)
- Piqueras, L., Henry, D., Jeandel, D., Scott, J., Wild, J., 2008. Three-dimensional modelling of electric-arc development in a low-voltage circuit-breaker. *International Journal of Heat and Mass Transfer* 51, 4973–4984. <https://doi.org/10.1016/j.ijheatmasstransfer.2008.02.035>

- Planche, M.-P., 1995. Contribution à l'étude des fluctuations dans une torche à plasma. Application à la dynamique de l'arc et aux mesures de vitesse d'écoulement (Ph.D. dissertation). Limoges.
- Planche, M.P., Coudert, J.F., Fauchais, P., 1998. Velocity Measurements for Arc Jets Produced by a DC Plasma Spray Torch. *Plasma Chemistry and Plasma Processing* 18, 263–283. <https://doi.org/10.1023/A:1021606701022>
- Potapov, A.V., 1966. Chemical equilibrium of multi-temperature systems *High Temp.* 4 48–51. *Thermophysics of High Temperature*, in Russian 4, 55–58.
- Prevosto, L., Kelly, H., Mancinelli, B., Chamorro, J.C., 2015. On the Gas Heating Mechanism for the Fast Anode Arc Reattachment in a Non-transferred Arc Plasma Torch Operating with Nitrogen Gas in the Restrike Mode. *Plasma Chem Plasma Process* 35, 1057–1070. <https://doi.org/10.1007/s11090-015-9644-7>
- Rahmane, M., Soucy, G., Boulos, M.I., 1995. Analysis of the enthalpy probe technique for thermal plasma diagnostics. *Review of Scientific Instruments* 66, 3424–3431. <https://doi.org/10.1063/1.1145517>
- Ramakrishnan, S., 1995. Technological challenges in thermal plasma production. *Australian Journal of Physics* 48, 377. <https://doi.org/10.1071/PH950377>
- Rat, V., Coudert, J.F., 2011. Improvement of Plasma Spray Torch Stability by Controlling Pressure and Voltage Dynamic Coupling. *J Therm Spray Tech* 20, 28–38. <https://doi.org/10.1007/s11666-010-9555-3>
- Rat, V., Coudert, J.F., 2010a. Acoustic stabilization of electric arc instabilities in nontransferred plasma torches. *Appl. Phys. Lett.* 96, 101503. <https://doi.org/10.1063/1.3354007>
- Rat, V., Coudert, J.F., 2010b. Pressure and arc voltage coupling in dc plasma torches: Identification and extraction of oscillation modes. *Journal of Applied Physics* 108, 043304. <https://doi.org/10.1063/1.3466982>
- Rat, V., Mavier, F., Coudert, J.F., 2017. Electric Arc Fluctuations in DC Plasma Spray Torch. *Plasma Chem Plasma Process* 37, 549–580. <https://doi.org/10.1007/s11090-017-9797-7>
- Reimann, A.L., 1934. *Thermionic Emission*. Chapman & Hall, Ltd., London.
- Rhie, C.M., Chow, W.L., 1983. Numerical study of the turbulent flow past an airfoil with trailing edge separation. *AIAA Journal* 21, 1525–1532. <https://doi.org/10.2514/3.8284>
- Saad, Y., Schultz, M., 1986. GMRES: A Generalized Minimal Residual Algorithm for Solving Nonsymmetric Linear Systems. *SIAM J. Sci. and Stat. Comput.* 7, 856–869. <https://doi.org/10.1137/0907058>
- Saifutdinov, A.I., Timerkaev, B.A., Ibragimov, A.R., 2018. Numerical Simulation of Temperature Fields in a Direct-Current Plasma Torch. *Tech. Phys. Lett.* 44, 164–166. <https://doi.org/10.1134/S1063785018020281>
- Sanders, N.A., Pfender, E., 1984. Measurement of anode falls and anode heat transfer in atmospheric pressure high intensity arcs. *Journal of Applied Physics* 55, 714–722. <https://doi.org/10.1063/1.333129>
- Sansonens, L., Haidar, J., Lowke, J.J., 2000. Prediction of properties of free burning arcs including effects of ambipolar diffusion. *J. Phys. D: Appl. Phys.* 33, 148–157. <https://doi.org/10.1088/0022-3727/33/2/309>
- Schlitz, L.Z., Garimella, S.V., Chan, S.H., 1999a. Gas dynamics and electromagnetic processes in high-current arc plasmas. Part I. Model formulation and steady-state solutions. *Journal of Applied Physics* 85, 2540–2546. <https://doi.org/10.1063/1.369572>

- Schlitz, L.Z., Garimella, S.V., Chan, S.H., 1999b. Gas dynamics and electromagnetic processes in high-current arc plasmas. Part II. Effects of external magnetic fields and gassing materials. *Journal of Applied Physics* 85, 2547–2555. <https://doi.org/10.1063/1.369573>
- Selvan, B., Ramachandran, K., Sreekumar, K.P., Thiyagarajan, T.K., Ananthapadmanabhan, P.V., 2009. Numerical and experimental studies on DC plasma spray torch. *Vacuum* 84, 444–452. <https://doi.org/10.1016/j.vacuum.2009.09.009>
- Shannon, J.M., Nieuwesteeg, K.J.B.M., 1993. Tunneling effective mass in hydrogenated amorphous silicon. *Appl. Phys. Lett.* 62, 1815–1817. <https://doi.org/10.1063/1.109558>
- Speckhofer, G., Schmidt, H.-, 1996. Experimental and theoretical investigation of high-pressure arcs. II. The magnetically deflected arc (three-dimensional modeling). *IEEE Transactions on Plasma Science* 24, 1239–1248. <https://doi.org/10.1109/27.536571>
- Steenbeck, M., 1932. Energetik der Gasentladungen. *Physikalische Zeitschrift* 33, 809–815.
- Straeter, T.A., 1971. On the Extension of the Davidon-Broyden Class of Rank One, Quasi-Newton Minimization Methods to an Infinite Dimensional Hilbert Space with Applications to Optimal Control Problems (Ph.D. dissertation). North Carolina State Univ, Raleigh, NC, United States.
- Sun, X., Heberlein, J., 2005. Fluid dynamic effects on plasma torch anode erosion. *J Therm Spray Tech* 14, 39–44. <https://doi.org/10.1361/10599630522404>
- Tanaka, M., Ushio, M., 1999. Observations of the anode boundary layer in free-burning argon arcs. *J. Phys. D: Appl. Phys.* 32, 906–912. <https://doi.org/10.1088/0022-3727/32/8/011>
- Tanaka, M., Ushio, M., Wu, C.S., 1999. One-dimensional analysis of the anode boundary layer in free-burning argon arcs. *J. Phys. D: Appl. Phys.* 32, 605–611. <https://doi.org/10.1088/0022-3727/32/5/016>
- Tolias, P., 2017. Analytical expressions for thermophysical properties of solid and liquid tungsten relevant for fusion applications. *Nuclear Materials and Energy* 13, 42–57. <https://doi.org/10.1016/j.nme.2017.08.002>
- Transparency Market Research, 2018. High Performance Ceramic Coatings Market: Global Industry Analysis, Size, Share, Growth, Trends, and Forecast, 2017–2025 (No. TMRGL37931). Pune 411045 India.
- Trelles, J.P., 2007. Finite element modeling of flow instabilities in arc plasma torches (Ph.D. dissertation). University of Minnesota, Minneapolis and Saint Paul, Minnesota, United States.
- Trelles, J.P., Heberlein, J.V.R., Pfender, E., 2007. Non-equilibrium modelling of arc plasma torches. *J. Phys. D: Appl. Phys.* 40, 5937–5952. <https://doi.org/10.1088/0022-3727/40/19/024>
- Trelles, J.P., Modirkhazeni, S.M., 2014. Variational multiscale method for nonequilibrium plasma flows. *Computer Methods in Applied Mechanics and Engineering* 282, 87–131. <https://doi.org/10.1016/j.cma.2014.09.001>
- Trelles, J.P., Pfender, E., Heberlein, J., 2006. Multiscale Finite Element Modeling of Arc Dynamics in a DC Plasma Torch. *Plasma Chem Plasma Process* 26, 557–575. <https://doi.org/10.1007/s11090-006-9023-5>
- Tucker, R.C.Jr., 2013. *ASM Handbook, Volume 5A: Thermal Spray Technology* - ASM International. ASM International, Materials Park, Ohio.
- Vacquie, S., 2000. *L'arc électrique*, 1st ed, Sciences et techniques de l'ingénieur. Éditions Eyrolles.

- van de Sanden, M.C.M., Schram, P.P.J.M., 1991. Generalized law of mass action for a two-temperature plasma. *Phys. Rev. A* 44, 5150–5157. <https://doi.org/10.1103/PhysRevA.44.5150>
- van de Sanden, M.C.M., Schram, P.P.J.M., Peeters, A.G., van der Mullen, J.A.M., Kroesen, G.M.W., 1989. Thermodynamic generalization of the Saha equation for a two-temperature plasma. *Physical Review A* 40, 5273–5276. <https://doi.org/10.1103/PhysRevA.40.5273>
- Vardelle, A., Moreau, C., Akedo, J., Ashrafizadeh, H., Berndt, C.C., Berghaus, J.O., Boulos, M., Brogan, J., Bourtsalas, A.C., Dolatabadi, A., Dorfman, M., Eden, T.J., Fauchais, P., Fisher, G., Gaertner, F., Gindrat, M., Henne, R., Hyland, M., Irissou, E., Jordan, E.H., Khor, K.A., Killinger, A., Lau, Y.-C., Li, C.-J., Li, L., Longtin, J., Markocsan, N., Masset, P.J., Matejicek, J., Mauer, G., McDonald, A., Mostaghimi, J., Sampath, S., Schiller, G., Shinoda, K., Smith, M.F., Syed, A.A., Themelis, N.J., Toma, F.-L., Trelles, J.P., Vassen, R., Vuoristo, P., 2016. The 2016 Thermal Spray Roadmap. *J Therm Spray Tech* 25, 1376–1440. <https://doi.org/10.1007/s11666-016-0473-x>
- Vardelle, A., Moreau, C., Themelis, N.J., Chazelas, C., 2015. A Perspective on Plasma Spray Technology. *Plasma Chem Plasma Process* 35, 491–509. <https://doi.org/10.1007/s11090-014-9600-y>
- Vardelle, M., Fauchais, P., Vardelle, A., Li, K.-I., Dussoubs, B., Themelis, N.J., 2001. Controlling particle injection in plasma spraying. *J Therm Spray Tech* 10, 267–284. <https://doi.org/10.1361/105996301770349367>
- Venkatramani, N., 2002. Industrial plasma torches and applications. *Current Science* 83, 254–262.
- Wang, C., Sun, L., Sun, Q., Zhang, Z., Xia, Weiluo, Xia, Weidong, 2019a. Experimental Observations of Constricted and Diffuse Anode Attachment in a Magnetically Rotating Arc at Atmospheric Pressure. *Plasma Chem Plasma Process* 39, 407–421. <https://doi.org/10.1007/s11090-019-09954-z>
- Wang, C., Sun, Q., Sun, L., Lu, Z., Xia, Weiluo, Xia, Weidong, 2019b. Spot and diffuse mode of cathode attachments in a magnetically rotating arc plasma generator at atmospheric pressure. *Journal of Applied Physics* 125, 033301. <https://doi.org/10.1063/1.5081113>
- Westhoff, R., Szekely, J., 1991. A model of fluid, heat flow, and electromagnetic phenomena in a nontransferred arc plasma torch. *Journal of Applied Physics* 70, 3455–3466. <https://doi.org/10.1063/1.349238>
- Wright, D.A., 1953. A survey of present knowledge of thermionic emitters. *Proceedings of the IEE - Part III: Radio and Communication Engineering* 100, 125–139. <https://doi.org/10.1049/pi-3.1953.0030>
- Wutzke, S.A., Pfender, E., Eckert, E.R.G., 1968. Symptomatic behavior of an electric arc with a superimposed flow. *AIAA Journal* 6, 1474–1482. <https://doi.org/10.2514/3.4791>
- Wutzke, S.A., Pfender, E., Eckert, E.R.G., 1967. Study of electric arc behavior with superimposed flow. *AIAA Journal* 5, 707–713. <https://doi.org/10.2514/3.4051>
- Yang, G., Cronin, P., Heberlein, J.V., Pfender, E., 2006. Experimental investigations of the anode boundary layer in high intensity arcs with cross flow. *J. Phys. D: Appl. Phys.* 39, 2764–2774. <https://doi.org/10.1088/0022-3727/39/13/020>
- Yang, G., Heberlein, J., 2007a. Instabilities in the anode region of atmospheric pressure arc plasmas. *Plasma Sources Sci. Technol.* 16, 765–773. <https://doi.org/10.1088/0963-0252/16/4/011>

- Yang, G., Heberlein, J., 2007b. Anode attachment modes and their formation in a high intensity argon arc. *Plasma Sources Sci. Technol.* 16, 529–542. <https://doi.org/10.1088/0963-0252/16/3/012>
- Yershow, A.V., Panevin, I.G., 1973. Negative anodic drop of potential in arc discharges. Presented at the Proc. 21th Intern.Conf. on Phenomena in Ionized Gases, Praha, p. 83.
- Yin, F., Hu, S., Yu, C., Li, L., 2007. Computational simulation for the constricted flow of argon plasma arc. *Computational Materials Science* 40, 389–394. <https://doi.org/10.1016/j.commatsci.2007.01.008>
- Yuan, X.Q., Li, H., Zhao, T.Z., Wang, F., Guo, W.K., Xu, P., 2004. Comparative Study of Flow Characteristics Inside Plasma Torch with Different Nozzle Configurations. *Plasma Chem Plasma Process* 24, 585–601. <https://doi.org/10.1007/s11090-004-7934-6>
- Yuen, M.C., 1966. Stability of the Poiseuille Plasma Arc in an Axial Magnetic Field. *Physics of Fluids* 9, 1140–1150. <https://doi.org/10.1063/1.1761813>
- Zang, Y., Street, R.L., Koseff, J.R., 1994. A Non-staggered Grid, Fractional Step Method for Time-Dependent Incompressible Navier-Stokes Equations in Curvilinear Coordinates. *Journal of Computational Physics* 114, 18–33. <https://doi.org/10.1006/jcph.1994.1146>
- Zhang, D., Zheng, L., Hu, X., Zhang, H., 2016. Numerical studies of arc plasma generation in single cathode and three-cathode plasma torch and its impact on plasma spraying. *International Journal of Heat and Mass Transfer* 98, 508–522. <https://doi.org/10.1016/j.ijheatmasstransfer.2016.03.038>
- Zhou, X., Heberlein, J., 1994. Analysis of the arc-cathode interaction of free-burning arcs. *Plasma Sources Sci. Technol.* 3, 564–574. <https://doi.org/10.1088/0963-0252/3/4/014>
- Zhu, P., Lowke, J.J., Morrow, R., 1992. A unified theory of free burning arcs, cathode sheaths and cathodes. *J. Phys. D: Appl. Phys.* 25, 1221–1230. <https://doi.org/10.1088/0022-3727/25/8/011>
- Zhu, P., Lowke, J.J., Morrow, R., Haidar, J., 1995. Prediction of anode temperatures of free burning arcs. *J. Phys. D: Appl. Phys.* 28, 1369–1376. <https://doi.org/10.1088/0022-3727/28/7/014>
- Zhukov, M.F., 1980. *Electric-Arc Plasmatrons*, 3rd ed. Inst. Teplofiziki, Academy of Sciences of the Soviet Union, Novosibirsk.
- Zhukov, M.F., 1972. Electric arc generators of low temperature plasma. *Thermophysics of High Temperature*, in Russian 10, 1295–1307.
- Zhukov, M.F., Anshakov, A.S., Zasyupkin, I.M., Kurochkin, Iu.V., Lukashov, V.P., Pustogarov, A.V., 1981. *Electric-arc generators with interelectrode inserts*. Nauka, Siberian Branch, Novosibirsk, in Russian.
- Zhukov, M.F., Zasyupkin, I.M., 2007. *Thermal Plasma Torches: Design, Characteristics, Application*. Cambridge Int Science Publishing.

## Annexes

---

Annex A. Argon plasma composition .....	168
Annex B. Argon plasma transport properties .....	171
Annex B.1. Electrical conductivity .....	171
Annex B.2. Thermal conductivity .....	172
Annex B.2.1. Electron translational thermal conductivity .....	172
Annex B.2.2. Heavy species translational thermal conductivity .....	172
Annex B.2.3. Reaction thermal conductivity .....	173
Annex B.2.4. Results of thermal conductivity computation .....	175
Annex B.3. Viscosity .....	176
Annex B.4. Collision integrals .....	177
Annex B.5. Basic data for collisions in argon .....	177
Annex B.6. Exchange coefficient .....	178
Annex B.7. Volumetric net radiation energy losses .....	179



## Annex A. Argon plasma composition

Following the method presented in (Fretton et al., 2012), the plasma composition is computed according to the Saha equation (4.1) given by the formulation of (van de Sanden and Schram, 1991), Dalton equation for pressure (4.2) and the electrical neutrality equation (4.3).

$$\frac{n_e \cdot n_h^{\zeta+}}{n_h^{(\zeta-1)+}} = 2 \cdot \left( \frac{2\pi m_e k_B T_e}{h_p^2} \right)^{3/2} \cdot \frac{Q_\zeta^{\text{int}}(T_e)}{Q_{\zeta-1}^{\text{int}}(T_e)} \cdot \exp\left(-\frac{E_\zeta - \delta E_\zeta}{kT_e}\right) \quad (4.1)$$

$$p = n_e k_B T_e + \sum_{\zeta=0}^N n_h^{\zeta+} k_B T_h \quad (4.2)$$

$$n_e = \sum_{\zeta=1}^N \zeta \cdot n_h^{\zeta+} \quad (4.3)$$

Where  $n_e$  and  $m_e$  are the electron number density and mass respectively;  $n_h^{\zeta+}$  and  $m_h^{\zeta+}$  the number density and mass of the ion  $Ar^{\zeta+}$ ;  $E_\zeta$  the ionization energy of the particle  $Ar^{(\zeta-1)+}$  to  $Ar^{\zeta+}$ ;  $k_B$  the Boltzmann constant;  $N$  the maximum ion charge in the plasma composition.

The first term in parentheses on the right-hand side of Saha equation (4.1) is the translational partition function which is evaluated over the volume available for the monoatomic particle (Drellishak et al., 1963). The internal partition function  $Q_\zeta^{\text{int}}(T_e)$  for the ion  $Ar^{\zeta+}$  is given by the formula (4.4).

$$Q_\zeta^{\text{int}}(T_e) = \sum_{i=0}^{\infty} g_i e^{-\varepsilon_i/kT_e} \quad (4.4)$$

Where  $g_i$  is the degeneracy factor of the energy level  $\varepsilon_i$ . The factor  $g_i$  is given by  $2J+1$ , where  $J$  is the total angular momentum quantum number. The data for the energy levels was obtained from (Kramida et al., 2018). The partitioning functions presented in (Drellishak et al., 1963) deviate from the NIST data in (Kramida et al., 2018) above 15000 K, and thus the plasma compositions obtained from these two different sources differ significantly above 20000 K. However, comparison of different sources and their effect on the plasma torch simulation is beyond the scope of this study, therefore we chose the most recent available data.

The lowering of the ionization energy  $\delta E_\zeta$  is given by formula (4.5) following (Hingana, 2010).

$$\delta E_\zeta = (\zeta + 1) \cdot 2.087 \cdot 10^{-11} \cdot \sqrt{\frac{n_e + \sum_{\zeta=0}^N \zeta^2 \cdot n_h^{\zeta+}}{T_e}} \quad (4.5)$$

During the computation of plasma composition the temperature step in the set of equations (4.1), (4.2) and (4.3) is 1 K. The initial temperature  $T_e$  in the computation is 300 K. The initial number densities of the ions are equal to unity per  $\text{m}^3$ . The maximum ion charge considered during the computation is dependent on the temperature, since the lower temperature, the

lower number density of each ion, and number densities lower than unity per  $\text{m}^3$  do not hold any statistical importance. Thus during the following temperature ranges were considered:

1. [300 K; 1700 K) the argon gas is considered as non-ionized, i.e. only  $\text{Ar}^0$ . The number densities  $n_h^{1+}$  to  $n_h^{4+}$  are equal  $1 \text{ m}^{-3}$ ;
2. [1700 K; 5000 K) with only atoms  $\text{Ar}^0$  and singly ionized particles  $\text{Ar}^+$ ,  $N = 1$ ;
3. [5000 K; 10000 K) the considered particles are  $\text{Ar}^0$ ,  $\text{Ar}^+$  and  $\text{Ar}^{2+}$ ,  $N = 2$ ;
4. [10000 K; 17000 K) where ion with maximum charge is  $\text{Ar}^{3+}$ ,  $N = 3$ ;
5. [17000 K; 35000 K) with the biggest set of particles:  $\text{Ar}^0$ ,  $\text{Ar}^+$ ,  $\text{Ar}^{2+}$ ,  $\text{Ar}^{3+}$ ,  $\text{Ar}^{4+}$ ,  $N = 4$ .

The plasma composition was computed for numerous ratios of temperatures  $\theta = T_e / T_h$ , more precisely [1.0; 1.1; 1.2; 1.3; 1.4; 1.5; 1.6; 1.7; 1.8; 2.0; 2.5; 3.0; 4.0; 5.0; 6.0; 7.0; 8.0; 9.0; 10.0; 12.0; 15.0; 17.0; 19.0; 21.0; 23.0; 25.0; 30.0]. Later in the simulation each cell of the computational domain is assigned with one of the presented values of  $\theta = T_e / T_h$ . The computed plasma composition for several values of  $\theta$  is illustrated in Figure 138. The plasma density computed similarly to the LTE model is given in Figure 139.

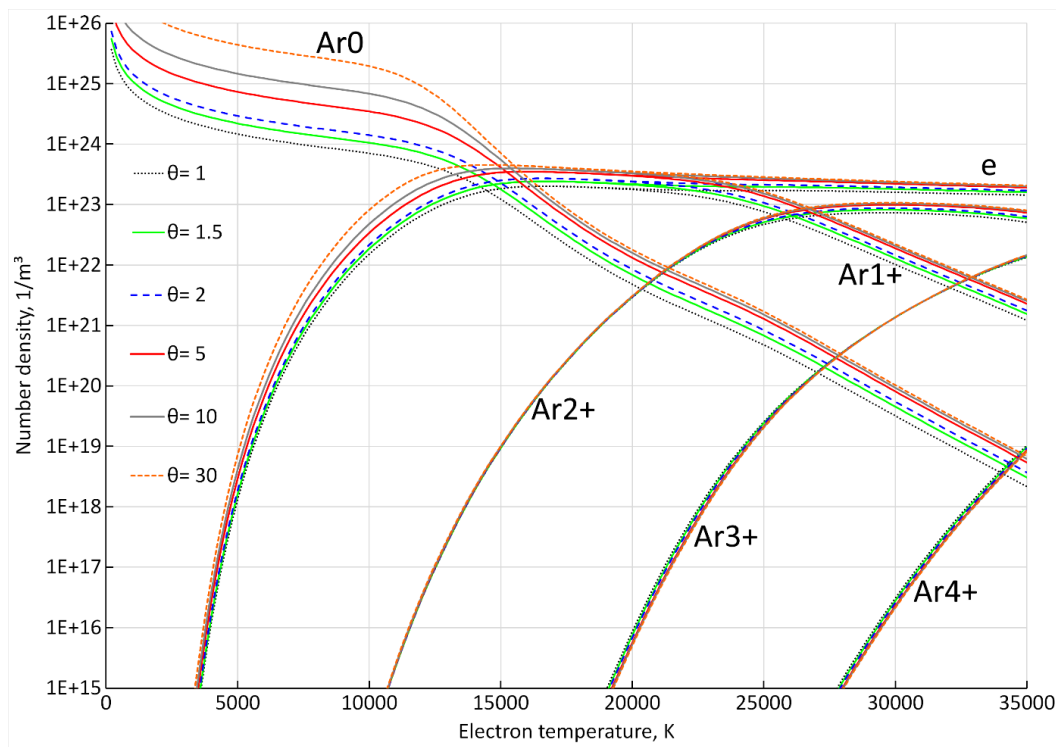


Figure 138 Computed 2T argon plasma composition

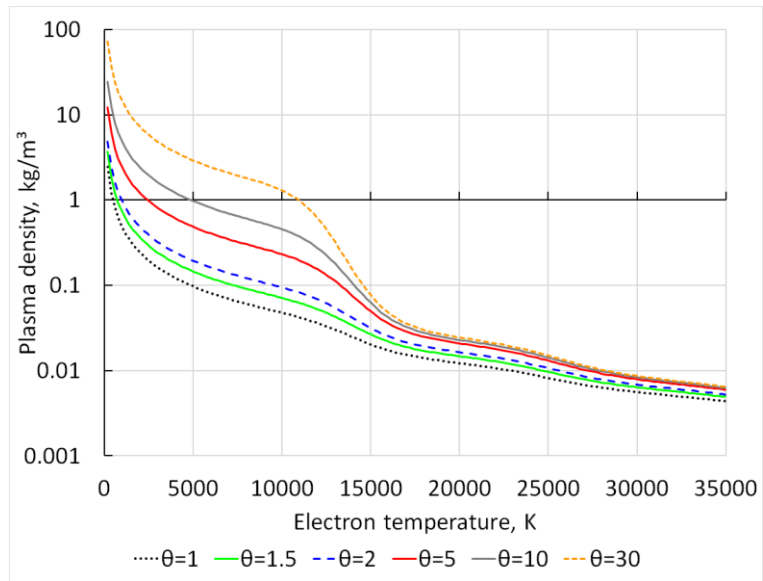


Figure 139 Computed 2T argon plasma density

## Annex B. Argon plasma transport properties

### Annex B.1. Electrical conductivity

The electrical conductivity is calculated according to the Bonnefoi's approach (Bonnefoi et al., 1983) that is initially based on the derivation given by Devoto (Devoto, 1965).

The electrical conductivity is calculated to the third order as follows:

$$\sigma = 3n_e^2 e^2 \left( \frac{\pi}{2m_e k_B T_e} \right)^{1/2} \frac{q^{11} q^{22} - (q^{12})^2}{D} \quad (4.6)$$

where  $D$  is the determinant  $D = \begin{vmatrix} q^{00} & q^{01} & q^{02} \\ q^{10} & q^{11} & q^{12} \\ q^{20} & q^{21} & q^{22} \end{vmatrix}$ .

The matrix elements  $q^{ij}$  found in the electrical conductivity are detailed below:

$$\begin{aligned} q^{00} &= 8n_e \sum_{i=2}^N n_i \bar{Q}_{ei}^{(1,1)} \\ q^{01} &= 8n_e \sum_{i=2}^N n_i \left( \frac{5}{2} \bar{Q}_{ei}^{(1,1)} - 3 \bar{Q}_{ei}^{(1,2)} \right) \\ q^{02} &= 8n_e \sum_{i=2}^N n_i \left( \frac{35}{8} \bar{Q}_{ei}^{(1,1)} - \frac{21}{2} \bar{Q}_{ei}^{(1,2)} + 6 \bar{Q}_{ei}^{(1,3)} \right) \\ q^{11} &= 8\sqrt{2} n_e^2 \bar{Q}_{ee}^{(2,2)} + 8n_e \sum_{i=2}^N n_i \left( \frac{25}{4} \bar{Q}_{ei}^{(1,1)} - 15 \bar{Q}_{ei}^{(1,2)} + 12 \bar{Q}_{ei}^{(1,3)} \right) \\ q^{12} &= 8\sqrt{2} n_e^2 \left( \frac{7}{4} \bar{Q}_{ee}^{(2,2)} - 2 \bar{Q}_{ee}^{(2,3)} \right) + 8n_e \sum_{i=2}^N n_i \left( \frac{175}{16} \bar{Q}_{ei}^{(1,1)} - \frac{315}{8} \bar{Q}_{ei}^{(1,2)} + 57 \bar{Q}_{ei}^{(1,3)} - 30 \bar{Q}_{ei}^{(1,4)} \right) \\ q^{22} &= 8\sqrt{2} n_e^2 \left( \frac{77}{18} \bar{Q}_{ee}^{(2,2)} - 2 \bar{Q}_{ee}^{(2,3)} + 5 \bar{Q}_{ee}^{(2,4)} \right) + \\ &+ 8n_e \sum_{i=2}^N n_i \left( \frac{1225}{64} \bar{Q}_{ei}^{(1,1)} - \frac{735}{8} \bar{Q}_{ei}^{(1,2)} + \frac{399}{2} \bar{Q}_{ei}^{(1,3)} - 210 \bar{Q}_{ei}^{(1,4)} + 90 \bar{Q}_{ei}^{(1,5)} \right) \end{aligned}$$

The index e stands for the electrons. Note that  $q^{ij} = q^{ji}$ .

The collision integrals  $\bar{Q}_{ij}^{(l,s)}$  will be defined below.

The electrical conductivity in the fluid phase is bounded from below as in (Bolot et al., 2011). The resulting expression for electrical conductivity is given by (4.7). The used infimum  $\sigma(3000K)$  of electrical conductivity was chosen in a series of simulations in order to mitigate the numerical fluctuations of electric potential in the periphery and enhance convergence. The computed argon plasma electrical conductivity is illustrated in Figure 140.

$$\sigma = \max(\sigma(3000K); \sigma(T)) \quad (4.7)$$

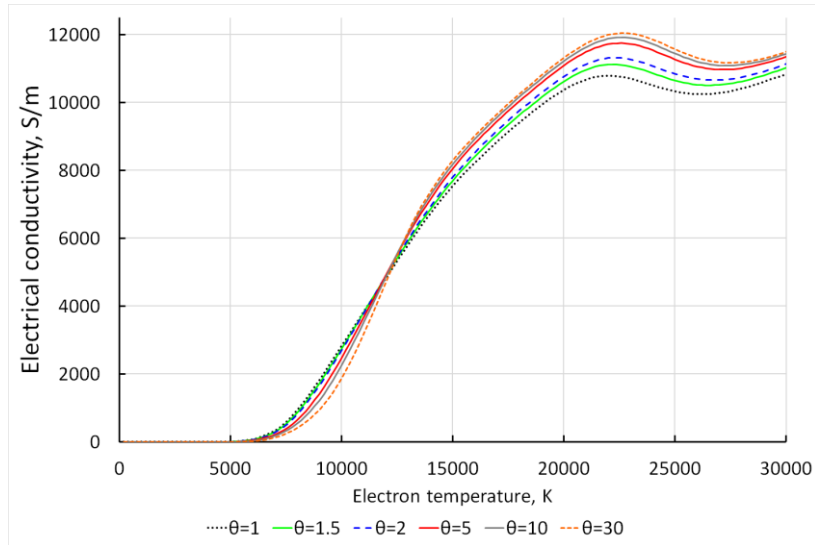


Figure 140 Electrical conductivity of argon plasma

## Annex B.2. Thermal conductivity

### Annex B.2.1. Electron translational thermal conductivity

The electron translational thermal conductivity is also given by the Bonnefoi's derivation as follows:

$$\lambda_e^{tr} = \frac{75}{8} n_e^2 k_B \left( \frac{2\pi k_B T_e}{m_e} \right)^{1/2} \frac{q^{22}}{q^{11} q^{22} - (q^{12})^2} \quad (4.8)$$

### Annex B.2.2. Heavy species translational thermal conductivity

The heavy species translational thermal conductivity is obtained to the second order given by (Muckenfuss and Curtiss, 1958) and detailed by (Cressault, 2001):

If N is the total number of species in the mixture, only the N-1 heavy species are considered within the summation of the next relationships:

$$\lambda_h^{tr} = 4 \frac{\begin{vmatrix} L_{11} & \dots & L_{1N} & X_1 \\ \vdots & L_{ii} & \vdots & \vdots \\ L_{N1} & \dots & L_{NN} & X_N \\ X_1 & \dots & X_N & 0 \end{vmatrix}}{\begin{vmatrix} L_{11} & \dots & L_{1N} \\ \vdots & L_{ii} & \vdots \\ L_{N1} & \dots & L_{NN} \end{vmatrix}} \quad (4.9)$$

The  $L_{ij}$  terms are given by (the  $k$  summation is made over heavy species only):

$$L_{ii} = -4 \frac{X_i^2}{K_{ii}} - \sum_{\substack{k=1 \\ k \neq i}}^{N-1} \left( \frac{2X_i X_k}{K_{ik}} \cdot \frac{1}{(M_i + M_k)^2} \cdot \frac{1}{A_{ik}^*} \cdot \left[ \frac{15}{2} M_i^2 + \frac{25}{4} M_k^2 - 3M_k^2 B_{ik}^* + 4M_i M_k A_{ik}^* \right] \right)$$

$$L_{ij} = \frac{2X_i X_j}{K_{ij}} \cdot \frac{M_i M_j}{(M_i + M_j)^2} \cdot \frac{1}{A_{ij}^*} \left[ \frac{55}{4} - 3B_{ij}^* - 4A_{ij}^* \right]$$

where  $X_i$  is the molar fraction of the species  $i$  and  $M_i$  is its molar mass ( $\text{g}\cdot\text{mol}^{-1}$ ).

$$K_{ij} = 8.3224 \times 10^{-2} \frac{\pi T_h^{1/2}}{\overline{Q_{ij}^{(2,2)}}} \left( \frac{M_i + M_j}{2M_i M_j} \right)^{1/2}$$

$$K_{ii} = 8.3224 \times 10^{-2} \frac{\pi T_h^{1/2}}{\overline{Q_{ii}^{(2,2)}}} \frac{1}{M_i^{1/2}}$$

$$A_{ij}^* = \frac{\overline{Q_{ij}^{(2,2)}}}{\overline{Q_{ij}^{(1,1)}}}$$

$$B_{ij}^* = \frac{5\overline{Q_{ij}^{(1,2)}} - 4\overline{Q_{ij}^{(1,3)}}}{\overline{Q_{ij}^{(1,1)}}}$$

The collision integrals  $\overline{Q_{ij}^{(l,s)}}$  are in  $\text{\AA}^2$  in the previous relationships.

### Annex B.2.3. Reaction thermal conductivity

The reaction thermal conductivity was calculated from the Bonnefoi's approach (Bonnefoi et al., 1983).

By definition, the reaction heat flux  $\vec{q}_R$  corresponds to the enthalpy brought by species during chemical reactions:

$$\vec{q}_R = \sum_{i=1}^N H_i \vec{\omega}_i = -\lambda_r \nabla T_e \quad (4.10)$$

where  $H_i$  and  $\vec{\omega}_i$  are respectively the molar enthalpy ( $\text{J/mol}$ ) and the molar flux ( $\text{mol/m}^2/\text{s}$ ) of species  $i$ .

The non-equilibrium parameter  $\theta = T_e / T_h$  is supposed to be constant so that  $\nabla T_e = \theta \nabla T_h$ .

The method consists in linking the molar flux  $\vec{\omega}_i$  to the partial pressure gradient  $\nabla p_i$  of species  $i$ . It implicitly implies that diffusion due to the total pressure and the external forces is neglected. The thermal diffusion is also supposed to be negligible.

Afterwards,  $\nabla p_i$  can be related to the temperature gradient  $\nabla T_e$  by the use of the two-temperature Saha law derived by van de Sanden (van de Sanden and Schram, 1991). This means that the choice made on the Saha law affects the reaction thermal conductivity. Bonnefoi used a 2T Saha law derived from Potapov's work (Potapov, 1966).

In the argon plasma, we consider 4 chemical reactions ( $k=1,2,3,4$ ) written with two dependent components, i.e. Ar and electron:

$$Ar^+ = Ar - e$$

$$Ar^{2+} = Ar - 2e$$

$$Ar^{3+} = Ar - 3e$$

$$Ar^{4+} = Ar - 3e$$

It can be written according to these 4 independent chemical reactions:

$$-\lambda_r \nabla T_e = \sum_{k=1}^4 \Delta H_k \vec{\omega}_k$$

where  $\Delta H_k$  is the reaction enthalpy of  $k^{\text{th}}$  chemical reaction above, and  $\vec{\omega}_k$  is the molar flux of the  $k^{\text{th}}$  independent species, i.e.  $Ar^+$ ,  $Ar^{2+}$ ,  $Ar^{3+}$  and  $Ar^{4+}$ .

The reaction enthalpies are:

$$\Delta H_1 = RT_e^2 \left( \frac{\partial \ln Q_{Ar}^{\text{int}}}{\partial T_e} - \frac{\partial \ln Q_{Ar^+}^{\text{int}}}{\partial T_e} \right) - E_{1+} - \frac{5}{2} RT_e$$

$$\Delta H_2 = RT_e^2 \left( \frac{\partial \ln Q_{Ar}^{\text{int}}}{\partial T_e} - \frac{\partial \ln Q_{Ar^{2+}}^{\text{int}}}{\partial T_e} \right) - E_{1+} - E_{2+} - \frac{5}{2} RT_e$$

$$\Delta H_3 = RT_e^2 \left( \frac{\partial \ln Q_{Ar}^{\text{int}}}{\partial T_e} - \frac{\partial \ln Q_{Ar^{3+}}^{\text{int}}}{\partial T_e} \right) - E_{1+} - E_{2+} - E_{3+} - \frac{5}{2} RT_e$$

$$\Delta H_4 = RT_e^2 \left( \frac{\partial \ln Q_{Ar}^{\text{int}}}{\partial T_e} - \frac{\partial \ln Q_{Ar^{4+}}^{\text{int}}}{\partial T_e} \right) - E_{1+} - E_{2+} - E_{3+} - E_{4+} - \frac{5}{2} RT_e$$

where  $Q_i^{\text{int}}$  is the internal partition function of the species  $i$ .  $E_{\zeta}$  is the ionization energy of the particle  $Ar^{(\zeta-1)+}$  to  $Ar^{\zeta+}$ . Note that the ionization potential lowering is not considered.

The derivation of the partial pressure gradient as a function of  $\nabla T_e$  by the use of the van de Sanden law gives:

$$\nabla p_e + \nabla p_{Ar^+} - \nabla p_{Ar} = -\frac{\Delta H_1}{RT_e^2} \nabla T_e$$

$$2\nabla p_e + \nabla p_{Ar^{2+}} - \nabla p_{Ar} = -\frac{\Delta H_2}{RT_e^2} \nabla T_e$$

$$3\nabla p_e + \nabla p_{Ar^{3+}} - \nabla p_{Ar} = -\frac{\Delta H_3}{RT_e^2} \nabla T_e$$

$$4\nabla p_e + \nabla p_{Ar^{4+}} - \nabla p_{Ar} = -\frac{\Delta H_4}{RT_e^2} \nabla T_e$$

Following the Bonnefoi's derivation, the reaction thermal conductivity is then:

$$\lambda_r = -\frac{1}{RT_e^2} \frac{\begin{vmatrix} 0 & \Delta H_1 & \dots & \Delta H_4 \\ -\Delta H_1 & A_{11} & \dots & A_{14} \\ \vdots & \vdots & A_{ij} & \vdots \\ -\Delta H_4 & A_{41} & \dots & A_{44} \end{vmatrix}}{\begin{vmatrix} A_{11} & \dots & A_{14} \\ \vdots & A_{ij} & \vdots \\ A_{41} & \dots & A_{44} \end{vmatrix}}$$

where  $A_{ij}$  the matrix elements derived from (Bonnetoi et al., 1983).

The total thermal conductivity in LTE case is  $\lambda = \lambda_e^{tr} + \lambda_h^{tr} + \lambda_r$ . The internal thermal conductivity is neglected.

#### Annex B.2.4. Results of thermal conductivity computation

The computed thermal conductivity component of argon plasma are illustrated in Figure 142, Figure 143 and Figure 140.

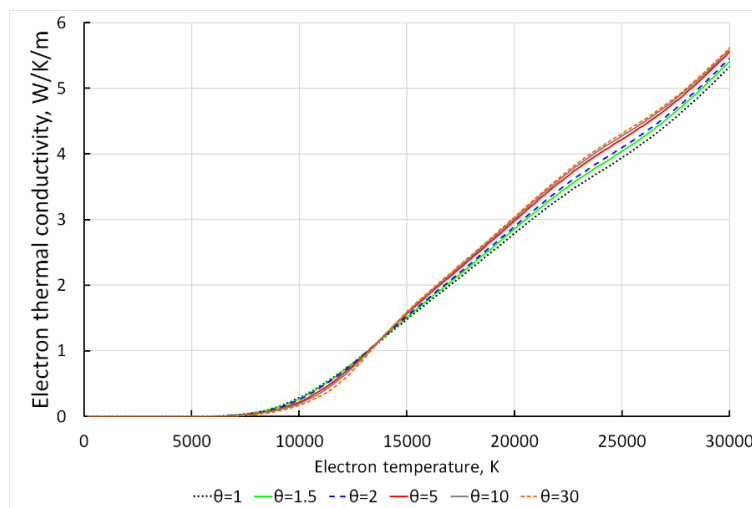


Figure 141 Electron thermal conductivity of argon plasma

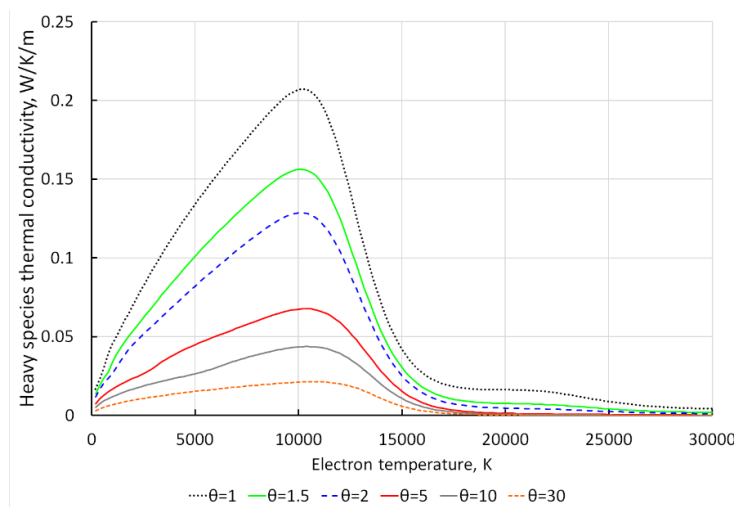


Figure 142 Heavy species thermal conductivity of argon plasma



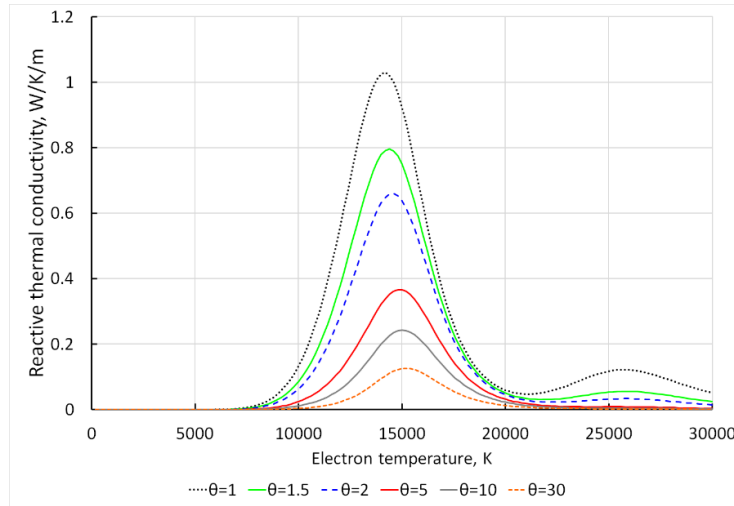


Figure 143 Reactive thermal conductivity of argon plasma

### Annex B.3. Viscosity

The viscosity  $\mu$  is calculated to the first order as shown by (Hirschfelder et al., 1964) and also detailed by (Cressault, 2001). As for the heavy species translational thermal conductivity, the contribution of the electrons to the viscosity is neglected. The results for the viscosity computation are illustrated in Figure 144.

$$\mu = - \frac{\begin{vmatrix} H_{11} & \dots & H_{1N} & X_1 \\ \vdots & H_{ii} & \vdots & \vdots \\ H_{N1} & \dots & H_{NN} & X_N \\ X_1 & \dots & X_N & 0 \end{vmatrix}}{\begin{vmatrix} H_{11} & \dots & H_{1N} \\ \vdots & H_{ii} & \vdots \\ H_{N1} & \dots & H_{NN} \end{vmatrix}} \quad (4.11)$$

$$H_{ii} = \frac{X_i^2}{\mu_i} + \sum_{\substack{k=1 \\ k \neq i}}^{N-1} \left( \frac{2X_i X_k}{\mu_{ik}} \cdot \frac{M_i M_k}{(M_i + M_k)^2} \cdot \left[ \frac{5}{3A_{ik}^*} + \frac{M_k}{M_i} \right] \right)$$

$$H_{ij} = - \frac{2X_i X_j}{\mu_{ij}} \cdot \frac{M_i M_j}{(M_i + M_j)^2} \cdot \left[ \frac{5}{3A_{ij}^*} - 1 \right]$$

$$\mu_i = 2.6693 \times 10^{-6} \frac{\pi (M_i T_h)^{1/2}}{\bar{Q}_{ii}^{(2,2)}}$$

$$\mu_{ij} = 2.6693 \times 10^{-6} \frac{\pi \left( \frac{M_i M_j}{M_i + M_j} T_h \right)^{1/2}}{\bar{Q}_{ij}^{(2,2)}}$$

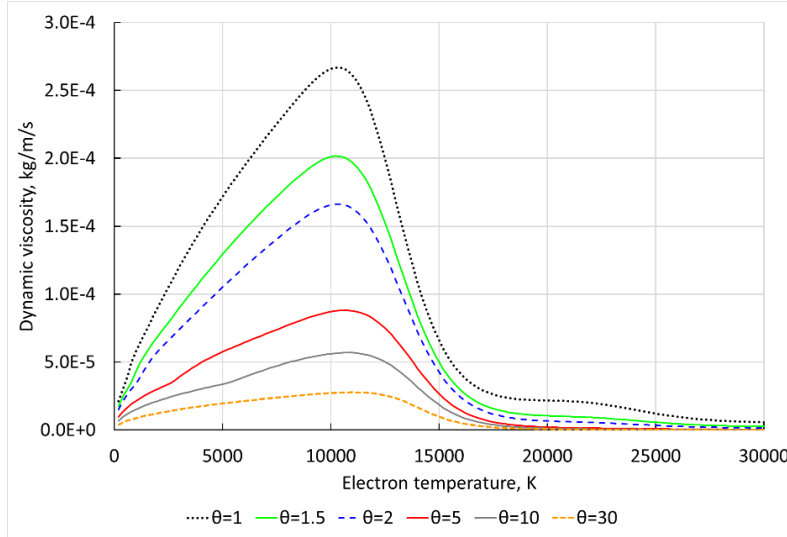


Figure 144 Dynamic viscosity of argon plasma

### Annex B.4. Collision integrals

The collision integral  $\bar{Q}_{ij}^{(l,s)}$  are defined by:

$$\bar{Q}_{ij}^{(l,s)} = \frac{4(l+1)}{(s+1)!(2l+1-(-1)^l)} \int_0^{+\infty} e^{-\gamma^2} \gamma^{2s+3} Q_{ij}^{(l)} d\gamma \quad (4.12)$$

where  $\gamma = \frac{\mu_{ij} g^2}{2k_B T^*}$ ,  $\mu_{ij} = \frac{m_i m_j}{m_i + m_j}$  is the reduced mass,  $g$  is the relative speed between species  $i$  and  $j$  when colliding and  $T^*$  an effective temperature.

When an electron is involved within a collision  $T^* = T_e$ , otherwise  $T^* = T_h$ . This implies that the collision integrals are only function of  $T_e$  when an electron is involved. In other cases, the collisions integrals depends on  $T_h$ . This assumption is backed by the fact that the electrons have much higher kinetic energy than the heavy species so that any electron/heavy species collision is ruled by the temperature  $T_e$ .

The quantities  $Q_{ij}^{(l)}$  are transport cross section defined by Hirschfelder (Hirschfelder et al., 1964) and depends on interaction potentials of the  $ij$  collision.

### Annex B.5. Basic data for collisions in argon

For the Ar-Ar collision, we use the polynomial fitting for the collision integrals  $\bar{Q}_{ArAr}^{(l,s)}$  ( $l=1,2$  and  $s=1,2,3$ ) given in (Aubretton and Fauchais, 1983) which was extended to higher temperatures than 15 000 K.

Aubretton and Fauchais also permit to properly evaluate the e-Ar collision integrals  $\bar{Q}_{eAr}^{(l,s)}$  ( $l=1,2$  and  $s=1,2,3,4,5$ ).

The Ar-ArZ<sup>+</sup> charge transfer collision integrals results from the polynomial fitting of Aubretton and Fauchais for the couples  $(l, s) = (1, 1)$  and  $(l, s) = (2, 2)$ . For the couples  $(1, 1)$  and  $(1, 3)$ , the collision integrals were recalculated from the formula given in (Devoto, 1967) and fitted with a polynomial approximation for subsequent use.

The collision integrals between charged species were basically obtained from (Mason et al., 1967) and (Devoto, 1973). Note that this calculation requires the prior knowledge of the electron number density since it relies on a screened Coulomb potential involving the Debye length. As recommended in (Murphy, 2000), the latter only considers the electrons  $\lambda_D = (\epsilon_0 k_B T_e / e^2 n_e)^{1/2}$ .

### Annex B.6. Exchange coefficient

The exchange coefficient  $K_{exchange}$  is computed by the formula (4.13). The exchange term is not allowed to be negative because the negative exchange term would mean an energy transfer from a heavy and slow particle to electron which is much lighter and still faster. Thus the exchange term is considered to be zero in case when  $T_e < T_h$ .

$$K_{exchange} = \sum_{\zeta=0}^N \frac{2}{3} \cdot \left( \frac{2m_h^{\zeta+} + m_e}{(2m_h^{\zeta+} + m_e)^2} \right) k_B n_e v_{eh}^{\zeta+} \delta_{eh}^{\zeta+} \quad (4.13)$$

Where  $\delta_{eh}^{\zeta+}$  is the inelastic collision factor which is assumed to be equal to 1 for monoatomic gas.  $v_{eh}^{\zeta+}$  is the collision frequency between electrons and atoms or ions with charge  $\zeta +$ .

The computed exchange term  $Q_{exchange}$  for some values of  $\theta = T_e / T_h$  as a function of  $T_e$  is illustrated in Figure 145.

The collision frequency between atoms and electrons  $v_{eh}^0$  is calculated by the formula (4.14).

$$v_{eh}^0 = n_h^0 \sqrt{\frac{8k_B T_e}{\pi m_e}} \overline{Q_{eh}^0} \quad (4.14)$$

Where  $\overline{Q_{eh}^0}$  is a mean elastic cross section which is calculated by the formula (4.15).

$$\begin{aligned} \overline{Q_{eh}^0} &= \frac{2}{3} \int_0^\infty \left( \frac{m_{eh} (v_e - v_{Ar})^2}{2k_B T} \right)^2 \exp\left( -\frac{m_{eh} (v_e - v_{Ar})^2}{2k_B T} \right) Q_{eh}^0 (|v_e - v_{Ar}|) d \frac{m_{eh} (v_e - v_{Ar})^2}{2k_B T} \\ x &= \frac{E}{k_B T} = \frac{m_{eh} g^2}{2k_B T} = \frac{m_{eh} (v_e - v_{Ar})^2}{2k_B T} \\ \overline{Q_{eh}^0} &= \frac{3}{2} \int_0^\infty x^2 e^{-x} Q_{eh}^0 \left( \sqrt{\frac{2k_B T}{m_{eh}}} x \right) dx \end{aligned} \quad (4.15)$$

Where  $m_{eh} = \frac{m_e m_{Ar}}{m_e + m_{Ar}} \approx m_e$  is the reduced mass of the considered two-body collision.

$Q_{eh}^0(|v_e - v_{Ar}|)$  is the elastic momentum transfer cross section which is a function of the relative speed  $|v_e - v_{Ar}|$ . The elastic momentum transfer cross section is usually found as a function of the collision energy and was taken from the Biagi-v7.1 (Magboltz version 7.1) database (Biagi, 2004).

The collision frequency between ions and electrons is given by the formula (4.16) taken from (Mitchner and Kruger, 1973).

$$v_{eh}^{\zeta+} = n_h^{\zeta+} \frac{4\sqrt{2\pi}}{3} \left( \frac{m_e}{k_B T_e} \right)^{3/2} \left( \frac{\zeta e^2}{4\pi\epsilon_0 m_e} \right)^2 \ln\Lambda \quad (4.16)$$

Where  $\ln\Lambda = \frac{\lambda_D}{b_0}$ ,  $\lambda_D = \left( \frac{\epsilon_0 k_B T_e}{n_e e^2} \right)^{1/2}$  and  $b_0 = \frac{\zeta e^2}{12\pi\epsilon_0 k_B T_e}$ .

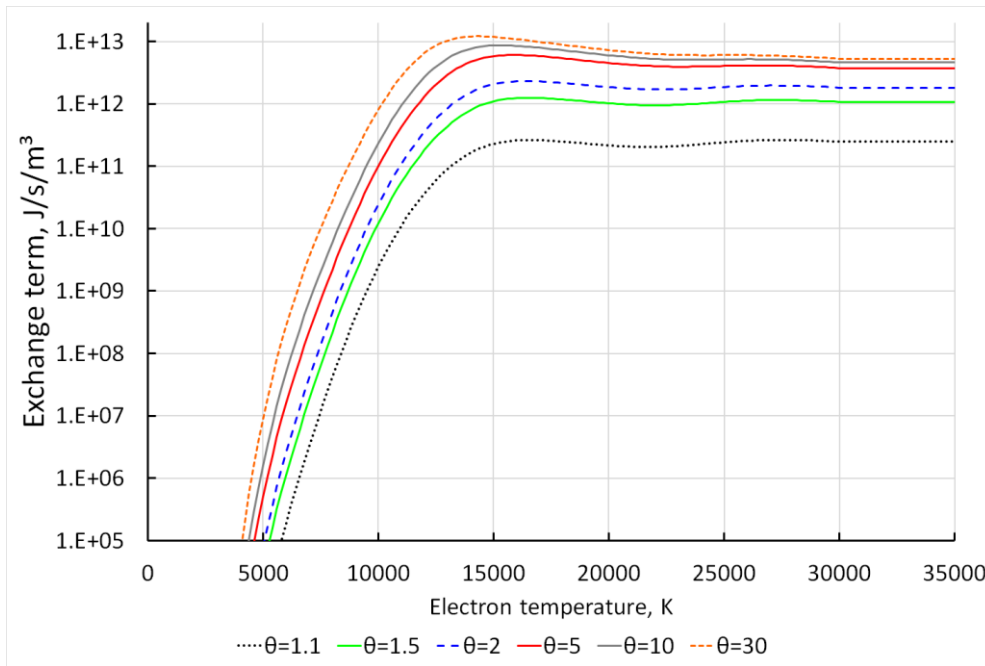


Figure 145 Computed exchange term used in the 2T model

## Annex B.7. Volumetric net radiation energy losses

The volumetric net radiation energy losses  $Q_R$  for argon plasma is taken from (Beulens et al., 1991) by analogy with (Trelles, 2007) and computed according to the formula (4.17). The same values are used in the LTE and 2T models in order to have proper comparison of the results. The temperature dependency of the radiation losses is shown in Figure 146.

$$Q_R = 53.759 \cdot \frac{n_0}{10^{24}} \cdot \left( \frac{n_e}{10^{20}} \right)^{1.25} + 910 \cdot \left( \frac{n_e}{10^{20}} \right)^2 + 2572 \cdot \left( \frac{n_e}{10^{20}} \right)^{1.57} \quad (4.17)$$

Where  $n_0$  and  $n_e$  are number densities given in  $m^{-3}$ . The value  $Q_R$  is given in  $W/m^3$ .

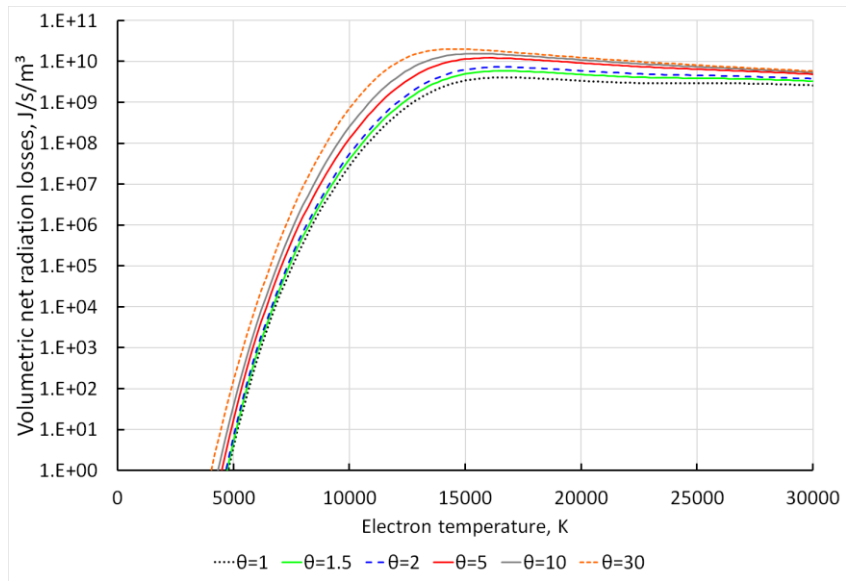


Figure 146 Volumetric net radiation energy losses of argon plasma

## List of Illustrations

---

Figure 1: Schematic drawing of a typical conventional plasma spray gun (Fauchais et al., 2014).....	19
Figure 2: Examples of conic tip cathodes erosion in F4 plasma torch (by courtesy of IRCER, University of Limoges).....	27
Figure 3: Examples of anode erosion with 600 A, 45 NLPM of argon plus 15 NLPM of H <sub>2</sub> (Planche, 1995).....	28
Figure 4 E-I characteristics of the arc in the initial section of the channel of plasma torch with stabilized arc length. Air, nozzle diameter 30 mm, gas flow rate 1) 36 g/s; 2) 70 g/s; 3) 84 g/s; 4) calculated for 36 g/s (Zhukov and Zasytkin, 2007).....	29
Figure 5: The simplest electric arc: straight discharge between two pin-type electrodes.....	33
Figure 6: Principle diagram of the shunting of the electric arc in the channel of a plasma torch.....	40
Figure 7 Anode arc attachment modes: restrike mode 100 A, 12/40 slpm of Ar/He; take-over mode 500 A, 40/20 slm of Ar/He; steady mode 900 A, 60 slm of Ar (Duan, 2000).....	42
Figure 8 Fluctuations of arc voltage and pressure in the cathode cavity for 600A and Ar-H <sub>2</sub> 45-6 slm (Rat and Coudert, 2010b).....	44
Figure 9 Time sweep of raw signal of pressure and voltage and their decomposition into several components with different frequencies (Rat and Coudert, 2011).....	45
Figure 10 Torch with a mounted acoustic stub (Rat and Coudert, 2010a).....	46
Figure 11 Plasma torch with sudden expansion of the anode diameter and arc length smaller than in the conventional plasma torch. (Zhukov and Zasytkin, 2007).....	47
Figure 12 Plasma torch with inter-electrode insert and arc length greater than in the conventional plasma torch. 1: cathode, 2: anode, 3: inter-electrode insert, G <sub>0</sub> is the flow rate of the injected plasma-forming gas. (Zhukov and Zasytkin, 2007).....	48
Figure 13 Electric arc photographs in a long cylindrical channel. a) the arc in the initial section of the gas flow; b) random oscillations of the arc in the transition section; c) arc-arc shunting; d) splitting of the arc (Zhukov and Zasytkin, 2007).....	48
Figure 14 Plasma torch with cascaded anode and arcing between the neutrodes (Ramakrishnan, 1995).....	49
Figure 15 Example of the Lorentz force created by an axial external magnetic field in the arc in a conventional DC plasma torch. Black lines and black arrows represent the electric current lines. Red arrows represent the Lorentz force. The absolute values of electric current density and Lorentz force are not presented.....	51
Figure 16 Time sweep of arc luminosity with external magnetic field in the plasma torch with interelectrode inserts. Current intensity of 160 A, pressure of 10 <sup>5</sup> Pa and 10 <sup>4</sup> Pa (Zhukov et al., 1981).....	51
Figure 17 LTE argon plasma enthalpy as a function of temperature.....	68
Figure 18 Computed heavy species and electron enthalpy in the <b>2T(I)</b> model.....	71

Figure 19 Computed heavy species and electron enthalpy in the <b>2T(II)</b> model .....	71
Figure 20 Lines and continuum radiation shares in argon plasma (Erraki, 1999) .....	72
Figure 21 Translation of electron enthalpy to electron temperature in the 2T(I) model.....	75
Figure 22 Translation of heavy species enthalpy to heavy species temperature in the 2T(I) model .....	75
Figure 23 Simulated plasma torch SinplexPro™ manufactured by Oerlikon Metco. 1 is a ceramic electrode insulator. 2 is a gas injector ring. ....	76
Figure 24 Comparison of the arc voltage time sweeps in the LTE model for time steps of $1 \cdot 10^{-7}$ s and $1 \cdot 10^{-8}$ s. Arc current of 500 A, gas flow rate of 60 NLPM. The anode and cathode sheath voltage drops are not taken into account.....	77
Figure 25 Computational domain of the model .....	78
Figure 26 Example of model of constricted transferred arc for which the checkerboard order oscillations may appear in the outlet tank. The distributions below are given for the red cross section.....	79
Figure 27 Example of checkerboard order oscillations of plasma and velocity.....	79
Figure 28 Mesh near the cathode tip. Cells in grey are a part of the cathode. ....	80
Figure 29 Mesh at the torch nozzle exit. Cells in grey are a part of the anode. ....	81
Figure 30 Mesh at the outlet tank. Size of the cells in the periphery of the outlet tank is 0.8 mm. ....	81
Figure 31 Relative fluctuations of the input mass flow rate. The rough mesh has a cell size of 4 mm in the periphery; the fine mesh has a cell size of 0.8 mm.....	82
Figure 32 Relative fluctuations of the spatial mean total pressure. The rough mesh has a cell size of 4 mm in the periphery; the fine mesh has a cell size of 0.8 mm.....	82
Figure 33 Boundary conditions of the <b>LTE</b> model .....	83
Figure 34 Boundary conditions of <b>2T(I)</b> and <b>2T(II)</b> models .....	84
Figure 35 Magnetic vector potential stream lines inside the plasma torch in the LTE model .	86
Figure 36 Electric current density stream lines inside the plasma torch in the LTE model ....	86
Figure 37 Divergence of magnetic vector potential .....	87
Figure 38 Magnetic vector potential stream lines at the “bottleneck” of the computational domain where the magnetic vector potential is far from being constant .....	88
Figure 39 Derivative of magnetic vector potential $\frac{\partial A_y}{\partial y}$ .....	88
Figure 40 Derivative of magnetic vector potential $\frac{\partial A_z}{\partial z}$ .....	89
Figure 41 Example of a cross shape of the cathode arc attachment that appears in case of improper initialization of the boundary condition for magnetic vector potential.....	90

Figure 42 Computed distribution of magnitude of the boundary condition for the magnetic vector potential.....	90
Figure 43 Temperature discontinuity in LTE model in the case without the custom fluid-electrodes coupling .....	92
Figure 44 External and internal boundaries of the computational domain. The internal boundaries are used in the fluid-electrode coupling.....	92
Figure 45 Temperature distribution at the cathode tip in LTE model in the case with the custom fluid-electrodes coupling .....	93
Figure 46 Two-cell case considered at every face of the electrode-fluid interface.....	93
Figure 47 Distribution of the MPI rank of parallel subdomains. Discontinuity of the parallel subdomain at the fluid-electrode interface which raises the problem of the fluid-electrode coupling in multiple-processor computation .....	95
Figure 48 Artificial electrical conductivity (0-195-0 S/m) domain behind the anode arc attachment intended to mimic the disequilibrium effect.....	98
Figure 49 Computed magnetic field with the <b>BS</b> boundary condition for magnetic vector potential. 500 A and 60 NLPM of argon.....	104
Figure 50 Computed magnetic field with the <b>PVNF</b> boundary condition for magnetic vector potential. 500 A and 60 NLPM of argon.....	104
Figure 51 Computed velocity distribution with the <b>PVNF</b> boundary condition for magnetic vector potential. 500 A and 60 NLPM of argon .....	104
Figure 52 Computed temperature distribution with the <b>PVNF</b> boundary condition for magnetic vector potential. 500 A and 60 NLPM of argon .....	104
Figure 53 LTE arc voltage fluctuations for the BS and PVNF boundary conditions for the magnetic vector potential. 500 A and 60 NLPM of argon. Sheath voltage drops are not included in the predicted arc voltage .....	105
Figure 54 Computed electric current density with the <b>BS</b> boundary condition for magnetic vector potential. 500 A and 60 NLPM of argon .....	105
Figure 55 Computed electric current density with the <b>PVNF</b> boundary condition for magnetic vector potential. 500 A and 60 NLPM of argon .....	106
Figure 56 Electric current density profile predicted by the LTE model with electrodes. 500 A and 60 NLPM of argon .....	106
Figure 57 Predicted temperature distribution on the cathode tip with the LTE model. 500 A and 60 NLPM of argon .....	107
Figure 58 Photos of worn cathodes of the of the SinplexPro™ plasma torch with molten patterns on the top surface. The cathodes were used for extended period of time with various parameters (courtesy of Oerlikon Metco (US) Inc.).....	107
Figure 59 SinplexPro™ cathodes erosion after 5 minutes and 60 minutes of operation with 500 A and 60 NLPM of argon (courtesy of Oerlikon Metco (US) Inc.) .....	107



Figure 60 Cathode and anode electrode temperature predicted by the LTE model after 10 ms of operation with a stable angular position of the anode arc attachment. 500 A and 60 NLPM of argon.....	108
Figure 61 Computed magnetic field without electrodes with the BS boundary condition for the magnetic vector potential and without the electrodes in the computational domain .....	108
Figure 62 Computed electric current density with the BS boundary condition for the magnetic vector potential and without the electrodes in the computational domain.....	109
Figure 63 Computed velocity distribution inside the plasma torch with the BS boundary condition for the magnetic vector potential. <b>Without</b> the electrodes in the computational domain. 500 A and 60 NLPM of argon.....	109
Figure 64 Computed velocity distribution inside the plasma torch with the BS boundary condition for the magnetic vector potential. <b>With</b> the electrodes in the computational domain. 500 A and 60 NLPM of argon .....	109
Figure 65 Computed temperature distribution inside the plasma torch with the BS boundary condition for the magnetic vector potential. <b>Without</b> electrodes in the computational domain. 500 A and 60 NLPM of argon .....	110
Figure 66 Computed temperature distribution inside the plasma torch with the BS boundary condition for the magnetic vector potential. <b>With</b> electrodes in the computational domain. 500 A and 60 NLPM of argon .....	110
Figure 67 Instantaneous electric current streamlines in the LTE model for 500 A, 60 NLPM of argon and BS boundary condition for the magnetic vector potential .....	111
Figure 68 Instantaneous electric current streamlines and distribution on the anode surface for 500 A, 60 NLPM of argon and BS boundary condition for the magnetic vector potential.....	111
Figure 69 Electric current streamlines at the cathode tip for 500 A, 60 NLPM of argon and BS boundary condition for the magnetic vector potential.....	112
Figure 70 Joule power distribution for 500 A, 60 NLPM of argon and BS boundary condition for the magnetic vector potential.....	112
Figure 71 Instantaneous computed temperature distribution in LTE model for 500 A, 60 NLPM of argon and BS boundary condition for the magnetic vector potential.....	112
Figure 72 Electric current streamlines and constricting Lorentz force vectors near the cathode tip.....	113
Figure 73 Pressure gradient near the cathode tip in the direction perpendicular to the torch axis.....	113
Figure 74 Lorentz force near the cathode tip in the direction perpendicular to the torch axis. ....	113
Figure 75 Instantaneous computed plasma velocity in the LTE model for 500 A, 60 NLPM of argon and BS boundary condition for the magnetic vector potential .....	114
Figure 76 Velocity streamlines in the LTE model for 500 A, 60 NLPM of argon and BS boundary condition for the magnetic vector potential.....	114
Figure 77 Instantaneous distributions of the enthalpy flux [ $J/m^2/s$ ] and mass flux [ $kg/m^2/s$ ] at the nozzle exit .....	114

Figure 78 Full arc voltage time sweep in the LTE model with anode and cathode sheath voltage drops. The experimental voltage is $76.5 \pm 4$ V.....	115
Figure 79 Velocity streamlines with a gas injection angle of $10^\circ$ .....	117
Figure 80 Velocity streamlines with a gas injection angle of $25^\circ$ .....	117
Figure 81 Velocity streamlines with a gas injection angle of $45^\circ$ .....	118
Figure 82 Time-azimuthal distribution of the electric current density on the anode surface plotted over time. Without swirling gas injection and without external magnetic field. ....	118
Figure 83 Time-azimuthal distribution of the electric current density on the anode surface. The swirling gas injection angle is $10^\circ$ .....	119
Figure 84 Time-azimuthal distribution of the electric current density on the anode surface. The swirling gas injection angle is $25^\circ$ .....	119
Figure 85 Photos of worn anodes with the arc traces parallel to the torch axis. The anode were used for extended period of time with various parameters (courtesy of Oerlikon Metco (US) Inc.).....	120
Figure 86 Electric current lines and temperature distribution on surface of anode and cathode at several times with a $25^\circ$ swirling gas injection. ....	120
Figure 87 Time-azimuthal distribution of the electric current density on the anode surface. The swirling gas injection angle is $45^\circ$ .....	121
Figure 88 Circumferential velocity of the anode arc attachment as a function of the gas injection angle .....	122
Figure 89 Maximum anode temperature as a function of the gas injection angle .....	122
Figure 90 External magnetic field streamlines created by a coil around the torch.....	123
Figure 91 Electric current streamlines in the computational domain and boundary value of electric current density on the electrode surface for an external magnetic field of <b>0.05 T</b> and time step of <b><math>10^{-8}</math> s</b> .....	123
Figure 92 Lorentz force exerted on the plasma shown by the electric current streamlines for an external magnetic field of <b>0.05 T</b> and time step of <b><math>10^{-8}</math> s</b> .....	124
Figure 93 Time-azimuthal distribution of the electric current density on the anode surface for an external magnetic field of <b>0.01 T</b> and time step of <b><math>10^{-7}</math> s</b> .....	125
Figure 94 Velocity streamlines for an external magnetic field of <b>0.01 T</b> and time step of <b><math>10^{-7}</math> s</b> .....	125
Figure 95 Time-azimuthal distribution of the electric current density on the anode surface for an external magnetic field of <b>0.03 T</b> and time step of <b><math>10^{-7}</math> s</b> .....	126
Figure 96 Time-azimuthal distribution of the electric current density on the anode surface for an external magnetic field of <b>0.03 T</b> and time step of <b><math>10^{-8}</math> s</b> .....	127
Figure 97 Time-azimuthal distribution of the electric current density on the anode surface for an external magnetic field of <b>0.05 T</b> and time step of <b><math>10^{-7}</math> s</b> .....	128
Figure 98 Velocity streamlines for an external magnetic field of <b>0.05 T</b> and time step of <b><math>10^{-7}</math> s</b> .....	128

Figure 99 Time-azimuthal distribution of the electric current density on the anode surface for an external magnetic field of <b>0.05 T</b> and time step of <b><math>10^{-8}</math> s</b> .....	129
Figure 100 Velocity streamlines for an external magnetic field of <b>0.05 T</b> and time step of <b><math>10^{-8}</math> s</b> .....	129
Figure 101 Time-azimuthal distribution of the electric current density on the anode surface for an external magnetic field of <b>0.1 T</b> and time step of <b><math>10^{-8}</math> s</b> .....	130
Figure 102 Velocity streamlines for an external magnetic field of <b>0.1 T</b> and time step of <b><math>10^{-8}</math> s</b> .....	130
Figure 103 Swirl numbers at the channel center and nozzle exit for various values of the external magnetic field.....	131
Figure 104 Circumferential velocity of the anode arc attachment as a function of the external magnetic field.....	131
Figure 105 Maximum anode temperature as a function of the external magnetic field.....	132
Figure 106 Computed electric current density streamlines in the <b>2T(I)</b> model for 500 A and 60 NLPM of argon.....	133
Figure 107 Computed electric current lines in the <b>2T(II)</b> model for 500 A and 60 NLPM of argon.....	133
Figure 108 Electric current density profiles at the cathode tip predicted by the 2T(I), 2T(II) and LTE models with 500 A and 60 NLPM of argon.....	134
Figure 109 Predicted temperature distribution on the cathode tip in the 2T(II) model with 500 A and 60 NLPM of argon.....	134
Figure 110 Joule power in the 2T(I) and 2T(II) models for 500 A and 60 NLPM of argon....	134
Figure 111 Computed electron temperature $T_e$ at the axial cross section in <b>2T(I)</b> model ....	135
Figure 112 Computed heavy species temperature $T_h$ at the axial cross section in <b>2T(I)</b> model.....	135
Figure 113 Computed $T_e$ and $T_h$ distribution at the nozzle exit in <b>2T(I)</b> model.....	135
Figure 114 Recomputed $\theta=T_e/T_h$ in the <b>2T(I)</b> model after the governing equations are solved.....	136
Figure 115 Comparison of the various thermal energy terms in the <b>2T(I)</b> model along the torch axis.....	136
Figure 116 Recomputed $\theta=T_e/T_h$ in the <b>2T(I)</b> model along the torch axis.....	136
Figure 117 Computed electron temperature $T_e$ in the axial cross section with the <b>2T(II)</b> model.....	137
Figure 118 Computed heavy species temperature $T_h$ in the axial cross section with the <b>2T(II)</b> model.....	137
Figure 119 Computed $T_e$ and $T_h$ distribution at the nozzle exit with the <b>2T(II)</b> model.....	138
Figure 120 Recomputed $\theta=T_e/T_h$ in the <b>2T(II)</b> model after the governing equations are solved.....	138

Figure 121 Comparison of the various thermal energy terms in the <b>2T(II)</b> model along the torch axis.....	139
Figure 122 Recomputed $\theta=T_e/T_h$ in the <b>2T(II)</b> model along the torch axis .....	139
Figure 123 Recomputed $\theta=T_e/T_h$ in the <b>2T(I)</b> model with <b>200 A</b> and <b>60 NLPM</b> of argon after the governing equations are solved .....	139
Figure 124 Electron temperature in the <b>2T(I)</b> model with <b>200 A</b> and <b>60 NLPM</b> of argon .....	139
Figure 125 Recomputed $\theta=T_e/T_h$ in the <b>2T(II)</b> model with <b>200 A</b> and <b>60 NLPM</b> of argon after the governing equations are solved .....	140
Figure 126 Electron temperature in the <b>2T(II)</b> model with <b>200 A</b> and <b>60 NLPM</b> of argon ....	140
Figure 127 Plasma velocity distribution in the axial cross section predicted by the <b>2T(I)</b> model .....	141
Figure 128 Plasma velocity distribution in the axial cross section predicted by the <b>2T(II)</b> model .....	141
Figure 129 Plasma velocity distribution at the nozzle exit predicted by the 2T(I) and 2T(II) models .....	141
Figure 130 Comparison of the experimental and predicted full arc voltage with the LTE model for various arc current intensity and gas flow rates .....	142
Figure 131 Comparison of the experimental and predicted cooling loss with the LTE model for various arc current intensity and gas flow rates .....	142
Figure 132 Predicted electric current density on the anode surface with the 2T(II) model. 500 A and 60 NLPM of argon. Most of the electric current density is concentrated on the upstream edge .....	144
Figure 133 SinplexPro™ anode erosion on the upstream edge <b>after 5 minutes</b> of operation with 500 A and 60 NLPM of argon. (courtesy of Oerlikon Metco (US) Inc.).....	144
Figure 134 SinplexPro™ anode erosion on the upstream edge <b>after 60 minutes</b> of operation with 500 A and 60 NLPM of argon. (courtesy of Oerlikon Metco (US) Inc.).....	144
Figure 135 Comparison of the arc voltage time sweeps predicted by the 2T models and LTE model. With anode and cathode sheath voltage drops. The experimental voltage is $76.5\pm 4$ V. ....	145
Figure 136 Comparison of the experimental voltage with predicted full voltage with the LTE, 2T(I) and 2T(II) models for various current intensity and <b>60 NLPM</b> of argon.....	145
Figure 137 Comparison of the experimental voltage with the predicted full voltage in LTE and 2T(II) models for various arc current intensity and <b>120 NLPM</b> of argon .....	146
Figure 138 Computed 2T argon plasma composition .....	169
Figure 139 Computed 2T argon plasma density .....	170
Figure 140 Electrical conductivity of argon plasma .....	172
Figure 141 Electron thermal conductivity of argon plasma.....	175
Figure 142 Heavy species thermal conductivity of argon plasma.....	175
Figure 143 Reactive thermal conductivity of argon plasma.....	176

Figure 144 Dynamic viscosity of argon plasma.....	177
Figure 145 Computed exchange term used in the 2T model.....	179
Figure 146 Volumetric net radiation energy losses of argon plasma .....	180

## List of Tables

---

Table 1: Characteristics of some recent models of plasma torches .....	54
Table 2: Swirl numbers in different parts of the torch for various gas injection angles .....	121
Table 3: Swirl numbers in different parts of the torch for various values of the external magnetic field .....	131



## Towards a reliable numerical model of DC plasma spray torch

La projection plasma est une technologie de dépôt qui utilise un jet de plasma pour accélérer, chauffer, fondre et déposer des particules de poudre sur un substrat et ainsi, élaborer un revêtement. La reproductibilité du procédé dépend en grande part des fluctuations d'enthalpie et de vitesse du jet de plasma et de l'usure des électrodes. Les torches à plasma à anode cascadée permettent une longueur d'arc stabilisée et ainsi d'atteindre le premier objectif. Cependant, leur géométrie ne garantit pas l'absence d'érosion des électrodes. L'étude des processus électromagnétiques et thermiques à l'intérieur de la torche peut aider à contrôler les propriétés du jet de plasma et à réduire l'érosion des électrodes, et en particulier de l'anode. Ce travail porte sur la simulation d'une à plasma commerciale (la torche SinplexPro™ d'Oerlikon Metco) fonctionnant à l'argon sous pression atmosphérique. Il a été mené en deux étapes. La première a consisté à développer un modèle à l'équilibre thermodynamique local (ETL) du comportement dynamique de l'arc dans la torche. La tension d'arc et les pertes thermiques de la torche prédites par ce modèle sont en bon accord avec celles mesurées pour un faible débit de gaz et un courant électrique élevé. Pour de telles conditions de fonctionnement, le modèle prédit un pied d'arc constricté à l'anode. Le modèle ETL a ensuite été utilisé pour tester deux méthodes pour faire tourner le pied d'arc sur la paroi de l'anode: une injection du gaz en vortex et un champ magnétique externe axial. L'injection du gaz avec un angle de 45° tourbillonnaire s'est avérée plus efficace qu'avec l'angle de 25° actuellement utilisé sur ce type de torche. La seconde étape de ce travail a consisté à développer un modèle à deux températures. Ce modèle considère deux formulations pour l'enthalpie des électrons et celle des espèces lourdes, qui diffèrent par l'attribution de l'énergie d'ionisation à l'une ou l'autre des particules. Le modèle 2T avec les deux formulations prédit un pied d'arc diffus à l'anode et des tensions d'arc en bon accord avec les valeurs expérimentales pour une large plage de courant et de débit de gaz. Le mode diffus du pied d'arc anodique semble confirmé par l'observation d'anodes usées ayant fonctionné dans les mêmes conditions. La formulation de l'équation de l'énergie avec l'énergie d'ionisation assignée aux électrons a un coût de calcul acceptable et présente des résultats plus raisonnables en termes de température des électrons et des espèces lourdes. Cette formulation sera utilisée pour le développement ultérieur du modèle et son extension à des gaz diatomiques.

Mots-clés: torche plasma, arc électrique, électrode, modèle à l'ETL et à 2T, simulation numérique  
**Towards a reliable numerical model of DC plasma spray torch operation**

DC plasma spraying is a coating technology that utilizes the energy of a plasma flow to accelerate, heat up, melt and deposit the coating powder on a substrate. For a high reproducibility in coating production, the plasma flow should have low fluctuations of enthalpy and velocity, and the erosion of electrodes should be limited. Plasma torches with a cascaded anode yield a more stabilized arc length and could achieve the first goal. However, a stabilized arc does not guarantee a low erosion rate of electrodes and in particular anode. An insight into the electromagnetic and thermal processes inside the plasma torch could help to control the properties of the plasma flow issuing from the torch and extend the lifetime of the torch parts. This work dealt with the simulation of the commercial plasma torch SinplexPro™ manufactured by Oerlikon Metco operated in argon under atmospheric pressure. It involved two steps. The first consisted in developing a LTE model with the inclusion of the electrodes in the computational domain. The arc voltage and cooling loss predicted by this model were in good agreement with the experimental values for a low gas flow rate and high electric current. For such operation conditions, the model predicted a constricted anode arc attachment. Then, two methods were tested to rotate the constricted anode arc attachment: gas swirling injection and axial external magnetic field. The swirling gas injection was found to be more efficient for a gas injection angle of 45° than for an angle of 25°, which is the angle used in the actual plasma torch. The second step of this study was about the development of a two-temperature model. The latter considered two formulations for the enthalpy of electrons and heavy species differing in the attribution of the ionization energy to electrons or heavy species. The 2T model with both formulations projected a diffuse anode arc attachment and arc voltage that agreed with the experimental values for a wider range of arc current and gas flow rate. The mode of anode arc attachment was confirmed by the observation of tested anodes. The formulation of the energy equation with the ionization energy assigned to the electrons had an acceptable computational cost and yielded reasonable results in terms of electron and heavy species temperature. It will be used to develop further the model and apply it to diatomic gases.

Keywords: plasma torch, electric arc, electrode, LTE model, 2T model, numerical simulation

